Astronomy Unit
School of Physics and Astronomy
Queen Mary University of London

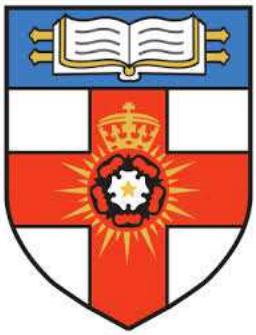

Simulations of Electron Kinetics in Solar Wind Turbulence

Christopher Thomas Haynes

July 2014

Submitted in partial fulfillment of the requirements of the Degree of Doctor of Philosophy

Declaration

I, Christopher Thomas Haynes, confirm that the research included within this thesis is my own work or that where it has been carried out in collaboration with, or supported by others, that this is duly acknowledged below and my contribution indicated. Previously published material is also acknowledged below.

I attest that I have exercised reasonable care to ensure that the work is original, and does not to the best of my knowledge break any UK law, infringe any third party's copyright or other Intellectual Property Right, or contain any confidential material.

I accept that the College has the right to use plagiarism detection software to check the electronic version of the thesis.

I confirm that this thesis has not been previously submitted for the award of a degree by this or any other university.

The work in this thesis resulted from collaborations with David Burgess, Enrico Camporeale, and Torbjorn Sundberg.

The results presented in Chapter 4 have been published in the article:
C. T. Haynes, D. Burgess, and E. Camporeale (2014), Reconnection and electron temperature anisotropy in sub-proton scale plasma turbulence, *The Astrophysical Journal*, Volume 783, Number 1, 38.

Christopher Thomas Haynes
Date: 30/6/2014

Abstract

Solar wind plasma is a turbulent medium, with processes that operate on many scales. Observations below proton scales are rare. Future spacecraft missions will have the required resolution to make these observations, so theoretical experiments and simulations at these scales will become increasingly important in order to match observations to theory. In this thesis, kinetic simulations are used to study electron dynamics within a turbulent electron-proton plasma.

Firstly in this thesis, a study of the formation of electron temperature anisotropy due to magnetic reconnection is presented using particle in cell (PIC) simulations of the turbulent decay of sub-proton scale fluctuations. A fluctuation power spectrum with approximately power law form down to scales of order the electron gyroradius is formed. The signatures of collisionless reconnection within the turbulent field are generally associated with regions of strong parallel electron temperature anisotropy. Electrons from spatially different locations, can mix at reconnection sites, generating multi-peaked velocity distribution functions, which could become unstable to further instabilities. This is evidence of an important role for reconnection in the dissipation of small scale turbulent fluctuations.

Secondly, a new type of electron scale vortex is discussed, which can spontaneously form during the simulations of turbulence. These are generated by electrons in (quasi) trapped orbits, which diamagnetically reduce the local magnetic field, creating a coherent structure. The properties of these vortices are categorized and compared to observations of similar structures called "magnetic holes" observed within the Earth's plasma sheet.

Finally, we look to understand what dissipation is in a collisionless plasma. We examine signatures of dissipation in the previous simulations, and in simulations where electrostatic electron-electron beam modes are generated within the turbulence.

Acknowledgements

I would like to sincerely thank Prof. David Burgess for all the guidance he has provided me with, over that last few years. I hope that all those knocks on your office door with random questions were not too distracting! (That's if I could find your office, given all the building works going on!) I've always found our talks very useful, and your more relaxed attitude to supervision let me thrive.

I also have to thank all the wonderful friends I've made over my PhD years. Far too many to name them all, but some deserve special mention: Arianna, Meike, Pavlos, Elena and the rest of the gang. Exotic names from wonderful far away lands! Thankyou for always putting a smile on my face, and I hope to visit you all soon.

To my old flatmate, Stephen. Your never ending patience with my antics is thoroughly appreciated, and your kitten fostering idea was simply inspired!!! May the fourth live on as a glorious tradition.

Roman. A true inspiration during the last three years, and a great friend. I hope we will continue to have many great adventures together and a cheeky Laphroaig from time to time.

Last but by no means least, to my family: Mum, Dad, Ant, and Fluffy (where would I be without therapeutic cat cuddles?) You have always been the best family I could ever have hoped for, kind, caring, patient and always supportive. This hard work is all for you.

This work was supported by the Science and Technology Facilities Council (STFC).

Contents

List of Figures

List of Tables

1. Introduction

1.1. The solar wind

The solar corona is the outermost layer of the solar atmosphere, consisting of high temperature ($\sim 1 \times 10^6$ K) plasma with structures, such as loops, which are due to the magnetic field. Parker [1958] proposed that the solar corona could not be in static equilibrium with interplanetary space, and predicted it must have a steady flow of plasma coming out from it, which we call the solar wind. Using the equations of hydrodynamics, he derived the following solar wind equation:

$$\left(v - \frac{c_s^2}{v}\right)\frac{dv}{dr} = \frac{2c_s^2}{r} - \frac{GM_\odot}{r^2}. \tag{1.1}$$

If we define the critical radius, r_c, as the radius where the solar wind velocity, v, equals the sound speed, c_s, then we find $r_c = \dfrac{GM_\odot}{2c_s^2}$. Solar wind speeds at radii below r_c are sub-sonic, and are supersonic beyond it. r_c is predicted to lie at $\sim 5R_\odot$, where $R_\odot$ is the solar radius. This expression for r_c can be used to rewrite Eq. 1.1 as:

$$\left(v - \frac{c_s^2}{v}\right)\frac{dv}{dr} = \frac{2c_s^2}{r^2}(r - r_c). \tag{1.2}$$

Solutions to this separable ODE, using different boundary conditions, are shown in Fig. 1.1. The red lines represent mathematical solutions to Eq. 1.2 that are non-physical, as they have two values of velocity at a specific radius. The green lines show physical solutions where the wind speed close to the Sun is assumed to be supersonic, which does not match solar wind observations. The remaining grey and blue lines are possible solutions. The blue line represents a set of solutions that are never supersonic and have slowly decreasing speed with radial distance, which also does not match observations. The solution suggested by Parker (the dark grey line) has an increasing solar wind expansion speed with radial distance from the Sun, and the rate of increase becomes smaller with distance. Beyond another radius, known as the Alfvén critical point, r_A, the solar wind expansion speed becomes faster than

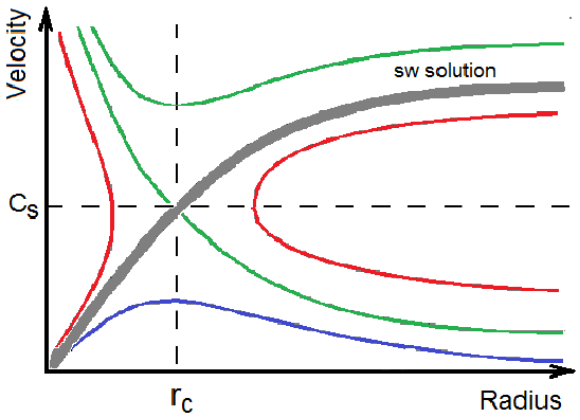

Figure 1.1.: Solutions to Parker's solar wind equation (Eq. 1.2).

the Alfvén wave speed, and the flow becomes "super-Alfvénic." This distance is predicted to be further out from the Sun than r_c at $\sim 13R_\odot$ (Verdini et al. [2009]).

The solar wind drags the interplanetary magnetic field (IMF) out with it as it travels away from the Sun, due to the high conductivity, high R_m flow (R_m is the magnetic Reynolds number), and it interacts with the planets of the solar system whether they have a magnetic field or not. Planets with dipolar magnetic fields, such as the Earth, dynamically interact with the solar wind, creating localised magnetospheres around them. The solar wind plasma is shocked around the Earth, defining the magnetopause as the boundary between the solar wind and magnetospheric plasma. The magnetosphere extends out on the nightside to form a geomagnetic tail, and the bow shock lies ahead of the magnetosphere in the supersonic solar wind.

The solar wind expands until it reaches the outer edges of the solar system, where it interacts with the interstellar medium (ISM), which fills the space between stars in our galaxy. The radial velocity of the solar wind plasma eventually slows to zero due to the external pressure of this medium, and this defines the heliopause as the boundary between the solar wind and ISM. Since the solar wind travels away from the Sun in all directions, the heliosphere can be thought of as a bubble carved out by the solar wind, with the heliopause marking the boundary of the Sun's (plasma) influence in the galaxy.

Observations of the solar wind began with the Soviet Union's Luna-1 probe, launched in 1959. The probe measured a continual outflow of ions/plasma from the sunward direction, confirming the existence of the solar wind, and Parker's theory. Since then, many observations have been made of the solar wind, mainly in the ecliptic plane, due to the smaller number of spacecraft that have been sent into

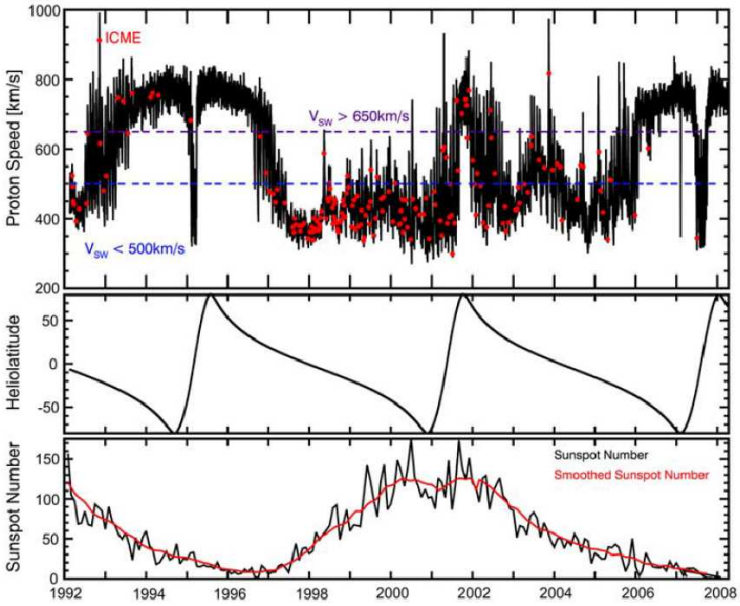

Figure 1.2.: Measurements of the fast and slow solar wind by the Ulysees spacecraft. (Figure from Ebert et al. [2009].)

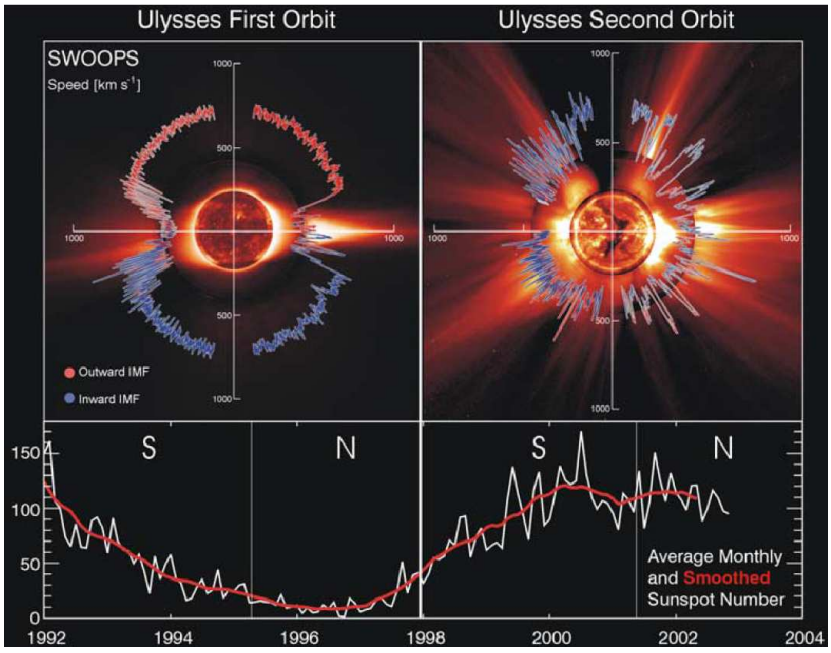

Figure 1.3.: Polar plots of solar wind speed as a function of latitude for Ulysses' first two orbits. (Figure from [McComas et al., 2003].)

an out of ecliptic orbit. The solar wind was found to be composed of two main states; a "fast" and "slow" wind, as shown in Fig. 1.2. The top panel shows proton speed, and areas of fast and slow wind are easily identifiable. The slow wind has a speed of $\sim 350\,\mathrm{km\,s^{-1}}$ whereas the fast wind has a speed of $\sim 750\,\mathrm{km\,s^{-1}}$. A table

of typical solar wind parameters at 1 au is shown in Table 1.1. Derived solar wind

Wind Parameter	Slow wind	Fast wind
number density	$\sim 15\,\mathrm{cm}^{-3}$	$\sim 4\,\mathrm{cm}^{-3}$
bulk velocity	$\sim 350\,\mathrm{km\,s}^{-1}$	$\sim 600\,\mathrm{km\,s}^{-1}$
proton temperature	$\sim 5 \times 10^4\,\mathrm{K}$	$\sim 2 \times 10^5\,\mathrm{K}$
electron temperature	$\sim 2 \times 10^5\,\mathrm{K}$	$\sim 1 \times 10^5\,\mathrm{K}$
magnetic field	$\sim 6\,\mathrm{nT}$	$\sim 6\,\mathrm{nT}$

Table 1.1.: Typical solar wind parameters at 1 au. (Data from Bruno and Carbone [2013].)

parameters can be calculated from the above values (Table 1.2). The fast and slow

Derived parameter	Slow wind	Fast wind
Alfvén Speed	$\sim 30\,\mathrm{km\,s}^{-1}$	$\sim 60\,\mathrm{km\,s}^{-1}$
proton thermal speed	$\sim 20\,\mathrm{km\,s}^{-1}$	$\sim 40\,\mathrm{km\,s}^{-1}$
electron thermal speed	$\sim 1700\,\mathrm{km\,s}^{-1}$	$\sim 1200\,\mathrm{km\,s}^{-1}$
proton cyclotron frequency	$\sim 0.1\,\mathrm{Hz}$	$\sim 0.1\,\mathrm{Hz}$
electron cyclotron frequency	$\sim 2 \times 10^2\,\mathrm{Hz}$	$\sim 2 \times 10^2\,\mathrm{Hz}$
Debye length	$\sim 8\,\mathrm{m}$	$\sim 11\,\mathrm{m}$
proton gyroradius	$\sim 35\,\mathrm{km}$	$\sim 70\,\mathrm{km}$
electron gyroradius	$\sim 2\,\mathrm{km}$	$\sim 1\,\mathrm{km}$

Table 1.2.: Derived solar wind parameters at 1 au using values from Table 1.1.

wind originate from different regions of the Sun. The different regions correspond to open field line regions, where the fast wind is observed, or regions dominated by loops (closed field lines), associated with the slow wind. In terms of latitude, the fast wind is generally considered to originate from the polar regions of the Sun, from coronal holes, whereas the slow wind originates from lower latitudes. The correlation between "fast" wind speeds and high heliolatitude is clearly visible in Fig. 1.2.

Coronal holes (and therefore the fast wind) are almost always present at the polar regions of the Sun, unlike Coronal holes at lower latitudes, which are generally only seen during solar maximum. Figure 1.3 shows solar wind speed, as measured by Ulysses, on a polar plot as a function of latitude for solar minimum (left hand panel) and solar maximum (right hand panel). The left hand panel shows that the fast wind is confined to high latitudes during solar minimum. The right hand panel shows that the distinction between fast and slow wind is much less defined at solar maximum.

Due to the anticlockwise rotation of the Sun, the IMF is wound up into a spiral shape, known as the Parker spiral, as shown in Fig. 1.4. The solar wind expands

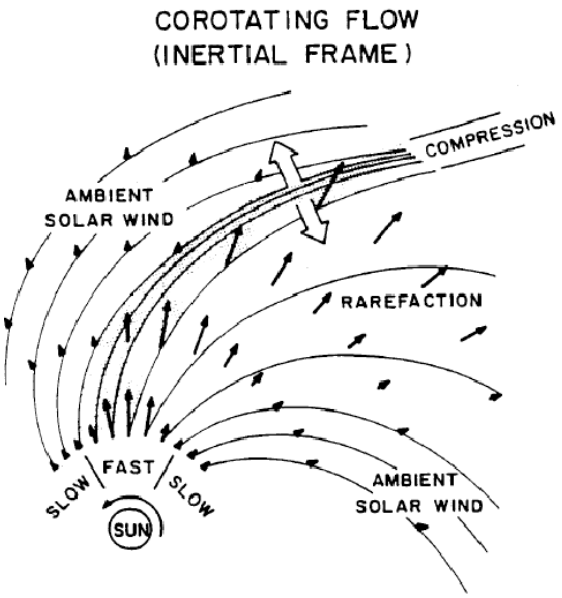

Figure 1.4.: Fast and slow wind interaction in the ecliptic plane. (Figure from [Gosling and Pizzo, 1999].)

radially, but the fast and slow components interact with each other as they flow out causing more structure. The relative speeds of the fast and slow winds result in areas of compression and rarefaction in solar wind density (Fig. 1.4). These are called co-rotating interaction regions (CIRs) and like the IMF, they rotate anti-clockwise with the Sun. The differential flows in the CIRs can lead to instabilities, such as the Kelvin-Helmholtz instability (KHI) [Karimabadi et al., 2013], as well as shocks, heating and turbulence.

The theory provided by Parker predicts that an adiabatic expansion of the solar wind from the corona should have a consequent decrease in proton temperature, but observations in the inner and outer solar system show that the actual decrease in temperature is less than expected. This suggests that another source of heating is present in the solar wind as it expands. The current scientific consensus is that turbulence provides this extra heating mechanism. Turbulence will be covered in Chapter 2. However, the turbulent heating of the plasma cannot be due to viscosity, because the solar wind is effectively collisionless. In the time the solar wind takes to travel from the Sun to the radius of Earth's orbit at 1 au, there will only have been one collision between protons, so the heating must come from another collisionless process, such as wave damping.

The absence of collisions results in the evolution of non-Maxwellian features in solar wind velocity distribution functions (VDFs), such as beams, relative streaming of components, and temperature anisotropies. Figure 1.5 shows examples of proton

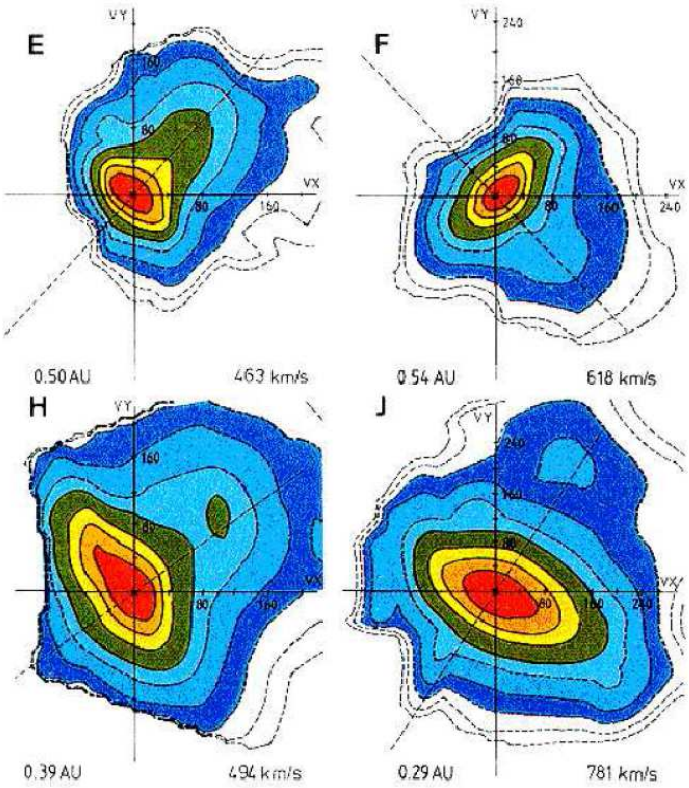

Figure 1.5.: Proton VDFs in the solar wind. (Figure from Marsch [2006].)

velocity distributions (VDFs) in the fast and slow wind. The beam-like features are clearly visible. Marsch et al. [1982] analysed proton temperature anisotropies in the fast and slow solar wind as a function of radius. The slow solar wind was observed to have $T_{\perp p} < T_{\parallel p}$, where $T_{\perp p}$ is perpendicular proton temperature, and $T_{\parallel p}$ is parallel proton temperature. The fast wind has the opposite temperature anisotropy with $T_{\perp p} > T_{\parallel p}$.

The processes that control the shape of these VDFs must be plasma instabilities and the affects of solar wind expansion. The main parameters governing plasma (ion) instabilities are, the plasma β, temperature anisotropy $\dfrac{T_{\perp p}}{T_{\parallel p}}$, and the relative drift speeds of any beam populations. Careful analysis of these parameters in solar wind measurements can link observations back to linear theory, which states that deviations from isotropic Maxwellian distributions should be sources of free energy for instabilities and wave generation.

Hellinger et al. [2006] used data from the Helios spacecraft to plot the relative observation frequencies of $(\beta_{\parallel p}, T_{\perp p}/T_{\parallel p})$ for the fast and slow wind. Figure 1.6 shows that the observations all lie outside but close to the contours of the linear stability thresholds. (Note, the fast wind data contained beam populations, so only the main

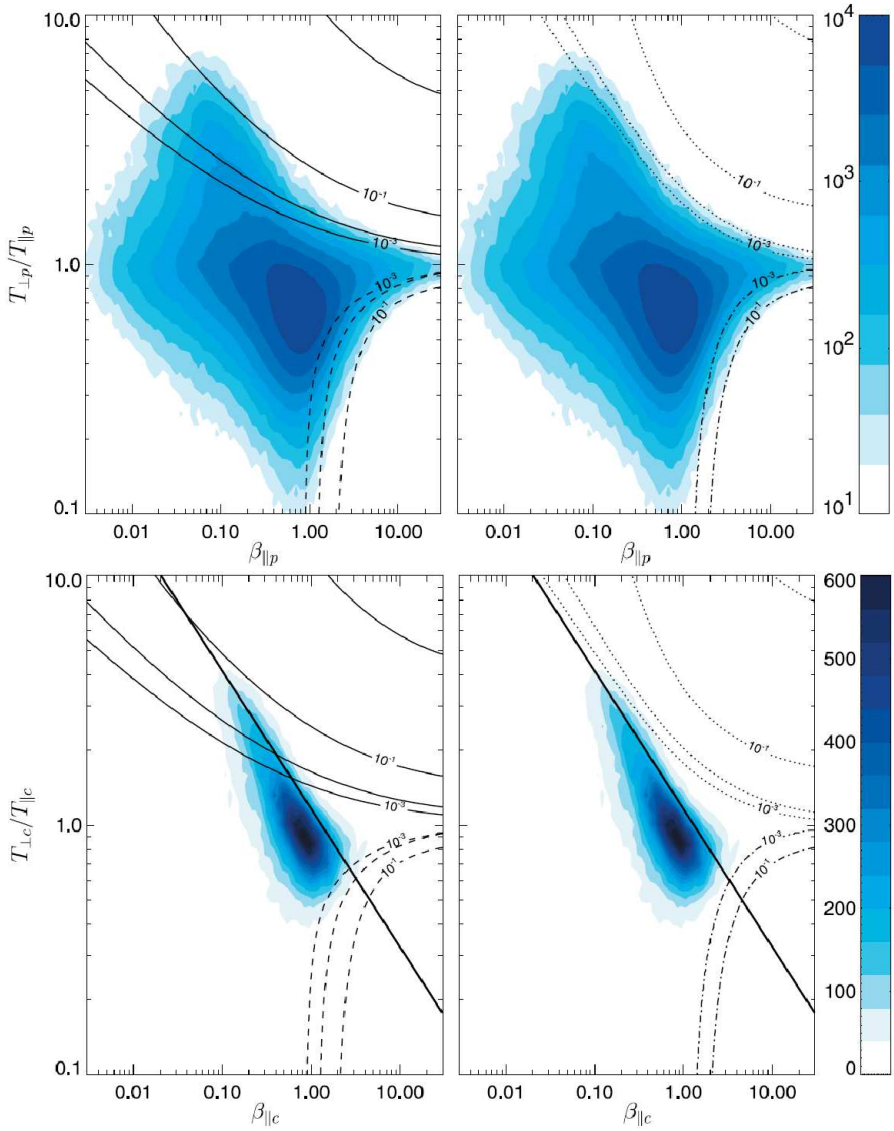

Figure 1.6.: Relative observation frequencies for the solar wind. The upper panels show slow wind data, and the lower panels show fast wind data. The left panels shows proton cyclotron instability (solid) and the parallel firehose thresholds (dashed). The right panels shows the mirror mode thresholds (dotted) and oblique firehose thresholds (dashed-dot). The black line shows a similar trend found by Marsch et al. [2004]. (Figure from Hellinger et al. [2006].)

core was used when measuring fast wind temperature.) The instability thresholds plotted in the right hand panel seem to better constrain the observations, indicating that both the fast and slow solar wind are constrained by the proton mirror mode and oblique firehose instabilities.

Matteini et al. [2007] expanded on this work by examining the radial evolution of the observations. They showed that both the oblique and parallel firehose in-

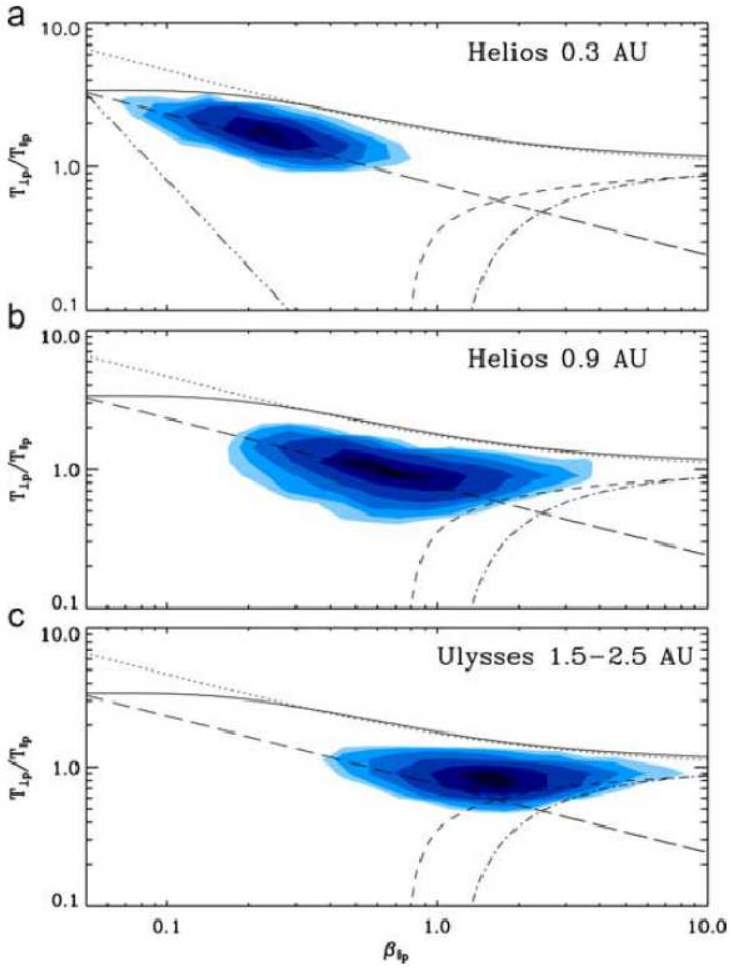

Figure 1.7.: Relative observation frequencies vs radial distance for the fast solar wind. Instability thresholds are shown for the ion-cyclotron (solid), the mirror (dotted), the parallel (dashed), and the oblique (dash-dotted) firehose instabilities. In Panel (a) the dash-dot-dot-dotted straight line refers to the adiabatic prediction. (Figure from Matteini et al. [2007].)

stabilities appear to constrain the observations as distance from the Sun increases (Fig. 1.7). This work also shows how the plasma temperature evolves in the expanding solar wind. Theoretical models of an adiabatic expansion of the solar wind, assuming no parallel heat flux and the conservation of magnetic moment, predict that temperature anisotropy should evolve radially as $T_{\perp p}/T_{\parallel p} \propto r^{-2}$. Therefore if the temperature of the plasma (at the Sun) is initially isotropic, then it should become anisotropic if the expansion is collisionless. This prediction is indicated by the dash-dot-dot-dotted line in Fig. 1.7(a). The observations form a shallower slope (larger dashed line) than this prediction, indicating that the ions have experienced perpendicular heating. Further evidence of (turbulent) perpendicular heating is provided from measurements by the Helios spacecraft in high speed streams, showing

that average magnetic moment increases with radial distance (Fig. 1.8).

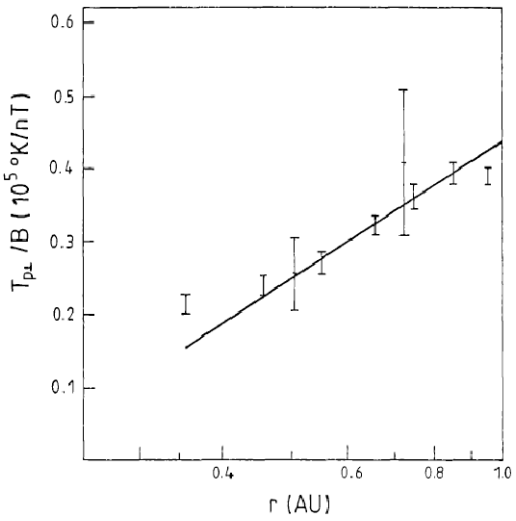

Figure 1.8.: Average magnetic moment against radial distance from the Helios spacecraft in high speed streams (Figure from Marsch [1991].)

The VDFs of electrons in the solar wind also have non-Maxwellian features. An example electron velocity distribution function is shown in Fig. 1.9. The electron VDF has a structure containing three components; the core, halo and strahl. The core represents the main distribution of electrons. The strahl is a high energy field aligned beam. The halo is a separate distribution that is at higher energy than the other two components. As with the ion instabilities, the electron VDFs appear to be constrained by electron instabilities. For example the electron firehose instability (EFI), which generates waves when $T_{\|e} > T_{\perp e}$ [e.g., Camporeale and Burgess, 2008].

In summary, the solar wind is not simply an expanding fluid as described by Parker, but is a complex and dynamic medium. We must examine the plasma using the correct physical model for the phenomena of interest. The fluid equations of MHD are used to describe large-scale systems such as global simulations of magnetospheres, or solar flare models, and low frequency plasma waves, such as Alfvén waves. Below ion length scales, the ion gyro-radius or ion inertial length, the equations of kinetic plasma physics must be used. In this regime, the electron dynamics become important, and must be taken into account. The Vlasov-Maxwell system of equations allows an accurate description of collections of particles using distribution functions. Between these two scale extremes are the intermediate models, such as two fluid MHD, and hybrid codes, where the electrons are treated as a fluid and the ions are modelled as particles.

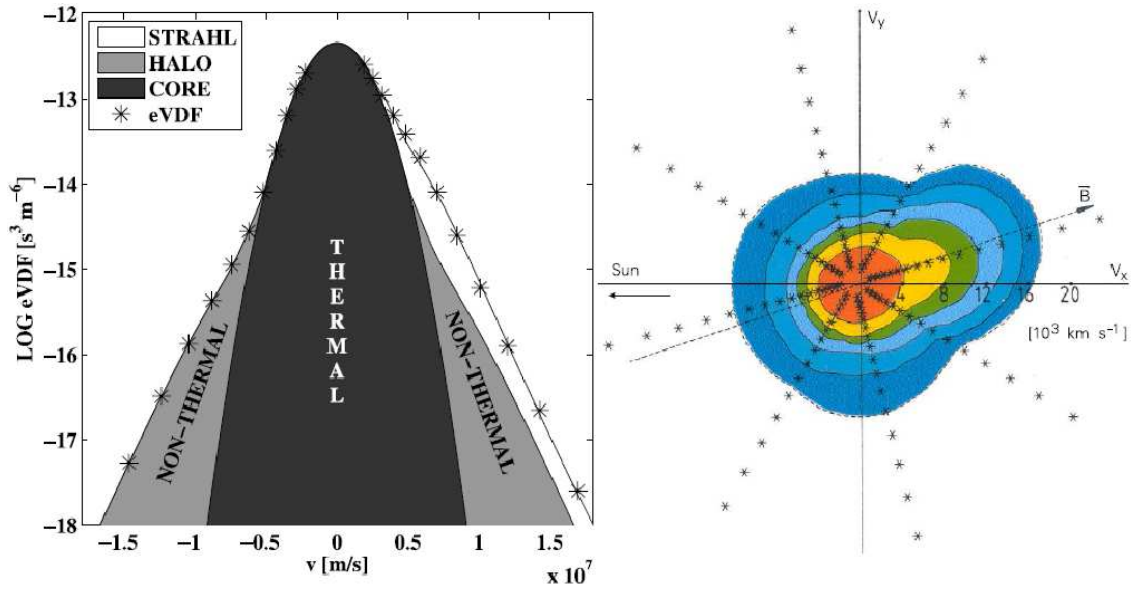

Figure 1.9.: Left: Cross section of an electron VDF along **B**. (Figure from Štverák et al. [2009].)
Right: Electron VDF at 1 au. (Figure from [Marsch, 2006].)

1.2. Outline of the thesis

Due to the non-linearities associated with the equations governing plasma dynamics, my work has been focused on performing simulations and analyzing data from a kinetic particle in cell (PIC) code. My primary interest has been in the behaviour of plasma within turbulence at sub-proton scales. Large scale (MHD) solar wind simulations have been studied for many years, but small/kinetic scale plasma turbulence is a relatively new topic of interest. There is little solar wind observational data at kinetic scales due to the resolution required, but forthcoming missions will have the resolution to begin probing this intriguing medium at electron scales, providing the motivation for this work.

This thesis is divided into seven chapters. In the next chapter (Chapter 2) I will review the theories and properties of plasma turbulence, and how they relate to the current observations of the solar wind. Then in Chapter 3, I will review the theories governing the process of magnetic reconnection. This is relevant as this process operates on many scales in plasmas, allowing the conversion of magnetic energy to kinetic energy. This multi-scale phenomenon is important for a complete understanding of plasma turbulence and also, turbulence becomes an important process in understanding "fast" reconnection.

In Chapters 4 - 6, I will review three projects: The first project looks at the affect that electron scale turbulence, induced by a magnetic perturbation, has on plasma

properties, with a focus on electron temperature anisotropy. A new mechanism to generate parallel electron temperature anisotropy around small scale reconnection sites is described in detail.

The second project studies the properties of a type of sub-proton scale coherent structure that can spontaneously form within a turbulent field. I will show that these structures can explain some of the observations of "magnetic holes" in the Earth's plasma sheet.

In the third project, I look to understand what dissipation is in a collisionless plasma, by examining signatures of dissipation in the previous simulations. I then show how the plasma behaviour changes when the parallel direction is supported in the simulations, and find evidence for electron-electron beam modes within the turbulence.

Together these projects demonstrate the richness and complexity of turbulence in the solar wind, with magnetic fluctuations generating multiple waves, that can cascade energy to smaller scales, and coherent structures all interacting within the turbulent plasma. Finally, in Chapter 7, I will draw conclusions and discuss possible future work.

2. Turbulence physics

2.1. Introduction

The term "turbulence" is often used in everyday life to describe something that is not regular, or apparently random. Examples being the turbulent air experienced by aircraft, waves on a rough sea, or even the vortices created after stirring a mug of coffee. Turbulence is often referred to as the last unsolved problem in classical physics. Since we can treat plasma as a type of magnetized fluid, it is necessary to briefly review the hydrodynamic concepts of turbulence, as these are often borrowed by the space plasma community when describing the observations of solar wind turbulence.

In hydrodynamics, "laminar" or streamline flow, refers to a fluid that flows in parallel layers or sheets. The velocity of the flow is smoothly varying in space and time, in some regular and predictable way. "Turbulent flow" is where the flow becomes irregular, with "eddies", swirls and cross currents between flow layers. The localized movement of the fluid appears to become random, and appears chaotic in space and time. However examination of a static image of turbulent flow reveals vortices and structure at many scales. An image taken at another time would appear remarkably similar, except the specifics of the flow at any given point would be different. Therefore a statistical approach is used to describe turbulent fluid properties. Statistically, the long time averages of the system are reproducible, whereas the actual (localised) flows are random, and sensitive to perturbations.

The dimensionless parameter that determines if a fluid flow is laminar or turbulent is the Reynold's number,

$$R_e = \frac{\rho u l}{\mu} = \frac{u l}{\nu}, \tag{2.1}$$

where u is the bulk motion of the fluid, l is the length scale of the system, ρ is the density of the fluid, μ and ν are the dynamic and kinematic viscosities of the fluid. The Reynold's number is derived from the Navier-Stokes equation, which describes the evolution of flow in a incompressible fluid. It is the ratio between the inertial

and viscous forces acting on the fluid. For low values of R_e (e.g. < 2300) the flow is regular, or laminar, as the higher viscous forces damp out any random velocity perturbations. When R_e is high enough (e.g. > 4000), viscous forces are overcome, and the flow transitions to turbulent flow. Between these two values the fluid would contain areas of both laminar flow, mixed with areas of turbulent motion. In other words, for a given system size, density and type of fluid, the bulk velocity must be greater than a certain value, in order to overcome viscous forces.

A key assumption in the theories of turbulence (Section 2.2) is that the fluid is non-intermittent. Intermittency refers to large amplitude, localized departures from homogeneity. This can give one dimensional time-series of parameters (e.g. velocity, density, magnetic field strength) the appearance of being "bursty" and irregular. It is usually associated with coherent structures. For example, in hydrodynamics, the eddies may not fill all of the available space, so there will be areas of turbulent motion and laminar motion. This would mean that the energy contained in the fluid is unevenly distributed in space, and can also result in uneven energy cascade rates, and dissipation rates. However, intermittency seems to be a generic property of turbulent flows, so departures from theoretical values for the cascade power spectrum can be attributed to this property. I will discuss this property, in relation to the solar wind in Section 2.3.3.

2.2. Theoretical models of turbulence

2.2.1. Kolmogorov's model of isotropic hydrodynamic turbulence

The fundamental theory of turbulence was outlined by Kolmogorov [1941]. The theory (K41 hereafter) assumes that the turbulent velocity fluctuations are statistically isotropic, i.e. the same in all directions, and homogeneous, or the same everywhere, and as previously mentioned, the statistical properties, such as the mean, variance (and power spectrum) are time stationary.

The fluid has an injection of energy at some scale, L, called the stirring scale. This motion will drive large eddies, and those large eddies will break up into smaller ones, and transfer energy to vortices of a similar size. This transfer is through nonlinear wave "triad" interactions. If two eddies have wavenumbers $\mathbf{p}$ and $\mathbf{q}$ one way they can interact to create a new wavenumber, is via $\mathbf{k} = \mathbf{p} + \mathbf{q}$ as shown in Fig. 2.1 (in two dimensions). Wavenumber interactions can also subtract so $\mathbf{l} = \mathbf{p} - \mathbf{q}$ is

also possible. New wavenumbers can then interact with previously generated waves, until the entire range of wavenumber space is filled. This mathematical description allows interactions between any sized wavenumbers, but a key idea in Kolmogorovs theory is the "locality, in wavenumber space, of interactions," i.e. interactions are between vortices of a similar length scale, and are local triads, as shown on the left in Fig. 2.1. This makes some physical sense: consider the interaction of a large eddy on a much smaller one. The flows of a large eddy will seem, at the small scale, like regular flow, and the smaller eddy will be dragged around the larger one, without much energy exchange. The net effect of the locality assumption will be the transfer of energy from the large stirring scale to smaller ones. This is defined as a "forward cascade" of energy. (An "inverse cascade" would transfer energy from small to large scales.)

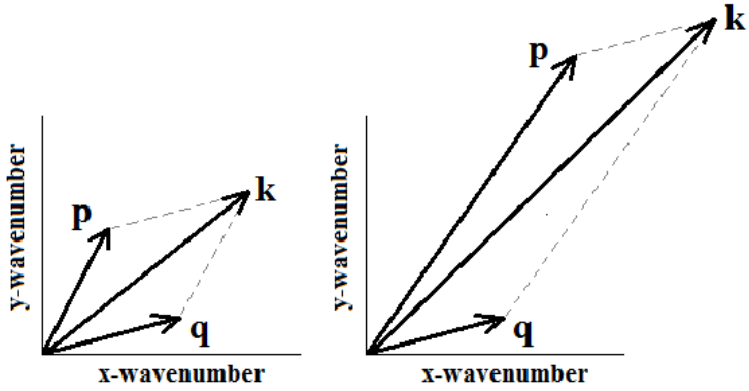

Figure 2.1.: Nonlinear triad interactions. Left is a local triad where $\mathbf{p} \approx \mathbf{q}$. Right is a non-local triad. In both diagrams $\mathbf{k} = \mathbf{p} + \mathbf{q}$.

The transfer of energy to smaller scales continues until, at some small scale, viscosity damps out the small fluctuations and dissipates the fluid motion into heat energy. This is called the "dissipation scale", l_ν. Between the stirring scale and the dissipation scale is the "inertial range." In this range of scales where $L \gg l_I \gg l_\nu$ energy cascades from large to small scales. The rate of energy input at the stirring scale is defined as ϵ. Assuming that the resulting energy spectrum is in a steady state, then the energy transfer rate at each smaller scale must also be equal to ϵ. Additionally, the energy dissipation rate (or output rate), once the forward cascade reaches the dissipation scale, must also equal ϵ to maintain the steady state. Figure 2.2 shows a power spectrum of what a forward cascade would look like for a turbulent fluid. This is a snapshot in time, showing the energy at all wavenumbers. Given a constant energy input at the stirring scale, and the assumptions of Kolmogorovs theory, this spectrum should also remain constant in time. Kolmogorov predicted

that the power spectrum in the inertial range would be proportional to $k^{-5/3}$ (where k is the wavenumber.) This has been experimentally confirmed as a universal law of hydrodynamics.

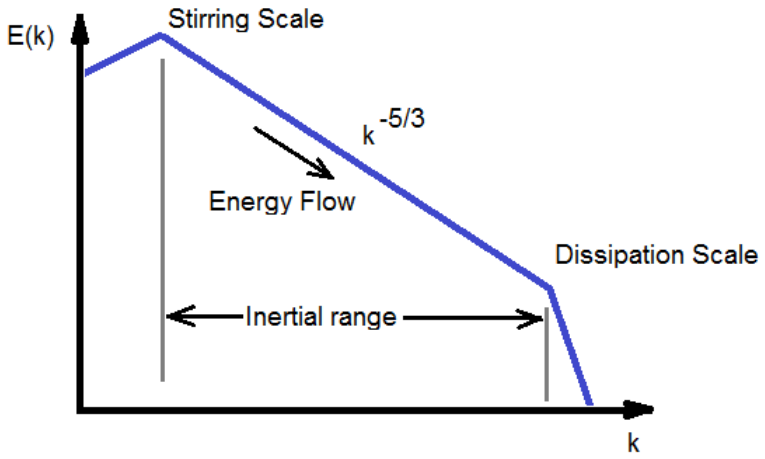

Figure 2.2.: Kolmogorov's Turbulent Power Spectrum Concept.

Using Parsevals theorem (that energy in Fourier space is conserved) the total energy, E, in the fluid can be expressed as,

$$E \sim \int_k E(k)\ dk, \tag{2.2}$$

$E(k)$ is the energy spectrum, so $E(k)dk$ is the energy in the infinitesimal wavenumber range δk. Taking unit mass and only considering the dimensions length (l) and time (t) the units of $E(k)$ are energy ($v^2 \sim l^2\ t^{-2}$) per unit wavenumber ($k \sim l^{-1}$), or ($l^3\ t^{-2}$). Defining the velocity fluctuations associated with eddies (in the inertial range) of a certain length scale, l_I, as δu_I and the timescale that the energy takes to transfer between scales (in the inertial range) as τ_I then,

$$\epsilon \sim \frac{\delta u_I^2}{\tau_I} \tag{2.3}$$

From Eq. 2.3, ϵ has units of energy ($l^2\ t^{-2}$) per second or $l^2\ t^{-3}$. Assuming that $E(k)$ is some function of ϵ and k only,

$$E(k) = g(\epsilon, k). \tag{2.4}$$

The left hand side of Eq. 2.4 has units ($l^3\ t^{-2}$), and the function g must also have the same units. Since ϵ is the only variable with the time dimension, it must be raised to the power of 2/3 to match the units of t^{-2}. So $\epsilon^{2/3}$ has the units of

$(l^2\ t^{-3})^{2/3} = l^{4/3}\ t^{-2}$. Rewriting Eq. 2.4 and redefining the function g to depend only on the variable, k,

$$E(k) = \epsilon^{2/3} g(k). \tag{2.5}$$

Equating dimensions of length reveals that $g(k)$ must have the units $l^{5/3}$. (So that $l^{4/3}.l^{5/3} = l^{9/3} = l^3$.) This is equivalent to $g(k)$ having dimensions $k^{-5/3}$. So finally (ignoring any dimensionless constants):

$$E(k) \sim \epsilon^{2/3} k^{-5/3}. \tag{2.6}$$

Equation 2.6 is the well known "Kolmogorov -5/3" power law spectrum for turbulent fluids within the inertial range.

2.2.2. Kraichnan's model of isotropic MHD turbulence

In 1965 Kraichnan attempted to derive a theory (K65 hereafter) similar to that of Kolmogorov, but for a plasma described by the equations of MHD. These equations are the same form as the fluid equations of hydrodynamics, with the addition of the Lorentz force, which gives rise to MHD waves. Kraichnan assumed that the nonlinear interaction (Fig. 2.1) of Alfvén wave packets were responsible for generating the turbulent cascade in the plasma.

Alfvén waves propagating at an angle θ to the magnetic field have the general dispersion relation $\omega^2 = k^2 v_A^2 \cos^2\theta$. Therefore the phase speed is given by $v_{ph} = \omega/k = \pm v_A \cos\theta$. Where v_A is the Alfvén velocity is given by $v_A = \dfrac{B}{\sqrt{4\pi n_i m_i}}$. The group velocity, which relates to the direction of energy flow, is given by $\mathbf{v_g} = \dfrac{\partial\omega}{\partial\mathbf{k}} = v_A\hat{\mathbf{z}}$, assuming the field direction is along $\hat{\mathbf{z}}$. Therefore Alfvén wave packets transport information and energy along the magnetic field direction at a speed of $\pm v_A$, whatever the direction of the wave itself. The incompressible MHD equations can also be rewritten in the form of Elsässer variables, which expresses them in terms of counter propagating Alfvénic fluctuations.

Kraichnan's argument was as follows. If the MHD waves are assumed to be Alfvénic, then only counter propagating wave packets will interact nonlinearly. This concept introduces a new set of time scales and length scales, and extra physics is needed in order to define a cascade scaling law. Introducing the Alfvén time, τ_A,

$$\tau_A(l_\parallel) \sim \frac{l_\parallel}{v_A}, \tag{2.7}$$

where the subscripts $\parallel$ and $\perp$ refer to the parallel and perpendicular directions to the magnetic field. The strain (or "eddy") time, τ_S, is defined as,

$$\tau_S(l_\perp) \sim \frac{l_\perp}{\delta u_I}, \tag{2.8}$$

where δu_I is, as in K41, the velocity fluctuation associated with the eddies. Two counter-propagating Alfvén wave packets are assumed to take approximately an Alfvén time, τ_A, to pass through each other. This ignores an extra factor of 2 for exactly parallel and anti-parallel interacting wave packets. In this time, the amplitude of the velocity fluctuations will have changed by:

$$\Delta\delta u_I \sim \frac{\delta u_I^2 \tau_A}{l_\perp} \sim \delta u_I \frac{\tau_A}{\tau_S}. \tag{2.9}$$

This assumes "weak interactions" so $\Delta\delta u_I \ll \delta u_I$ or $\tau_A \ll \tau_S$. In the time it takes for the waves to interact (τ_A) the velocity fluctuation will only have been changed by a small amount, proportional to the relative sizes of the timescales. Assuming the cascade time, τ_I is the time it takes for multiple nonlinear interactions to change the fluctuation, δu_I by an amount of the order of itself,

$$\sum^{\tau_I} \Delta\delta u_I \sim \delta u_I. \tag{2.10}$$

Now assuming the change in fluctuations behave like a random walk, then the overall change in fluctuation for N "steps/interactions" (which take a duration, τ_I) will be of the order $\sqrt{N}$ or $\sqrt{\frac{\tau_I}{\tau_A}}$ giving,

$$\sum^{\tau_I} \Delta\delta u_I \sim \delta u_I \frac{\tau_A}{\tau_S}\sqrt{\frac{\tau_I}{\tau_A}} \sim \delta u_I. \tag{2.11}$$

Equation 2.11 shows that:

$$\frac{\tau_A}{\tau_S}\sqrt{\frac{\tau_I}{\tau_A}} \sim 1, \tag{2.12}$$

or,

$$\tau_I \sim \frac{\tau_S^2}{\tau_A} \sim \frac{v_A}{l_\parallel}\frac{l_\perp^2}{\delta u_I^2}. \tag{2.13}$$

Equation 2.13 gives the dimensions of the cascade time as a function of MHD parameters. Using the original definition for the rate of energy cascade, ϵ (Eq. 2.3) we can write,

$$\delta u_I^2 \sim \epsilon \tau_I \tag{2.14}$$

substituting for τ_I from Eq. 2.13 gives:

$$\delta u_I^2 \sim \epsilon \frac{v_A}{l_\parallel} \frac{l_\perp^2}{\delta u_I^2}, \tag{2.15}$$

which can be rearranged to:

$$\delta u_I \sim (\epsilon v_A)^{1/4} \frac{l_\perp^{1/2}}{l_\parallel^{1/4}}. \tag{2.16}$$

Finally, Kraichnan assumed isotropic fluctuations. i.e. the length scales are the same in both the parallel and perpendicular directions, such that $l_\parallel \sim l_\perp \sim l$, so we can write:

$$\delta u_I \sim (\epsilon v_A)^{1/4} l^{1/4}, \tag{2.17}$$

or in terms of $l \sim 1/k$:

$$\delta u_I \sim (\epsilon v_A)^{1/4} k^{-1/4}. \tag{2.18}$$

This now constrains the units of the energy cascade. Recalling that $E(k)$ is energy per unit wavenumber, or $\sim \frac{\delta u_I^2}{k}$, we substitute in Eq. 2.18 giving:

$$E(k) \sim (\epsilon v_A)^{1/2} k^{-3/2}. \tag{2.19}$$

This shows that an isotropic MHD cascade should follow a slightly shallower $(-3/2)$ power law than that of hydrodynamic fluid turbulence $(-5/3)$.

2.2.3. Goldreich & Sridhar's (GS95) model of anisotropic MHD turbulence

Despite much progress in the theory of turbulence, K65 theory assumed isotropic fluctuations that are the same in any direction. Simulations (and observations) of Alfvénic turbulence showed that it is inherently anisotropic, with both wavevector and spectral anisotropy Section 2.2.5) in the parallel and perpendicular directions with respect to the global magnetic field, so an anisotropic theory was required.

Goldreich and Sridhar's theory [Goldreich and Sridhar, 1995] (GS95 hereafter) assumes that the nonlinear interactions between Alfvénic wave-packets are strong rather than weak. Firstly, the critical balance is defined, where the Alfvén time, τ_A, is assumed approximately equal to the eddy time, τ_S,

$$\frac{l_\parallel}{v_A} \sim \frac{l_\perp}{\delta u_I}. \tag{2.20}$$

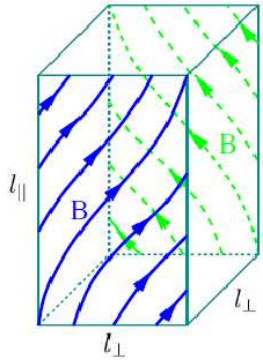

Figure 2.3.: A magnetic vortex with wavevector anisotropy, $k_\parallel > k_\perp$ (refer to Eq. 2.23). (Figure modified from Boldyrev [2006].)

This also means there is only one natural time-scale associated with the interactions, so the cascade time, τ_I, can be replaced with the eddy time, τ_S, in Eq. 2.3. The perturbations at the injection/stirring scale, L, are assumed to be isotropic, so that $L = l_\parallel = l_\perp$. Therefore the energy transfer rate, ϵ can be defined as,

$$\epsilon = \frac{\delta u_I^2}{\tau_S} = \frac{v_A^2}{\tau_A} = \frac{v_A^3}{L}. \tag{2.21}$$

The critical balance (Eq. 2.20) can also be re-written in terms of wavenumber yielding,

$$\delta u_I = \frac{k_\parallel}{k_\perp} v_A. \tag{2.22}$$

Substituting the above into Eq. 2.21, recognising $\tau_S = \tau_A = k_\parallel^{-1} v_A^{-1}$, reveals the following relationship between perpendicular and parallel wavenumber:

$$k_\parallel = k_\perp^{2/3} L^{-1/3}. \tag{2.23}$$

Equation 2.23 implies wavevector anisotropy, $k_\parallel < k_\perp$, within the inertial region in GS95 turbulence. This is shown diagrammatically in Fig. 2.3. A magnetic eddy will be longer in the parallel direction, and the same size in the two perpendicular directions. The spectral power laws in the parallel and perpendicular directions can be calculated using the equations,

$$E(k_\perp) = \frac{\delta u_I^2}{k_\perp}, \tag{2.24}$$

$$E(k_\parallel) = \frac{\delta u_I^2}{k_\parallel}. \tag{2.25}$$

Substituting Equations 2.22 and 2.23 into Equation 2.24 and 2.25 reveals the fol-

lowing power laws for the perpendicular and parallel directions:

$$E(k_\perp) \propto k_\perp^{-5/3}, \tag{2.26}$$

$$E(k_\parallel) \propto k_\parallel^{-2}. \tag{2.27}$$

In Eq. 2.26 the perpendicular power law returns to the K41 value of $-5/3$. However in Eq. 2.27 the parallel cascade has a slope of -2. The wavevector anisotropy (Eq. 2.23) describes magnetic eddies that are elongated in the $l_\parallel$ direction.

2.2.4. Boldyrev's model of anisotropic MHD turbulence

The problem with GS95 turbulence was that when the power spectra of magnetic fields from simulations were plotted (e.g. Maron and Goldreich [2001]) the 1D ($k_\perp$) spectra often show a power law of $k_\perp^{-3/2}$, corresponding to the K65 value, rather than $k_\perp^{-5/3}$ predicted by GS95 theory.

A modification to the theory was proposed by Boldyrev [2006]. As in GS95 theory, strong interactions are assumed. However the magnetic fluctuations and velocity perturbations are assumed to be separated by a (small) angle, ϕ_λ. This can be decomposed into the angles, θ_λ, and $\tilde{\theta}_\lambda$, where θ_λ is the angle between the local field perturbation and the velocity perturbation in the perpendicular plane. (Fig. 2.4.) This modifies the critical balance equation (Eq. 2.20):

$$\tau_S \sim \tau_A \sim \frac{l_\parallel}{v_A} \sim \frac{\lambda}{\delta u_I \theta_\lambda}, \tag{2.28}$$

where λ is the width of the eddy in one of the perpendicular directions (Fig. 2.5). $\delta u_I \theta_\lambda = \delta u_\lambda$, where δu_λ is the component of δu_I in the λ direction, assuming small angle approximations. As in Eq. 2.21, τ_S is substituted into the updated critical balance equation,

$$\epsilon = \frac{\delta u_I^2}{\tau_S} = \frac{\delta u_I^3 \theta_\lambda}{\lambda}. \tag{2.29}$$

Recognising that the energy flux is a constant then leads to the relation,

$$\delta u_I \propto \left(\frac{\lambda}{\theta_\lambda}\right)^{1/3}. \tag{2.30}$$

Since the turbulent fluctuations must be scale invariant, θ_λ must also be a power law function of λ. Boldyrev proposed the following parameterisation,

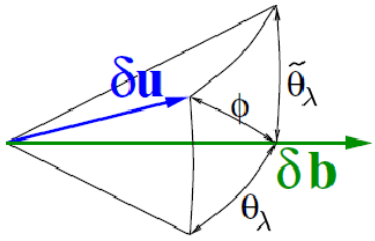

Figure 2.4.: Alignment of δB fluctuations to δu in Boldyrev's theory. (Figure modified from Boldyrev [2006].)

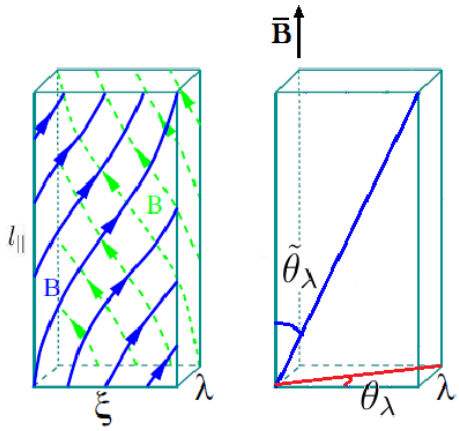

Figure 2.5.: A magnetic vortex with wavevector anisotropy, $k_\parallel < k_\perp$. These eddies have different lengths in both perpendicular directions, with $\xi < \lambda$. (Figure modified from Boldyrev [2006].)

$$\theta_\lambda \propto \lambda^{\alpha/(3+\alpha)}, \tag{2.31}$$

which using $\theta_\lambda = \lambda/\xi$ (Fig. 2.5) and Eq. 2.31 gives,

$$\begin{aligned} \delta u_I &\propto \lambda^{1/(3+\alpha)}, \\ \xi &\propto \lambda^{3/(3+\alpha)}, \\ l_\parallel &\propto \lambda^{2/(3+\alpha)}, \\ \tilde{\theta}_\lambda &\propto \lambda^{1/(3+\alpha)}. \end{aligned} \tag{2.32}$$

Note that this parameterisation yields the previous results of GS95 theory when $\alpha = 0$. Given the geometry, $\phi_\lambda = \sqrt{\theta_\lambda^2 + \tilde{\theta}_\lambda^2}$. Boldyrev's argument is that the fluctuations would attempt, on average, to minimize this angle during the cascade, so $\theta_\lambda \sim \tilde{\theta}_\lambda$. This leads to the conclusion that $\alpha = 1$ when comparing Eqs. 2.31 and 2.32. This gives the relation $\delta u_I \propto \lambda^{1/4}$, which using Eqs. 2.24 and 2.25 along with $k_{\perp\lambda} = \lambda^{-1}$ and $k_{\perp\xi} = \xi^{-1}$ yields,

$$E(k_{\perp\lambda}) \propto k_{\perp\lambda}^{-3/2}, \tag{2.33}$$
$$E(k_{\perp\xi}) \propto k_{\perp\xi}^{-5/3}, \tag{2.34}$$
$$E(k_{\parallel}) \propto k_{\parallel}^{-2}. \tag{2.35}$$

The perpendicular cascade returns to the K65 power law value of $-3/2$ in the λ direction, could be an explanation for the reduced values seen in simulations. Another important result is the 3D wavevector anisotropy predicted by this theory, which would result in ribbon like structures within MHD turbulence.

2.2.5. Anisotropy and turbulence

As seen in the previous section, there are several types of anisotropy that can develop within turbulence, so it is worth defining the appropriate terms here.

The scaling theories for the turbulent spectra discussed in sections 2.2.1 and 2.2.2 both assume that the fluctuations are isotropic. However, the GS95 and Boldyrev theories (sections 2.2.3 and 2.2.4) show the cascade power law may have different values depending on the direction of measurement. This is referred to as "spectral index anisotropy."

Eddies in hydrodynamics have isotropic wavelengths, and breakup into smaller ones, which are statistically the same, and circular with no preferential direction. Figures 2.3 and 2.5 in the previous sections show that in incompressible MHD turbulence, the eddies are expected to be elongated in the field parallel direction, and thinner in the perpendicular direction. This is called "wavevector anisotropy."

"Power anisotropy" is analogous to wavevector anisotropy, except that different power levels might be observed in certain different directions at a specific scale. For example, if a plot of the power spectra of $P(k_{\perp})$ and $P(k_{\parallel})$ is put onto the same axis, the two graphs might show different values of P(k) at a certain value of k.

Observations of the solar wind have shown that fluctuations perpendicular to the mean magnetic field direction tend to be larger than fluctuations in the parallel direction. i.e. $\dfrac{\delta B_{\perp}}{\delta B_{\parallel}} > 1$. This is called "amplitude (or variance) anisotropy".

2.3. Turbulence in the solar wind.

The power spectra of fluctuations in the solar wind has been a topic of intense research ever since Coleman [1968] first interpreted the magnetic spectrum of the

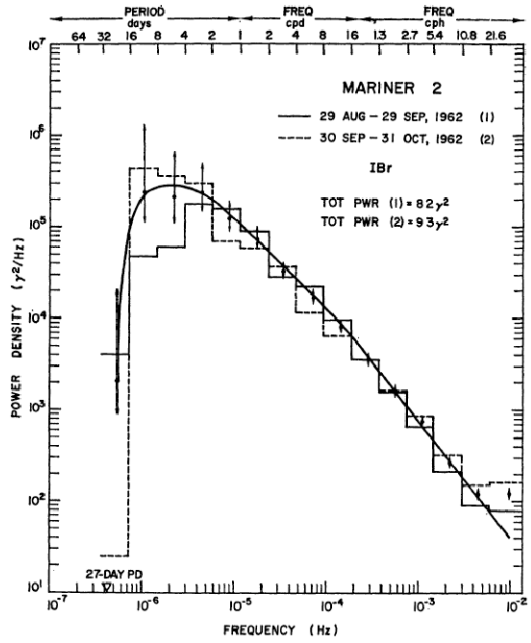

Figure 2.6.: Power spectrum of B_r as recorded by the Mariner 2 spacecraft. (Figure from Coleman [1968].)

solar wind as evidence of a turbulent cascade (Figure 2.6). These early observations measured solar wind parameters at frequencies corresponding to scales (via Taylor's hypothesis, see section 2.3.1) greater than the ion gyroradius ($\sim 0.1\,\mathrm{Hz}$ at $1\,\mathrm{au}$), and therefore allowed the K41 and K65 theorems discussed in Section 2.2 to be put into context. Theories were then developed for how energy could be injected into the solar wind, creating the observed cascade.

Due to the large magnetic Reynold's number, the magnetic field lines generated by the Sun are anchored to the photosphere, and have to move with the parcels of plasma due to flux-freezing. However, the photosphere itself is in a state of constant motion. This means that the surface will drag the field lines with them as they move, generating Alfvén waves.

The large scale motion of the magnetic footpoints means that the energy injection into the solar wind is at a large scales, so we expect the energy cascade to be from large to small scales, a forward cascade. As mentioned in Section 2.2.2 a turbulent cascade under the MHD framework requires parallel and anti-parallel Alfvén waves. Mechanisms exist to reflect outward propagating Alfvén waves in a radially stratified solar atmosphere, such as non-WKB reflection [Chandran and Hollweg, 2009].

The reflected (sunward) waves allow nonlinear interaction with the outward propagating wave-packets (Fig. 2.7), the generation of an energy cascade, and a "fluid-like" power spectrum to be observed in the solar wind. Beyond the Alfvén critical

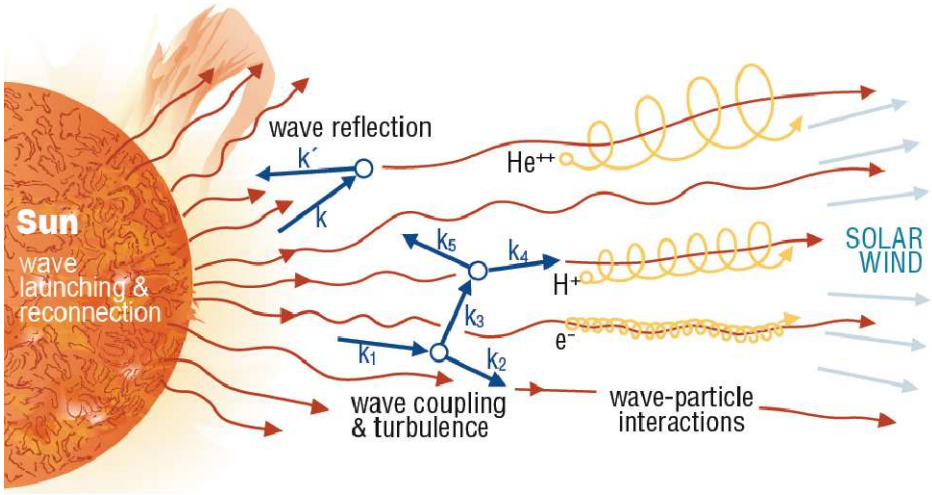

Figure 2.7.: The generation of Alfvénic turbulence in the solar wind. (Figure from Chandran [2011].)

point, even waves that are reflected sunward would be swept out with the solar wind, and have a net speed away from the Sun. However the relative speed of the reflected and anti-sunward waves still allows the Alfvén waves to interact. At present, the closest observations of the solar wind to the Sun have been provided by the Helios 1 spacecraft (1976) which travelled just inside the orbit of Mercury to a distance of 0.29 au. This is still outside the Alfvén critical point, and therefore there are no observations of the "birth" of solar wind turbulence, we have only observed supersonic flows, exhibiting developed turbulence. In the future, observations of the outer corona below this critical point (e.g. NASA's Solar Probe+ Mission will go to $8.5R_{\odot}$) will help us to understand this initial population of Alfvén waves and the nature of the energy injection scale in solar wind turbulence (Fig. 2.8).

2.3.1. Observations of solar wind power spectra

The interpretation and analysis of solar wind observations can be rather complex as one has to know the exact conditions under which the spacecraft measurements were taken. This is because the solar wind is not the simplified model as Parker envisaged, but is a dynamic and changing system, with features such as stream fronts between the fast and slow wind (CIRs), CMEs and shocks. Turbulence theory assumes a time independent process, in a homogeneous medium. Therefore observations used in turbulence studies have to be carefully filtered to isolate measurements of the "undisturbed" solar wind, with these localised time dependent features removed.

Once "undisturbed" solar wind data is filtered out, power spectra can be obtained

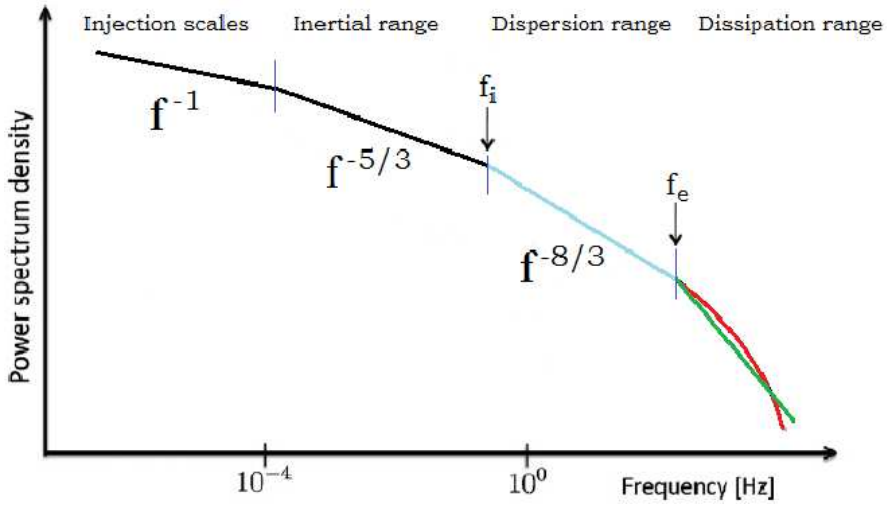

Figure 2.8.: Schematic power spectrum of (fast) solar wind magnetic fluctuations. (Image adapted from Bourouaine et al. [2012].)

by recording time series of the relevant variable (e.g. magnetic field, **B**, electric field, **E**, or velocity, **v**) using a single spacecraft, and converted to frequency space by using a fast Fourier transform (FFT) or similar algorithm. Frequency data can then be converted to wavenumber using "Taylor's hypothesis" [Taylor, 1938]. This assumes that a time-series of a signal can be interpreted as a spatial cross-section provided that spacecraft motion relative to the plasma frame is much faster than the wave speeds. For most spacecraft, we can consider it stationary compared to the solar wind, as the solar wind can travel at several hundred $\mathrm{km\,s^{-1}}$, whereas spacecraft are usually moving at only a few $\mathrm{km\,s^{-1}}$. Since MHD wave (Alfvén) speeds are, in most cases, only a few tens of $\mathrm{km\,s^{-1}}$, this hypothesis is valid, and a probe in the solar wind observes a spatial cross section of the solar wind. Spacecraft frequency, f, can be converted to a plasma frame wavenumber using $k = 2\pi f / v_{SW}$, where v_{SW} is the measured solar wind speed. Therefore spectra are often plotted against frequency, and interpreted as functions of wavenumber, as illustrated in Fig. 2.8.

However, a one dimensional spectrum measured by a single spacecraft can only give information about the spectrum along the direction of travel. Such a spectrum is called a "reduced" power spectrum. If the power of fluctuations is only contained in directions parallel to the direction of travel, then the exact plasma spectra will be measured. But if power is contained in wavevectors at any other angle to the direction of travel, then wavefronts of different wavelengths become indistinguishable, (Fig. 2.9) and all contribute to the measured power. This can make it difficult to interpret observations, and distinguish between spectral theories (Section 2.2), particularly if the mean magnetic field varies.

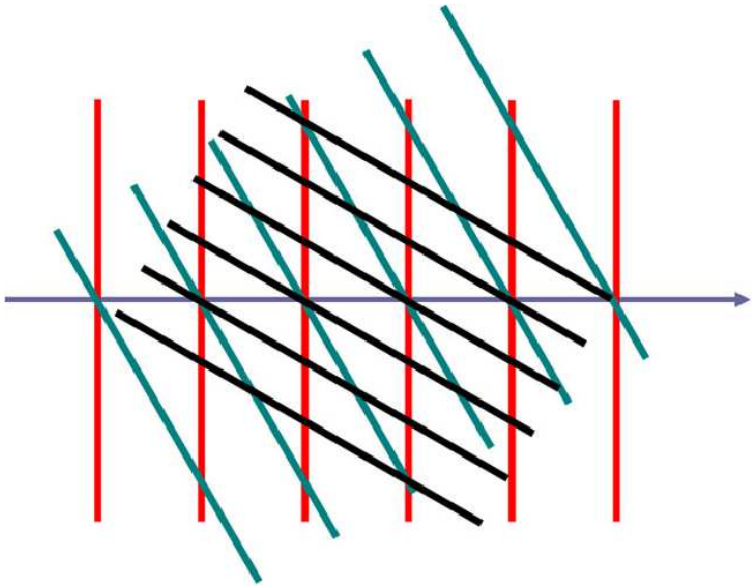

Figure 2.9.: Visualization of a reduced spectrum, as measured by a single spacecraft. The spacecraft travels along the blue line and travels through the wavefronts of three planar waves (red green and black). Each wave will contribute power at the same observed frequency despite them all having different wavelengths. (Figure from Horbury et al. [2012].)

Despite these difficulties, observational papers have shown that the slow wind often has a Kolmogorov $-5/3$ spectrum at all radial distances from the sun [Bruno and Carbone, 2013] and is considered to be in a state of fully developed turbulence [Horbury et al., 2005]. The fast wind shows more evolution and has at least two "breaks" in the magnetic power spectrum (Fig. 2.8). At the largest length scales, the fast wind spectrum appears to follow a power law of k^{-1}. This is attributed to a population of large wavelength Alfvén waves being generated by the Sun, that originate in the Corona [Bourouaine et al., 2012]. (Labelled as "injection scales" in Fig. 2.8.) Beyond the injection scales, the first change of slope can be seen in the data, where the fast wind's spectrum changes to follow a power law $\sim k^{-5/3}$, like a Kolmogorov spectrum. (Note that distinguishing between a Kolmogorov and Kraichnan spectrum can be difficult in some datasets, due to the similarity of the two power law values.) In this thesis I shall refer to this part of the spectrum as the "inertial range."

Example observations of the magnetic field spectra, (near the inertial range) taken in the ecliptic plane of the solar system are shown in Fig. 2.10. Notice that only the fast wind has a low frequency break in the power spectra. The location (in frequency space) of this breakpoint moves to lower values as radial distance from the Sun increases, corresponding to a larger wavelength. (See Fig. 3 of Horbury et al.

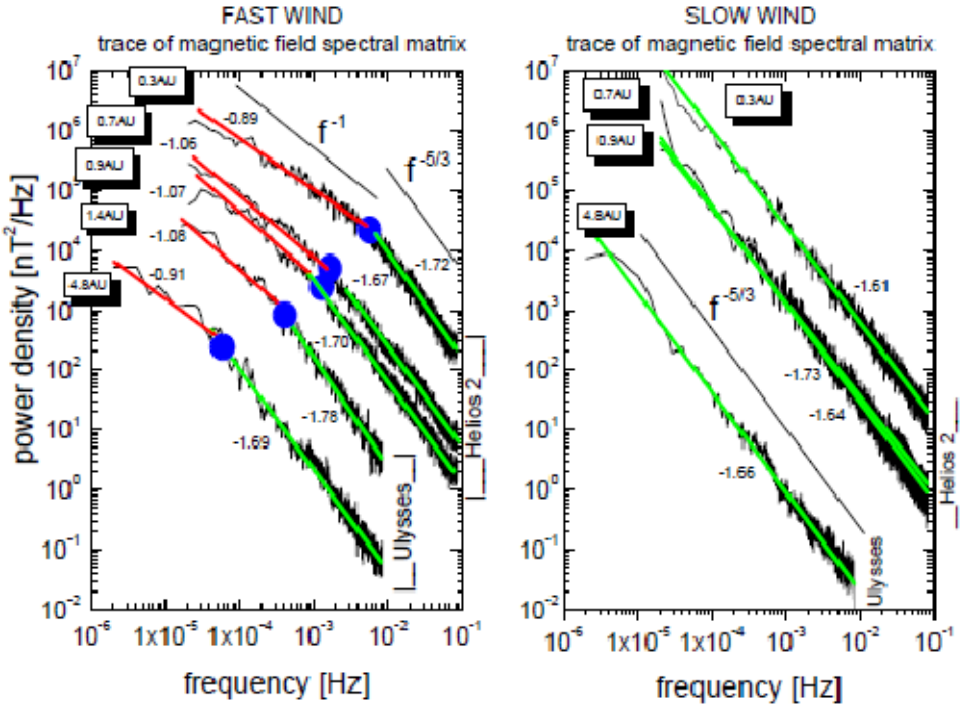

Figure 2.10.: Magnetic spectra vs radial distance (in au). (Figure from Bruno and Carbone [2013].)

[2005].) This is further evidence of an active turbulent cascade. If the k^{-1} part of the spectrum is interpreted as the energy source for the turbulent cascade (as described in Section 2.3) then the moving breakpoint suggests that increasingly larger Alfvén waves have given their energy to the cascade as radial distance increases. In the turbulence physics framework, we assume that energy would take a characteristic timescale to transfer. At larger radial distances, since the solar winds speed is finite, more time has elapsed allowing more energy to be distributed, moving the breakpoint to lower frequencies [Horbury et al., 2005].

The location of the breakpoint in the fast solar wind, as shown in Fig. 2.10, follows a power law of $R^{-1.5}$. This differs from fast solar wind observations in the polar regions which has a breakpoint location that follows a power law of $R^{-1.1}$ [Bruno and Carbone, 2013]. This implies that the turbulence in the fast polar wind has a slower rate of evolution than the fast wind in the ecliptic, and emphasizes the need to put measurements in their correct context due to the complexity of the structure of the solar wind.

Observations of the velocity spectrum also provide information about the cascade in inertial range of the solar wind. The velocity spectra in the heliosphere is observed to have a value closer to the K65 value of $-3/2$, whereas magnetic fluctuations show

the K41 scaling of $-5/3$ [Podesta et al., 2007]. This is confusing as the turbulence theories outlined in Section 2.2 are assumed to be universal energy scaling laws.

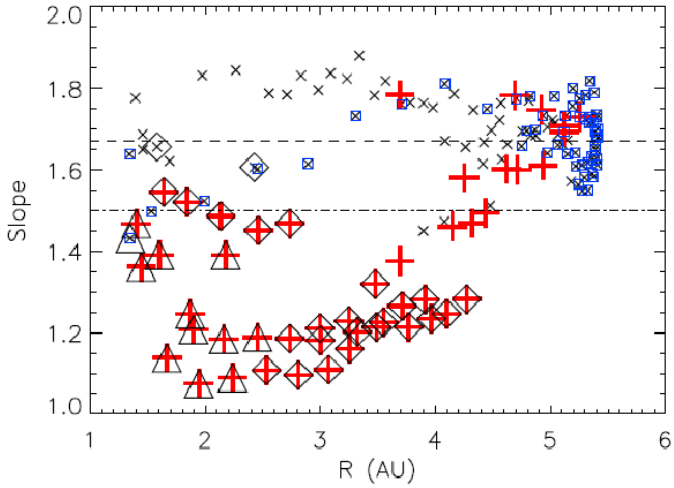

Figure 2.11.: Velocity spectra power law slope vs. radial distance (in au). Points for which the speed is greater than 675 km s^{-1} are shown as red plusses, with all other points shown as black crosses. Points with a (signed) Alfvénicity between 0.33 and 0.5 are enclosed in black diamonds, those with Alfvénicity greater than 0.5 are enclosed in black triangles, and points that are within 20° of the ecliptic are shown in blue squares. Horizontal lines are drawn at slope values of -1.5 and -1.67. There is a convergence with radial distance to slopes near $-5/3$ for both slow and fast wind. (Figure from Roberts [2010].)

There are several explanations available for this discrepancy. Roberts [2010] argued that the spectra measured at 1 au is in a transient state, (not steady state as assumed in turbulence theories) and only achieves a steady cascade at a greater distance from the Sun, once more time has elapsed. This argument was reinforced by plotting velocity spectra power law value as a function of radius which seems to eventually converge to the K41 value at ~ 5 au, with some unconvincing scatter (Fig. 2.11).

A more convincing argument was put forward by Boldyrev et al. [2011], who state that an imbalance between magnetic energy and kinetic energy is a natural part of incompressible MHD turbulence, and is related to the driving conditions at the energy injection scale. They showed through numerical simulation, and comparison to observations that the total energy (magnetic energy plus kinetic energy) spectrum follows a power law close to $-3/2$ in agreement with the K65 and Boldyrev theories. They also plot spectra of residual energy, defined as $E_R(k) = E_V(k) - E_B(k)$, where $E_V(k)$ and $E_B(k)$ are the velocity and magnetic spectra respectively. The residual

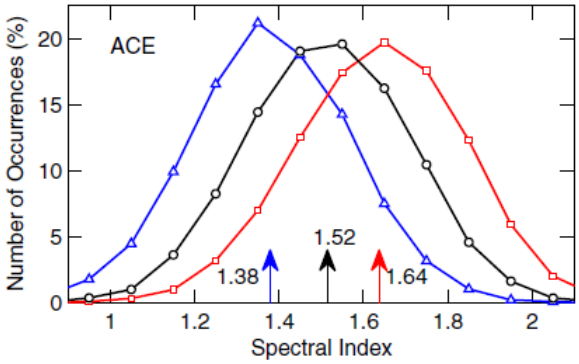

Figure 2.12.: Histograms of measured spectral indices for the velocity spectrum (blue triangles), magnetic field spectrum (red squares), and total energy spectrum (black circles) in the solar wind using data from the ACE spacecraft. The average spectral indices are indicated by the arrows. (Figure from Boldyrev et al. [2011].)

energy spectrum follows a power law, $E_R(k) \propto k^{-2}$. They state that the presence of residual energy tends to steepen the magnetic spectrum, ($< -3/2$) whilst making the velocity spectrum more shallow. The steeper slope of the residual energy means that at larger wavenumber, its value will become negligible, restoring both magnetic and kinetic energy to the $\sim 3/2$ power law. (Which could also explain the convergence of Fig. 2.11.) The measured variability at 1 au in spectral indices (using the ACE spacecraft) for total energy (black), velocity (blue) and magnetic spectra is shown in Fig. 2.12, which matched results from numerical simulations.

After the inertial range, the fast solar wind is observed to have a second break in the power spectrum, labelled f_i in Fig. 2.8. This break corresponds to the location, below ion scales, where the equations of MHD are no longer valid. At this scale ion kinetic processes may become important, providing additional sources of dissipation. Whether the change in slope is due to this additional damping and/or dissipation is subject of much research. Another argument is that below ion scales the Alfvén wave mode must convert into other kinetic waves, such as the whistler mode, or kinetic Alfvén mode. These modes, unlike Alfvén waves, are dispersive, and this property alters the cascade power law. I will therefore refer to the region beyond f_i as the "dispersion range," as suggested by Stawicki et al. [2001] (Fig. 2.8), as recent observations indicate that the cascade continues even further into electron scales. The true dissipation range (where the magnetic energy is finally converted to heat within the plasma) is thought to be located at even smaller scales, but observations here are limited.

Historically, it was thought that the location of the "ion-scale breakpoint," f_i,

should be associated with the ion inertial length, λ_i or the ion gyroradius, ρ_i. When the solar wind properties at 1 au are converted to frequencies using Taylor's hypothesis, these spatial scales are close to each other, making it difficult to distinguish which parameter is of more importance. A study by Bourouaine et al. [2012] looked at how the location of f_i changed with radial distance from the Sun. As the value of ρ_i and λ_i differ with radial distance, they were able to conclude that the location of f_i depends on the ion inertial length and not the ion gyroradius.

Within the dispersion range the spectrum is observed to have a power law with values ranging from -2 to -4 [Bale et al., 2005, Leamon et al., 1998, Smith et al., 2006]. The exact value appears variable and depends on which spacecraft data-set was used to calculate the spectrum, the analysis technique and sensitivity of the instruments used. For example, Sahraoui et al. [2009], using the Cluster spacecrafts instruments, report a spectrum proportional to $k^{-2.3}$ in the dispersion range followed by another break in the spectrum at the electron Larmor radius, ρ_e. The spectrum beyond this was reported to follow a power law of $k^{-4.1}$. Alexandrova et al. [2008] suggested that the variability of the values of the spectrum in the dispersion range depends on the plasma compressibility, whilst implying that the cascade proceeds down to electron scales. A typical value often reported in this region is $\sim -8/3$ as shown in Fig. 2.8.

Beyond the dispersion range, lies the dissipation range. Observational data becomes limited, but several studies have suggested a third breakpoint may exist as the cascade approaches electron scales [Camporeale and Burgess, 2011]. This breakpoint is labelled f_e in Fig. 2.8 and is often linked to the electron Larmor radius, ρ_e. This is a hotly debated subject. Alexandrova et al. [2009] using the Cluster spacecraft, argued for a power law of $k^{-2.8}$ in the dispersion range and, in the dissipation range (within the range $k\rho_e \sim [0.1, 1]$), an exponential function of the form $\sim -a\exp(\sqrt{k\rho_e})$ (rather than a power law) is fitted to the spectrum. (See red curve in Fig. 2.8.) Alexandrova et al. [2012] later refined this model to the form $E(k) = k^{-8/3}\exp(-k\rho_e)$ to fit both the dispersion and dissipation ranges. This more general form maintains the $-8/3$ value in the dispersion range, with the exponential factor changing the spectrum to a curved shape near and beyond the electron gyroradius (Fig. 2.13).

On the other hand, Sahraoui et al. [2013] showed a similar power law exponent in the dispersion range of $k^{-2.8}$ with a break at ρ_e, followed by a straight line power law below electron scales. (See green line in Fig. 2.8.) They argue that this can only be done with data that has a sufficiently large signal to noise ratio. The spectrum below the electron Larmor radius in the dissipation region then follows a power law

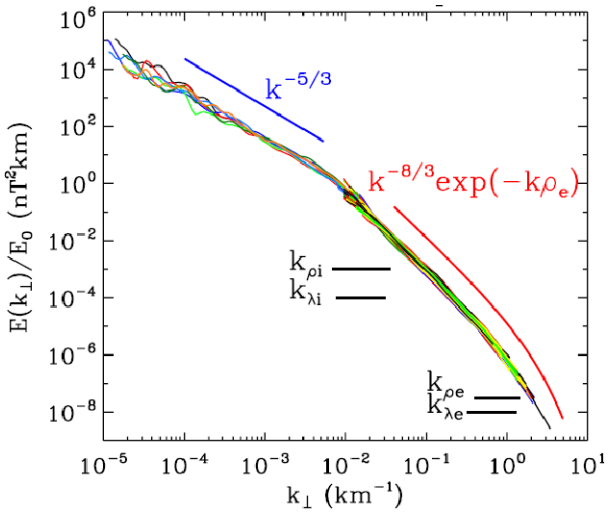

Figure 2.13.: Superposed solar wind spectra, covering fluid and kinetic scales. The blue line indicates $\propto k_\perp^{-5/3}$ and the red line shows $\propto k_\perp^{-8/3}$ which represents well all the spectra. (Caption and figure from Alexandrova et al. [2012].)

with values in the range of $\sim [-3.5, -5.5]$ with a peak of -4.

2.3.2. Observations of anisotropy

Observations of the solar wind has shown it exhibits many types of anisotropy. For example it is well known that the solar wind demonstrates variance anisotropy, where the amplitude of perpendicular fluctuations are greater than the parallel ones. This can be demonstrated by plotting the local field direction (in angles) and the minimum variance direction, which is the direction where the field varies least. These are often seen to be in alignment, indicating $\delta B_\perp > \delta B_\parallel$ (E.g. Fig. 4 of Horbury et al. [2005]).

A more complex question is what is the distribution of spectral power in wavevector space (or spectral anisotropy). Again, the solar wind is known to show spectral anisotropy, and was best illustrated by Matthaeus et al. [1990], who used multiple data sets of magnetic field data from the ISEE3 spacecraft (International Sun-Earth Explorer) to plot a 2D spatial correlation function (Fig. 2.14). A correlation function shows how similar the fluctuations are between two timeseries of data. This 2D version was built up using combinations of data recordings from a single spacecraft, noting the mean field direction. The time series can be interpreted as a spatial cut (using Taylor's hypothesis) at an angle to the magnetic field, and the correlation function computed in the direction of the solar wind flow. Combining multiple sets of data which had different field-flow angles allowed the authors to build up this 2D

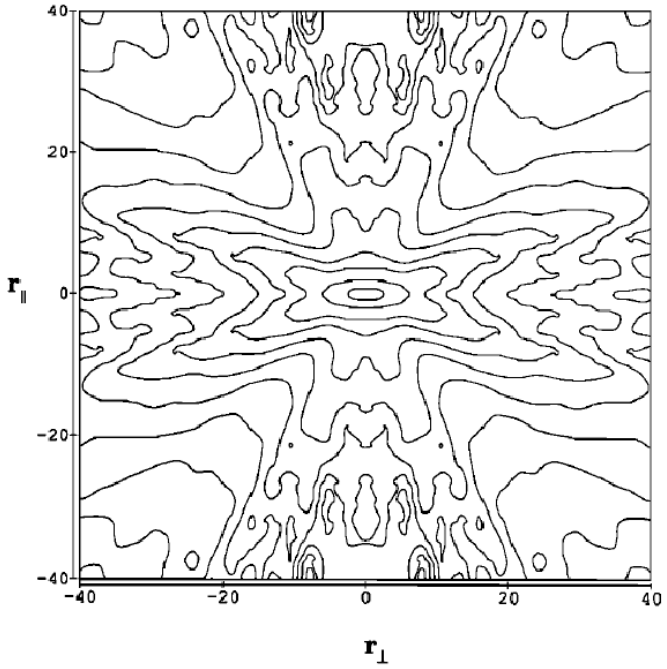

Figure 2.14.: The maltese cross. (Figure from Matthaeus et al. [1990].)

plot, which was initially only the upper right hand corner, reflected to fill in the other quadrants, assuming cylindrical symmetry. This figure was generated using a minimum separation distance of $\sim 1 \times 10^5$ km which is larger than the ion gyroradius, so it only reveals information about fluctuations in the inertial range, at MHD scale sizes. This figure is often referred to as the Maltese cross due to its appearance.

The figure shows where the power lies in 3D space in the magnetic fluctuations at 1 au. Clearly there appears to be two distinct types of fluctuations, a population of quasi-parallel fluctuations and another population of quasi-perpendicular fluctuations. A "pure" Alfvén wave ($\mathbf{k} \parallel \mathbf{B}$) propagates along the field. The perturbations of δB and δV would be perpendicular to this, and the phase fronts of these waves, could be thought of as infinite "slabs" propagating along the field. Therefore contours of the 2D correlation function that are parallel to the $r_\perp$ axis show these "Alfvénic-like" fluctuations. The other component is referred to as the "quasi-2D" component. These are waves that propagate nearly perpendicularly to the field, hence the 2D name. The wave fronts of these fluctuations could be thought of existing in infinitely long cylinders with its axis aligned parallel to the mean field direction. Therefore these appear in the correlation function as contours parallel to the $r_\parallel$ axis. If the fluctuations were isotropic, then the contours would be circular.

Since its publication there have been many papers attempting to explain the Maltese cross. For example Dasso et al. [2005] used 5 years worth of spacecraft data

to recalculate the correlation function for the fast and slow wind. They found that the fast streams are dominated by quasi-parallel fluctuations (Alfvénic) and the slow wind, which as previously discussed shows a more developed (Kolmogorov) power spectrum is dominated by quasi-perpendicular fluctuations ("quasi-2D").

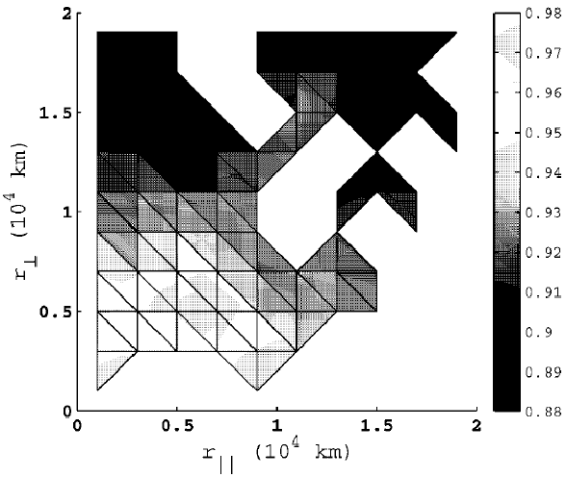

Figure 2.15.: Spatial autocorrelation function of the z-component of Cluster magnetic field fluctuations. The function is anisotropic: it does not decay equally in all directions, but rather the decay with increasing $r_\perp$ is more rapid than the corresponding decay with increasing $r_\parallel$, which is consistent with a dominant 2D component. (Figure from Osman and Horbury [2007].)

More recently Osman and Horbury [2007] used a similar technique with multiple spacecraft to calculate correlation functions, with a spacecraft separation of 10 000 km. They again found that the fluctuations are anisotropic, with the correlations decreasing faster in the perpendicular direction, than in the parallel one. This indicates that 2D fluctuations were dominant in the measurements (Fig. 2.15).

Chen et al. [2012] used structure functions to measure the power in the turbulent fluctuations in 3D. A structure function is defined by the equation, $S_m\langle|u(x+\Delta S)-u(x)|^m\rangle$, where m is the order, $u(x)$ is a variable that depends on spatial position, and ΔS is a spatial separation. Using magnetic field data as the variable and the order $m = 2$, this equation becomes related to the power of the fluctuations. They used these second order structure functions to plot contours of constant fluctuation power at different scale-lengths (Fig. 2.16). This showed that the fluctuation power is also three dimensionally anisotropic, with fluctuation power increasing along the field direction as scale size decreased. The plots in Fig. 2.16 are referred to as eddy shapes, although they don't represent dynamic shapes as such. This figure provides evidence that Boldyrev's theory of strong anisotropic turbulence is correct (Section

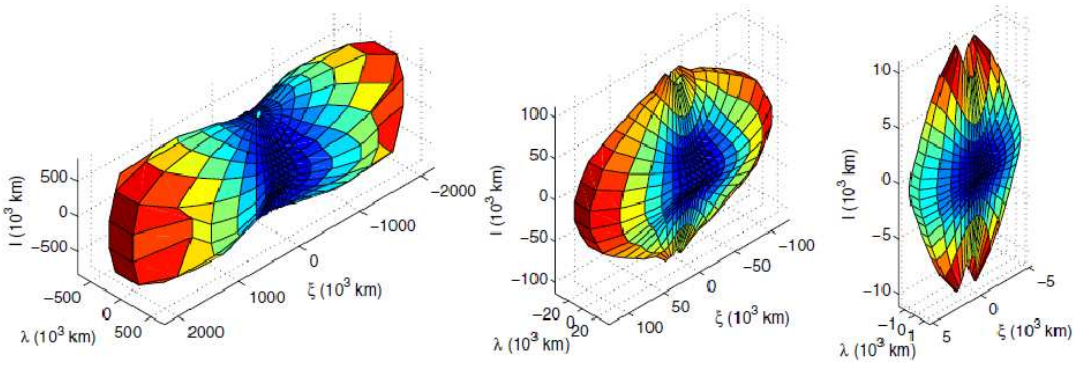

Figure 2.16.: Surfaces of constant B-trace power (statistical Alfvénic eddy shapes) from large (left) to small (right) scales, in which color represents distance from the origin. The vertical axis is field aligned. The typical proton gyroradius is $\sim 360\,\mathrm{km}$. (Figure from Chen et al. [2012].)

2.2.4).

2.3.3. Observations of intermittency

Intermittency (Section 2.1) is also a property seen in solar wind turbulence. Several studies [Greco et al., 2009, Osman et al., 2011, Sorriso-Valvo et al., 1999] have used statistical methods to identify intermittency in the solar wind. One method involves plotting the probability distribution function (PDF) of the normalised partial variance of increments (PVI). For any time series of data, e.g. magnetic field B_t, (where the subscript, t, in this notation means it is a time series) a spatial scale, $\Delta\tau$ (by use of Taylor's hypothesis) is chosen and a new time series can be created, formed of the difference between the points in the original sample data, as shown below:

$$\Delta B_t = B_t(t + \Delta\tau) - B_t(t). \tag{2.36}$$

This new time series is then normalised by its standard deviation, σ, giving the PVI, ξ, defined as:

$$\xi = \frac{\Delta B_t}{\sigma}, \tag{2.37}$$

where the standard deviation, $\sigma = \langle |\Delta B_t|^2 \rangle^{1/2}$ ($\langle\rangle$ represents the average value) and B_t is a time series of a measured variable. Plotting PDFs of ξ shows the statistical properties of the turbulence. When $\Delta\tau$ is large the PDF is Gaussian. At smaller scales the distribution departs from the Gaussian shape, and develops strong "wings" indicating increased probability of large ΔB from the average. This behaviour is attributed to intermittency. Note, that the value $\langle \xi^4 \rangle$ is related to the Kurtosis

(pointyness) of the PDF, and so assigns a quantitative value to the property of intermittency. A example of an intermittent PDF is shown in blue in Fig. 2.17, plotted using solar wind measurements from the ACE and Wind spacecraft [Osman et al., 2011]. A Gaussian probability density distribution with unit variance is shown in red.

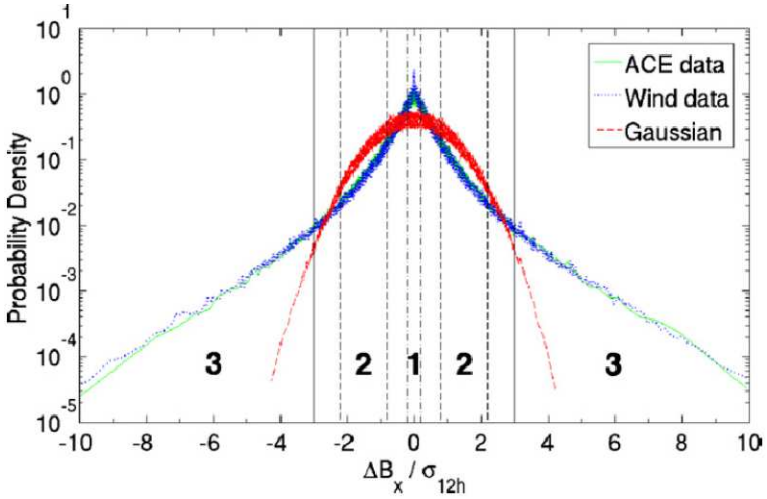

Figure 2.17.: PDFs of the Geocentric Solar Ecliptic (GSE) coordinate system x-component magnetic field increment, using a 96 s separation, normalized by the 12 h standard deviation. Magnetic field data from the MFI instrument on board Wind (3 s resolution) and from the MAG instrument on board ACE (16 s resolution) are used. Each bin contains 100 data points. The other GSE coordinate components behave in a similar manner. For comparison, a unit variance Gaussian is also shown. Three regions are identified: (1) super-Gaussian core, (2) sub-Gaussian mid-section, and (3) super-Gaussian tails. (Figure from Osman et al. [2011].)

Figure 2.17 highlights super-Gaussian (1 & 3) and sub-Gaussian regions (2). Matching these regions to locations in 2D MHD simulations reveals information about which structures contribute to intermittency. Greco et al. [2009] showed that region 3 corresponds in MHD turbulence to small scale coherent structures, (e.g. current sheets near reconnection sites) whereas region 1 corresponds to areas of low value fluctuations usually between magnetic islands, and the areas of region 2 are associated with the centres of magnetic islands.

Therefore, turbulence in plasma naturally causes intermittency, and high values of PVI usually indicate coherent structures. So what other kinds of structures can exist in the solar wind? The literature discusses two main types of 1D structure that creates discontinuities (e.g., large $\Delta\mathbf{B}$) in the measured properties: one dimensional

current sheets, where the value of the magnetic field changes sign across it, and shock waves [Bruno and Carbone, 2013]. Current sheets can also form in 2D structures, and can be related to magnetic reconnection events (Chapter 3).

Another type of structure relates back to the Alfvénic properties of the plasma that is believed to generate the energy for the turbulent spectrum, namely flux tubes (Fig. 2.18). These are large filament structures, described by Bruno et al. [2001] and later by Borovsky [2008] that are convected with the expanding solar wind. Each tube has its own marginally different field direction, and within each tube Alfvénic fluctuations make the local field wander randomly about its own direction. This concept of tangled ropes, or spaghetti like structures fits with the discussion in Section 2.3 about the generation of Alfvén waves at the footpoints of the Sun's magnetic field lines. Any twisting of these footpoints on the photosphere would naturally create these tangled structures.

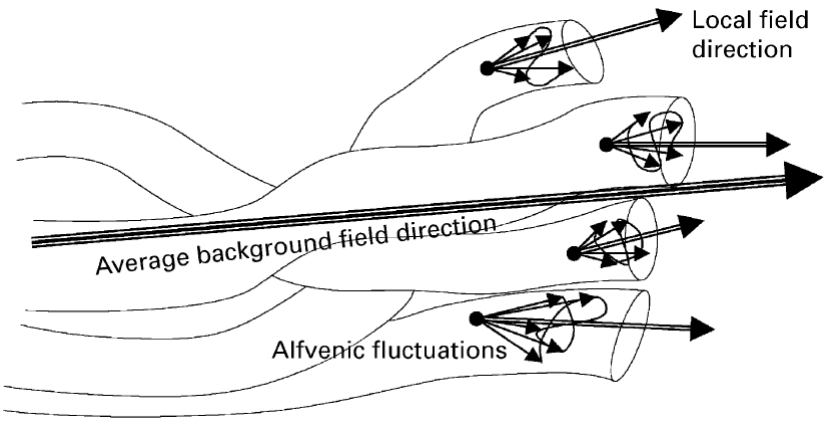

Figure 2.18.: Visualization of a flux tube filament structure. (Figure from Bruno et al. [2001].)

Other types of coherent structures can also form within plasma such as magnetic holes, and vortices, that also contribute to its intermittent nature. This will be the subject of new research described in detail in Chapter 5.

2.4. Simulations of turbulence

There are many examples of simulations of turbulence over the years, far too many to cover all of them in this thesis. Early, historically speaking, works used MHD codes to simulate inertial range turbulence. More recently attempts have been made to try and explain the observation within the dispersion range of turbulence, and beyond. Given the success of MHD at explaining the inertial range spectra, the question

remains what wave modes can be responsible to the turbulence interactions at sub-ion scales. The two likely candidates are whistler waves, and kinetic Alfvén waves. It has proven difficult to isolate these waves in observations due to the similarity of their dispersion relations. However, a recent paper [Chen et al., 2013] uses density fluctuations of the two waves to establish a difference between the two. The ratio $\delta n^2/\delta B^2$ should be of the order ~ 1 for KAW and ~ 0.03 for whistler waves [Chen et al., 2013]. The values seen in observations and KAW simulation is closer to 0.75 hinting that KAWs are the more likely candidate. The following section discusses some example simulations selected from the literature, in order to give an impression of the range of simulation types and how they are used.

2.4.1. Whistler turbulence

Gary et al. [2008] investigated plasma turbulence in the regime after the ion scale breakpoint f_i (Fig. 2.8), in the dispersion range, using a PIC code. They pointed out that MHD is not a complete description of plasma and only allows for long wavelength, low frequency waves. Additional physics is included in Hall MHD models, and ion kinetic processes can be investigated using hybrid codes. However, a full investigation into the change in slope in the dispersion range can only be done with fully kinetic codes with both ions and electrons treated as particles. They argued that there is not a great deal of evidence to suggest that the change in slope after f_i is associated with dissipation, but it is more likely to be associated with a change in the wave interactions within the cascade from non-dispersive MHD scale Alfvén waves to waves which are dispersive such as kinetic Alfvén modes, [Bale et al., 2005, Leamon et al., 1998] and/or whistler modes [Beinroth and Neubauer, 1981, Lengyel-Frey et al., 1996].

To demonstrate this, the authors generated an initial population of whistler waves using a 2D PIC simulation in a square periodic box, with a length of $102.4\lambda_e$, where λ_e is the electron inertial length. The grid size was 1024×1024 cells, so the cell size was $0.1\lambda_e$. The simulation used realistic mass ratio, $m_i/m_e = 1836$ with 64 particles per cell, initially loaded with an isotropic Maxwellian distribution, with equal ion and electron temperatures, $T_i = T_e$. The plasma ion beta is quoted as $\beta_p = 0.1$. With temperatures equal, and assuming charge neutrality, $n_e = n_i$, gives the electron beta, $\beta_e = 0.1$. Using the relation $\frac{\rho_e}{\lambda_e} = \sqrt{\frac{\beta_e}{2}}$,where ρ_e is the electron Larmor radius, gives $\rho_e = 0.224\lambda_e = 2.24$ cells, so the electron gyro-radius is resolved. The ion Larmor radius, $\rho_i = \rho_e \times \sqrt{1836} \sim 96$ cells. The background magnetic field is initially set in the in-plane x direction only, $\mathbf{B} = B_0\hat{\mathbf{x}}$.

The simulation domain was initialized with 42 different whistler wave mode perturbations. The $k_{\|}$ wavevectors used were equivalent to the largest three wavemodes the box could support (in each direction). The k_y wavevectors were the same size as the parallel modes, including the additional $k = 0$ mode. The magnetic perturbation was limited to a maximum value of $|\delta B^2| = 0.1B_0^2$. The electric field was perturbed according to Faradays equation, and the necessary current was induced by adding bulk drifts to the electron Maxwellian distributions. The simulation was then allowed to evolve for a time-period of $T = 447\Omega_e^{-1}$.

The simulation results show that power cascades to smaller wavevectors, with more power in the perpendicular fluctuations. Power law fits to graphs of $|\delta B^2|$ give spectral indices of $k_{\|} \propto 6.8$ and $k_{\perp} \propto 4.6$. The preference for energy to flow in the perpendicular direction is shown in Fig. 2.19.

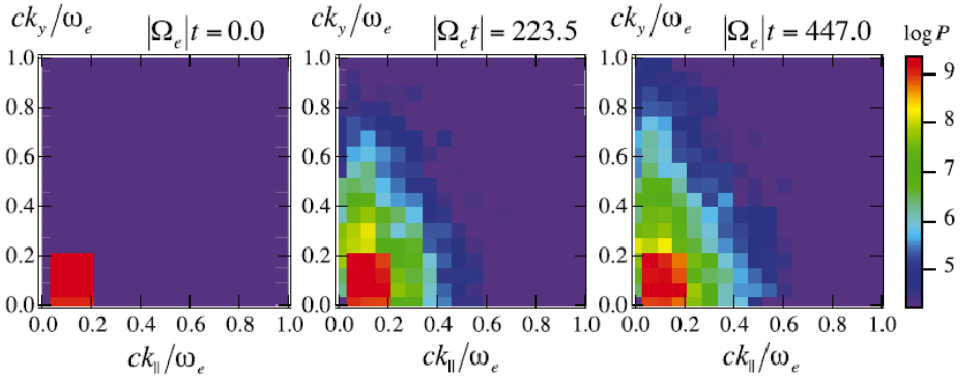

Figure 2.19.: Magnetic field fluctuation energy density as a function of $k_{\|}$ and $k_{\perp}$ at $t = 0$ and two subsequent times. (Figure from Gary et al. [2008].)

The authors also performed 1D simulations, with only the parallel dimension included. They found, in this case, that no evidence of a cascade to smaller energy scales, which indicates the whistler modes preference to cascade in the perpendicular direction.

The main simulation also showed that the electrons are preferentially heated in the parallel direction, as demonstrated by plotting the difference of initial and final electron VDFs. The heating mechanism proposed is the damping of the parallel propagating whistler waves via Landau resonance. This would transfer the wave energy of the whistlers into kinetic energy of the electrons.

In conclusion, these simulations show that a cascade of whistler waves can contribute to the steeper spectra seen in the "dispersion" range of solar wind turbulence, below ion scales, where MHD is no longer valid.

The simulation is useful at examining the properties of a "pure" whistler cascade

below ion scales, and being a PIC simulation, all kinetic effects such as wave-particle interactions are fully modelled. The weakness of this simulation is that the solar wind may not just contain whistler waves. It is known that both kinetic Alfvén waves and whistler waves are both possible modes below ion scales [Chen et al., 2013]. Perhaps an improvement to this work might have been the use of a perturbation that generates larger scale Alfvén waves, and analyse its cascade to the sub-proton scales, and look for evidence of mode changes into either the whistler mode, or the kinetic Alfvén mode.

2.4.2. Kinetic Alfvén wave turbulence

Boldyrev and Perez [2012] also investigated the cascade of plasma turbulence below the ion scale breakpoint, f_i. However, the authors used a two fluid model of kinetic Alfvén waves (KAWs), in the regime of strong turbulence. This approach allows for a cascade of waves, but effectively removes Landau damping or any other wave-particle interactions from the simulation. This enabled a more direct comparison of undamped KAW turbulence to the theories of MHD turbulence, which are heavily based on a fluid description of the plasma (Section 2.2).

The authors formulated a system of equations to describe KAW waves/turbulence using two-fluid MHD. A guide field is assumed to be out of the plane (z direction). The magnetic field is assumed much stronger than the turbulent fluctuations in the system. Electrons are treated as an isothermal fluid, and ion parallel motion is neglected. A scale size for the system is chosen, specific for the KAW regime, that is scales smaller than the ion gyroscale, $k_\perp \rho_i \gg 1$, where ρ_i is the ion thermal larmor radius. A nonlinear (fluid) system of equations are formulated which includes the critical balance between parallel and perpendicular fluctuations, which are anisotropic as in GS95 (Section 2.2.3). The equations are linearized in such a way so that they only include fluctuations matching the KAW dispersion relation, $\omega = k_z k_\perp$. Using this system, they derived a scaling law of $E(k_\perp) \propto k_\perp^{-7/3}$ that they would expect from the system of equations. Then they used a pseudo-spectral code to numerically simulate that system.

The numerical simulation was performed in a 3 dimensional cube, in a grid of 512^3 cells. The length of the cube, L, was $L = \rho_s$ (spatial scales were normalised to ρ_s and $L = 1$) where ρ_s is the ion acoustic scale $\rho_s = \dfrac{v_S}{\Omega_{ci}}$ and the sound speed, $v_S = \sqrt{\dfrac{k_b T_e}{m_i}}$. (Note for equal ion and electron temperatures, $T_e = T_i$, the sound speed is equal to the ion thermal velocity.) The simulation was periodically driven

by randomised forces at large scales, in order to provide a constant input of energy, driving a forward cascade of KAWs, through nonlinear interactions of the driven and existing waves. Damping and dissipation is provided by introducing plasma resistivity and electron diffusivity, which are quoted as being small but necessary for stability of the code.

The results of the numerical simulation showed that the energy spectra which resulted was $E(k_\perp) \propto k_\perp^{-8/3}$. The reason for this discrepancy in spectral index is shown in Fig. 2.20. The numerical model showed that the nonlinear KAW interactions only occurred in localised 2D structures, an assumption not incorporated into the previous calculations of the model's spectral index. Applying a filter to remove large wavelength fluctuations revealed the shape of these structures. These were organized into elongated, 2D "sausage" shapes or sheets, of magnetic and density fluctuations (Fig. 2.20). Introducing a space-filling fraction to the theoretical scaling law calculations allowed the authors to match their theory to the numerical simulation result of $E(k_\perp) \propto k_\perp^{-8/3}$.

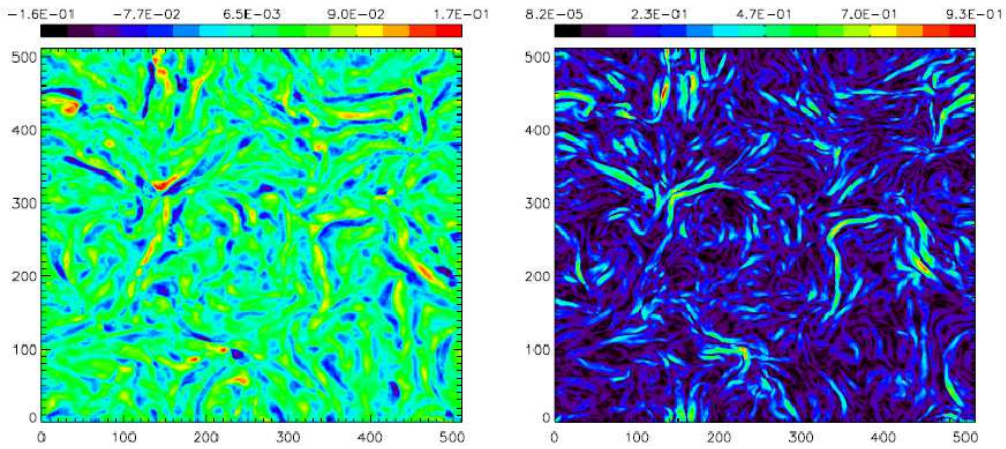

Figure 2.20.: Density fluctuations (left) and amplitude of magnetic-field fluctuations (right) in a field-perpendicular cross section of a KAW simulation. The large-scale harmonics with $k < 2\pi/12$ have been filtered out; the plot thus represents fluctuations in the inertial interval. The plot suggests that both density and magnetic fluctuations are concentrated along two-dimensional structures. Corresponding field-parallel cross sections (not shown here) are consistent with this picture. (Caption and figure from Boldyrev and Perez [2012].)

In conclusion, the authors state that $E(k_\perp) \propto k_\perp^{-8/3}$ should be the theoretical spectral slope of (two-fluid) KAW turbulence below ion scales. Since this value tends to agree with observations, [Alexandrova et al., 2008, Chen et al., 2010] and their model does not include Landau damping or wave-particle interactions, they

suggest that these additional physical processes may not be as important as thought for solar wind turbulence.

The advantages of this simulation is that it allows us to examine a "pure" cascade of KAW turbulence, below ion scales, which provides evidence to backup theoretical predictions for the cascade in turbulent plasma. There are, however many disadvantages to this technique. Firstly, it does not allow us to examine the mode transition from the large scale, Alfvén wave cascade to the KAW regime. Secondly the electrons are assumed thermally isotropic, and fluid-like. In Chapter 4 we will show evidence that electron temperatures fluctuate and are inherently anisotropic at sub-proton scales. In Chapter 6 we will show that non-fluid/kinetic effects, such as beam mode generation in non-maxwellian VDFs can play a large role in sub-proton scale plasma. Thirdly, the code inherently does not include the effects of wave-particle interactions and Landau damping. As we shall discuss in Chapter 6 these are potential sources of dissipation in the plasma, so they do have an impact on turbulence. In terms of a collisionless plasma, the "extra" terms of resistivity and diffusion that the authors had to include for stability do not make physical sense. The authors have added artificial dissipation in their simulation, and the physics of wave-particle interactions, which they do not simulate, is essential for understanding this in collsionless plasma. Despite this, the description of a space filling fraction for KAW is a useful tool, when understanding measurements of spectra in turbulent cascades.

2.4.3. Shear driven turbulence

Karimabadi et al. [2013] used a kinetic PIC simulation on a huge (computational) scale to span both ion and electron scales to investigate the nature of dissipation in a hot turbulent plasma. The authors make the point that studies focusing on models with one type of wave (Section 2.4.1) or fluid descriptions of a single/reduced wave modes (Section 2.4.2) are valuable for studying specific processes, but are missing important physics at kinetic scales.

In this study turbulence was initiated by means of a shear flow in an initially neutral electron proton plasma. This generated the well known Kelvin-Helmholtz instability (KHI), and created large scale vortices that "rolled up" and generated smaller and smaller vortices in a wide range of scale sizes (Fig. 2.21).

The simulation used a non-realistic mass ratio, $m_i/m_e = 100$. The magnetic field was set in the yz plane with an angle of $\theta = 2.86$ to the z axis. The simulation domain was rectangular in the x-y plane with a size of $50 \times 100\lambda_i$, and 8192×16382 cells, and a cell size of $0.77\lambda_D$. The particles were initially loaded with Maxwellian

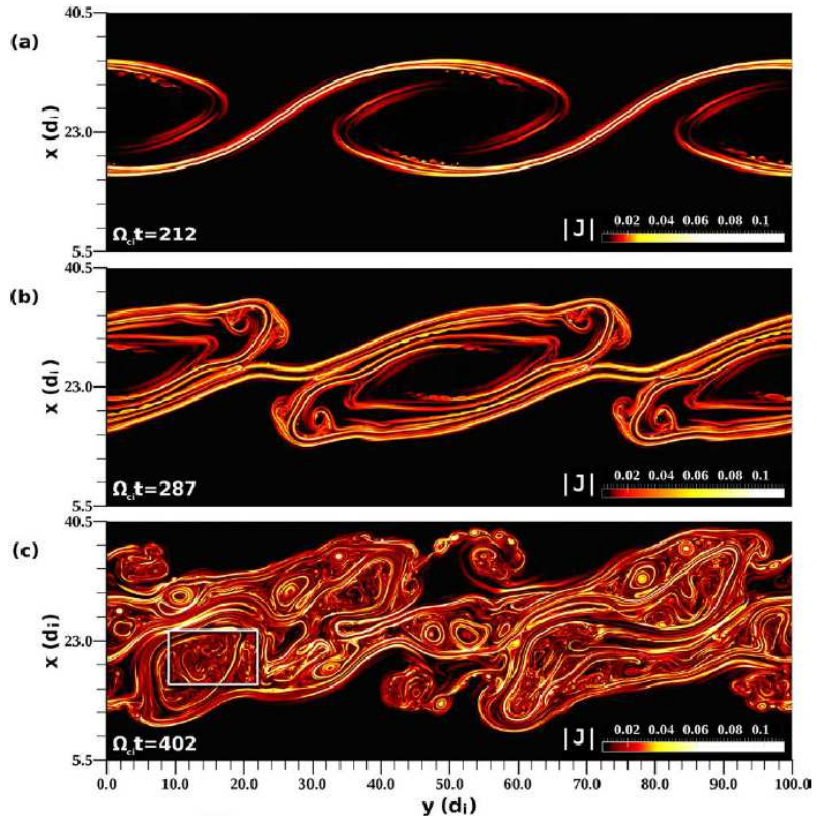

Figure 2.21.: Development of KHI induced turbulence in physical space. (a) Formation of current sheets on the edge of the vortex. Current is normalized to en_0c. (b) Wrapping of current sheets inside the vortex and continuation of secondary instabilities. (c) Full development of turbulence. (Caption and figure from Karimabadi et al. [2013].)

velocity distributions. The temperature was set the same for each species, $T_i = T_e$, with 150 particles per cell per species. A large scale KHI was initiated by introducing a bulk velocity shear of form $\tanh(y)$, with a shear layer half-thickness, $L_V = 4\lambda_i$. An electric field to support the cross field flow was also introduced , along with a small excess of electrons to support this electric field. The plasma beta was 0.1. The simulation was run for a time period of $T = 507\Omega_{ci}^{-1}$. Where Ω_{ci} is the ion gyro-frequency.

The KH perturbation first developed vortices on a large scale (Fig. 2.21(a)) followed by current sheet formation, and secondary instabilities, such as the tearing mode (Fig. 2.21(b)). This is where a thin current sheet between anti-parallel magnetic field lines undergoes filamentation into smaller magnetic islands, via diffusion and reconnection. Eventually, the simulation transitioned to a state of fully developed turbulence, which was confirmed by the fluid-like appearance of the simulation, multi-scale vortices and the development of a power spectrum with a $k^{-5/3}$ power

law (Fig. 2.21(c)). Movement of the large scale structures was shown to generate compressional magneto-sonic waves, and (low compressional) shear Alfvén waves, that propagated outside of the largest scale KH vortex. FFT analysis in this area showed that these modes matched overlays of the appropriate dispersion relation for that mode.

The magnetic fluctuations formed a Kolmogorov power law ($k^{-5/3}$) before the ion inertial length and a power law of $k^{-8/3}$ between the ion inertial and electron inertial lengths. Beyond this there was no clear power law, but the gradient did increase further as it approached smaller (electron) scales. The ion and electron velocity spectra initially followed the magnetic spectra, and showed a break at the ion inertial length. However, between this and the electron inertial length the electron velocity spectra was much steeper. The implication of this is that the onset of kinetic effects has affected the electron energy cascade.

The authors presented probability distribution functions (PDFs) of the increments of the magnetic fluctuations, in order to show the presence of coherent structures, associated with intermittency (Section 2.3.3). As in previous studies, the probability of finding large fluctuations becomes larger than that given by a Gaussian distribution, as the separation distance is reduced, indicating the presence of intermittency and coherent structures.

The authors used electron VDFs to show that the electrons are preferentially heated in the parallel direction (to the magnetic field). Cross sections of electron temperature anisotropy, $T_{\perp e}/T_{\parallel e}$ ranged from 0.5 to 3, with an average of ~ 1. Ion temperature anisotropy, $T_{\perp i}/T_{\parallel i}$, ranged from 0.5 to 4, with an average value slightly above 1.

The authors also used the diagnostic $\mathbf{E}_{\parallel}.\mathbf{J}_{\parallel}$ to show areas of dissipation. This is because the energy budget showed a large proportion of the energy conversion from the initial ion bulk flows had gone into heating the electrons ($\sim 50\%$). Since $\mathbf{E}_{\parallel}.\mathbf{J}_{\parallel}$ is the rate of work done per unit volume on the particles by the electric field (in the parallel direction) then this diagnostic represents a large proportion of the total dissipation. Spatial plots of this diagnostic showed it was localized within the thin current sheets. As we will discuss in Chapter 6, this diagnostic is a useful tool, however care should be taken with its interpretation. Negative values indicate that energy has been transferred from the particles to the electric field. If dissipation is defined as the process of transferring energy back to the medium, then the authors should have specifically plotted only positive values of $\mathbf{E}_{\parallel}.\mathbf{J}_{\parallel}$, and no indication of this is mentioned in the paper. It would have also been useful to compare the positive values of this diagnostic against positive regions of $\mathbf{E}.\mathbf{J}$. This indicates

regions of "dissipation" regardless of direction. Comparison of just the parallel and total diagnostics can indicate where only parallel dissipation occurs, and can reveal information about which processes are occurring where in space.

The authors also showed that the dissipation levels in their simulation matched the theoretical Taylor-von Karman estimate $\epsilon \sim U^3/L$ for a chosen length scale L and turbulence amplitude U, showing that the simulation can be matched to turbulence theory.

2D and 3D simulations of shear turbulence were also compared. The spectra of these comparison simulations were shown to be qualitatively similar. The main difference was that more instabilities were excited in the 3D simulation, because of the addition of the extra dimension, such as an increased amount of tearing modes. In conclusion the authors compared the electric potential energy of a KAW to that of the heating potential of reconnection sites (associated with current sheets). The potential of the reconnection sites were 100 times greater than KAWs. The suggestion therefore is that the formation of reconnection and thin current sheets could entirely explain the currently observed heating rates in the solar wind.

This work is visually impressive, but its main flaw (in addition to the dissipation diagnostics) is that although strong shear layers do exist in the solar wind (e.g. at CIRs) they are not anticipated to be everywhere within the wind. Therefore shear induced turbulence only applies to localised phenomena in the heliosphere, e.g. at magnetospheric and other plasma boundaries. The concept of nonlinearly interacting counter-propagating Alfvén waves (Section 2.3) is not addressed, which would be the more likely mode of turbulence generation in the solar wind. Also the question of the what the actual "local" dissipation mechanism is, in a collisionless plasma medium is not fully addressed. Localising positive values of $\mathbf{J}.\mathbf{E}$ and $\mathbf{J}_{\parallel}.\mathbf{E}_{\parallel}$, and examining localised electron and ion VDFs in these regions would help to isolate the kinetic modes/waves/instabilities that could be occurring at the kinetic level.

2.4.4. Hybrid-Vlasov turbulence

Servidio et al. [2012] investigated kinetic effects within turbulence using a hybrid-Vlasov code. In this code the electrons were treated as a charge neutralising fluid, and the ions were described using the Vlasov-Maxwell system of equations. The simulation was 2D in physical space and 3D in velocity space. This approach allowed the authors to investigate the kinetic effects of just the ion population within a turbulent field, using statistical methods.

Turbulence was initiated by perturbing both the magnetic field (initially in the

out of plane z direction) and velocity field with random fluctuations with wavenumbers ranging from $2 <= L_0 k/2\pi <= 6$, with random phases. The simulation used periodic boundary conditions. These conditions initiate a decaying simulation of turbulence, where no additional energy is injected into the system after $t = 0$.

Several runs were made, with different sizes ranging from $L_0 \approx 63$ to $189\lambda_i$. Initial values of $\delta B/B_0$ ranged from 1/3 to 1/7. The authors used the parameter $\langle j_Z \rangle$ (where $\langle\rangle$ is a spatial average over the 2D domain, and j is the current density) to measure the amount of turbulent activity. This parameter had a maximum at different times in the simulations, with the peak time defined as τ^*.

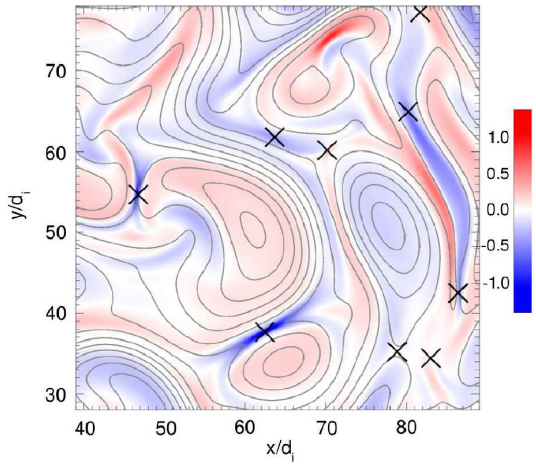

Figure 2.22.: Shaded contours (zoom) of j_Z together with A_Z (isolines) and its X-points (black crosses). (Caption and figure from Servidio et al. [2012].)

Magnetic field lines are plotted as contours of constant A_z, where $\mathbf{A}$ is the magnetic vector potential. Areas of magnetic reconnection are identified in Fig. 2.22 as crosses, which usually occur at the saddle points of A_z. The colour map in Fig. 2.22 shows j_Z is most intense between magnetic islands, and are several λ_i wide.

Figure 2.23 shows power spectra of the magnetic, electric fields, alongside bulk ion velocity and ion density. The electric magnetic and velocity spectra all show a power law form slightly steeper than Kolmogorov's $-5/3$ value, consistent with other studies. The magnetic, electric and velocity spectra are all parallel (with slope $\sim -5/3$) until the ion inertial length, λ_i where the gradients begin to deviate from each other, indicating the onset of kinetic effects. All spectra steepen after this scale, and appear to have a curved, non-power law shape.

The authors used the following technique to analyse the ion temperature anisotropy in three dimensions: The stress tensor is computed for each position in the simulation at $t = \tau^*$. Then the eigenvalues $(\lambda_1, \lambda_2, \lambda_3)$ and eigenvectors $(\mathbf{e_1}, \mathbf{e_2}, \mathbf{e_3})$ of the stress tensor are calculated. The normalized eigenvectors represent the minimum

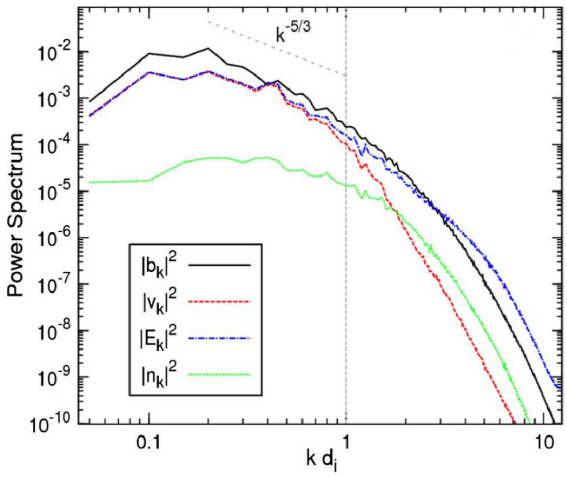

Figure 2.23.: Power spectra of ion density (green dotted), ion bulk velocity (red dashed), magnetic field (black solid), and electric field (dot dashed blue). The Kolmogorov expectation $k^{-5/3}$ (gray dashed) is reported as a reference, while the vertical dashed line represents the ion skin depth wave number. (Caption and figure from Servidio et al. [2012].)

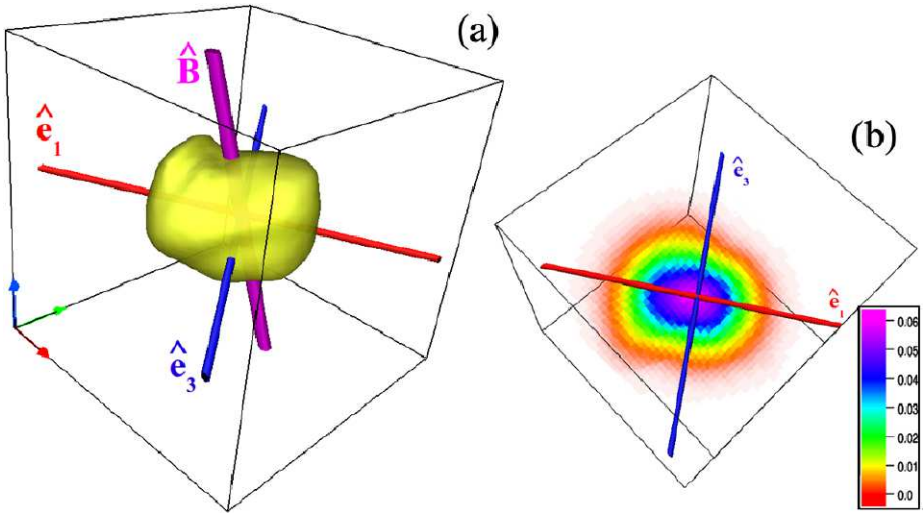

Figure 2.24.: Isosurfaces of the velocity distribution function $f(\mathbf{x}^*, \mathbf{v})$, at a given spatial position $\mathbf{x}^* \approx (60, 119)\lambda_i$. (b) Two-dimensional cut of f in the minimum variance frame. Thin (red) and thicker (blue) axis indicate $\hat{e}_1$ and $\hat{e}_3$, respectively. The magnetic field direction $\hat{B}$ is represented with a thick (magenta) tube. (Figure from Servidio et al. [2012].)

variance frame (MVF). The eigenvalues are defined so that $\lambda_1 > \lambda_2 > \lambda_3$. These represent the temperature in the direction specified by the corresponding eigenvector. The authors then defined the anisotropy as λ_1/λ_3. Using this technique they show that maximum anisotropy values occur in thin sheet structures, and are comparable to the current sheets identified in Fig. 2.22.

Figure 2.24(a) shows an example ion VDF, by plotting a single isosurface, with corresponding eigenvectors and magnetic field direction shown. The structure resembles an elongated potato shape, stretched in the $\hat{\mathbf{e}}_1$ direction. Note that, in this example, this would represent a perpendicular temperature anisotropy, with the largest temperature, $\lambda_1 \perp \mathbf{B}$. A cross section of the VDF is also shown in Fig. 2.24(b).

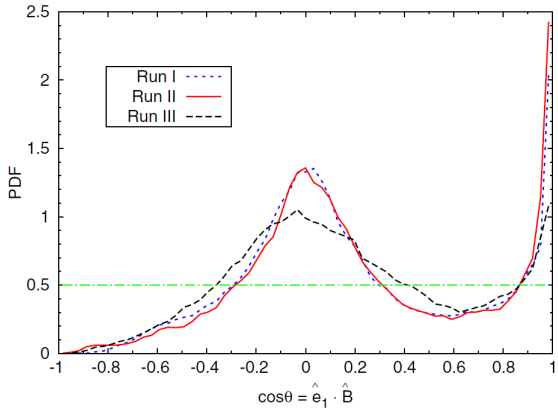

Figure 2.25.: PDF of the cosine angle given by $\cos\theta = \hat{\mathbf{e}}_1.\hat{\mathbf{B}}$ for all runs. The horizontal (green) dot-dashed line represents the distribution in the case of random variables. (Figure from Servidio et al. [2012].)

Finally, the authors show a PDF for all runs of $\cos\theta = \hat{\mathbf{e}}_1.\hat{\mathbf{B}}$ (Fig. 2.25). For randomly distributed $\cos\theta$, the PDF would have a constant value of 0.5. However a clear pattern emerges showing two peaks where the maximum temperature is parallel to the mean field ($\cos\theta = 1$), or perpendicular to it ($\cos\theta = 0$). The authors conclude that kinetic effects in turbulent plasmas are strongly inhomogeneous, due to complex interactions between the velocity distribution functions and the turbulent background. This is described as "kinetic intermittency", and the implication is that fully kinetic descriptions of plasma (including a kinetic description of electrons) will be necessary to fully understand turbulent plasma behaviour. This is generally an interesting paper, which shows new and novel analysis techniques. It demonstrates that in order to understand the mechanisms of turbulence, we must plot distribution functions locally, in regions which have macro-scale properties of interest, and then use the distribution function to look for kinetic effects. Its main drawback is the lack of kinetic electrons, so it is still only concerned with ion-scale kinetics. applying such techniques to full Vlasov (with kinetic electron) and or PIC simulations might reveal more underlying physics.

2.4.5. Lessons from simulations

These example simulations, demonstrate the scale of the plasma turbulence problem. Even with the fastest supercomputers (Section 2.4.3) a full kinetic description using PIC codes still required the use of non-physical mass ratio, in order to be able to simulate across ion and electron scales. It is therefore necessary to use other codes such as MHD, hybrid and Vlasov codes, to explore specific regions of the plasma scale regime. Authors must therefore bear in mind the limitation of the code being used, and make conclusions accordingly.

Theoretical models (Section 2.4.2) are useful tools to investigate turbulent cascades in controlled environments, where certain physical properties are removed or neglected, but their focus seems primarily on explaining the expected slopes of the spectra, rather than the physical mechanisms of dissipation.

Models that simulate only one wave mode have the problem of applicability, since we are still unsure if KAW or whistler waves are responsible for the sub-proton scale cascades seen in the actual solar wind. Despite this, simulations with one type of wave mode (Section 2.4.1 and 2.4.2) might prove useful when identifying wave-modes in actual observations, or more complex simulations where multiple wave modes might exist. Multi-scale simulations (Section 2.4.3) are best suited to attempt to observe mode transitions from Alfvén waves to kinetic scale waves, and if they are fully kinetic (Section 2.4.1 and 2.4.3) then they can probe the small scale physics of actual collisionless reconnection, and dissipation mechanisms. Fully kinetic codes that examine the electron scale regime should make full use of their kinetic nature and plot local electron VDFs in order to link macro-scale properties to kinetic scale phenomena.

3. Magnetic reconnection physics

3.1. Introduction

Magnetic reconnection is a prime example of a nonlinear process in plasmas that is ubiquitous throughout the heliosphere. It involves a change in magnetic topology, into a state with lower energy, converting the released magnetic energy into kinetic energy. In the collisionless case, this can be kinetic or thermal energy, resulting in energetic particles (and possibly waves). The basic concept involves anti-parallel field lines (or an anti-parallel component) moving together until they meet creating an "X" shape. Conceptually, at this point, the field lines can be thought to break and "reconnect" (hence the name) to one part of the opposing field line. This idea is shown diagrammatically in Fig. 3.1. The area where the field is reorganized is indicated by a grey box in the figure. Outside this box, the plasma is assumed to obey the laws of ideal MHD where convection dominates and the plasma is frozen to the magnetic field lines. However, in this small region conductivity is no longer assumed infinite, resulting in the breakdown of ideal MHD, and magnetic diffusion dominates, allowing the field lines to slip and change connection. This area is known as the diffusion region.

There are many examples of reconnection in our solar system, e.g. the solar wind, when the IMF is southward, is deflected around the Earth's magnetic field. This interaction creates several reconnection sites at the sunward interface, and again when the field re-configures toward the geomagnetic tail. There are also suggestions that the unexplained high solar corona temperature (in excess of 1×10^6 K) could be due to micro-reconnection events in the coronal atmosphere, as there is abundant magnetic energy closer to the Sun to provide the necessary energy source. However the main drive to find a suitable model for reconnection rate was through the study of solar flares. Solar flare models are largely based around hot flux tubes in hydrostatic equilibrium which are ejected out into the solar system when the magnetic field suddenly changes configuration due to reconnection. Observations of these events, and comparison to MHD models showed that they occurred on timescales much

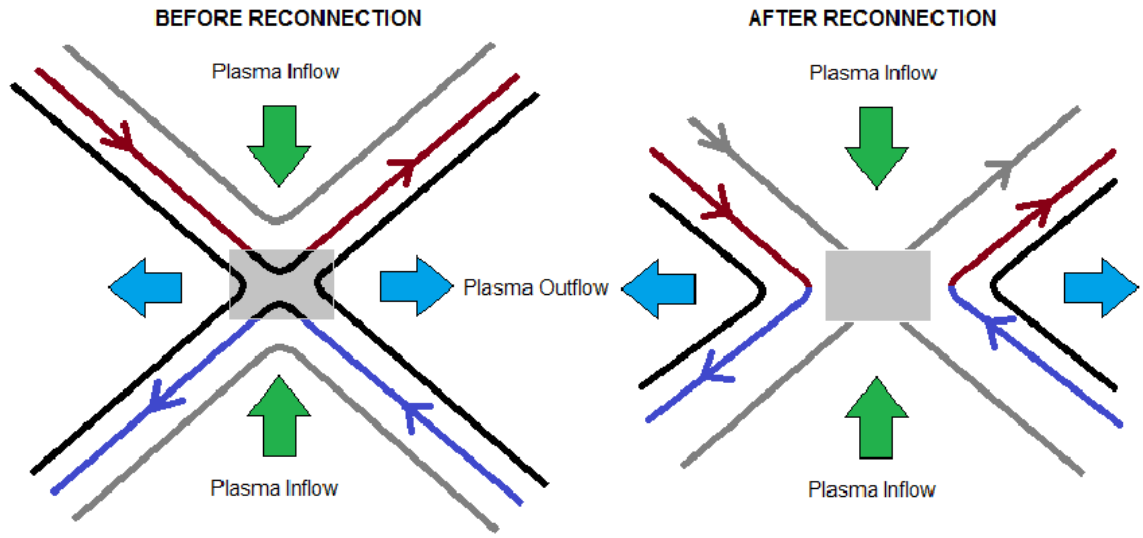

Figure 3.1.: Basic concept of field line breaking at "X" shaped magnetic field lines.

faster than predicted. This is believed to be a result of the collisional, dissipative nature of the MHD equations, and therefore the ultimate quest is to understand how fast, collisionless, kinetic reconnection occurs in such systems, and in the solar wind.

3.2. Sweet-Parker reconnection

Sweet and Parker were the first to describe a model based on MHD that could explain the essential plasma physics of reconnection phenomena, and this was used to make predictions for how fast reconnection should occur. The basic model involved ideal MHD plasma with anti-parallel field lines, flowing together into a diffusion region. The diffusion region is assumed to be long and thin, with the shorter width being the outflow region. Anti-parallel field lines create a current between them, due to Ampere's law, as shown in Fig. 3.2. This current sheet has a length $2L$ and a width/thickness $2l$. In-flow velocities are V_i and outflow velocities are V_o. Reconnection speeds/rates are often defined by the speed of the inflow, but can also be defined by the perpendicular electric field, depending on preference. I will now calculate the reconnection rate (inflow speed) for the Sweet Parker model.

The width of the current sheet can be estimated by evaluating the magnitude of the electric field generated by the plasma inflow: Using one fluid Ohm's law, and assuming the electrical conductivity, σ, outside the diffusion region is very large (ideal MHD) then the electric field reduces to $\mathbf{E} = -\mathbf{V} \times \mathbf{B}$. Given the uniform geometry as shown in Fig. 3.2, the magnitude of the electric field is $B.V_i$. Inside

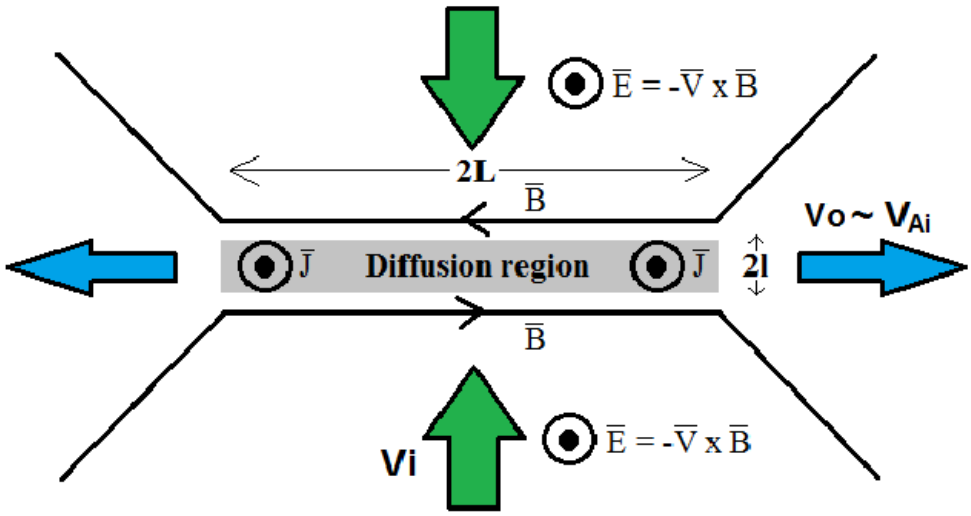

Figure 3.2.: Sweet-Parker reconnection configuration.

the diffusion region, we assume a steady state and use Ampere's law to estimate the value of the current, **J**. Since the velocity of the inflow must become stationary (or change direction towards the outflow) towards the centre of the diffusion region, the electric field can be found using, $\mathbf{J}/\sigma$. Assuming a constant electric field inside and outside the diffusion region, we can find an expression for the approximate width/thickness for the current sheet:

$$l \approx \frac{1}{\mu_0 \sigma V_i}. \tag{3.1}$$

This instantly has implications for most astrophysical plasmas, which have a high, sometimes assumed infinite, electrical conductivity, (or small resistivity $\eta = 1/\sigma$) as the size of l will be very small.

If we attribute the kinetic energy of the outflow (ignoring any heating or other effects) to the flux of incoming electromagnetic energy we find that the outflow velocity must be $V_o \approx V_{Ai}$, where V_{Ai} is the Alfvén velocity associated with the inflow region. Conserving plasma mass flow, into and out of the region, we can write $V_i L = V_o l$, and end up with the following expression for the inflow velocity:

$$V_{S-P} \approx \sqrt{\frac{V_{Ai}}{\mu_0 \sigma L}} = \frac{V_{Ai}}{\sqrt{S}} = \frac{V_{Ai}}{\sqrt{R_m}}, \tag{3.2}$$

where S is the Lundquist number, the ratio of the local Alfvén timescale to diffusion timescale, given by $S = \mu_0 \sigma L V_{Ai}$. (This is equivalent to the magnetic Reynolds number, R_m, the ratio of the convection and diffusion terms of the MHD induction

equation.)

Equation 3.2 is the Sweet-Parker reconnection rate. This model was a great leap forward in understanding reconnection, but its main drawback is that the rates it predicts are too slow to explain the observations solar flare events. In the solar corona, R_m is very large, typically 1×10^{12} to 1×10^{14}. Using a characteristic V_A of $1 \times 10^8\,\mathrm{cm\,s^{-1}}$ and length scale of $1 \times 10^8 - 1 \times 10^9\,\mathrm{cm}$, the Alfvén time, $t_A = 1 - 10\,\mathrm{s}$. Therefore the Sweet-Parker model yields a figure of $1 \times 10^6 - 1 \times 10^7\,\mathrm{s}$ (optimistically) or several days. This is far too slow to explain flare observations of several minutes to hours.

Equation 3.2 also reveals information about the relative sizes of the length to width of the diffusion region. Using the conservation of mass flows, it can be shown that:

$$l = \frac{L}{\sqrt{S}}. \tag{3.3}$$

Equation 3.3 shows that for plasmas with large S (as in most astrophysical plasmas) the thickness of the diffusion region will be very small compared to its length. This gives Sweet-Parker reconnection sites an elongated and flat geometry rather than the symmetric X pattern that might be naively expected.

3.3. Petschek reconnection

The limiting factor in the Sweet-Parker model is that the narrow outflow region (small l) only allows limited mass flow through the system, which severely limits the maximum reconnection rate. A modification to this model was suggested by Petschek [1964] who attempted to increase the rate of reconnection by adding slow mode shocks in the outflow region, which would allow a higher mass flow through the site. This led to the reconnection rate being a significant proportion of the Alfvén speed (typically $\approx 0.1 V_A$) with the maximum rate given by:

$$V_{Petschek} = \frac{\pi V_A}{8\ ln(S)}. \tag{3.4}$$

Using the plasma parameters in Section 3.2, Eq. 3.4 yields a flare time of $700 - 800\,\mathrm{s}$, which is fast enough to explain the reconnection speeds observed in large scale solar flares events. Therefore the Petschek model was the commonly accepted explanation for observations of fast reconnection until Biskamp [1986] performed MHD simulations with uniform resistivity. He showed that Petschek's X-point shaped geometry eventually collapsed back into Sweet-Parker's elongated shape, when the

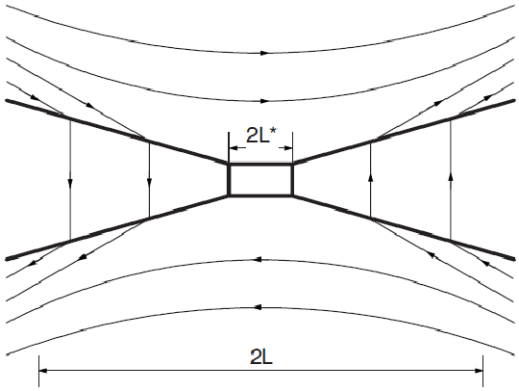

Figure 3.3.: Petschek reconnection configuration. (Figure from Yamada et al. [2010].)

reconnection rate was fast enough. This was later supported by the numerical simulations of Uzdensky and Kulsrud [2000], again with constant resistivity (Fig. 3.4).

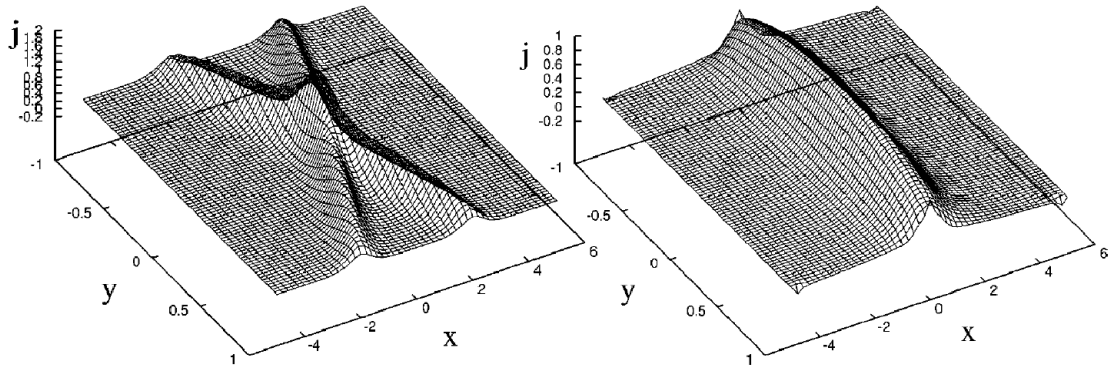

Figure 3.4.: (Left) The current density $j(x, y)$ at $t = 0$ for Petschek-like initial conditions.
(Right) The current density $j(x, y)$ in the steady state. (Figures from Uzdensky and Kulsrud [2000].)

Simulations of the Petschek model could be stabilized by using an non-uniform resisitivity, i.e., a larger value of resisitivity at the point of reconnection. This allowed Petschek-like simulations to remain stable and X-shaped. However, in a collsionless system, resistivity should be zero, therefore this was called "anomalous resistivity." Parker [1973] suggested that the intense currents in the diffusion region could cause localised turbulence, micro-instabilities, and particle scattering due to wave particle interactions, i.e. collision-like processes, creating the effects of increased resistivity in the area. Since these processes are not described by MHD additional terms can be added locally to simulate this additional resistivity. This has been used since

in many numerical simulation studies [Forbes, 2001, Scholer, 1989, Shibata and Magara, 2011, Ugai, 1992, Ugai and Tsuda, 1977, Yan et al., 1992], but many of these produced reconnection rates that depend on the resistivity, so these are still not truly "fast" collisionless kinetic reconnection.

3.4. Multi-species reconnection

If the width of the Sweet-Parker current layer is allowed to be thinner than an ion-inertial length, then the MHD equations would not be applicable in this region. The next logical step was to include multi-fluid effects. Essentially the fluid description of MHD still applies but the ions and electrons are treated as separate species. The equation of motion for each species is shown below:

$$n_s m_s \left(\frac{\partial}{\partial t} + \mathbf{V_s}.\nabla \right) \mathbf{V_s} = -\nabla P_s + n_s q_s (\mathbf{E} + \mathbf{V_s} \times \mathbf{B}) + K_s. \tag{3.5}$$

V_s is the species bulk velocity. n_s is the species number density. m_s is the species mass. P_s is the species pressure (scalar). q_s is the species charge. $\mathbf{E}$ and $\mathbf{B}$ are the electric and magnetic field. K_s is a term that describes momentum exchange between the species, which essentially acts like resistivity, η. The fluid equations are determined in a frame moving with each separate species, and the two sets (or more if additional species are included) of equations are then coupled via Maxwell's equations. Assuming an electron-proton plasma, the two equations of motion can be combined into the following form:

$$\begin{aligned} \mathbf{E} + \mathbf{V_e} \times \mathbf{B} = \; & + \frac{\mathbf{j}}{\sigma} - \frac{\mu}{enm_i}(\mathbf{j} \times \mathbf{B}) \\ & - \frac{1}{ne}\nabla \left(\frac{\mu P_e}{m_e} - \frac{\mu P_i}{m_i} \right) \\ & + \mu \frac{\partial}{\partial t} \left(\frac{\mathbf{j}}{ne^2} \right) + \frac{\mu}{e} \left(\mathbf{V_i}.\nabla \mathbf{V_i} - \mathbf{V_e}.\nabla \mathbf{V_e} \right), \end{aligned} \tag{3.6}$$

where I have assumed $n_i = n_e = n$ (i.e. charge neutrality, because the characteristic length scale is larger than the Debye length). $e = q_i = -q_e$, resulting in $\mathbf{j} = ne(\mathbf{V_i} - \mathbf{V_e})$ and $\mu = (m_i m_e)/(m_i + m_e)$. Equation 3.6 is known as generalized Ohm's law. It is easy to see why, as ignoring all but the first term on the right hand side, the equation is of the same form as for single-fluid, resistive, MHD. In this case the $\mathbf{V_e} \times \mathbf{B}$ term is the motional electric field for the electrons, where the moving electrons "see" an additional electric field due to the transformation of

that field into the moving frame. In the electron fluid frame $\mathbf{j} = \sigma \mathbf{E}'$ returning to the stationary Ohm's laws. Assuming ideal MHD, conductivity is infinite, all other terms are discarded and we simply have $\mathbf{E} + \mathbf{V_e} \times \mathbf{B} = 0$. This means that in ideal two fluid MHD, the magnetic field is frozen into the electron fluid. This parameter can be used to examine departures from ideality in multi-species simulations and will be used later in Chapter 4, 5 and 6. The "$\mathbf{j} \times \mathbf{B}$" term is called the "Hall term" and is responsible for the "Hall field" that appears in reconnection models that include it. The pressure gradient term on the second line in Eq. 3.6 will be dominated by the electron pressure (as $\mu \approx m_e$), and essentially says that an electric field will be generated by electron pressure gradients in order to counteract their formation. The terms on the remaining line are from the inertial parts of the equations of motion, and are typically small.

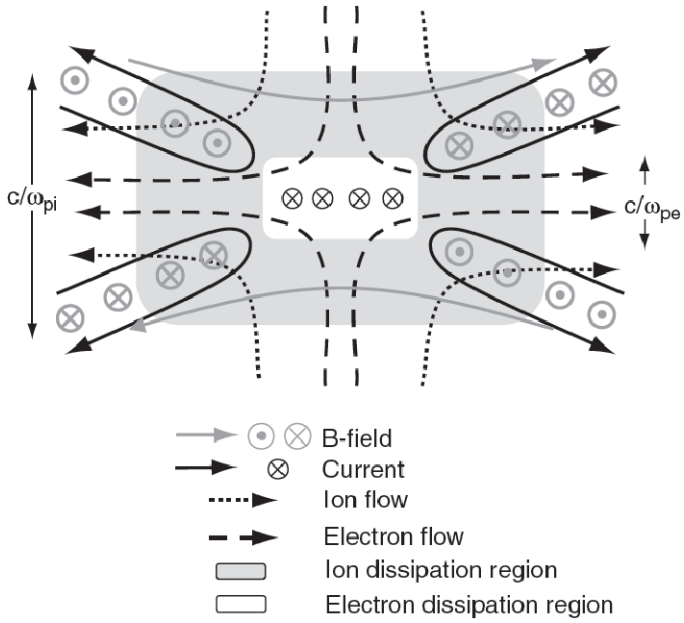

Figure 3.5.: The structure of the dissipation region during antiparallel two species reconnection. Electron (ion) dissipation region in white (grey) with scale size λ_e (λ_i). Electron (ion) flows in long (short) dashed lines. In-plane currents marked with solid dark lines and associated out of plane magnetic quadrupole field in grey. (Figure from Drake and Shay [2007].)

When these additional terms are included in a multi-species model, what affect will they have on reconnection? The two-fluid reconnection model is shown in Fig. 3.5. The diffusion region is now split into two separate zones, an ion diffusion region and an electron diffusion region located within it, due to the different ion and electron motion when considered at different length scales. The ion diffusion region has a thickness of an ion inertial length, as below this scale it can no longer

be treated as a fluid. The electron inertial length defines the outflow width of the electron diffusion region, as it is below this scale that the electrons decouple from the magnetic field. The electrons can reach a velocity equal to the electron Alfvén speed $V_{Ae} = B/\sqrt{\mu_0 m_e n_e}$, but eventually must drop back to the regular/ion Alfvén speed once they re-couple to the magnetic field [Drake and Shay, 2007].

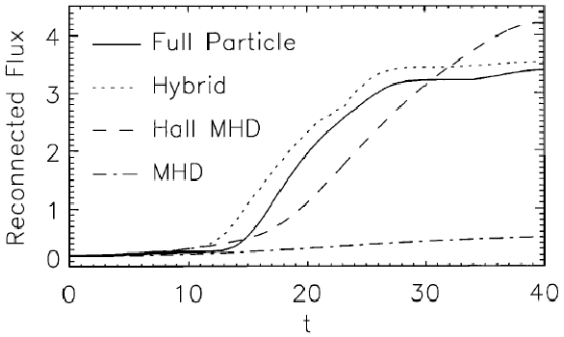

Figure 3.6.: The reconnected magnetic flux versus time from a variety of simulation models: full particle, hybrid, Hall MHD, and MHD (for resistivity $\eta = 0.005$). (Figure from Birn et al. [2001].)

The decoupled electrons result in an additional signature of two fluid reconnection, called the Hall field. This is a magnetic field with a quadrupole signature, and a direction perpendicular to the reconnection plane. (Fig. 3.5: the Hall field is directed towards the reader for clockwise electron flows, and into the page for anti-clockwise flows.) Is it often observed in two fluid or Hall-MHD models [Karimabadi et al., 2004, Sonnerup, 1979, Terasawa, 1983]. Of course, MHD models are not the only option for simulating multiple species. Hybrid codes also exist that treat one of the species as fluid (usually the electrons) and another as kinetic (particles), and these also see the Hall field [Karimabadi et al., 1999]. Fully kinetic codes can be used too, and also show Hall field signatures [Lapenta et al., 2011].

Despite the type of code used, the effect that resolving both species has on reconnection is qualitatively similar. Even without Petschek shocks, the reconnection rate is increased. This was demonstrated in the Geospace Environment Modelling (GEM) challenge, which compared the reconnection rates of different model types, and showed that all models that include the Hall term (therefore excluding single fluid MHD) allowed faster reconnection rates [Birn et al., 2001]. This shows that the inclusion of the Hall term, in order to break the frozen in condition of ions is critical to achieving fast collisionless reconnection, and does not depend strongly on the model used to describe this effect (Fig. 3.6). However, there is also evidence that the rate of collisionless reconnection may depend on the off-diagonal terms

(non-gyrotropic terms) of the pressure tensor [Hesse et al., 2011] and therefore these terms must be included in any realistic study of reconnection rate.

Beyond two fluid models, collisionless reconnection has also been studied in fully kinetic PIC simulations. These allow for additional physics, such as acceleration or heating of particles, non-gyrotropic pressure (off diagonal terms in the pressure tensor) and instabilities due distributions in velocity space, all of which results in contributions to the non-ideal electric field, **E**, which leads to reconnection. [Ricci et al., 2002, Shay and Drake, 1998, Shay et al., 2007].

3.5. Turbulent reconnection

The concept of turbulent reconnection [Lazarian and Vishniac, 1999] describes how reconnecting field lines behave in a turbulent fluid. It is often referred to simply as LV99. This theory has many applications as turbulence is believed to be a fundamental process, present in most astrophysical systems. The concept allows for field lines to wander in the turbulent fluid, so they are not "well ordered" when the field lines approach each other (Fig. 3.7). Due to the turbulence, specifically the diffusivity of the magnetic field lines, the plasma is not confined to the current sheet, allowing for a broader outflow region and thus faster reconnection. The elongated "Sweet-Parker" diffusion region is replaced with multiple reconnection sites, each with a much shorter length, each reconnecting simultaneously. Importantly the equation governing the reconnection speed now only depends on the properties of the turbulence, and is independent of resistivity, so this is true "fast reconnection" applicable to many types of plasma. The reconnection rate for this scenario is shown in Eq. 3.7. L is the whole system length as before. λ_I is the turbulent energy injection scale. V_I is the velocity at the injection scale. The turbulence is assumed to be strong, and the terms comprising of velocities (on the left hand side) equate to the velocity of the largest eddies at the stirring scale.

$$V_{TURB-RECON} = V_A \left(\frac{V_I}{V_A}\right)^2 \left(\frac{\lambda_I}{L}\right)^{1/2}. \tag{3.7}$$

Usually the ratio λ_I/L is of the order of one, so the reconnection speed occurs at the strong turbulent eddy speed. This also means that for weak turbulence (where the eddy speed is slow) the reconnection rate will once again be slow.

Simulations have been run using codes based on isothermal non-ideal MHD equations [Kowal et al., 2012]. These models introduced random turbulent eddies at a

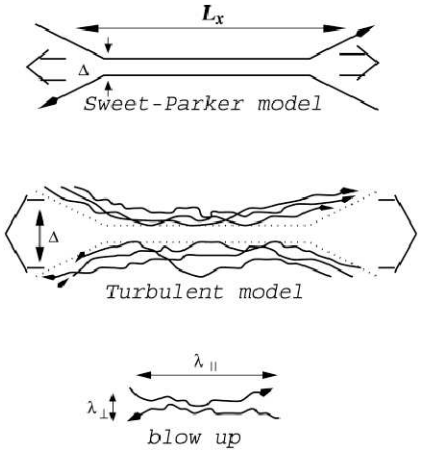

Figure 3.7.: Turbulent Reconnection Concept. Top: Sweet Parker Scaling. Middle: turbulence adds noise to field lines, allowing for a broader plasma outflow than a laminar/well defined current sheet. Bottom: Reconnection occurs on smaller scales simultaneously. (Figure from Lazarian et al. [2004].)

specific wavenumber corresponding to the power injection scale. The simulation results confirmed that the addition of turbulent power in the MHD fluid does increase reconnection rate (Fig. 3.8) offering a global explanation for why the observed rates can be larger than the Sweet-Parker "laminar" reconnection rates. Figure 3.8 also shows that the reconnection rate does not depend on whether the turbulent power (P_{inj}) is induced by magnetic or velocity perturbations.

The advantages of this model is that it quickly proves the turbulent reconnection concept by introducing turbulent-like features to an MHD model, without replicating the microphysics of turbulence. The turbulence can be driven by the addition of power in velocity space or magnetic potential, so it is possible to investigate if there is any difference in the method of producing turbulence. It is also independent of resistivity, so that the MHD equations, and the numerical results are applicable to collisionless reconnection.

The disadvantages are that, because the the authors are only interested in the reconnection rate of the large scale magnetic field structure, it still lacks kinetic scale effects, so the electron scale physics and dissipation mechanisms cannot be analysed using this scheme.

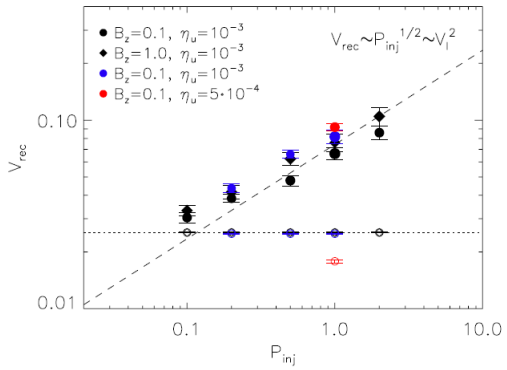

Figure 3.8.: The dependence of the reconnection speed, V_{rec}, on turbulent power, P_{inj}. Blue symbols show models with driving in which the eddies where injected in magnetic field instead of velocity (black symbols). The dotted line corresponds to the Sweet-Parker reconnection rate for models with $\eta_u = 10^{-3}$. A unique red symbol shows the reconnection rates from model with driving in velocity performed with higher resolution ($512 \times 1024 \times 512$) and resistivity coefficient reduced to $\eta_u = 5e10^{-4}$. Error bars represent the time variance of V_{rec}. The size of symbols corresponds to the error of V_{rec}. (Figure from Kowal et al. [2012].)

3.6. Reconnection within turbulence

Reconnection is not just a process that occurs in isolation, the plasma it occurs in is usually turbulent. In the previous section the reconnection geometries are assumed to be extremely large compared with the scale of the turbulent magnetic fluctuations. However, even when the mean field in a turbulent plasma contains less large scale structure, (and is more homogeneous) the fluctuating magnetic fields will always create topologies favourable to reconnection at multiple points in space, as shown in Fig. 3.9.

Servidio et al. [2010] studied the reconnection rates of multiple reconnection sites, within several incompressible 2D MHD simulations of turbulence. They show that turbulence and reconnection are intrinsically linked. They state "It is, in fact, difficult to envision a turbulent cascade without change of magnetic topology."

The simulation sizes vary, and the plasma parameters are not disclosed, as the simulation is generalized to a large scale, L_0. The equations are written in terms of magnetic vector potential, A, stream function, ϕ with uniform mass density $\rho = 1$. The simulation domain is periodic, and turbulence was initiated by perturbing both the magnetic field and velocity field with random fluctuations with wavenumbers ranging from $5 <= k <= 30$, (k in units of $1/L_0$) with random phases. This perturbation creates a sea of magnetic islands, as shown in Fig. 3.9.

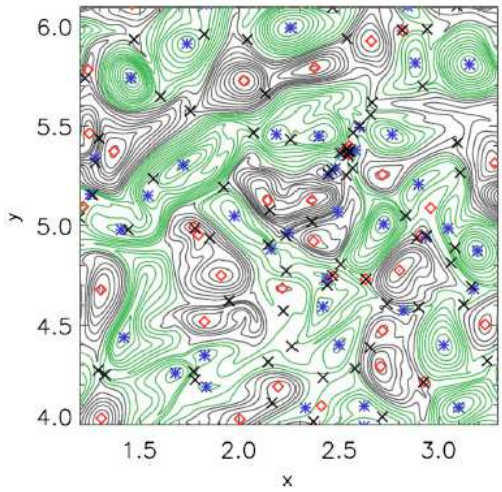

Figure 3.9.: 2D MHD simulation of turbulence. (Figure from Servidio et al. [2010].)

The authors primarily focus on the statistics of the multiple reconnection sites generated within the simulation. Reconnection sites are identified using a geometrical technique involving calculation of the Hessian matrix of A_Z. (This will be discussed in detail in Chapter 4.) This method identifies all the critical points in the simulation, which can be divided into maxima, minima (both located at the centre of magnetic islands) or saddle points, which are potential regions for reconnection. Saddle points are shown by black crosses in Fig. 3.9. The authors state that the following relation between the numbers of critical points in the 2D periodic domain is true:

$$\#(Maxima) + \#(Minima) - \#(Xpoints) = 0. \tag{3.8}$$

Equation 3.8 is a general topological feature of divergence-free vector fields. This geometric approach also allowed measurement of the size of each local diffusion region, length, l and width δ. These statistics allowed comparison of the simulated reconnection rates to theory. The authors measured reconnection rate using E_z (using $\mathbf{E} = -\mathbf{V_i} \times \mathbf{B}$) and show that for strong reconnection sites, there is the following scaling law for reconnection rate:

$$E_z \approx \frac{l}{\delta}. \tag{3.9}$$

This is the opposite of what is expected from "laminar" Sweet-Parker reconnection. (Using Eqs. 3.2 and 3.3, the Sweet Parker reconnection rate is $V_{SP} = V_{Ai}\ \delta/l$.) The authors point out that the Sweet-Parker reconnection rates were derived under

conditions with assumptions of symmetry (of both magnetic field, density) and this is not likely in a turbulent domain. Therefore another approach is needed for this problem. Cassak and Shay [2007] derived a system of equations for asymmetric Sweet-Parker reconnection using the equations of collisional MHD. The magnetic field strength and plasma density, ρ, were assumed to be different on opposite sides of the dissipation region. Using the conservation of mass, energy and magnetic flux, and assuming the system is in a steady state (time derivatives zero), they show that the equation expressing asymmetric reconnection rate for an incompressible plasma is:

$$E \propto \sqrt{\frac{\eta V_{out} B_1 B_2}{4\pi l}}, \tag{3.10}$$

where B_1 and B_2 are the reconnecting magnetic fields, and no longer have the same magnitude. The paper also specifies $V_{out} = \sqrt{B_1 B_2 / 4\pi\rho}$ for incompressible conditions. Substituting this into Eq. 3.10, and ignoring any constants:

$$E \propto \sqrt{\frac{B_1^{3/2} B_2^{3/2}}{R_m l}}, \tag{3.11}$$

where $\eta = R_m^{-1}$ (ignoring the constants L_0 and V_0).

The authors show this new equation for reconnection within turbulence matches measured reconnection rates at saddle points (Fig. 3.10). This good correlation shows that reconnection within turbulence follows scaling laws for asymmetric Sweet Parker reconnection, as outlined by Cassak and Shay [2007]. These simulations also show, that given the number of reconnection sites, reconnection should be considered an integral part of plasma turbulence.

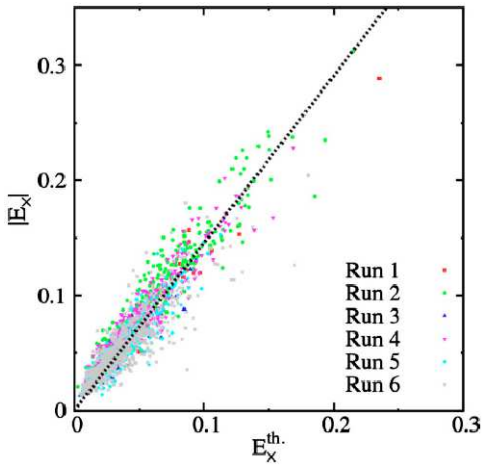

Figure 3.10.: Computed reconnection rates vs expected values from Eq. 3.11. (Figure from Servidio et al. [2010].)

These results are important as they show that reconnection and turbulence are intrinsically linked. We expect to see a wide range of reconnection rates within a turbulent plasma, and if those reconnection sites are in a steady states, then their reconnection rates are predictable based on the upstream properties of the plasma. however, the equations used resistivity as a dissipation mechanism, so are collisional in nature. It would be an interesting question to see if these scaling laws apply for collisionless reconnection events, and for reconnection on kinetic scales.

4. Reconnection and electron temperature anisotropy in sub-proton scale plasma turbulence

Note: The majority of the work presented in this chapter has been published in the Astrophysical Journal (ApJ) under the title "Reconnection and electron temperature anisotropy in sub-proton scale plasma turbulence" (see Haynes et al. [2014]).

4.1. Introduction

In Chapter 2 we discussed the general concepts of hydrodynamic turbulence, including non-linear wave-wave interactions, the formation of a forward cascade of energy, and the termination of this cascade via viscosity in small scale shear flows. Viscosity is the mechanism that dissipates the cascade energy, heating the fluid. In Section 2.3 we saw how these concepts have been applied to observations of solar wind turbulence, and that this cascade proceeds down to electron scales. However, in a collisionless plasma, there is no viscosity, so this must be replaced by other dissipative mechanisms at electron scales such as cyclotron or Landau damping. In Section 3.6 we saw, through simulation, how reconnection is also an integral part of plasma turbulence at MHD scales. Therefore, one might expect to see reconnection in the solar wind wherever you see plasma turbulence.

Observations of reconnection within turbulence in the solar wind have been rare, but there is an increasing body of evidence that reconnection does occur in the turbulent solar wind downstream of Earth's bow shock, in the magnetosheath [Retinò et al., 2007, Sundkvist et al., 2007]. In this location, large amplitude turbulence occurs as the plasma is shocked and deflected around the Earth's magnetic field. Figure 4.1 shows the location of the observations by Retinò et al. [2007] using the

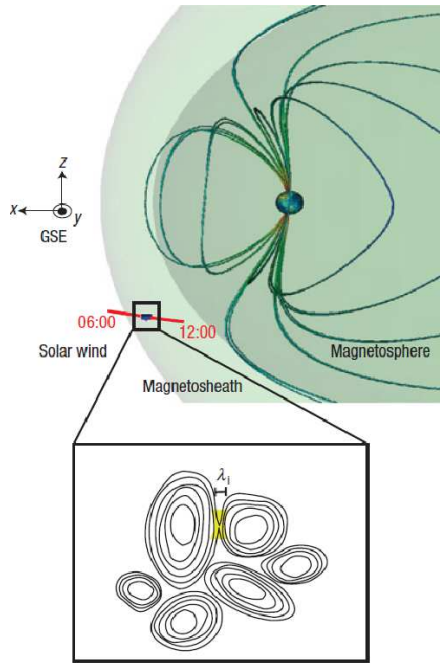

Figure 4.1.: The quasi-parallel bow-shock crossing. Spacecraft orbit (red line). Inset: Schematic diagram of current-sheet formation between magnetic islands. (Figure from Retinò et al. [2007].)

Cluster spacecraft, and the concept of reconnection occurring between magnetic islands. Retinò et al. [2007] show evidence for a planar current sheet at a scale size of $\sim 1\lambda_i$, whereas Sundkvist et al. [2007] show evidence for current sheets a few λ_i wide. Evidence of reconnection is provided in both observations by the change in sign of the components of magnetic field data. In both sets of data, the relative change in magnetic field strength is large, and is quoted in Sundkvist et al. [2007] as $\delta B/B_0 = 1$. Other observations have offered indirect evidence of reconnection contributing to solar wind dissipation [Bourouaine et al., 2012, Osman et al., 2011]. There is also strong evidence for quasi-steady reconnection associated with solar wind discontinuities [Gosling and Szabo, 2008].

Given this evidence, this raises an interesting question: If the turbulent cascade also transports or creates topological complexity at small scales, to what extent does reconnection at kinetic/electron scales affect or contribute to turbulent dissipation?

In Section 2.3 we have seen how the power spectrum of solar wind turbulence steepens at sub-proton scales, and the data does suggest that the cascade does proceed down to electron scales [Alexandrova et al., 2009, Kiyani et al., 2009, Sahraoui et al., 2009]. In these cases the spectra above the frequency corresponding to ρ_e steepen with a slope of ~ -4 on average. This is roughly in agreement with the results of 2-D and 3-D PIC simulations [Camporeale and Burgess, 2011, Chang et al.,

2011, Gary et al., 2012]. However none of these studies discuss reconnection in relation to electron scale turbulence.

In this chapter, we present results of fully kinetic plasma simulations with realistic mass ratio and plasma parameters (such as the ratio of plasma frequency to gyrofrequency) which are relevant to the solar wind and magnetosheath. We focus on the turbulent relaxation at sub-proton scales, and the resulting electron flows and velocity distributions. We will show that reconnection sites within turbulence can be responsible for strong electron temperature anisotropy via a velocity space mixing mechanism. The development of electron temperature anisotropy is well documented for individual reconnection sites in isolated current sheets, such as those observed in the magnetotail, and is explained by a model of passing and trapped electrons [e.g., Egedal et al., 2012]. Electron temperature anisotropy has also previously been reported in PIC simulations of turbulence [Camporeale and Burgess, 2011, Karimabadi et al., 2013]. Based on analysis of the electron dynamics, we will describe a mechanism for creating electron temperature anisotropy that requires multiple magnetic reconnection sites within the turbulent field. Electrons are accelerated in the reconnection electric field, but in magnetic turbulence the sense of reconnection (and direction of the reconnection electric field) varies between the reconnection sites. The topology of the magnetic field linking the different reconnection sites allows them to also act as mixing zones for the accelerated particles. This leads to the formation of multi-peaked distributions in electron velocity space, which may be a source of further waves and particle coupling via instabilities. The reconnection sites within the turbulence lead to electron energy gain, nonlocal velocity space mixing and the formation of strong temperature anisotropy, all of which may contribute to the dissipation of turbulent fluctuations at sub-proton scales.

In Chapter 1 we discussed the frequency distribution of solar wind observations in a parameter space such as $T_\parallel/T_\perp$ against $\beta_\parallel$ is constrained within boundaries related to the marginal growth of linear instabilities. Here, we make the argument that an additional driver for the electron temperature anisotropy in an expanding plasma flow might be magnetic reconnection occurring as an element within turbulence.

4.2. Methodology

4.2.1. Simulation

We use the particle-in-cell (PIC) code Parsek2D [Markidis et al., 2009] based on the implicit moment method for time advance of the electromagnetic fields, and

a predictor-corrector method for the particle mover. The implicit method allows larger time steps and cell sizes compared with explicit PIC methods, which are usually constrained (for numerical stability) by the condition $\omega_{pe}\Delta t < 2$, where Δt is the time step, and ω_{pe} is the electron plasma frequency. Also Parsek2D allows a relaxation of the Courant-Friedrichs-Lewy (CFL) condition $c\Delta t/\Delta x < 1$, where c is the speed of light and Δx is the cell size. The time step $\Delta t = 0.05\Omega_e^{-1}$, where Ω_e is the electron gyrofrequency (so that the electron cyclotron motion is fully resolved), and the cell size $\Delta x = \Delta y \sim 17\lambda_D$, where λ_D is the Debye length. The code is two dimensional in the x-y plane but retains all three vector components for velocities and fields. The electron-proton plasma is initially loaded with a uniform, isotropic Maxwellian distribution. The simulation box is 200×200 cells, with periodic boundary conditions and 6400 simulation particles per cell for each species. This large number of particles reduces the statistical particle noise so that the dynamic range in Fourier space is large enough to resolve the formation of a turbulent cascade. The simulation box is sized to resolve wave vectors ranging from $k\rho_e = 0.1$ to $k\rho_e = 10$, where k is wave vector and ρ_e the thermal electron gyroradius. The box length is about 1 ion inertial length, and the electron gyro-motion is resolved with ~ 3 cells per electron gyroradius (based on the initial guide field strength). We used plasma parameters which are appropriate to the solar wind and magnetosheath: the ion plasma frequency to ion cyclotron frequency ratio $\omega_{pi}/\Omega_i \sim 1650$, and the ion to electron mass ratio is physical with $m_i/m_e = 1836$. The ions and electrons are initialized to the same normalised temperature, i.e. $\beta_e = \beta_i = 0.5$. The simulation was run until $t = 200\Omega_e^{-1}$. Unless quoted otherwise, simulation results are shown in Gaussian CGS units with the following normalizations: Velocities are normalized to the speed of light, time is normalized to $10\omega_{pe}^{-1}$, and charge per unit mass is normalized to the proton charge per unit mass (see Appendix B). Temperatures are the variance of velocities in each simulation cell. Initial particle density is assumed to be equivalent to 10 particles per cm^3. A more detailed description of the code, and normalisation techniques are outlined in Appendices A and B.

Similar to the method of Camporeale and Burgess [2011], the simulation was initialised with a background magnetic field $\mathbf{B_0}$ and random long wavelength magnetic field fluctuations were added. For the simulations shown here the background field was set in the out-of-plane z direction. The intention is to provide an initial input of energy at low values of k with properties that mimic a turbulent field, and then follow the decay of this initial perturbation and the development of power at larger wave numbers. The magnetic field was initialized with random fluctuations in all three components for wave vectors $k_x = 2\pi m/L_x$ and $k_y = 2\pi n/L_y$ for $m = -3, \ldots, 3$

and $n = -3, \ldots, 3$. No initial value of spectral slope was imposed on the initial fluctuations. The initial electric field was zero, but the abrupt perturbation of the magnetic field acted to initialize the self-consistent evolution of the turbulent decay after a short period at the start of the simulation. This method emphasizes the random nature of turbulence, and in particular has the advantage that no particular linear modes are assumed dominant. Other methods of initializing the decay of turbulent fluctuations are possible, such as initial equilibria [Karimabadi et al., 2013], Alfvénic-like fluctuations [Camporeale and Burgess, 2011], or superposition of linear modes [Chang et al., 2011]. The requirement to resolve the development of a turbulent cascade means that the initial perturbation has to be relatively large, and a value $\delta B/B_0 = 1$ was used here. The configuration with the background field perpendicular to the simulation plane does not support $k_\parallel$ wave vectors (at least on average), but creates magnetic field line topologies with islands and X-points with a guide field. We use the magnetic perturbation described in Camporeale and Burgess [2011], which can be expressed as:

$$\delta B_x = \sum_{k_x} \sum_{k_y} |k_x|^{-1} \cos(k_x x + k_y y + \phi_{x,y}) + \sum_{k_y} \left| \frac{L_x}{2\pi} \right| \cos(k_y y + \phi_x), \tag{4.1}$$

$$\delta B_y = -\sum_{k_x} \sum_{k_y} |k_y|^{-1} \cos(k_x x + k_y y + \phi_{x,y}) + \sum_{k_x} \left| \frac{L_y}{2\pi} \right| \cos(k_x x + \phi_y), \tag{4.2}$$

$$\delta B_z = \sum_{k_x} \sum_{k_y} \frac{1}{(k_x + k_y)} \cos(k_x x + k_y y + \phi_z). \tag{4.3}$$

4.2.2. Identification of reconnection sites

We use a method as described by Servidio et al. [2009], to identify points in the simulation where reconnection was likely to occur. To confirm the algorithm is correctly locating X-lines of magnetic field geometry, animations of field line motion were also created, by plotting constant contours of the z component of vector potential, A_z (see Appendix C). The method described by Servidio et al. [2009], was then used to calculate and plot the locations of reconnection within this field: First, the areas where $\nabla A_z = 0$ are found, in order to identify critical points. Since the simulation is discrete in space a threshold was used to indicate a possible zero gradient. X-point geometries are located where there are saddle points in A_z. These were identified

out of the list of critical points using the Hessian matrix, given by:

$$H(A_z) = \begin{bmatrix} \frac{\partial^2 A_z}{\partial x^2} & \frac{\partial^2 A_z}{\partial x \partial y} \\ \frac{\partial^2 A_z}{\partial y \partial x} & \frac{\partial^2 A_z}{\partial y^2} \end{bmatrix}. \tag{4.4}$$

The eigenvalues of H were then found by solving $det(H - \lambda I) = 0$. The eigenvalues represent the signs of the second derivatives. If both eigenvalues are positive, then the critical point is a minimum. If both eigenvalues are negative, then the critical point is a maximum. If the eigenvalues are of opposite sign, then the location is a saddle point (a minimum in one direction and maximum in the other) and is a potential location for reconnection. This technique usually finds multiple locations around a single reconnection point due to the threshold condition imposed on the gradient. In this case we use a recursive algorithm that finds all connected cells that match the gradient threshold and saddle criteria. The cell with the smallest magnitude gradient in this group of connected cells was then chosen to be the actual centre of reconnection.

Since the geometry of the turbulence simulation was unknown, we wanted to check that this detection algorithm could correctly identify reconnection sites on some known test data. This was tested using an Orszag-Tang vortex. This vortex is well known, as it is used in MHD simulations to generate a large reconnection site at its centre, with several smaller ones surrounding it, and therefore would be easy to see if the algorithm had selected the correct cells. The general form of an Orszag-Tang vortex [Orszag and Tang, 1979] is a magnetic field of the following form:

$$\mathbf{B} = -B_0 \sin(2\pi y/L_y)\hat{\mathbf{x}} + B_0 \sin(4\pi x/L_x)\hat{\mathbf{y}} + B_g \hat{\mathbf{z}}, \tag{4.5}$$

where x and y is the position in the 2D grid. L_x and L_y are the length of the simulation domain. B_0 is the in-plane maximum magnetic field strength, and B_g is the out of plane guide field. The velocity perturbation in this vortex is as follows:

$$\mathbf{V_d} = -V_0 \sin(2\pi y/L_y)\hat{\mathbf{x}} + V_0 \sin(2\pi x/L_x)\hat{\mathbf{y}}, \tag{4.6}$$

where $\mathbf{V_d}$ is the electron and ion drift velocity. V_0 is the maximum in-plane drift velocity. Of course, it was not necessary to run a complete simulation, as the detection algorithm could have been evaluated on a static field. However it was necessary in order to check that the field line plotting code correctly follows the same field lines in time.

A simulation was run with the same plasma parameters as in the turbulence

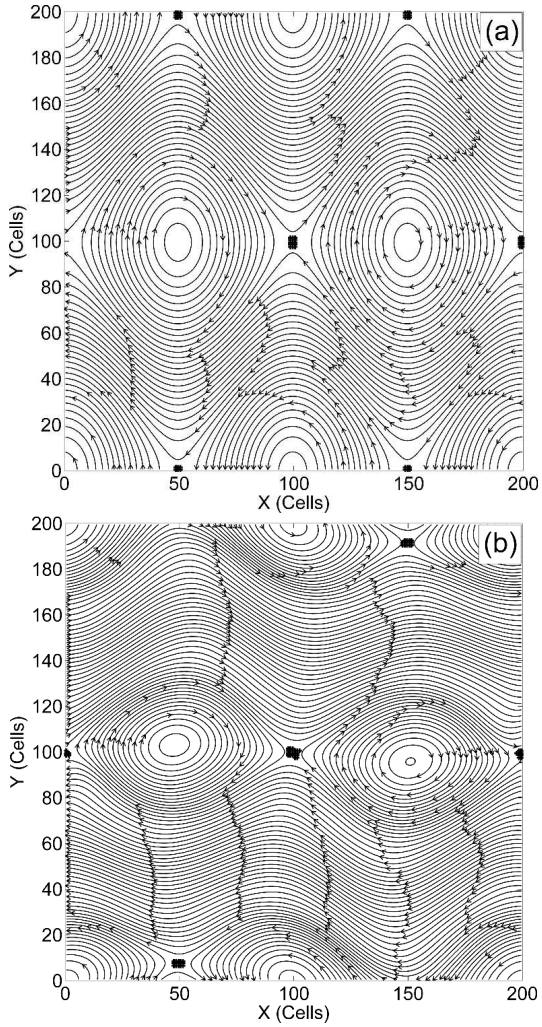

Figure 4.2.: Orszag-Tang in-plane field configuration at (a) $t = 0$ and (b) $t = 71\Omega_e^{-1}$. Black crosses show potential reconnection sites (these appear as black smudges where crosses from adjacent cells overlap).

simulation. V_0 was set to the Alfvén speed, $V_A = B_0/\sqrt{\mu_0\rho}$. We use a guide field, B_g, equal to $5B_0$. The initial in-plane magnetic field lines (black) generated are shown in Fig. 4.2(a). The black crosses show the locations of cells that have been selected as potential reconnection sites (these appear as black smudges where crosses from adjacent cells overlap). Several cells have been selected for each location. (The cell chosen as the reconnection centre has not been plotted.) Due to the periodic nature of the simulation, the Orszag-Tang initialisation produces four initial saddle points. One in the centre, another on the y-axis boundary, and two on the x-axis boundary. The same four reconnection sites were correctly identified by the algorithm, throughout the simulation, as shown in Fig. 4.2(b) which shows the magnetic field lines and selected reconnection regions at $t = 0$ and $t = 71\Omega_e^{-1}$.

Animations showed that the movement of the field lines also matched the value of E_z at each reconnection site. This in conjunction with Fig. 4.2 proved that the detection technique worked, so we then applied this same technique on the outputs from the turbulence simulation.

4.3. Turbulence simulation results

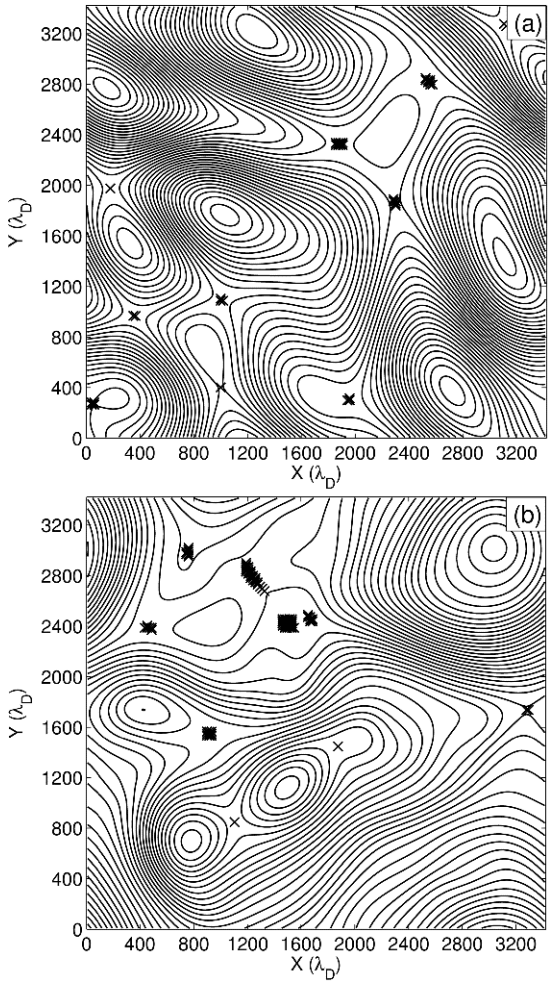

Figure 4.3.: Initial and final magnetic field line configurations at (a) $t = 0$ and (b) $t = 200\Omega_e^{-1}$. Lengths in units of λ_D.

We now discuss the results from simulations of decaying turbulence. Figure 4.3 shows magnetic field line configurations for the simulation at times $t = 0$ and $t = 200\Omega_e^{-1}$. Potential X-point reconnection sites are shown by black crosses where the threshold for the gradient is satisfied. The end state has a magnetic field which is topologically simpler with 8 X-point sites compared to 10 initially. When the simulation is run for longer times, beyond $t = 200\Omega_e^{-1}$, the number of X-points reduces

further, with a consequent reduction in the number of magnetic islands. During the simulation the field line evolution is highly dynamic, with X-points moving around the simulation region and interacting with magnetic islands and other X-points. Animations show that magnetic islands gain or lose flux via reconnecting field line motion through X-points, i.e., field lines with island-like connectivity become linked to other X-points or encircle more than one island. Thus an island may shrink until it disappears or is absorbed by another island, and at this point the separating X-point also disappears.

Occasionally new X-points are seen to form, but only temporarily as the field fluctuates. The sense of reconnection may reverse at an X-point, with the movement of field lines changing direction as the surrounding islands shrink or grow. Associated with a change in the sense of magnetic field reconnection there will also be a change in the sense of the reconnection electric field. In the final state there are some X-points which are in complex geometries and seem on the verge of disappearing if the simulation were run longer. By examining the time evolution of the local electron gyroradius we find that once an X-point region develops a scale less than about an electron gyrodiameter it is likely that the X-point will disappear, although sometimes disappearance occurs in more topologically complex regions with several X-points close to each other.

Figure 4.4 shows power spectra of $|\delta B|^2/|B_0|^2$ as functions of k_x and k_y at $t = 0$ (green) and $t = 200\Omega_e^{-1}$ (blue). The k_x and k_y directions are both perpendicular to the average guide field. The noise floor, as determined from a simulation with no applied perturbation, is shown in red. Starting from the initial energy input at small k values, the power at larger k evolves rapidly until $t = 100\Omega_e^{-1}$, after which the spectra are relatively time steady over the period simulated. There are no major differences between the spectra in the two directions. Simulations with an in-plane guide field show a similar rapid formation of approximately power law spectra, but with a power anisotropy in the parallel and perpendicular wave vector directions [Camporeale and Burgess, 2011] (Chapter 6). The simulation domain size is approximately one ion inertial length λ_i, and between this scale and $k\rho_e = 0.3$ the power spectrum is approximately proportional to $k^{-8/3}$ in agreement with other simulations and observational data [Alexandrova et al., 2008, Smith et al., 2006]. Beyond this driving scale, the spectra gradually steepens, roughly consistent with observations, until it reaches a power law of approximately $k^{-6.5}$, but there appears to be no obvious break point in wavenumber. Note that for $k\rho_e \geq 4$ the spectrum is not above the background noise level and is not meaningful.

In addition to the magnetic spectrum shown in Fig. 4.4 we have also examined the

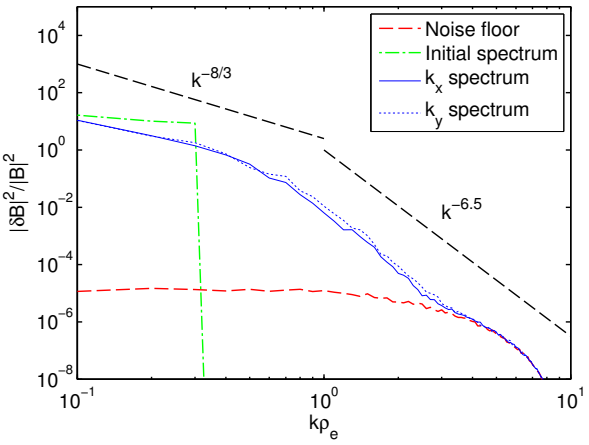

Figure 4.4.: Power spectra of $|\delta B|^2/|B_0|^2$ as functions of k_x and k_y, at $t = 200\Omega_e^{-1}$ (blue solid and dotted lines), initial spectrum (green dash-dot line) and noise floor (red dashed line). A $k^{-8/3}$ gradient is shown to indicate the typical gradient seen in other works where k extends to smaller values.

spectra of the electric field, number density and average ion and electron velocity. These spectra are qualitatively similar, showing a dual slope form of power law. These spectra also evolve until $t = 100\Omega_e^{-1}$, and show that an ensemble of stochastic fluctuations is present within the simulation, and has properties that are similar to turbulence. The transition from the initial power spectrum, with power only in small wavenumbers, to a relatively time steady power spectrum over a large range of k is consistent with the formation of a turbulent cascade, down to the noise level of the simulation and scales of order the electron gyroradius.

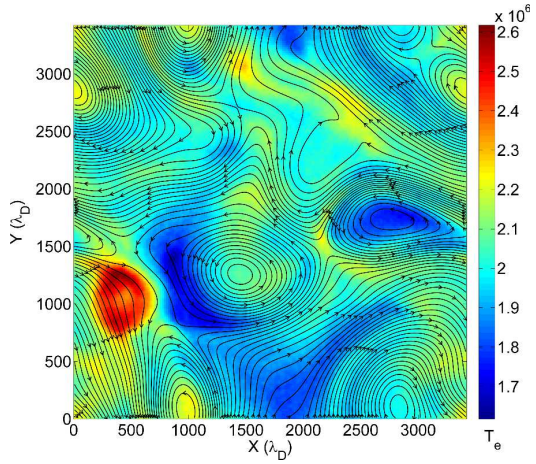

Figure 4.5.: Magnetic field lines (black) and electron temperature T_e at time $t = 97\Omega_e^{-1}$ for the full simulation domain.

Reconnection is usually understood to produce plasma heating, and so it might

be expected that electron temperature increases around magnetic field X-points. However, over the course of the simulation, the changes in electron temperature in the vicinity of the reconnection sites are not significantly different from those at other locations. This is shown in Fig. 4.5 (the circular region of hot electrons in the lower left hand corner is a coherent structure that will be discussed in Chapter 5). This indicates that energy dissipation occurring through the reconnection process does not dominate over dissipation elsewhere. The lack of a unique, strong correlation between T_e changes and the location of reconnection sites may be related to recent observations of magnetopause reconnection outflows that show a wide variability in bulk electron heating, explained by a dependence on the Alfvén speed of the inflow [Phan et al., 2013]. In order to illustrate the effects of reconnection around magnetic field X-points, we will concentrate on the electron drift velocities and electron temperature anisotropy.

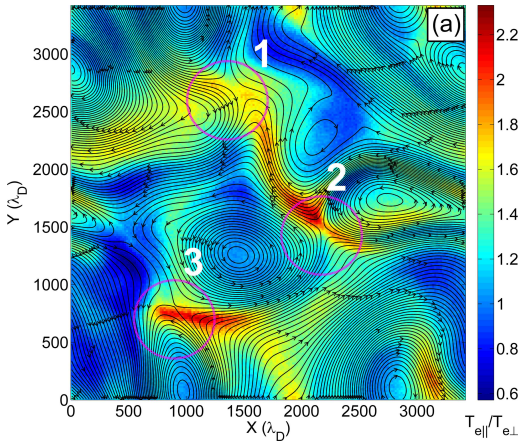

Figure 4.6.: Magnetic field lines (black) and electron temperature anisotropy ($T_{e\|}/T_{e\perp}$) at time $t = 97\Omega_e^{-1}$ for the full simulation domain. ($m_i/m_e = 1836$) The three X-point regions discussed in the text are marked.

Figure 4.6(a) shows the electron temperature anisotropy $T_{e\|}/T_{e\perp}$ for the simulation with $m_i/m_e = 1836$, over the full simulation domain at $t = 97\Omega_e^{-1}$, with magnetic field lines shown in black. Although T_e does not significantly increase at the reconnection sites, three reconnection sites have been labelled where there is a strong signature of parallel temperature anisotropy.

Our analysis will therefore focus on the three sites in Fig. 4.6(a), in order to understand how these strong temperature anisotropy signatures arise, and how they are linked to magnetic reconnection.

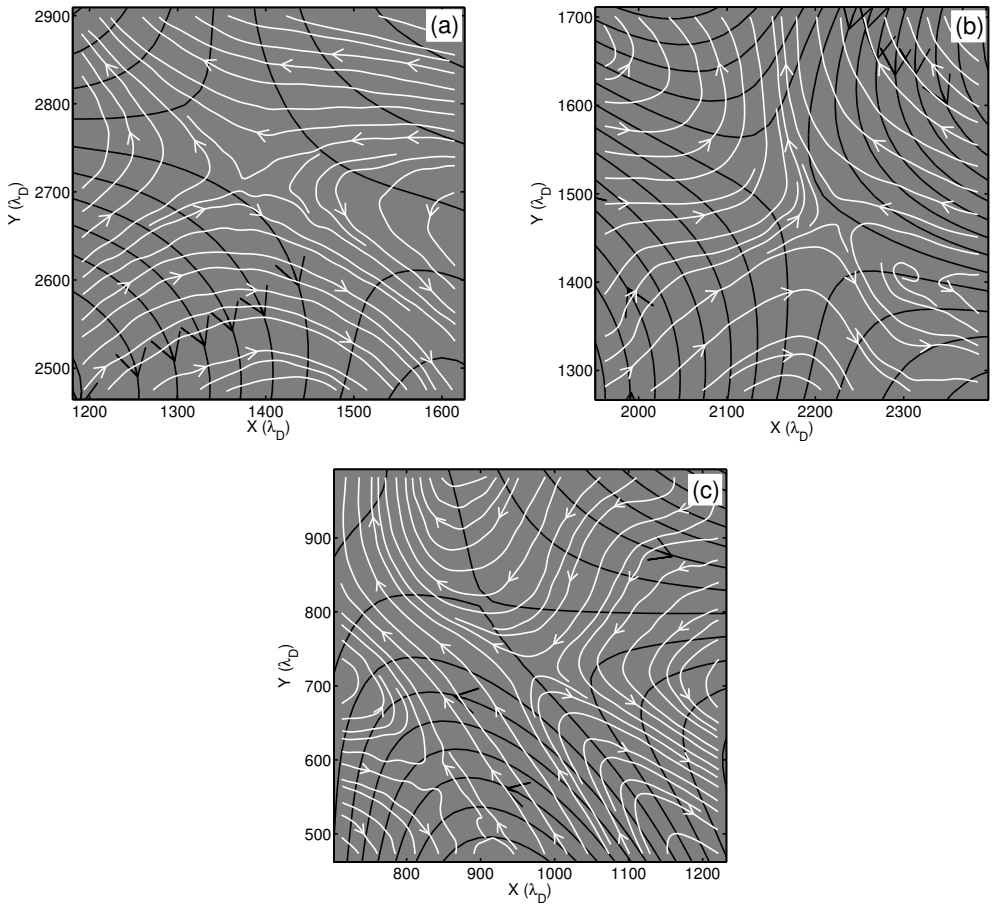

Figure 4.7.: Enlarged detail showing magnetic field lines (black) and electron streamlines (white) for (a) reconnection site 1,(b) reconnection site 2, and (b) reconnection site 3. The position of the reconnection sites are marked in Fig. 4.6.

4.3.1. Reconnection flows and asymmetry

Firstly, we will examine the electron bulk drifts in the reconnection regions. Due to the total simulation time, the ions do not have much time to accelerate, and the data shows that the currents are primarily the result of electron flows. Figure 4.7 shows an enlarged detail for all three reconnection sites. Electron average velocity streamlines are shown in white and magnetic field lines in black. The geometry of the magnetic field lines and electron flows resemble typical X-point reconnection with inflow and outflow regions. The regular flow configuration is perhaps surprising at this scale, given that the size of the reconnection site is $\sim 400\lambda_D$ (25 cells), compared to the electron thermal gyroradius, which varies over 3-5 cells due to the varying magnetic field strength (and can be 10 cells within magnetic holes, due to the low field strength. These are discussed in Chapter 5). The velocity and the magnetic

field patterns are not exactly symmetric, and for site 2 (Fig. 4.7(b)) the flow and field pattern centres are displaced from one another by $\sim 50\lambda_D$. The corresponding displacement is larger for site 3 (Fig. 4.7(c)) possibly due to the larger asymmetry imposed by the surrounding islands. Reconnection sites 2 and 3 are both at the junction of merging magnetic islands. Reconnection site 1 (Fig. 4.7(a)) is located within a more complex magnetic topology, and the sense of field line motion changes as the local islands around it disappear. Despite this, this site shows a large electron parallel temperature anisotropy and an electron flow signature similar to the other two sites.

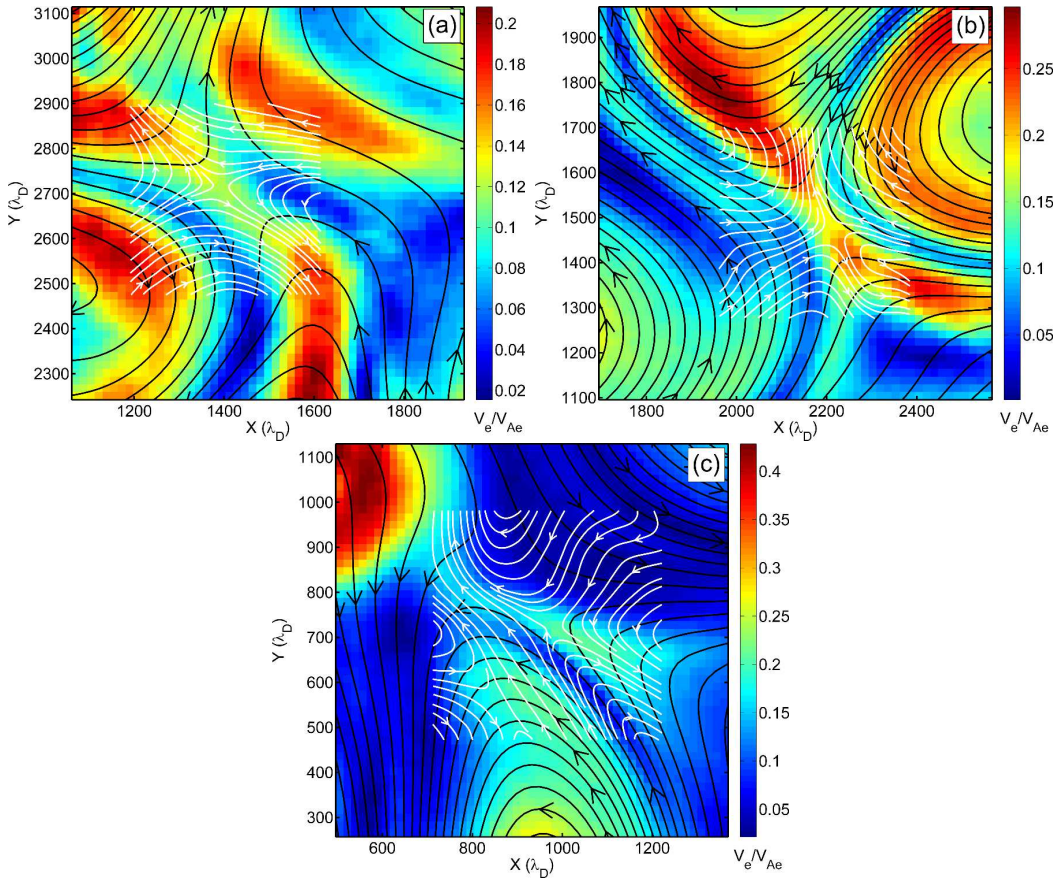

Figure 4.8.: Enlarged detail showing magnetic field lines (black) and electron streamlines (white). Background colour is electron bulk drift, V_e normalized to the cell electron Alfvén speed, V_{Ae}. (a) reconnection site 1, (b) reconnection site 2, and (c) reconnection site 3. The position of the reconnection sites are marked in Fig. 4.6.

Figure 4.8 shows enlarged areas around all three reconnection sites. Again magnetic field lines are shown in black, electron bulk velocity is shown in white. The magnitude of the electron bulk velocity is shown in the background colour. As the scale of the simulation is below the ion inertial length the electron flows can reach

up to the electron Alfvén speed, V_{Ae} defined as $B/\sqrt{\mu_0 m_e n_e}$, as discussed in Section 3.4. Inflow speeds are often used to measure reconnection rates (Section 3.2) but as shown in Fig. 4.8 the magnitude of the inflow velocity changes dramatically around the reconnection sites. Theoretical models of reconnection usually deal with spatially symmetric flows and frozen in magnetic fields, so inflows are a good measure of the rate of reconnected flux. Figure 4.8 shows why E_z, measured at the reconnection centre (see Appendix C, Eq. C.7) is a better measure of reconnection rate in 2D turbulence, as inflows can vary greatly even on small scales. Visual inspection of the three panels in Fig. 4.8 shows a similar configuration for all three reconnection sites. Outflows in each case are associated with higher magnitude flows, of $\sim 0.15 - 0.2 V_{Ae}$. The value of the reconnection inflows are $\sim 0.1 V_{Ae}$ or less. The region of increased flow in the top left corner of Fig. 4.8(c) is associated with a coherent structure that formed in the simulation, and is the topic of Chapter 5.

4.3.2. Electron diffusion region

Cassak and Shay [2007] derived a model of Sweet-Parker reconnection under asymmetric conditions, using the equations of MHD. The magnetic field strength and plasma density, ρ, were assumed to be different on opposite sides of the dissipation region. Using the conservation of mass, energy and magnetic flux they derive scaling laws for the outflow speed and reconnection rate. They also show that the flow stagnation point would not be located at the same location as the magnetic null point, but would be offset towards the side with lower ρ/B. This model was demonstrated applicable to MHD diffusion regions by Servidio et al. [2010] (See Section 3.6). Reconnection in turbulence is going to be asymmetric in nature, and we have already demonstrated in Section 4.3.1 that the flow stagnation points in our results are offset from the magnetic null point. Therefore, it is interesting to attempt this type of scaling analysis for the electron diffusion region.

The centres of the identified reconnection events were tracked during their motion in the course of the simulation. As mentioned earlier, reconnection sites are first identified through the Hessian matrix analysis, to locate saddle points. Reconnection sites are saddle points whose gradients are zero. Since a threshold was used to find near zero gradients, this selects multiple cells around the actual reconnection site centre, as shown in Fig. 4.9. Analysis code was developed to find the centre, by first finding all connected cells that are saddle points, and meet the zero gradient criteria. This was done by using a function, that searches the entire grid, and on finding the first cell meeting the criteria, labels it as an event in a complementary 2D

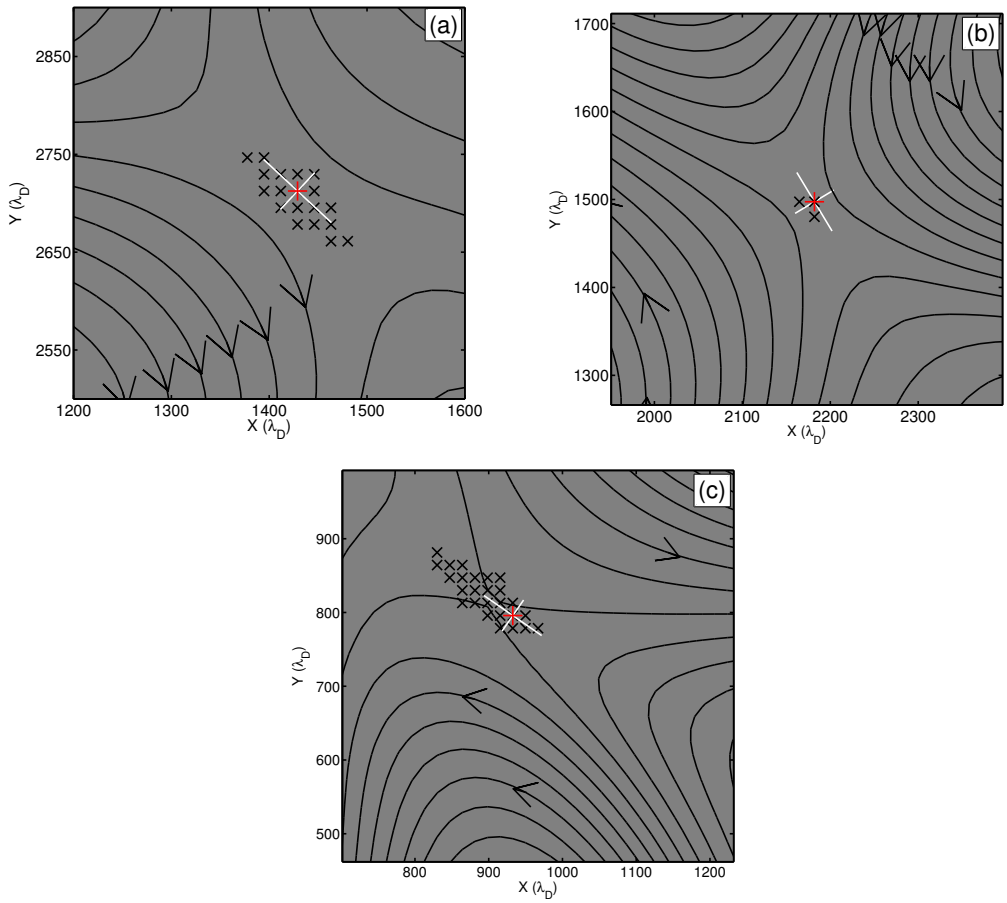

Figure 4.9.: (a) Reconnection site 1 (refer to Fig. 4.6). Magnetic field lines (black). Cells that meet the reconnection site criteria are marked by black crosses. The centre of reconnection (the cell with the minimum magnitude gradient) is marked by a larger red cross. Eigenvectors of the Hessian matrix are shown by white lines.
(b) Reconnection site 2 (refer to Fig. 4.6).
(c) Reconnection site 3 (refer to Fig. 4.6).

array. The routine then calls a recursive function that checks the same criteria in all 8 cells surrounding the first one. In each case (up, down, left, right and diagonals) if the neighbouring cell also meets the criteria and is not already labelled, then it is labelled (with the same number), before calling the same function. This continues recursively until a cell is found that does not match the criteria, at which point, the function checks the next in the list of 8 surrounding cells. This continues until the end of the function is reached. The function stack will then return back to the next line where it was called from and continue to call itself, eventually finding every connected grid points. This method has the advantage of being relatively simple to code, is quick, and will always find every connected cells regardless of the shape of

the reconnection site. The result is a list of connected cells. This is then used to find the cell with the minimum magnitude gradient, which is defined as the centre of reconnection (Fig. 4.9).

Once the centre of reconnection is identified, the eigenvalues and eigenvectors of the Hessian matrix at the reconnection centre were used as in Servidio et al. [2010]. The eigenvalue with the largest magnitude, λ_{max}, has a corresponding eigenvector associated with the width, δ of the reconnection site. The eigenvalue with the smaller magnitude, λ_{min} has a corresponding eigenvector associated with the length, l, of the reconnection site. The ratio of the eigenvalues determines the aspect ratio of the field line geometry, so information about the diffusion region can be inferred, through the equation:

$$\sqrt{|\lambda_{max}/\lambda_{min}|} \sim l/\delta. \tag{4.7}$$

Although this analysis was used for MHD turbulent reconnection (as discussed in Section 3.6), we will now show that this appears to work for reconnection within turbulence at sub-proton scales. In Fig. 4.9 the direction of both eigenvectors is indicated in the form of a white cross, plotted at the centre of reconnection. In all three sites, the shorter eigenvector corresponds to the inflow direction, and the longer eigenvector to the outflow direction. (Compare Figures 4.7 and 4.9.) At this scale, the term "diffusion region" is incorrect. This is the "electron dissipation region", or "electron diffusion region" (refer to Fig. 3.5). This should occur at scales below the electron inertial length. Using the initial parameters the electron inertial length, λ_e, is ~ 4.5 cells, therefore, when plotting the eigenvectors, we use a "diffusion region" width, δ, of 3 cells ($< \lambda_e$) and calculate the length of the diffusion region, l, using Eq. 4.7, so that the plotted eigenvector magnitudes are consistent with this concept.

Figures 4.10, 4.11 and 4.12 show the electron diffusion region in further detail, for reconnection sites 1, 2 and 3 respectively. Panel (a) in each figure shows the magnitude of the in-plane magnetic field, $|B(x, y)|$. Panel (b) shows electron charge density, ρ_{qe}. Panels (c) and (d) both show the parameter $-\rho_{qe}/|B(x, y)|$, with different colour bar scalings. Magnetic field lines are plotted in black and the centre of reconnection and eigenvectors/eigenvalues are plotted using a white cross. During asymmetric Sweet-Parker reconnection [Cassak and Shay, 2007] the flow stagnation point, should be offset in the direction of the smaller value of ρ/B. At these scales, due to approximate charge neutrality, $-\rho_{qe}$ is proportional to number density, and because there is a guide field, only the in-plane magnetic field is reconnecting, which is why we plot the parameter $-\rho_{qe}/|B(x, y)|$.

Firstly, Panel (a) in Figs. 4.10, 4.11 and 4.12 provides a verification that the

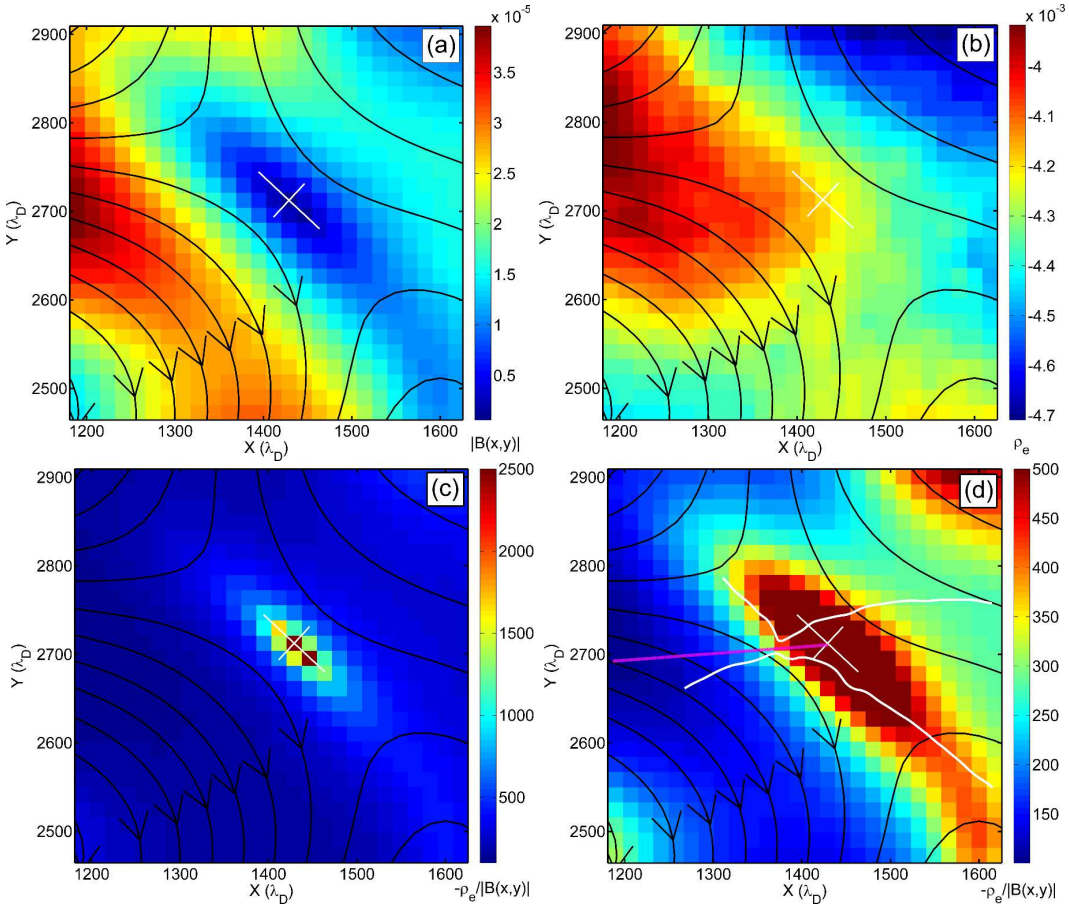

Figure 4.10.: Reconnection site 1 (refer to Fig. 4.6). Black lines are magnetic field lines. The white cross show the eigenvectors of the Hessian matrix. Background colour shows:
a) Magnitude B(x,y)
b) Electron charge density, ρ_{qe}
c) The parameter, $-\rho_{qe}/|B(x,y)|$, highlighting the electron diffusion region.
d) $-\rho_{qe}/|B(x,y)|$ (reduced color scale). White lines are streamlines of electron bulk velocity, showing the location of the electron stagnation point.

method of choosing the reconnection centre works, as all three white crosses are located at the cell with the lowest magnitude of in-plane field. Panel (c) shows that the parameter $-\rho_{qe}/|B(x,y)|$ is a useful diagnostic for the electron diffusion region, as its value increases sharply in the 3 cell width of the dissipation region, and the increased values occupy a region with a similar length to that chosen using the scaling from Eq. 4.7. This suggests that an equivalent of the MHD Sweet-Parker diffusion region scaling also applies at electron scales.

In Panel (d) of each figure the colour scale is chosen to exclude the higher values of

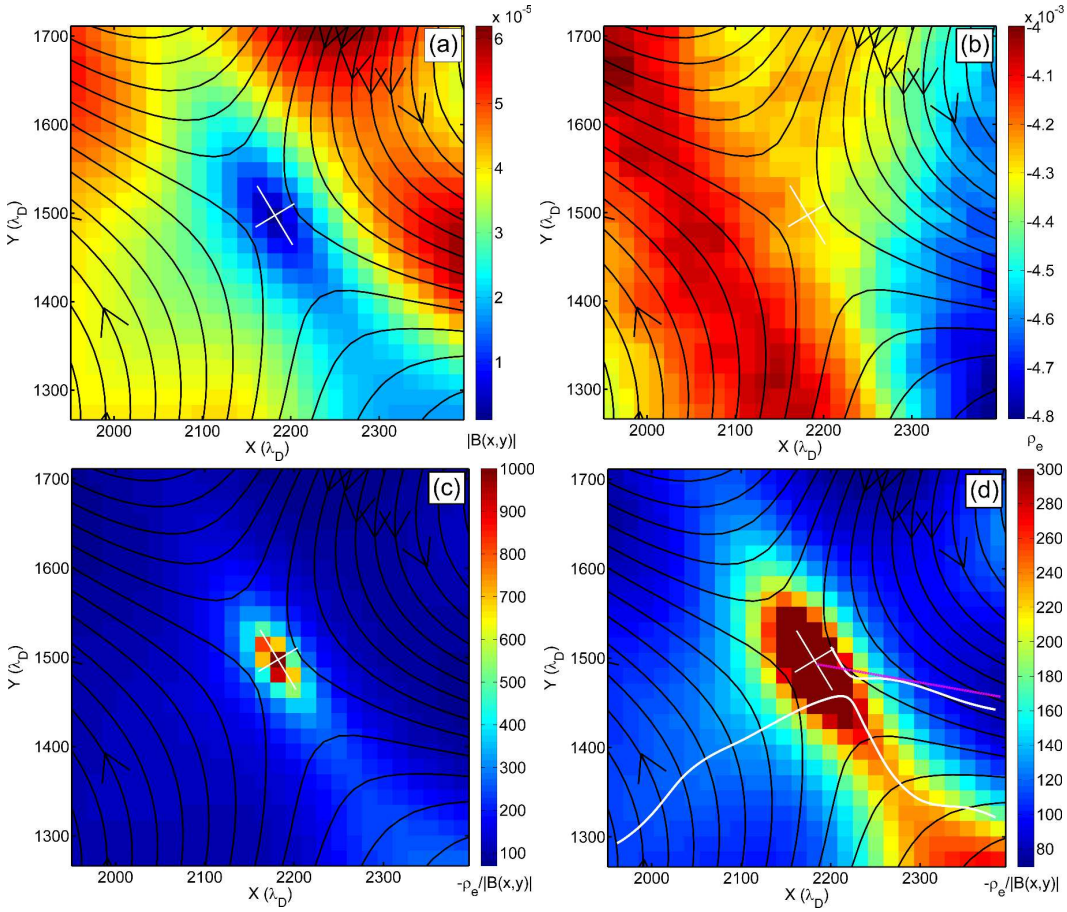

Figure 4.11.: Reconnection site 2 (refer to Fig. 4.6). Black lines are magnetic field lines. The white cross show the eigenvectors of the Hessian matrix. Background colour shows:
a) Magnitude B(x,y)
b) Electron charge density, ρ_{qe}
c) The parameter, $-\rho_{qe}/|B(x,y)|$, highlighting the electron diffusion region.
d) $-\rho_{qe}/|B(x,y)|$ (reduced color scale). White lines are streamlines of electron bulk velocity, showing the location of the electron stagnation point.

$-\rho_{qe}/|B(x,y)|$, in order to highlight lower values in the surrounding region. The approximate location of the electron drift stagnation point is indicated by the addition of the innermost streamlines from Fig. 4.7. Additionally a magenta line has been drawn from the centre of reconnection through the stagnation point. This shows that the stagnation point appears to be offset in the direction of lower $-\rho_{qe}/|B(x,y)|$, similar to the model of Cassak and Shay [2007]. This is more obvious for reconnection sites 1 and 3 where the offset is larger. The stagnation point is closer to the centre of reconnection in site 2, so this relation is less obvious. The Cassak and Shay

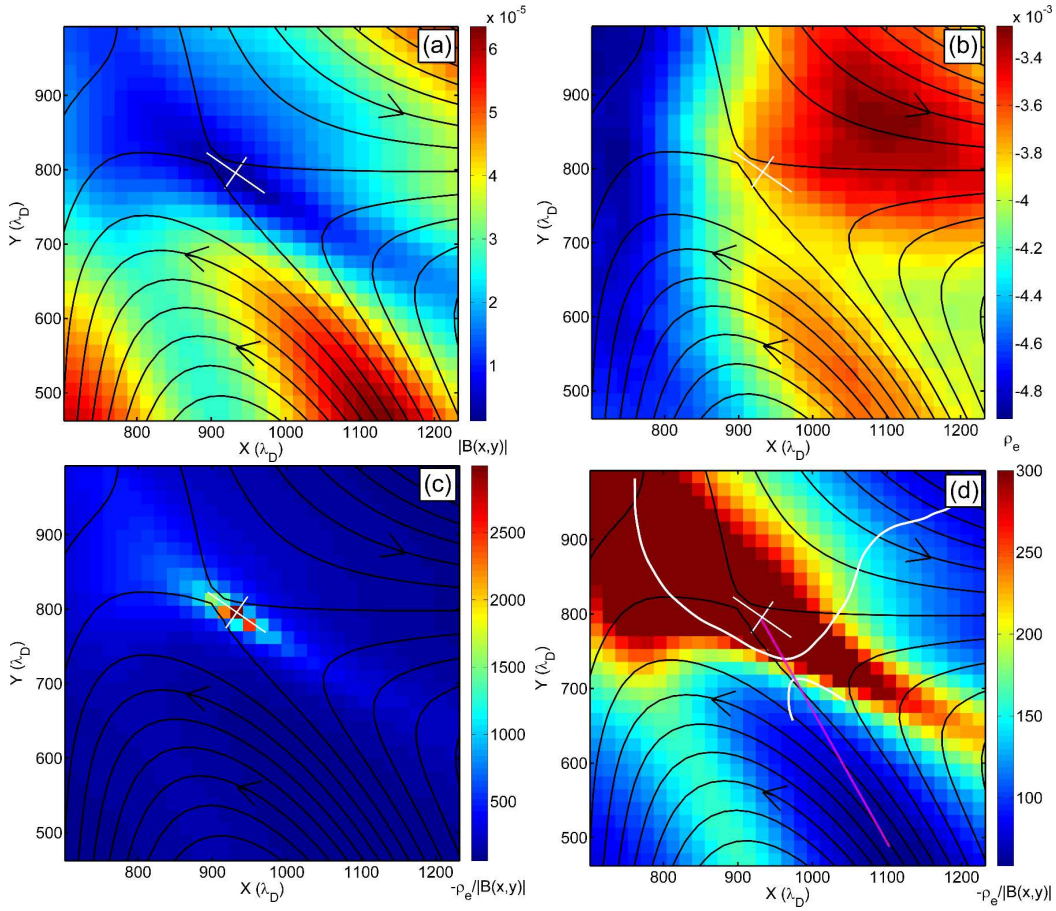

Figure 4.12.: Reconnection site 3 (refer to Fig. 4.6). Black lines are magnetic field lines. The white cross show the eigenvectors of the Hessian matrix. Background colour shows:
a) Magnitude B(x,y)
b) Electron charge density, ρ_{qe}
c) The parameter, $-\rho_{qe}/|B(x,y)|$, highlighting the electron diffusion region.
d) $-\rho_{qe}/|B(x,y)|$ (reduced color scale). White lines are streamlines of electron bulk velocity, showing the location of the electron stagnation point.

[2007] theory assumes steady state reconnection, whereas here the reconnection is not steady, but changes in both speed and reconnection direction as the field evolves and fluctuates within the turbulence. Therefore, the stagnation point will also move and fluctuate with the changing conditions, and the theory may not be valid until a relatively steady reconnection state is reached at any specific reconnection site.

4.3.3. Hall reconnection and its quadrupolar signature

Figure 4.13 again shows all three reconnection sites, with field lines plotted in black, electron streamlines plotted in white, and $B_z - B_0$ plotted as the background colour map. Subtracting the initial guide field from B_z reveals the shape of the out-of-plane quadrupolar signature, especially in Panel (b). This signature is usually seen in two-fluid Hall MHD simulations [Karimabadi et al., 2004, Sonnerup, 1979, Terasawa, 1983], hybrid simulations [Karimabadi et al., 1999], and full particle simulations simulations [Lapenta et al., 2011]. This quadrupolar signature arises from the circular motion of electron currents in the region, as they decouple from the ion flow, which enhances the out-of-plane magnetic field. Anti-clockwise electron motion creates a negative enhancement in the magnetic field, as can be seen in the top-left and bottom-right of Fig. 4.13(b), whereas clockwise electron motion creates a positive enhancement, as at top-right and bottom-left. Fig. 4.13(a) and 4.13(c) show less clear signatures. This is because the value of $B_z - B_0$ is close to zero at the flow stagnation point in Panel (b). In Panel (a), the value of $B_z - B_0$ at the stagnation point is $\sim -2 \times 10^{-5}$ and in Panel (c) it is $\sim 3.5 \times 10^{-5}$. Adding and subtracting these additional values from B_z to make the value of B_z at the stagnation point equal to zero reveals the positive and negative quadrupole signature. It is due to these signatures that the reconnection can be described as "Hall reconnection" (see Eq. 3.6) and is mainly due to the interaction of decoupled electron and ion flows. The reconnection arises spontaneously, driven by the plasma dynamics introduced by the initial magnetic perturbation.

The asymmetry of the X-point configuration is also seen in the asymmetric quadrupolar Hall signature. It is known that the presence of a guide field can result in an asymmetric reconnection field pattern due to the nonlinear interaction between guide field and Hall field components [Eastwood et al., 2010, Karimabadi et al., 1999]. However, asymmetry can be caused by other factors (as discussed in Section 4.3.1) such as density gradients and asymmetric inflows driving the reconnection, both of which are present in this simulation.

4.3.4. Temperature, anisotropy and reconnection rate

Figure 4.14 shows the distinctive shape of the region of increased electron temperature anisotropy generated around reconnection site 2. Two main areas of strong temperature anisotropy are located to the top-left and the bottom-right of the centre of reconnection in the outflow regions. An animation of the time development of the temperature anisotropy and magnetic field lines shows that the anisotropy

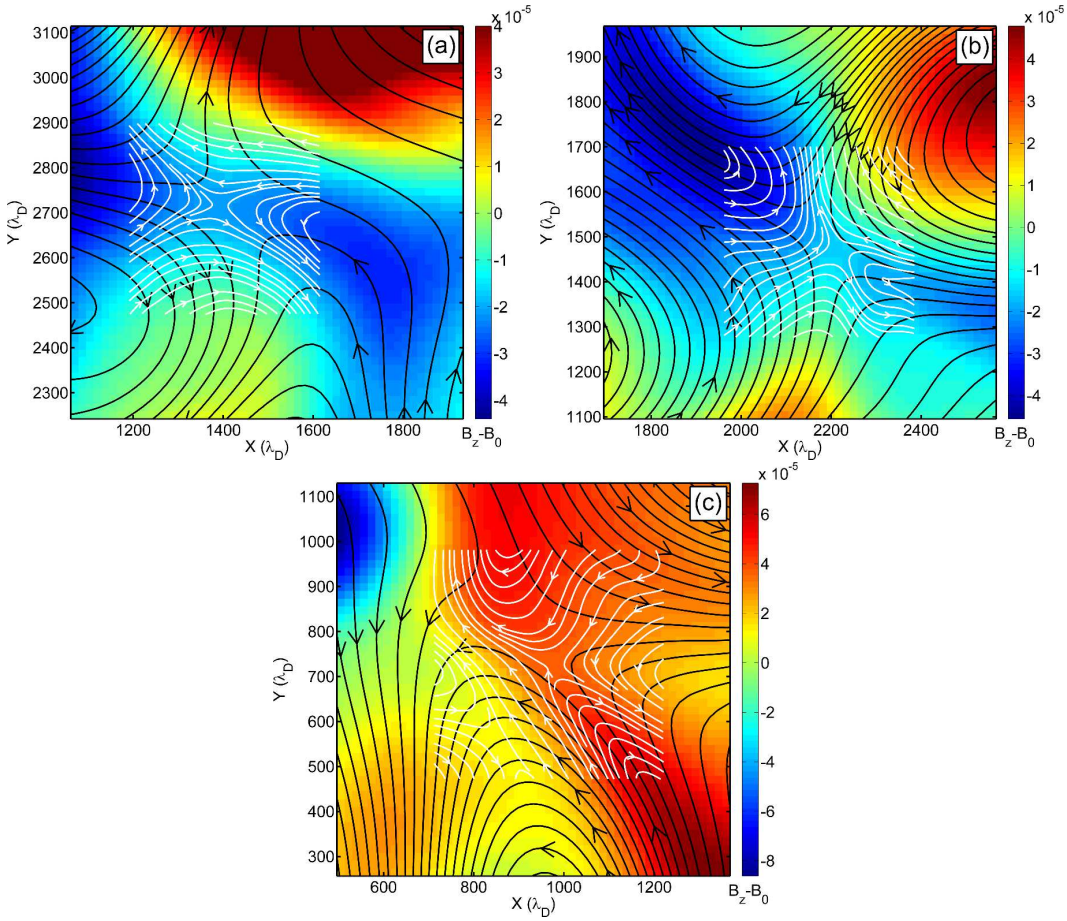

Figure 4.13.: Out of plane magnetic field component $(B_z - B_0)$ showing quadrupolar signature around a) reconnection site 1, b) reconnection site 2 and c) reconnection site 3. Magnetic field lines shown in black, and electron streamlines in white.

increases with the reconnection rate and appears to grow outwards from the centre of reconnection. Reconnection rate is equal to E_z in a 2-dimensional geometry.

To investigate if there is a link between reconnection and this anisotropy development, the reconnection sites were tracked, and the reconnection rate, E_z, at the centre of each recorded. Average plasma parameters in an area around each site was recorded, i.e. electron temperature and anisotropy. Values were averaged over a box size of 15 cells either side of the centre of reconnection (Fig. 4.15). Measured reconnection rates were consistent with the animations of magnetic field line motion, further evidence that reconnection was occurring. Figure 4.16 shows a time series of the data for reconnection site 2. Figure 4.16(a) shows reconnection rate, Fig. 4.16(b) average electron temperature and Fig. 4.16(c) average electron anisotropy in terms of the parameter $(1 - T_{e\parallel}/T_{e\perp})$. In this figure an anisotropy parameter value less than zero corresponds to a parallel temperature anisotropy.

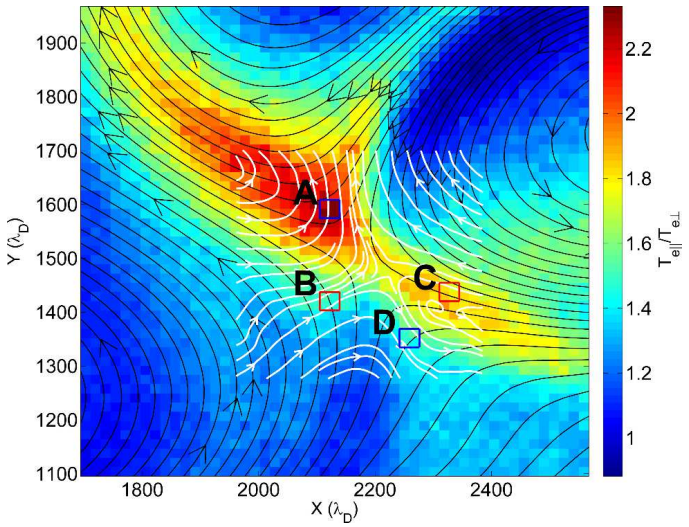

Figure 4.14.: Electron temperature anisotropy ratio $T_{e\parallel}/T_{e\perp}$ in the region of reconnection site 2 at $t = 97\Omega_e^{-1}$. Magnetic field lines are shown in black and electron streamlines are shown in white. The four marked regions are discussed in the text.

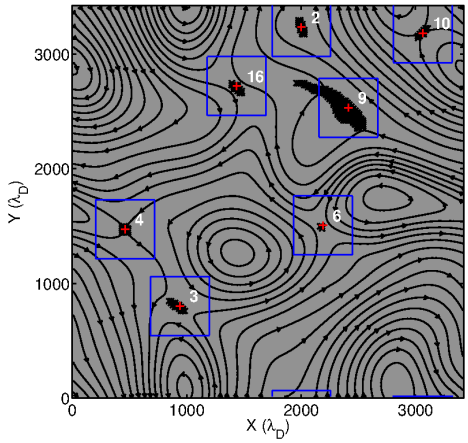

Figure 4.15.: Whole simulation domain at cycle = 1930. Event "labels" are shown in white. (Note: these are for computation only and do not match Fig. 4.6 labels.) The 30 cell width squares around the reconnection site centre (used for parameter averaging) are shown in blue.

As previously noted, the electron temperature is not distinctly greater around reconnection sites when compared with other temperature variations in the simulation. Comparing the time profiles of Fig. 4.16, T_e varies by ± 2 % of its initial value, before $t = 100\Omega_e^{-1}$. There is a small correlation with reconnection rate, but after this time the electrons around the reconnection site experience overall cooling and the correlation becomes weak. However, a correlation is evident between anisotropy and reconnection rate, throughout the entire simulation, indicating that

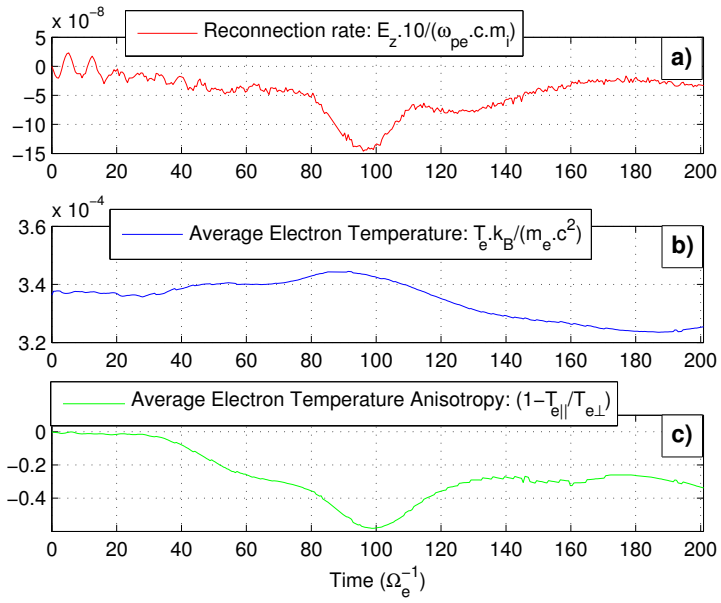

Figure 4.16.: Averaged values around reconnection site 2 for (a) reconnection rate, (b) electron temperature, and (c) temperature anisotropy parameter $(1 - T_{e\parallel}/T_{e\perp})$ as a function of time.

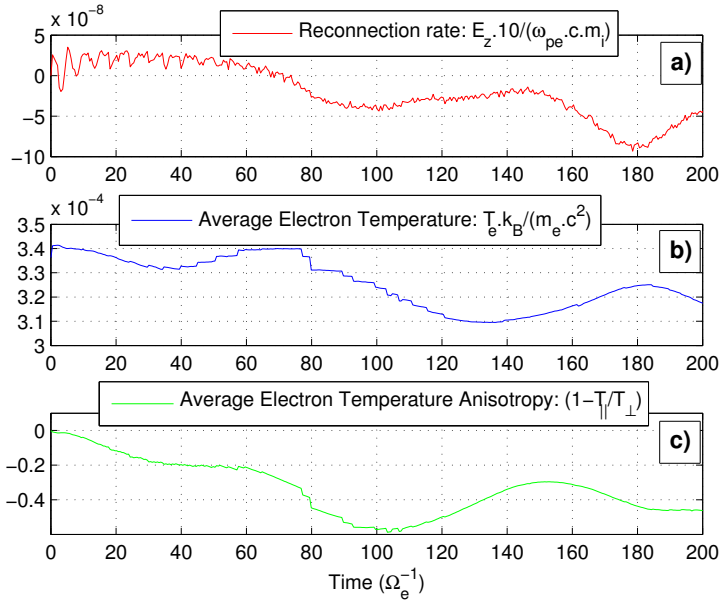

Figure 4.17.: Averaged values around reconnection site 3 for (a) reconnection rate, (b) electron temperature, and (c) temperature anisotropy parameter $(1 - T_{e\parallel}/T_{e\perp})$ as a function of time.

the reconnection process is responsible. A similar, but weaker correlation is evident in Fig. 4.17, which shows the same information, for reconnection site 3. In this time

series, electron temperature anisotropy increases shortly after the local reconnection rate increases.

As shown in Fig. 4.6 not all reconnection sites show such a marked increase in anisotropy, which suggests a more complex physical process is operating rather than a simple, local one which would produce an absolute correlation with reconnection rate.

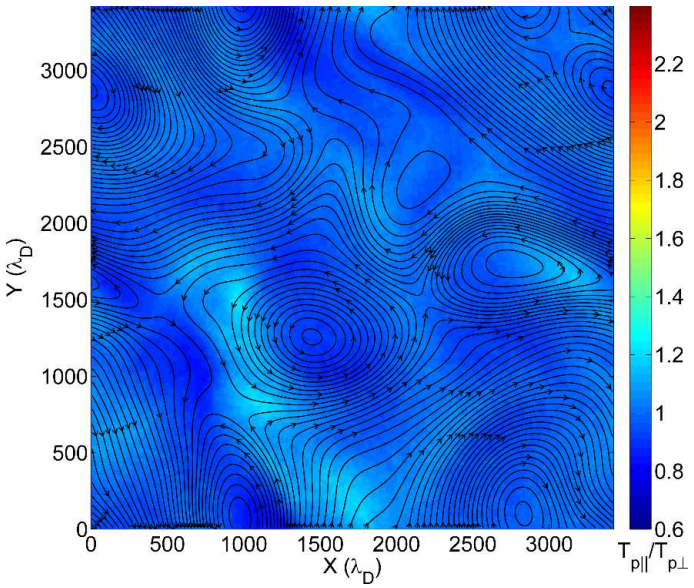

Figure 4.18.: Magnetic field lines (black) and proton temperature anisotropy $(T_{p\|}/T_{p\perp})$ at time $t = 97\Omega_e^{-1}$ for the full simulation domain for $m_i/m_e = 1836$.

An examination of the ion distribution functions in the vicinity of the reconnection sites, shows that there is no significant changes in ion temperature or temperature anisotropy (Fig. 4.18). The ion distribution function remains approximately isotropic, when averaged over ion gyro-scale. This is not unexpected considering the minor role of the ion dynamics over the timescale of the simulation.

4.3.5. Electron velocity distribution functions

We will now discuss the velocity distributions seen near reconnection site 2 shown in Fig. 4.14. Four sub-regions are chosen on different sides of the magnetic separatrices corresponding to electron inflow (B and C) and electron outflow (A and D).

Figure 4.19 shows the electron distribution in the region of inflow box A, where the anisotropy is highest. Figure 4.19(a) shows the distribution in the $v_y - v_x$ plane, with a black cross at the electron bulk velocity; Fig. 4.19(b) shows the distribution in the $v_z - v_x$ plane, with the black arrow indicating the direction of the magnetic

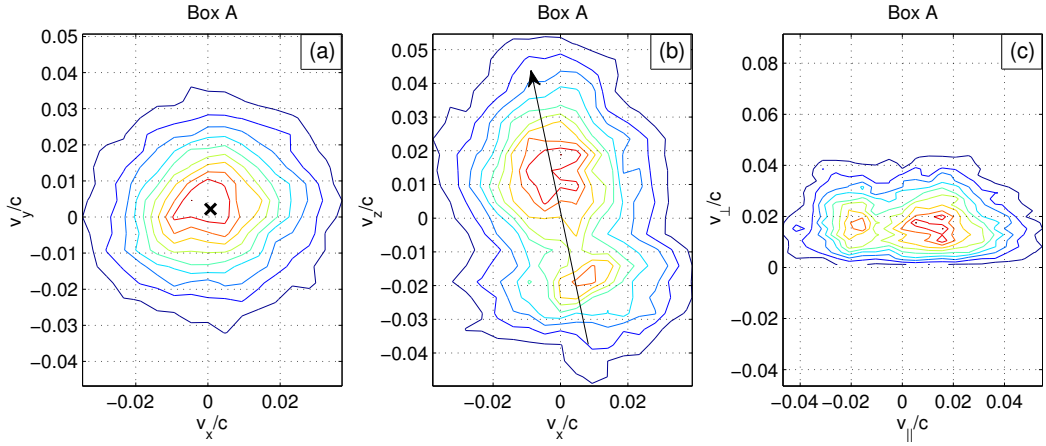

Figure 4.19.: Electron VDFs for reconnection site 2, box A (cf. Fig. 4.14) for (a) $v_x - v_y$, (b) $v_x - v_z$, and (c) $v_\parallel - v_\perp$ planes.

field; and Fig. 4.19(c) shows the distribution in the $v_\perp$ - $v_\parallel$ plane. All distributions are normalized to unity with red contours indicating higher particle density than blue; velocities are normalized to the speed of light c.

From Fig. 4.19(c) it can be seen that thermal width of the distribution in the parallel direction is approximately 1.5 times that in the perpendicular direction, in agreement with the anisotropy ratio of approximately 2.3 (cf. Fig. 4.14). Rather than a bi-Maxwellian shape, the distribution shows a double peaked, beam-like structure, with one peak on the negative $v_\parallel$ side and another on the positive $v_\parallel$ side of the distribution. The drift velocity in the positive y direction is consistent with the flow pattern of Fig. 4.14. The symmetry of the v_z - v_x distribution around the magnetic field direction seen in Fig. 4.19(b) indicates that the electron distributions are approximately gyrotropic.

Figure 4.20 shows plots of the $v_\perp$ - $v_\parallel$ distribution functions for the other three boxes B, C, and D marked in Fig. 4.14. These all show multi-peaked structures. For example, Fig. 4.20(c) box D has the appearance of a core plus beam distribution, as the peak on the positive $v_\parallel$ side of the distribution is much larger. The distribution for box C (Fig. 4.20(b)) even shows a triple peaked distribution. Thus the regions of largest temperature anisotropy in Fig. 4.6, which occur around reconnection sites, seem to correspond to the presence of distribution functions with a mix of multiple peaks. This, in itself, suggests that the reconnection process is forming one or both of these peaks, possibly by accelerating a subset of particles to form a second peak.

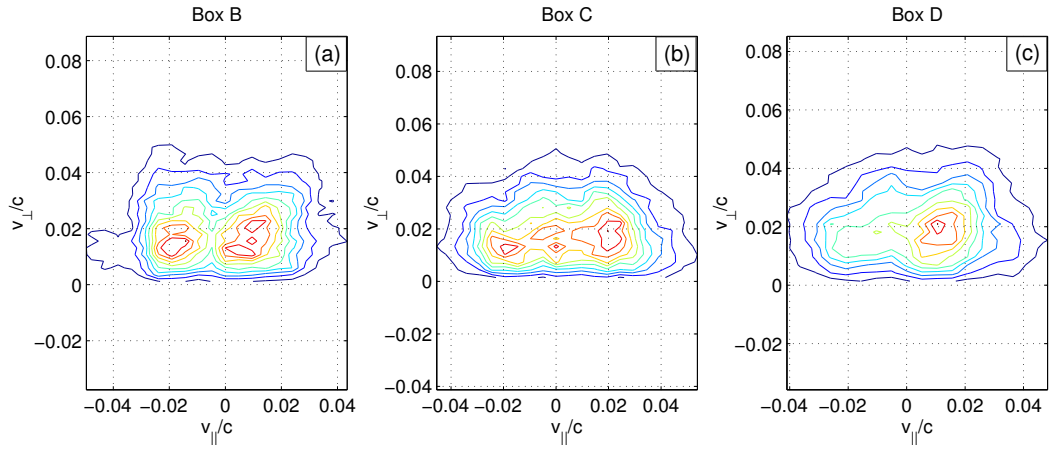

Figure 4.20.: Electron VDF in $v_{\parallel} - v_{\perp}$ plane for reconnection site 2, for (a) box B, (b) box C and (c) box D, as marked in Fig. 4.14.

4.3.6. Particle tracking

In order to determine the formation mechanism of these multi-peaked distributions, we tracked particle trajectories of electrons selected from the different peaks of the distributions, to determine whence these separate populations of electrons originate. Although the complex physics cannot be understood merely in terms of single particle motions, this exercise will allow us to see whether one or both of the distribution function peaks have been produced by electrons being accelerated or decelerated as they approach and interact with the reconnection site. We show here data for two electrons, labelled E1 and E2, which were tracked throughout the simulation. Both electrons were located in box A (Fig. 4.14), and were chosen from a large set of recorded particles that interacted with reconnection site 2. Electron E1 (Figs. 4.21 and 4.22) was chosen from the particles in the peak on the positive $v_{\parallel}$ side of the distribution shown in Fig. 4.19(c). Electron E2 (Figs. 4.23 and 4.24) was chosen from the particles in the peak on the negative $v_{\parallel}$ side of the distribution. In these figures time has been normalized to Ω_e calculated using magnetic field $\mathbf{B_0}$. Fig. 4.21(a) shows v_z versus time for electron E1. Velocity components v_x and v_y are shown in Fig. 4.21(b) in blue and green, respectively. The electric field as experienced by electron E1 is shown in the Fig. 4.21(c) and (d), with E_x and E_y plotted in blue and green, and E_z in red. Figure 4.22 shows the trajectory taken by electron E1 before and during its encounter with the reconnection site. Magnetic field line contours for the whole simulation box are shown in black at $t = 55\Omega_e^{-1}$. Traced in white is the electron position for the interval $t = 0$ to $t = 100\Omega_e^{-1}$. The green and blue crosses on the trajectory mark the start and end locations, respectively. In Fig. 4.21 the

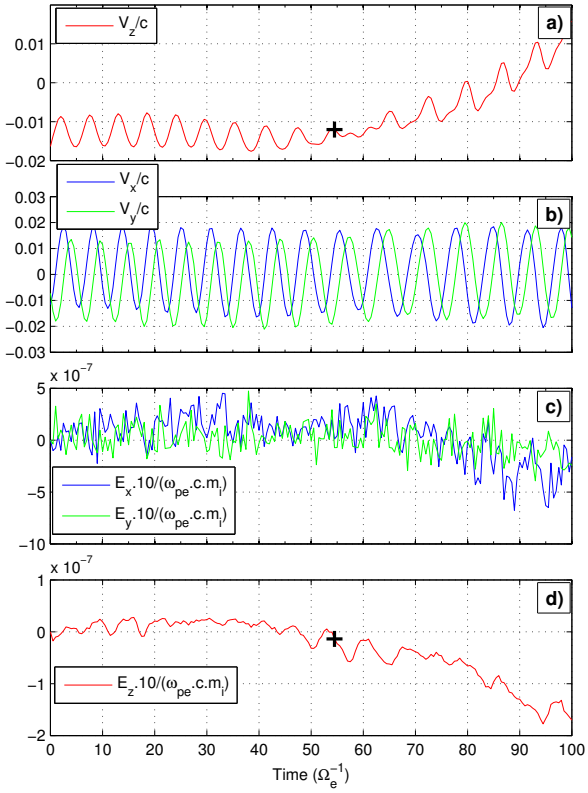

Figure 4.21.: Time series of particle velocity components and electric field components (as experienced by the particle) for electron E1 which is chosen from the positive $v_{\|}$ peak in the distribution function for box A (Figs. 4.14, 4.19).

black crosses marked on the v_z and E_z time-series, corresponds to the time at which the magnetic field lines are shown, with a corresponding red cross marked on the electron trajectory at the same time (Fig. 4.22). It is important to remember that the magnetic field evolves dynamically over the time interval of the electron trajectories. Thus, the magnetic field line configuration shown in these figures is only illustrative of the magnetic environment at a specific time late in the trajectories. Animations have been used extensively to analyse the electron trajectories relative to the dynamic field line geometry.

Figure 4.21(a) shows that as electron E1 encounters the reconnection region after $t = 55\Omega_e^{-1}$, the parallel z component of its velocity increases. This is one example of many particles that were tracked, and all show similar behaviour. Electrons experience an acceleration, due to E_z, along the guide field direction as they approach the reconnection site. The large increase in negative E_z in Fig. 4.21(d) results in a force on electron E1 in the positive z direction; E_z at reconnection site 2 is mainly

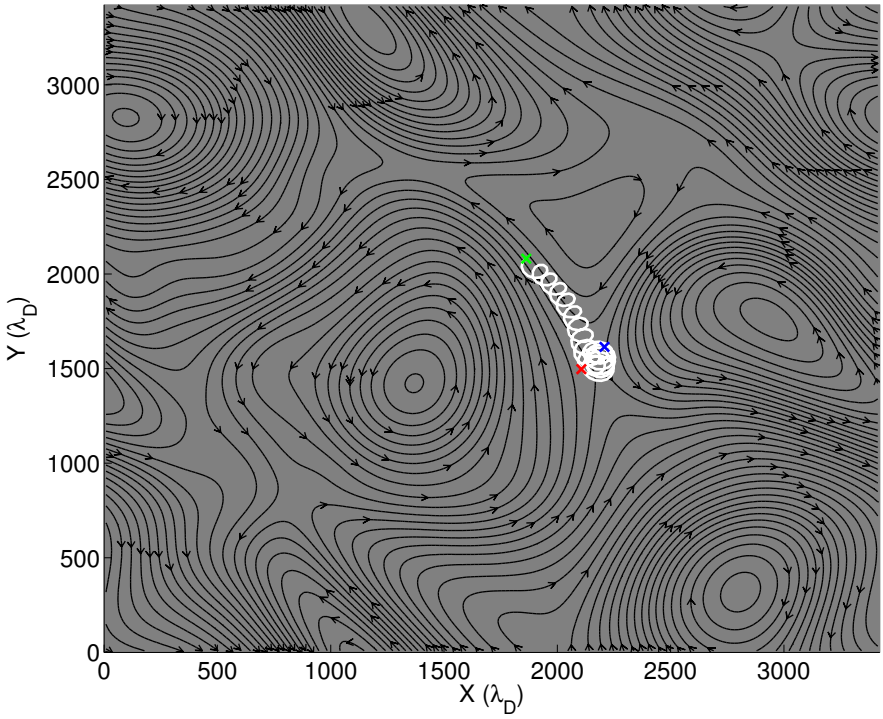

Figure 4.22.: Trajectory (white) of electron E1 as it approaches and interacts with reconnection site 2. The start and end locations are shown by green and blue crosses respectively. Magnetic field lines (black) are plotted at the time indicated by the black cross in Fig. 4.21. The position of electron E1 at the time of the plotted field lines is shown with a red cross.

negative throughout the simulation (Fig. 4.16(a)). Figure 4.21(a) also indicates that electron E1 passes very close to the center of reconnection, since the oscillation in v_z decreases in amplitude, indicating that the in-plane components of the magnetic field have become almost zero. In summary, reconnection site 2 is responsible for the positive parallel peaks in Figs. 4.19 and 4.20.

Figures 4.23 and 4.24, in the same format as Figs. 4.21 and 4.22 respectively, show trajectory information for electron number E2, which is from the peak on the negative $v_\parallel$ side of the distribution of Fig. 4.19. This particle has experienced acceleration in the negative z direction before it encounters the reconnection site at approximately $t = 85\Omega_e^{-1}$. However, similar to electron E1, it experiences a positive acceleration after it enters the region around reconnection site 2, consistent with the negative E_z. However, despite this acceleration the particle v_z remains negative. We have examined 181 particle trajectories taken from the negative $v_\parallel$ peak of the distribution and they all show a similar history; there are a total of 9901 simulation particles in the distribution with $v_\parallel < 0$. From Figs. 4.22 and 4.24 electrons E1 and

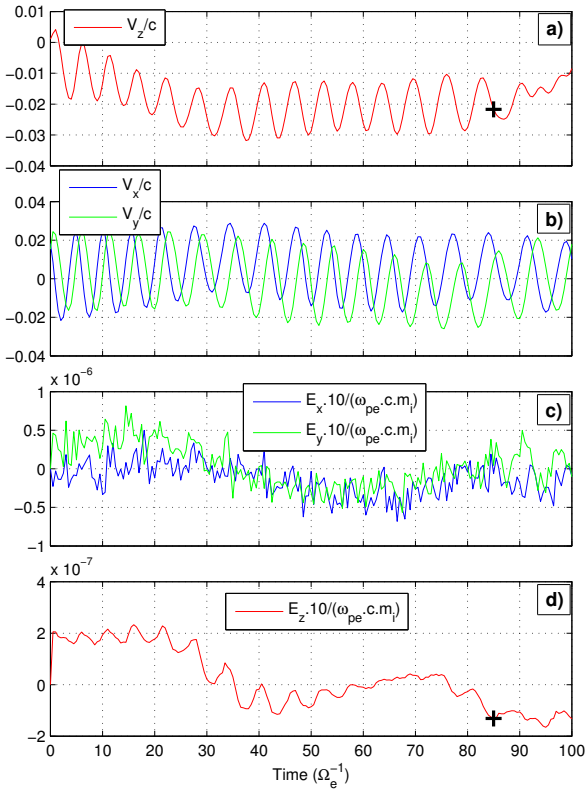

Figure 4.23.: Time series of particle velocity components and electric field components (as experienced by the particle) for electron E2 which is chosen from the negative $v_{\|}$ peak in the distribution function for box A (Figs. 4.14, 4.19).

E2 have very different trajectory histories, but are eventually colocated but with very different parallel velocities.

Since reconnection site 2 has mainly negative E_z for most of the simulation, it accelerates electrons in the positive z direction. We used this fact to confirm this mechanism of temperature anisotropy generation, by examining the positions at previous time-steps of groups of particles from the negative and positive peaks of Figs. 4.19 and 4.20. In this analysis, the two groups (electrons from the negative peak and the positive peak) are given label numbers; 1 for electrons from the negative peak, and 2 for electrons from the positive peak. We then used the position of these electrons, at a previous timestep, to create a numbered colour-map, see Fig. 4.25(a). Cells in the simulation domain are labelled 1 (cyan) if it contains only cells from the negative group, 2 (yellow) if it contains cells from just the positive group, zero (dark blue) if the cell contains no electrons from either group, and 3 (dark red) for a mix of both groups. Figures 4.25(a) and (b) are plotted at $t = 73\Omega_e^{-1}$. Figure 4.25(c)

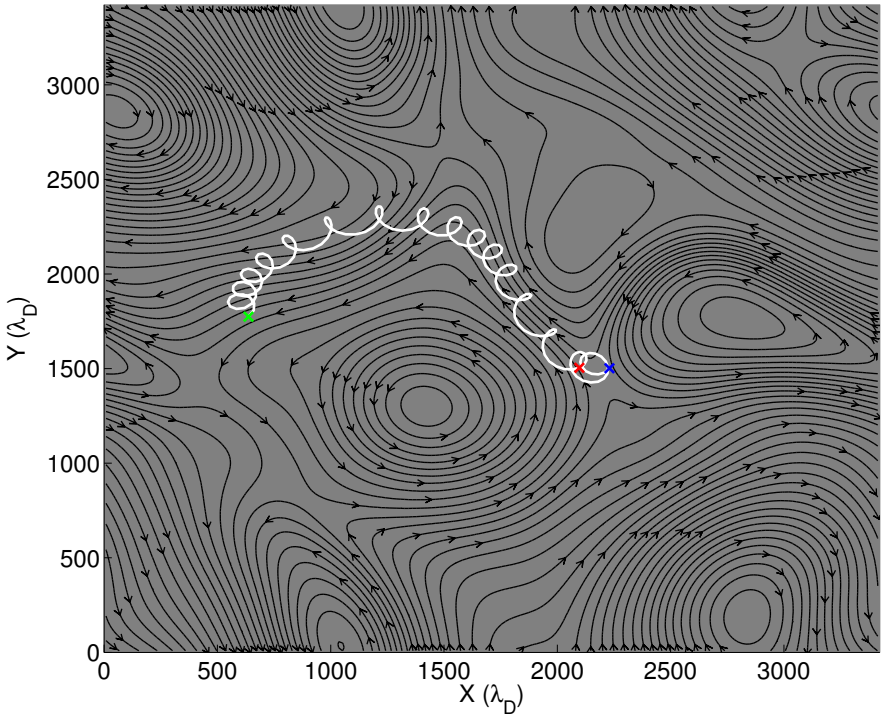

Figure 4.24.: Trajectory (white) of electron E2 as it approaches and interacts with reconnection site 2. The start and end locations are shown by green and blue crosses respectively. Magnetic field lines (black) are plotted at the time indicated by the black cross in Fig. 4.23. The position of electron E2 at the time of the plotted field lines is shown with a red cross.

is plotted just before $t = 97\Omega_e^{-1}$, and shows the 4 locations (boxes A, B, C and D) that the particles were originally selected from. (Compare Figs. 4.25 and 4.14.) This technique is useful, as it can show patterns or commonalities in the collective trajectory history of a group of particles.

As can be seen in Fig. 4.25(a) electrons that end up in the peaks at negative values of velocity in Figures 4.19 and 4.20 approach the reconnection site from the top left and bottom right. The trajectories of these particles trace a region whose shape is towards the center of reconnection only from the top left part of the separatrix and the bottom right part of the separatrix (Fig. 4.25(b)), consistent with the shape of the region of enhanced parallel anisotropies in these locations (Fig. 4.14). These particles, like electron E2, have experienced acceleration in the negative z direction elsewhere (perhaps from reconnection sites reconnecting in the opposite sense) and their presence in the reconnection outflow areas around the reconnection site, results in anisotropy and multi peaked distributions. In order to determine why a triple peaked distribution is formed, as shown in box C (Fig. 4.20), particles from the

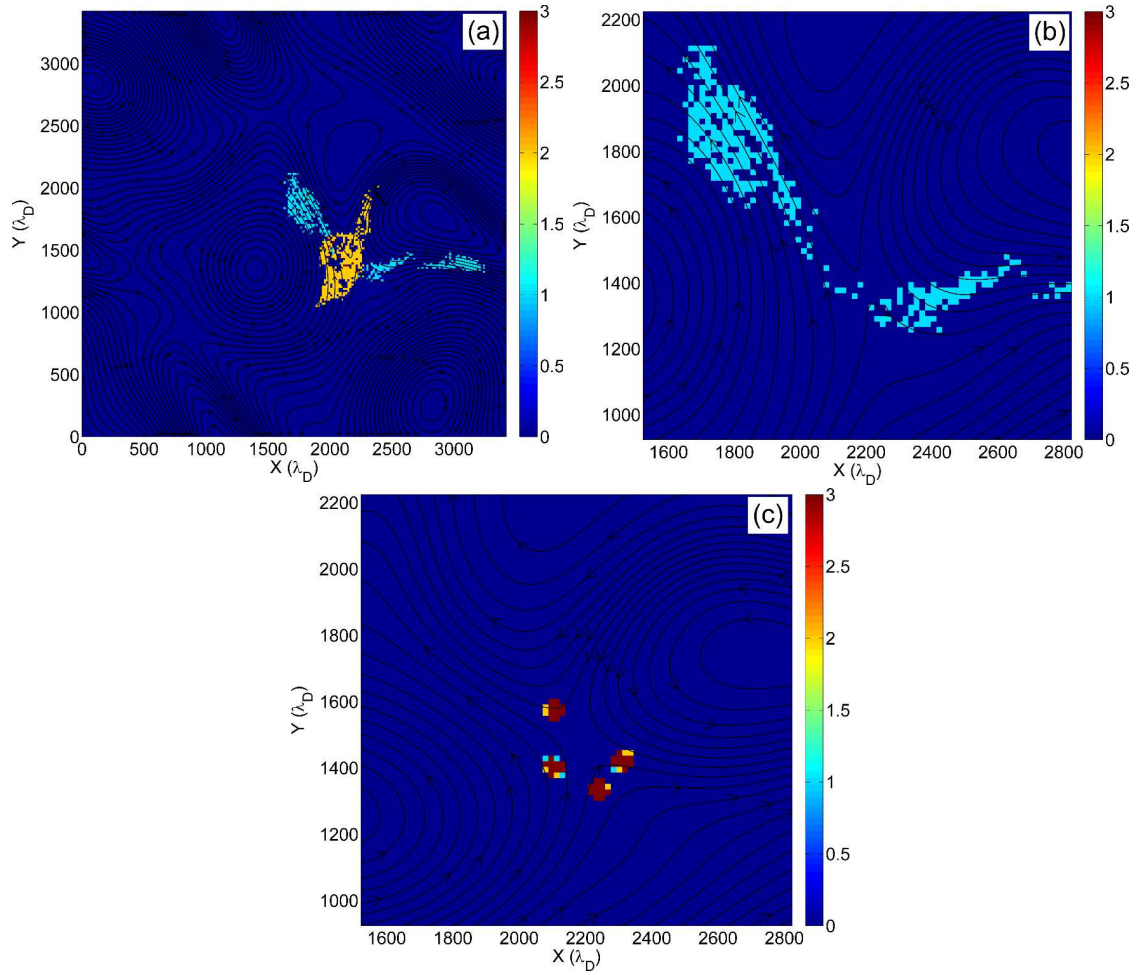

Figure 4.25.: Particle group trajectory plots around reconnection site 2. Value = 1 (cyan) show cells containing only electrons from the negative peaks of the VDFs of Figs. 4.19 and 4.20. Value = 2 (yellow) show cells containing only electrons from the positive peaks of the same VDFs. Value = 3 (dark red) show cells with electrons from positive and negative peaks. Panels (a) and (b) are plotted at $t = 73\Omega_e^{-1}$. Panel (c) is plotted just before $t = 97\Omega_e^{-1}$, and shows the locations of the boxes A ,B ,C and D. (cf. Fig. 4.14).

central peak were also tracked. Although not shown here, these particles again show positive increases in v_z near the reconnection site. So the central peak is formed of particles that start with a negative v_z but as they enter the reconnection site they are only accelerated enough to finish in the center of the distribution. So double or triple peaked distributions can be formed by electrons with different trajectory histories passing through multiple acceleration regions, but arriving at the same location within a reconnection site. This mixing mechanism is shown schematically in Fig. 4.30.

4.3.7. Small scale fluctuations

One unanswered question is what type of waves form the cascade extension to large k. As discussed in Section 2.2 theoretical models of turbulence rely on the nonlinear interactions of waves to create new waves at different wavenumbers, filling all of wavenumber space. Figure 4.4 has already demonstrated that energy in the initial long wavelength perturbations has cascaded to larger wavenumbers. In Section 2.4 we have already discussed that at sub-proton scales in the solar wind, there are two candidates: kinetic Alfvén waves (KAWs) and whistler waves. We will now present some evidence that the waves generated here are kinetic Alfvén waves. Although, it should be noted that this analysis is not yet conclusive, and further work is required.

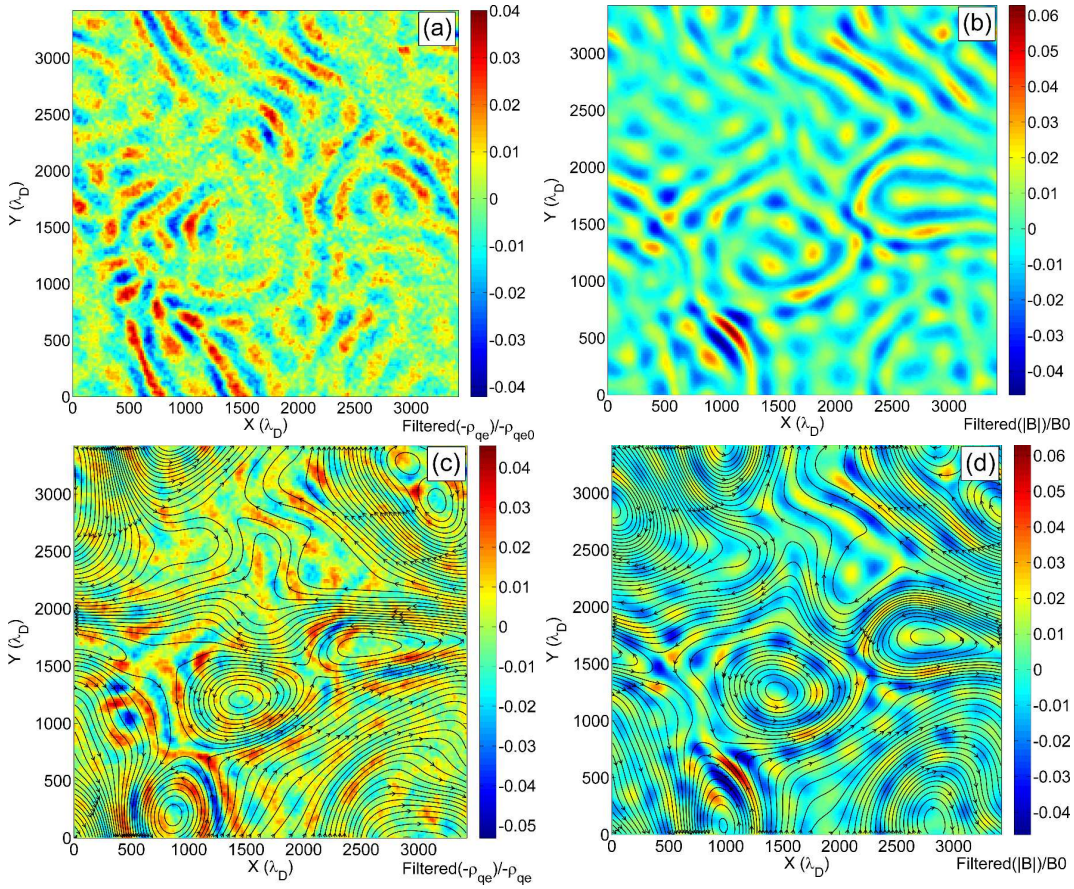

Figure 4.26.: FFT filtered parameters with wavenumber $k < 1$ removed for a) electron density at cycle 1930 ($t = 97\Omega_e^{-1}$), b) magnitude magnetic field at cycle 1930, c) electron density at cycle 2490 ($t = 125\Omega_e^{-1}$), d) magnitude magnetic field at cycle 1930. Original magnetic field lines are show in black. The fluctuations have been normalised to initial values.

We used Matlab's fast Fourier transform (FFT) routines to filter out large scale

fluctuations from electron density (multiplied by -1 so that is it proportional to density), $-\rho_{qe}$, and magnetic field strength, $|B|$. This involves taking an FFT of the data, and setting to zero coefficients that correspond to wavenumbers with $k < 1$, then an inverse FFT is performed. This procedure removes fluctuations near the injection scales, and the remaining fluctuations, with $k > 1$, correspond to wavenumbers within the steepest part of the turbulent cascade (Fig. 4.4).

Figure 4.26 shows the outputs from this analysis. In all panels the filtered parameter has been normalised by its initial value, $-\rho_{qe0}$ or $B0$. Figures 4.26(a) and (b) show data at $t = 97\Omega_e^{-1}$ (as Fig. 4.14). Figure 4.26(d) shows the same data as Fig. 4.26(b), but the unfiltered magnetic field lines are also plotted. This shows that the small scale magnetic fluctuations appear aligned with the in-plane field lines, suggestive of perpendicular propagation. Comparing Figs. 4.26(a) and (b), shows that density and field strength are not always correlated, although a similar pattern is visible. Both density and magnetic field fluctuations vary by $\sim \pm 4\%$.

These figures have a striking similarity to Fig. 2.20 which show a perpendicular cross section of filtered fluctuations from simulations of KAWs. Given that KAWs are quasi-perpendicular propagating waves and the similarity between these two figures, this is highly suggestive that the waves shown in Fig. 4.26 are KAWs. Additionally, the simulation has a strong guide field in the z direction, but no z spatial direction, so parallel propagating whistler waves cannot be supported.

To investigate further the correlation between density and field strength we performed a correlation analysis. In this analysis we calculate the sample Pearson correlation coefficient, r, for two matrices, X_{ij} and Y_{ij}, at two timesteps, t_1 and t_2, given by the equation,

$$r = \frac{\sum_{i=1}^{n_i}\sum_{j=1}^{n_j}[X_{ij}(t_1) - \bar{X}(t_1)][Y_{ij}(t_2) - \bar{Y}(t_2)]}{\sigma_X(t_1)\sigma_Y(t_2)}, \tag{4.8}$$

$$\sigma_X(t) = \left[\sum_{i=1}^{n_i}\sum_{j=1}^{n_j}(X_{ij}(t) - \bar{X}(t))^2\right]^{1/2}, \tag{4.9}$$

$$\sigma_Y(t) = \left[\sum_{i=1}^{n_i}\sum_{j=1}^{n_j}(\,Y_{ij}(t) - \bar{Y}(t)\,)^2\right]^{1/2}. \tag{4.10}$$

Where n_i and n_j are the size of the matrix in the i and j directions. $\bar{X}(t)$ and $\bar{Y}(t)$ are the mean values of each matrix at that timestep. (Note that Eqs. 4.9 and 4.10 are similar to the expression for the standard deviation.) In this case, each sample is considered to be a 2D matrix of numbers at a certain timestep. This was calculated

for the two filtered variables at all timesteps upto 4000 cycles ($t = 200\Omega_e^{-1}$) as follows; For each timestep, the "current" filtered electron density dataset was correlated with all previous timesteps of filtered magnetic field strength. At each previous timestep, Eq. 4.8 gives +1 for a perfect correlation, −1 for a perfect anti-correlation, zero for no correlation. The results of this analysis are shown in Fig. 4.27, as a colour map of the correlation values. The user should read horizontally across this graph, to find the correlation values at a certain timestep (of electron density) relative to previous values of magnetic field strength. A small black cross shows the location of the maximum magnitude correlation for that timestep. E.g. cycle 2000 ($t = 100\Omega_e^{-1}$) of charge density (vertical axis) has a maximum correlation with magnetic field strength at cycle ~ 1500 ($t = 75\Omega_e^{-1}$). Notice that the correlation coefficient, r, is nearly always negative, showing anti-correlation, and only shows positive correlation values below ~ 0.2. Additionally, the location of the maximum correlation value is ~ 500 cycles ($25\Omega_e^{-1}$) behind the current timestep, from the horizontal distance between the black cross in Fig. 4.27(a) and the $y = x$ line.

Figure 4.27(b) shows the value of r with the the maximum magnitude for each cycle, corresponding to the black cross in Panel (a). The data shows a strong anti-correlation (blue), of ~ -0.6 to -0.7. The anti-correlation increases after ~ 500 cycles ($t = 25\Omega_e^{-1}$) and then remains strong. As a check that the correlation function is working, Fig. 4.26(c) shows the filtered electron density variable at $t = 125\Omega_e^{-1}$, which has maximum anti-correlation to magnetic field strength at $t = 97\Omega_e^{-1}$ in Fig. 4.26(d). Careful inspection, particularly of the peaks in the density fluctuation, shows that the density fluctuations in Panel (c) have a strong anti-correlation to the magnetic fluctuations in Panel (d).

So the magnetic field strength and electron density are anti-correlated, with a time separation of ~ 500 cycles ($25\Omega_e^{-1}$) so that density fluctuations appear to lag behind the magnetic field fluctuations. While this is interesting, it does not help confirm the type of fluctuations.

4.4. Additional simulation results

Before we draw our conclusions we now briefly comment on simulations with different simulation parameters. When we ran the simulation with a different random seed value, used in the calculation of the initial the magnetic field perturbation, we find qualitatively the same results as presented in the previous sections, but with different field configurations. A simulation with a different initial field configuration is shown

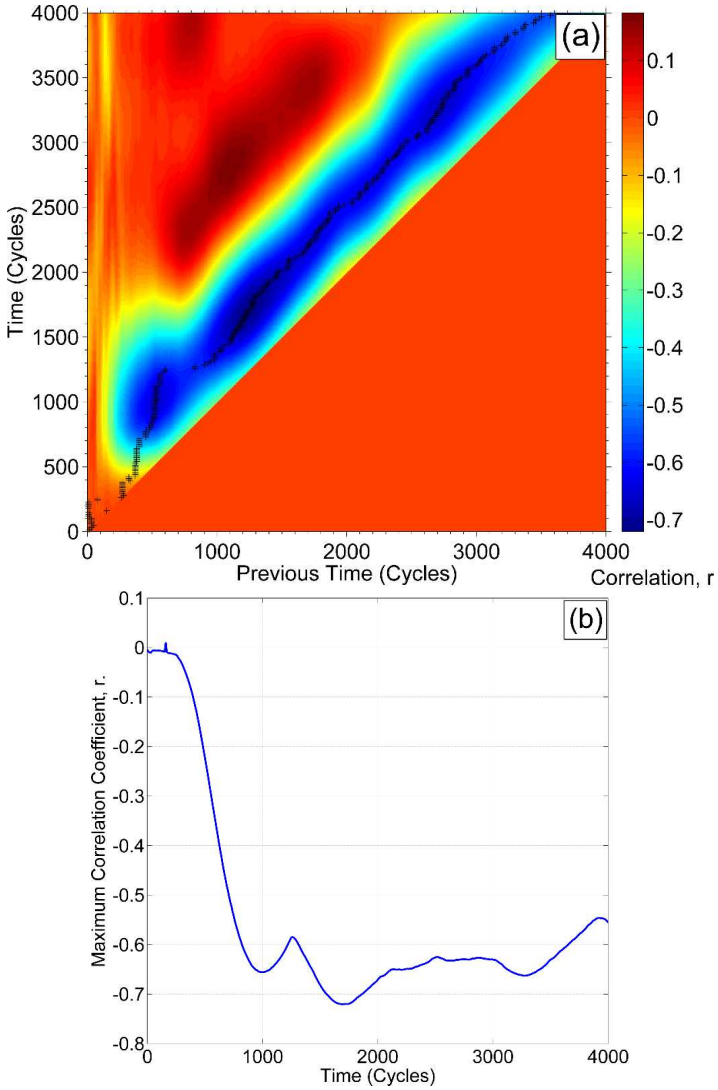

Figure 4.27.: a) Sample Pearson correlation coefficient for filtered ($k > 1$) electron density and all previous timesteps of filtered ($k > 1$) magnetic field strength. Maximum correlation time is marked by a black cross.
b) Time-series of maximum correlation value.

in Fig. 4.28. As in Fig. 4.6, only some reconnection sites show increased anisotropy (e.g. top left corner of Fig. 4.28), and the same anisotropy mechanism is responsible.

We have also investigated the effect of using a non-realistic proton-electron mass ratio. Many other PIC codes are explicit, which are computationally more expensive, and require many more steps per electron gyro-orbit when moving particles. Many users opt to use a lower m_i/m_e in order to reduce the total number of calculation steps required. Lowering the amount of computation may also allow the user to simulate physically larger areas of plasma for an equivalent grid size, as the mass

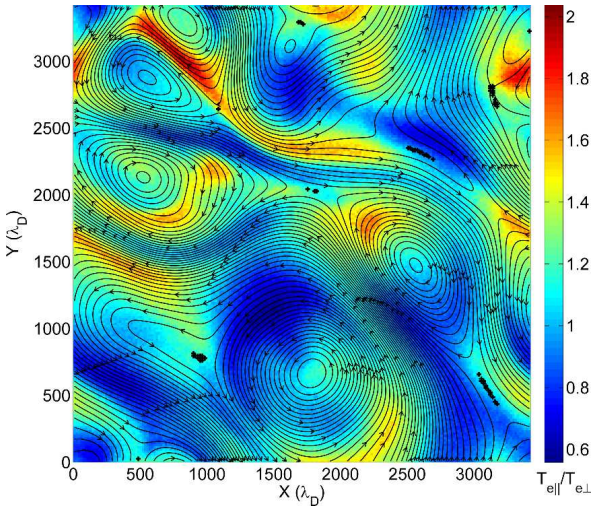

Figure 4.28.: Magnetic field lines (black) and electron temperature anisotropy ($T_{e\|}/T_{e\perp}$) at time $t = 50\Omega_e^{-1}$ for the full simulation domain.

ratio also adjust plasma length scales such as the proton larmor radius and ion inertial length. Therefore the question arises if this asymmetry generation mechanism we have described here depends on using a physical mass ratio.

We use $m_i/m_e = 400$ in this additional simulation, keeping the other plasma parameters such as plasma density and beta, the same as described in Section 4.2.1, except the ion super-particles were made lighter. The charge to mass ratio of particles were normalised to q/m_i, so the lighter mass ratio only changes the normalisations of ρ_q and $\mathbf{B}$ in this simulation (see Appendix B).

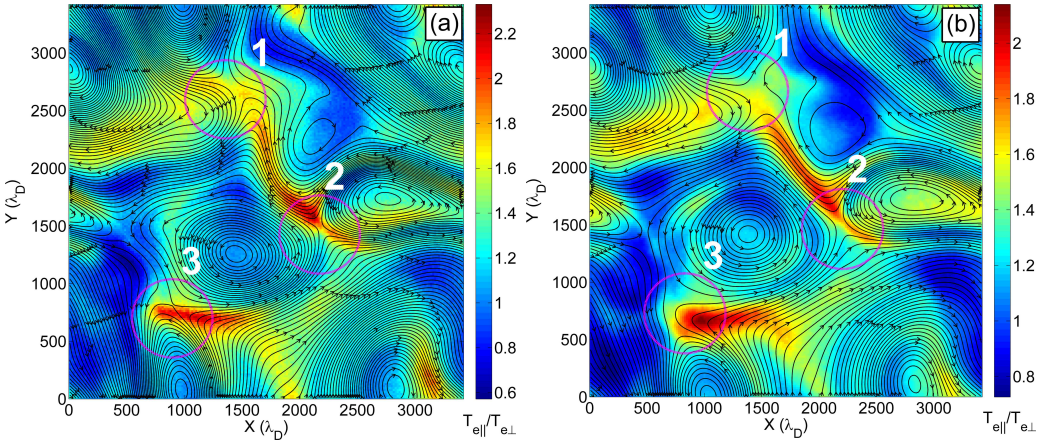

Figure 4.29.: Magnetic field lines (black) and electron temperature anisotropy ($T_{e\|}/T_{e\perp}$) at time $t = 97\Omega_e^{-1}$ for the full simulation domain for a) $m_i/m_e = 1836$ and b) $m_i/m_e = 400$. The three X-point regions discussed in the text are marked.

Figure 4.29 shows a comparison of the original physical mass ratio simulation,

and the simulation with $m_i/m_e = 400$. Panel (a) shows the electron temperature anisotropy at $t = 97\Omega_e^{-1}$ for the simulation with physical mass ratio. Panel (b) shows the electron temperature anisotropy at $t = 97\Omega_e^{-1}$ for the simulation with $m_i/m_e = 400$. There are only slight differences in the form of the in-plane field lines, and anisotropy, and the three reconnection sites with increased electron temperature anisotropy are visible in the corresponding locations in both simulations. This shows that the same mechanism is present, and that it does not depend on the mass ratio. We chose to focus our original analysis on the realistic mass ratio run so no doubt can be cast on any comparison to physical reality.

Additionally, we found that using $m_i/m_e = 400$ did not significantly change the form of the power spectra, the temperature, or temperature anisotropy signatures that were previously presented. The combination of these results means that in future work we could extend our simulations to larger box sizes, and cover both ion and electron scales, using $mi/m_e = 400$.

Finally, a repeat of the FFT analysis performed in Section 4.3.7, on the simulation data with $m_i/m_e = 400$ shows very similar results, except that the time lag of the correlation reduces to ~ 350 cycles ($18\Omega_e^{-1}$). The reduced time lag suggests that ion movement is still important, even at this scale, to the fluctuations involved in the turbulence. However more work is required to determine exactly what type of fluctuations are present.

4.5. Conclusions

We have presented the results of 2-D simulations using realistic proton to electron mass ratio of the turbulent decay of large scale fluctuations with an out-of-plane guide field. As in previous similar work with the guide field in the simulation plane [Camporeale and Burgess, 2011], a fluctuation power spectrum with approximately power law form quickly evolves, until $t = 100\Omega_e^{-1}$, after which the spectra are relatively time steady over the period simulated. The spectra extends to small scales of order the electron gyroradius. Animations of the magnetic field evolution show that X-points (i.e., potential reconnection sites) evolve dynamically, responding to the motion of surrounding magnetic islands in the turbulence. As reconnection occurs the topology of field lines can change as they move through the X-points, from closed within a single magnetic island to circulating around several islands. The sense and rate of field line motion can change at any one particular X-point as the islands surrounding it grow or shrink. During the course of the simulation a number of the

initial X-points disappear, and this is most likely to happen after the scale of the X-point becomes less than the local electron gyrodiameter. When the simulation is run for longer times the number of X-points reduces further, with a consequent reduction in the number of magnetic islands. Thus the simulation sees a relaxation of the initial magnetic topology, as well as a redistribution of power from large to short scales.

The regions around X-points have signatures which indicate that magnetic reconnection is occurring, with the motion of field lines and the pattern of electron bulk drifts consistent with reconnection inflows and outflows. Where there is a clear pattern of reconnection associated electron drifts there is a quadrupolar signature in B_z, similar to that found in Hall reconnection. This is consistent with the scale of the X-point region being smaller than the ion inertial and gyro-scales, so that the electron and ion motion are effectively decoupled. Generally there are asymmetries in the quadrupolar signature and flow pattern due to the guide field, density gradients and inflows. Because of the size of the simulation (the largest scale is of order the ion inertial length) and the initial number and shape of the islands, the simulations do not form narrow (small aspect ratio) current layers with embedded X-points. A larger simulation, with initial fluctuation injection at larger scales, or with initial power anisotropy may produce a different geometry of initial X-points in narrow current sheets as seen in MHD simulations [Servidio et al., 2009] and some PIC simulations [Karimabadi et al., 2013]

Applying the Hessian eigenvalue/vector analysis of Servidio et al. [2010] implies that the size of electron diffusion region also behaves as in asymmetric Sweet Parker reconnection. The smaller magnitude eigenvector indicates the direction of reconnection inflow, and the larger eigenvector indicates the reconnection outflow direction. As in the asymmetric model of Cassak and Shay [2007] reconnection sites appear to have electron flow stagnation points offset towards the lower value of density divided by reconnecting field strength, or $-\rho_{qe}/|B(x,y)|$.

Animations of the evolution of the electron temperature anisotropy ratio $T_{e\parallel}/T_{e\perp}$ indicate generation of enhanced parallel anisotropy at some X-points, and the dynamic appearance of regions of enhanced parallel anisotropy in reconnection outflow regions during periods of strong reconnection. There is not a unique one-to-one correspondence between X-points and regions of enhanced anisotropy, but this behaviour is frequently observed. We have shown that the enhanced anisotropy is due to multi-peaked velocity distribution functions. This is the first time that such velocity space structures have been reported at this scale and in turbulence. Further investigation reveals that such distributions are not unique to reconnection outflow

regions, but can be found elsewhere in the simulation.

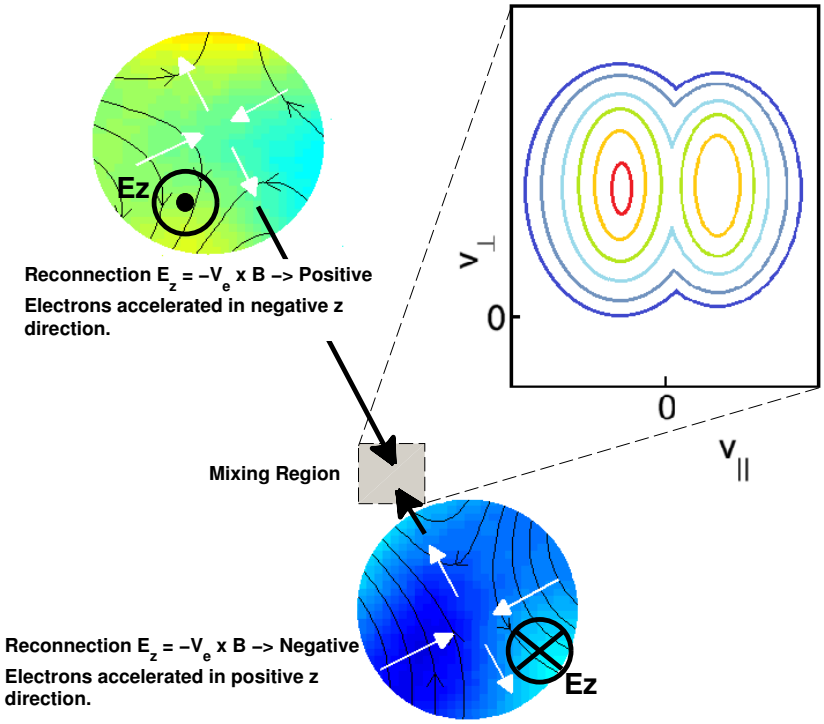

Figure 4.30.: Schematic of the mechanism for electron temperature anisotropy production due to reconnection in turbulence. Electrons accelerated at a region with a positive reconnection electric field E_z, gaining $v_{\parallel} < 0$, can propagate along reconnected field lines towards another reconnection site with E_z negative. Other electrons accelerated more locally gain $v_{\parallel} > 0$, and the two populations form a double peaked distribution in a mixing region in the reconnection outflow.

In order to determine how these velocity space features are formed, and whether reconnection sites are responsible, electrons from the peaks of the distribution were tracked. It was found that electrons are accelerated by the reconnection electric field E_z, in the direction of the guide field, when they are close to a reconnection site. Acceleration can occur in both positive and negative z directions depending on the sense of reconnection at a particular X-point. Particle tracking revealed the following explanation of the mechanism (see Fig. 4.30): The main peak of the distribution is generated by the local reconnection site, with the direction being set by the sense of reconnection, i.e. the sign of E_z. The outflow of electrons with the shifted v_z distribution will then potentially mix with the surrounding population of electrons. Large anisotropies therefore form around a reconnection site whose outflow area

already has a population of electrons, accelerated near another reconnection site, shifted in v_z in the opposite sense. This produces the double peaked distributions which are seen. This mechanism explains why not all reconnection sites in the simulation show this large temperature anisotropy signature, it depends on both the current direction of reconnection for the site, and the presence of a population of electrons oppositely shifted in velocity in its outflow region. This in turn depends on the magnetic topology of field lines allowing electron trajectories to connect different reconnection sites. In this model the reconnection sites act as both acceleration regions and mixing zones. It is also possible in this scenario to explain the presence of triple-peaked distribution functions, which are sometimes seen.

In a real plasma, the multi-peaked distributions may be unstable preferentially for parallel/oblique propagating waves, but given the guide field direction and 2-D nature of our simulation it is unlikely that the unstable waves are supported. In a full 3-D simulation we suggest that these multi-peaked distributions would produce additional waves via beam or anisotropy instabilities. It is not clear what the full effect of this would be in terms of electron scattering or magnetic field line topology, given that in a 3-D simulation the reconnection sites themselves would have their own three dimensional dynamics.

In Chapter 6 we will discuss similar distributions seen during a turbulence simulation with an in-plane guide field. In this case the simulation supports parallel propagating waves, and beam modes may be generated by multi peaked distributions.

The simulation results indicate that turbulence may play an active role in increasing electron parallel temperature anisotropy. This has implications for the study of the evolution of solar wind parameters which has highlighted the importance of kinetic linear instabilities in limiting temperature anisotropy in response to Coulomb collisions, and the expansion of the solar wind [Camporeale and Burgess, 2008, Matteini et al., 2012, Štverák et al., 2008]. These results indicate that reconnection can be another driver of electron temperature anisotropy, in localised areas of the turbulence. This paints a picture of electron scale turbulent dissipation that relies on multiple plasma mechanisms, depending on the local plasma parameters. The simulation has possible limitations due to the size of the simulation box and the large amplitude of the initial fluctuations. These have been adopted due to constraints of realistic mass ratio, and the requirement to resolve a turbulent cascade above the noise floor of the simulation. Thus these results are more appropriate to, for example, the large amplitude turbulence behind the quasi-parallel terrestrial bow shock [Retinò et al., 2007] or in current sheets in the solar wind where some evidence

of enhanced dissipation exists [Osman et al., 2011].

Finally, the power spectrum of fluctuations shown here, develops rapidly after the start of the simulation, and has a power law form which is relatively time-steady. It does not seem directly influenced by reconnection, the dynamic behaviour of X-points or the evolution of the electron temperature anisotropy.

The fluctuations contributing to the power spectrum, in the range $k > 1$ were isolated using a FFT technique in Section 4.3.7. This showed that the fluctuations appear aligned with the local magnetic field lines, and bear a striking resemblance to the KAW simulation data shown in Fig. 2.20. This, given with the lack of a parallel spatial direction to allow parallel propagating whistler waves is highly suggestive that these are kinetic Alfvén waves, although further work is required to get a definitive confirmation of this. A correlation analysis showed that electron density and magnetic field strength had a negative correlation, with the strongest correlation occurring when the electron density is 500 cycles ($25\Omega_e^{-1}$) behind the magnetic field. Further investigation is required to understand this effect, but the lower mass ratio run indicates the electron density fluctuations could be related to the speed of the ion movement.

In summary, the electron behaviour is crucially dependent on the topological evolution of the magnetic field via reconnection. It seems possible that dissipation at the smallest scales in a collisionless plasma might be strongly influenced by how topological complexity is carried to small scales, and also dissipation will depend on the instabilities that can occur locally as a result of the electron dynamics. We will discuss this further in Chapter 6.

5. Electron vortex magnetic holes (EVMHs)

Note: The work presented in this chapter is in preparation for publication in Physics of Plasmas.

5.1. Introduction

Intermittency, (Section 2.1) a fundamental property of hydrodynamic turbulence, is observed in astrophysical plasmas. It can give one dimensional time-series of parameters (e.g. velocity, density) the appearance of being "bursty" and irregular, and is often associated with coherent structures within the medium, such as current sheets or shocks. In hydrodynamics intermittency can be a result of the "eddies" not filling all of the available space, therefore Kolmogorov's assumption of homogeneity (Section 2.2.1) breaks down.

The plasma observed throughout the heliosphere, although turbulent, is not a homogeneous medium, and contains many types of coherent structures, all of which contribute to intermittency. These include current sheets, fast and slow streams, shocks, discontinuities, and magnetic holes. The term "magnetic hole" (MH) was first used by Turner et al. [1977] to describe 2-130 s depletions in magnetic field strength observed in the solar wind. MHs are isolated depressions in magnetic field strength in an otherwise uniform or undisturbed background field. Hole sizes were observed to range from tens to hundreds of proton larmor radii. Sometimes MHs were associated with a change in magnetic field direction across them.

Turner defined the term "linear hole" to describe holes that had little change in field direction, and a smoothly changing magnetic field strength. Winterhalter et al. [1994] later used this definition to describe isolated linear holes in observations in the solar wind. The selection parameters used were: a change in field direction of less than 5° and a drop in magnetic field strength greater than 50% for events with "widths" (using Taylor hypothesis to convert from spatial to temporal scales,

Section 2.3.1) of up to 150 s. They found that the most probable width was 10-15 s with a median of 22 s. The selection criteria meant that interplanetary discontinuities (large changes in magnetic field direction, often associated with magnetic reconnection or other processes) were not included in the analysis, implying that the holes were a new kind of coherent structure. Linear holes were found to occur near the leading edges of high-speed streams in the solar wind. Winterhalter et al. [1994] also found that the ambient plasma for linear MHs was marginally mirror stable, and many studies of MH observations in the solar wind, planetary magnetosheaths and heliosheath have all been explained in terms of this instability as a method of formation [Burlaga et al., 2006, Cattaneo et al., 1998, Génot et al., 2009, Tsurutani et al., 2011, Zhang et al., 2009]. Mirror mode waves are non-propagating, so any structures formed are stationary and convect with the local wind speed. Other proposed mechanisms have received much less attention, such as non-propagating diamagnetic structures [Burlaga and Lemaire, 1978] and MHD-solitons [Baumgärtel, 1999].

Franz et al. [2000] analyzed longer time durations, covering a wider range of hole size, and found MHs had a range of scales that formed a power law. The power law showed no indication of a lower limit for the size of MH, as the power law continued down to the limits of data resolution. So how small can a MH be? Recent observations by the THEMIS spacecraft showed that MHs exist in the Earth's plasma sheet with a scale size below the ion gyroradius [Ge et al., 2011]. There was some evidence that the MHs were associated with energetic electrons. Another survey of MH events in the plasma sheet [Sun et al., 2012] using TC-1 and Cluster observations also showed there is a population of smaller MHs with a range of sizes below the ion thermal gyroradius, with a peak in frequency distribution at $0.5\rho_i$. The search criteria for these observations was a drop in field strength $> 25\%$ and a small change in field direction across the MH of $< 15°$. This survey also indicated the events showed a increase in electron energy flux at a pitch angle of 90° inside the MH.

In this chapter we present results for a new type of MH, discovered whilst studying particle in cell (PIC) simulations of turbulent magnetic relaxation at sub-ion scales. These magnetic holes have a radius of approximately ~ 5.6 electron thermal gyroradii, high perpendicular electron temperature anisotropy, and a $\sim 50\%$ drop in magnetic field strength within the hole. We go on to show that the current in these structures are formed purely by a population of trapped/quasi-trapped, hot electrons. The collective trajectories of these electrons creates a current ring that diamagnetically induces a reduction in B_z with sufficient strength to maintain the

hole as a coherent structure. The magnetic holes have properties very similar to those observed by Sun et al. [2012] in the Earth's plasma sheet.

We aim to show that these self sustaining structures can form in the presence of magnetic depressions, (whether the result of mirror modes, or in-homogeneous turbulent magnetic fluctuations) and that they can naturally form within sub-proton scale plasma turbulence. Whilst we do not claim this work can replace the mirror mode theory for larger scale MHs, we suggest that the smaller sub-ion scale holes can be described by the theory outlined in this chapter. As such we will show that our simulations are consistent with observations, particularly in places that can have strong guide fields and quasi 2D geometries, such as in the plasma sheet.

This chapter will be split into the following sections. In Section 5.2 we seek to understand the properties of the magnetic holes that formed within the PIC simulation(s) of turbulence, and under what conditions they form, and show their link to the intermittency property of turbulence. In Section 5.3 we aim to understand the types of electron orbit possible within these structures using a test particle code, assuming static electric and magnetic fields. In Section 5.4 we use Parsek2D in an attempt to seed these structures in a self consistent model, without the presence of turbulence. Finally, in Section 5.5 we briefly present a comparison of our simulated results to observations of magnetic holes in the plasma sheet.

5.2. Turbulence simulations

In this section we use the same data from the PIC simulations of sub-proton scale turbulence, as discussed in Chapter 4. The plasma and simulation parameters are identical, but a different analysis was performed in an attempt to find any unusual kinetic effects occurring within the box. In Fig. 5.1 we plot the parameter $|\mathbf{E}+\mathbf{V_e}\times\mathbf{B}|$ which in Hall MHD should be equal to zero. In Hall MHD, the ideal equations of MHD are separated into separate electron and ion fluids, as discussed in Section 3.4. Revisiting the generalised Ohm's law equation (Eq. 3.6), assuming ideal conditions: infinite conductivity, no currents ($\langle V_i\rangle = \langle V_e\rangle$) and no pressure gradients in the fluid, then this term should be exactly zero. Hence the magnetic field should be frozen into the electron fluid, under these conditions. Therefore areas where $|\mathbf{E}+\mathbf{V_e}\times\mathbf{B}|$ shows large departures from zero will highlight where non-ideal (kinetic) effects are taking place. These effects could be caused by large currents, pressure gradients, wave activity, and any non-fluid-like behaviour of the electrons and/or ions.

Figure 5.1 clearly shows, using this parameter that two circular kinetic features

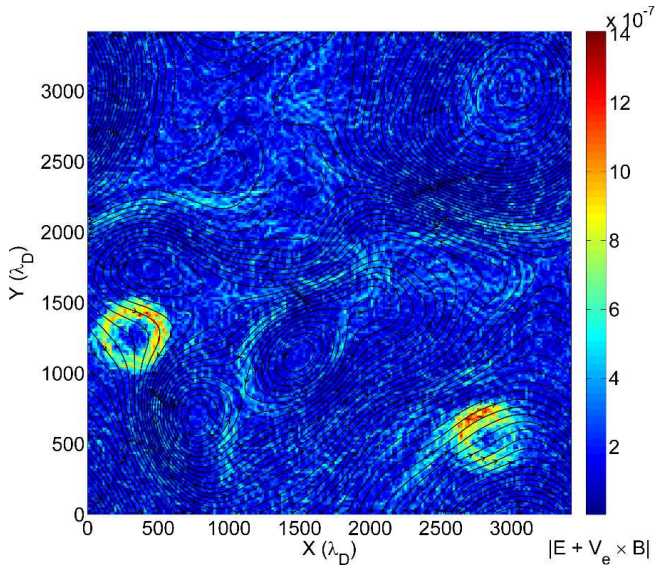

Figure 5.1.: Magnetic field lines (black) and the parameter ($|\mathbf{E} + \mathbf{V_e} \times \mathbf{B}|$) at time $t = 200\Omega_e^{-1}$.

have formed in the PIC simulation. Both of these features are coherent structures which remain relatively static in their appearance throughout the simulation, but they slowly drift in the $x-y$ plane as the simulation progresses. The structure on the left is persistent, and is present from near the start of the simulation, and is likely a result of the initial field perturbation/shape in that location. The circular feature on the right hand side of Fig. 5.1 spontaneously forms later on in the simulation, at $\sim t = 100\Omega_e^{-1}$, and slowly drifts left to the position shown at $t = 200\Omega_e^{-1}$ in Fig. 5.1. (This is also shown in Fig. 5.7.)

There are also some "worm-like" elongated features in this parameter, but these are out of the intended scope of this chapter. We will concentrate our analysis on the second structure that formed on the lower right hand side of the simulation box. We aim to describe the nature of this structure, and its formation.

5.2.1. Plasma parameters within the structure

Figure 5.2 shows plasma parameters in the local region of the structure on the right hand side of the simulation box as shown in Fig. 5.1. In all panels in-plane magnetic field lines are plotted as black contours, with the colour shading showing the value of different parameters. Figure 5.2(a) shows the out-of-plane magnetic field, B_z, and the direction of electron bulk flow is shown by magenta arrows. The structure is clearly characterized by a depletion in B_z of $\sim 50\%$, so we are justified in calling the structure a magnetic hole. Electron flow is in a circular anti-clockwise direction

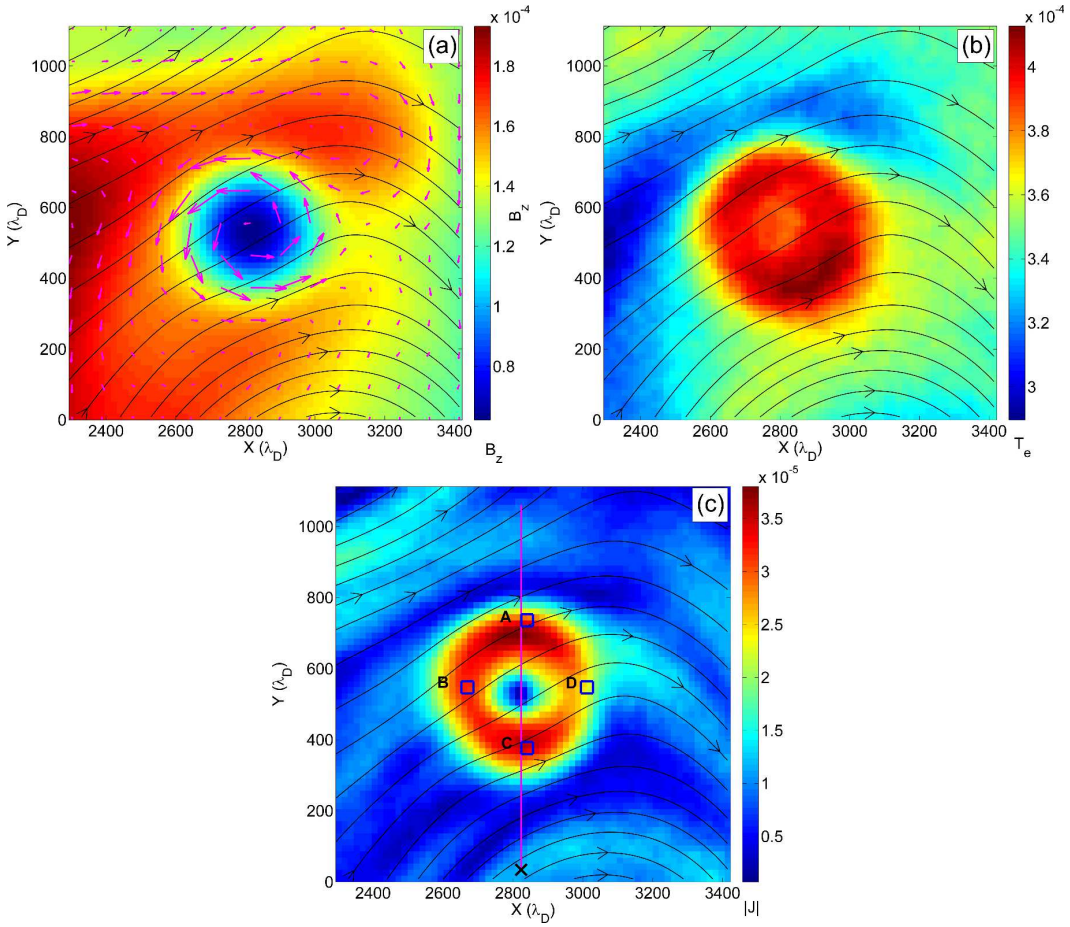

Figure 5.2.: Magnetic field lines (black) and (a) out-of-plane magnetic field B_z with electron flow vectors (magenta), (b) total electron temperature, T_e and (c) magnitude of current density, J. Data shown is for time $t = 200\Omega_e^{-1}$. Lengths units are in Debye lengths. The vertical line shows where cross sections of the parameters will be taken. The four marked regions are discussed in the text.

within the hole, much like a vortex, and therefore we shall refer to these structures as electron vortex magnetic holes (EVMHs).

Figure 5.2(b) shows the electron temperature, T_e, within the EVMH and Fig. 5.2(c) shows the magnitude of current density, J. These panels show that the depletion in B_z corresponds to a region of hot electrons. The current density in the region shows a characteristic ring shape. Also shown in Panel (c) are four boxes labelled A, B, C and D where we will later calculate electron velocity distribution functions (VDFs). The vertical line in Fig. 5.2(c) was used to generate a cross section of parameters through the structure, as shown in Figs. 5.3 and 5.4. The black cross in Fig. 5.2(c) indicates the start (left edge) of the displayed cross sections in Figs. 5.3 and 5.4.

The units of the horizontal axis in Figs. 5.3 and 5.4 are in Debye lengths, measured

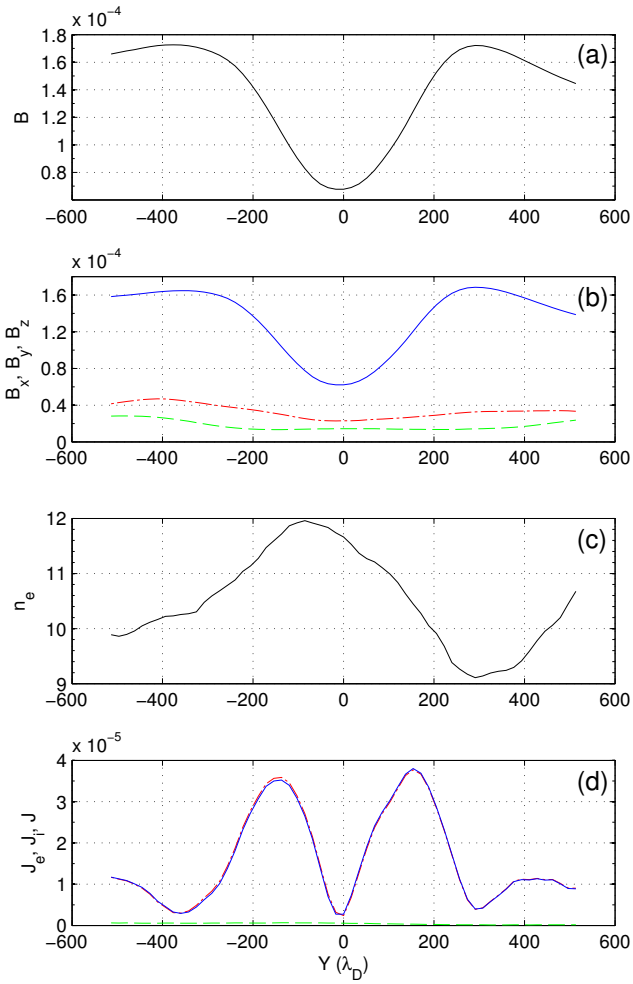

Figure 5.3.: Cross section of field and current parameters through the line indicated on Fig. 5.2(c). Multiple variables (see vertical axis) are coloured in the order, red (dash-dot line), green (dashed line) and blue (solid line).

from the centre of the EVMH. The hole's centre was determined by finding the location of minimum B_z in the region. The panels in Fig. 5.3 show from (a) to (d) B, (B_x, B_y, B_z), n_e, and (J_e, J_i, J). Number density is shown in particles cm^{-3}, and all other parameters are shown in normalised simulation units ($B \equiv \frac{B.10.q}{\omega_{pe}.c.m_i}$, and $J \equiv \frac{J.100.q}{\omega_{pe}^2.c.m_i}$). Where multiple parameters are plotted on a single axis, the variables are coloured in the order, red (dash-dot line), green (dashed line), blue (solid line) and black (solid line).

Figure 5.3(b) shows that the shape of the depletion in B_z between $\pm 300\lambda_D$. This appears to be approximately cosine in form (we will examine this later in Section 5.3). B_x and B_y are approximately constant within the structure. The depletion of B_z is $\sim 50\%$ at the hole's centre. As the system evolves the reduction in

B_z becomes larger. The magnetic field outside the hole makes an angle of $\sim$15° to the z-axis (see Fig. 5.3(b), at $+300\lambda_D$, $\theta \sim \arctan(1.6/0.4)$) which increases to $\sim$60° at the centre of the hole ($\theta \sim \arctan(0.6/0.3)$). The electron number density increases slightly within the hole (Fig. 5.3(c)) but does not appear to be completely anti-correlated with the field strength. The initial background simulation density was set to 10 particles per cm^3. The cross section shows local fluctuations of $\pm$10%, but the density within the hole peaks at +20%. Figure 5.3(d) shows the contribution to current density from both species, and the magnitude of the total current density, J. The ring shaped current is clearly visible as two sharp peaks in current, each at $\pm 200\lambda_D$ from the holes centre. The radius of the hole, determined from this current density cross section, is $\sim 300\lambda_D$. The magnitudes of the current density components show that the current is entirely generated by electron flow, as the J_e line (red) and J line (blue) completely overlap, and ion current (green) is negligible.

Figure 5.4 shows the details of the temperature and pressure properties of the EVMH. Both temperature and pressure are shown in simulation units ($T \equiv \dfrac{T\,k_B}{m_e\,c^2}$, and $P_i \equiv \dfrac{P_i\,100}{m_i\,\omega_{pe}^2}$, $P_e \equiv \dfrac{P_e\,100}{m_e\,\omega_{pe}^2}$, and magnetic pressure calculated using $P_B = B^2/8\pi$). Figure 5.4(a) shows there is a sharp increase in electron temperature within the hole. The temperature cross section is not symmetrical, with an elevated electron temperature at $-400\lambda_D$, compared to $+400\lambda_D$ (see Fig. 5.2(b)). There are two peaks in the temperature profile (Fig. 5.4(a)) which approximately match the location of the peaks in current at $\pm 200\lambda_D$. Perpendicular electron temperature anisotropy (Fig. 5.4(b)) increases within the EVMH from $\sim 0.7 - 0.9$ outside the structure (cf. Fig. 5.8) and increasing to ~ 1.4 inside the EVMH, remaining roughly constant between $\pm 200\lambda_D$ around its centre.

Figure 5.4(c) shows electron pressure, P_e (red), ion pressure, P_i (green), magnetic pressure, P_B (blue) and total pressure, P_t (black line). This figure shows that there is a reduction in total (gas plus magnetic) pressure within the structure, which is mostly due to the reduction in magnetic pressure within the hole where the total field strength is reduced (Fig. 5.3(a)). The magnetic pressure within the hole drops below both the electron and ion pressure. This results in a value of plasma beta, β, of ~ 5 within the EVMH, whilst outside the hole plasma beta remains at ~ 1.

Figure 5.4(d) shows the off-diagonal terms of the electron pressure tensor. These appear to become important within the EVMH as P_{xz} (green) takes on a large negative value, which is non-symmetric. Figure 5.4(e) shows the main components of the pressure tensor, rotated into the local parallel (to $\mathbf{B}$) and perpendicular

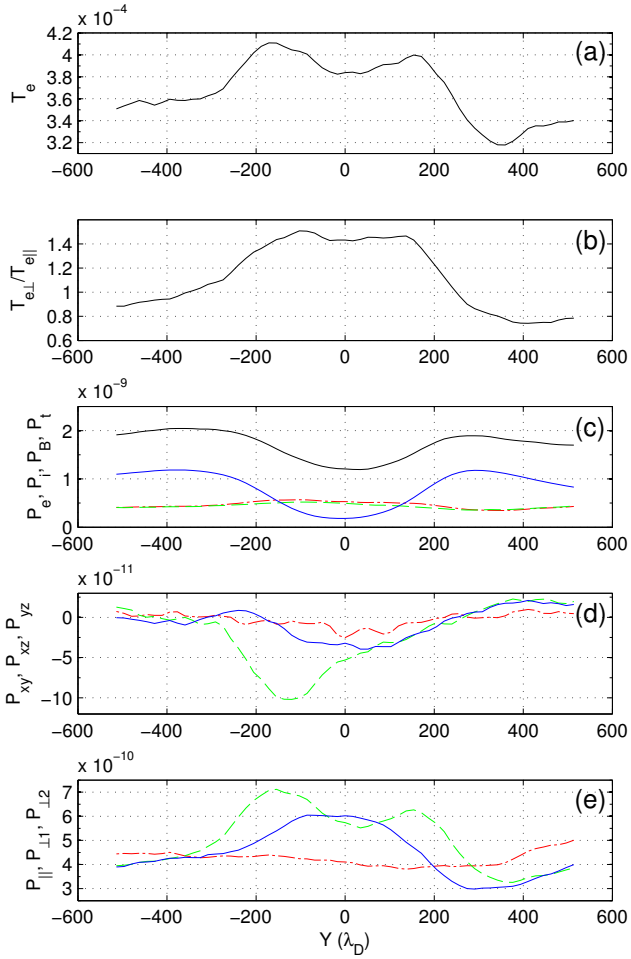

Figure 5.4.: Cross section of plasma temperature and pressure parameters through the line indicated on Fig. 5.2(c). Multiple variables (see vertical axis) are coloured in the order, red (dash-dot line), green (dashed line), blue (solid line) and black (solid line) respectively.

directions. This confirms that there is an increase in perpendicular pressure within the structure, as both the $P_{\perp 1}$ (green) and $P_{\perp 2}$ (blue) lines are larger than the parallel pressure (red). The clear difference in the $P_{\perp 1}$ and $P_{\perp 2}$ values indicates non-gyrotropic behaviour. The peaks in $P_{\perp 1}$ correspond to the peaks in current in Fig. 5.3, and therefore shows an increase in in-plane pressure due to the ring current.

This information indicates that the magnetic holes are being formed by a population of hot, possibly trapped electrons in the region, as there is little ion movement within the structure given the timescale of the simulation. The anti-clockwise electron drift (as indicated in Fig. 5.2(a)) would have a diamagnetic effect, and cancel out the magnetic field strength in the out-of-plane direction, hence the reduction in B_z.

5.2.2. Electron velocity distributions and particle tracking.

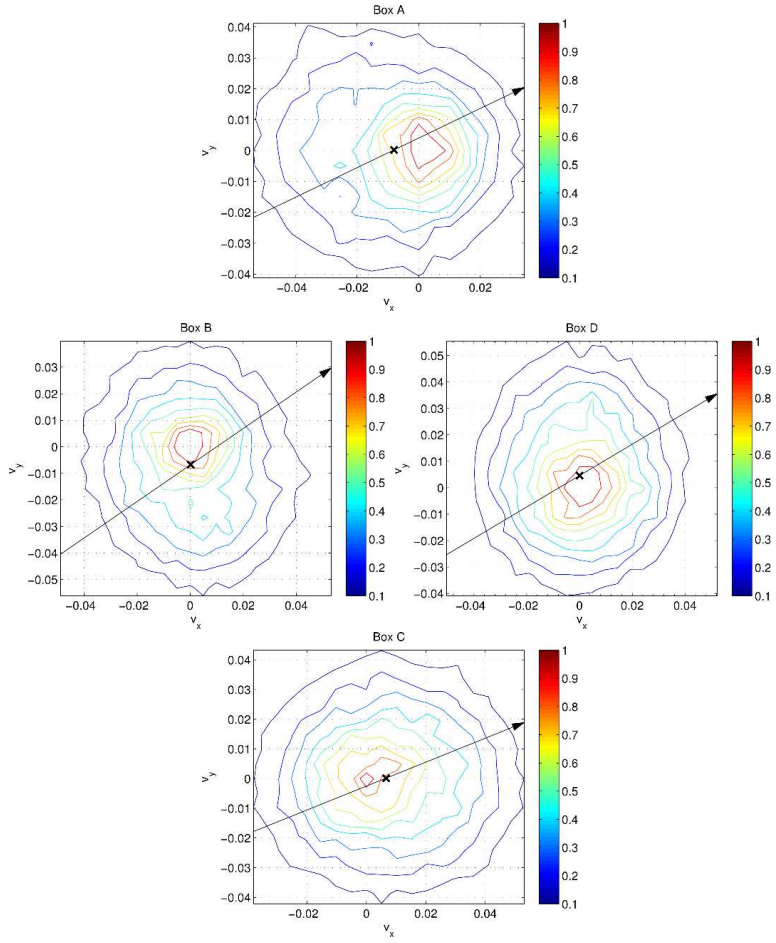

Figure 5.5.: Electron velocity distribution functions in the $v_x - v_y$ plane for Boxes A, B, C and D. (Refer to Fig. 5.2(c).)

Figure 5.2(c) shows the shape of the ring current formed within the EVMH. Four locations marked A, B, C, and D were selected around the structure in order to calculate electron velocity distribution functions (VDFs) at $t = 200\Omega_e^{-1}$ as shown in Fig. 5.5. The VDFs have been normalized to 1 and the direction of the in-plane magnetic field is shown by a black arrow. The small black cross in each figure represents the electron bulk velocity in the $x - y$ plane. All four VDFs show a similar shape, but with different orientations. The drift in Fig. 5.5 box A shows the electron bulk velocity in the negative x direction, in agreement with Fig. 5.2(a) which indicates anti-clockwise electron flows. Since box A is in a central, upper location of the vortex (Fig. 5.2(c)) the bulk velocity must be mainly in the negative x direction for the flow to be anti-clockwise. This pattern holds for all four VDFs, with Fig. 5.5 box B indicating negative y velocity, box C indicating positive x velocity and box

D indicating positive y velocity.

Each distribution shows a main peak, slightly offset in the opposite direction to the overall drift, and a plateau with extended tail of electrons in the appropriate anticlockwise direction. To illustrate this, an effective cross section of the distribution in box A is shown in Fig. 5.6. The data in this figure shows the maximum value of each column of data in the VDF for box A (Fig. 5.5). Since this VDF is roughly symmetrical around $V_y = 0$, it gives an impression of the cross section of this distribution along the V_x direction. The main peak and plateau are clearly visible in Fig. 5.6. The main peak appears to be Maxwellian. The excess electrons populating the plateaus, in any of the four boxes, will have a higher perpendicular velocity than particles populating the core, as the guide field is approximately in the z direction.

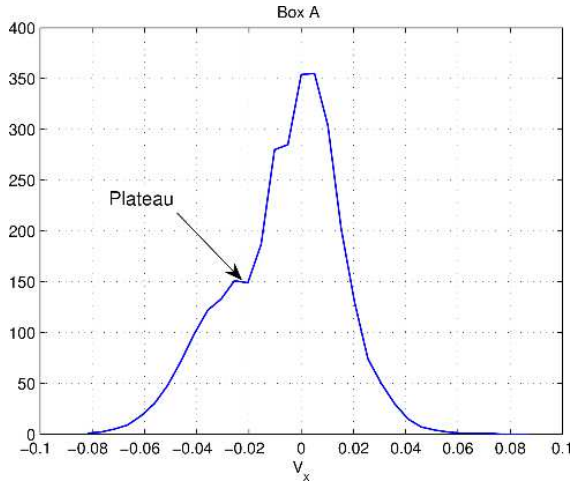

Figure 5.6.: Maximum value of electron VDF along the V_y direction, for Box A. (Refer to Fig. 5.2(c).)

In order to investigate the dynamics which have formed this structure, electrons were selected from the main peaks of all four boxes (A, B, C and D) and from a central location on each plateau, and their trajectories recorded from times $t = 100\Omega_e^{-1}$ to $t = 200\Omega_e^{-1}$.

Figure 5.7 shows an example trajectory for an electron from the plateau portion of the distribution in box B. The electron's start location is indicated by a green cross, and its last recorded position by a blue cross. In-plane magnetic field lines (black) are plotted at $t = 200\Omega_e^{-1}$, when the electron is at its last recorded position. The background colour shows B_z at the same time step. The purple line shows the trajectory of the centre of the EVMH as it moves. (Note that data was recorded at every 10th cycle, hence the jagged appearance in places.)

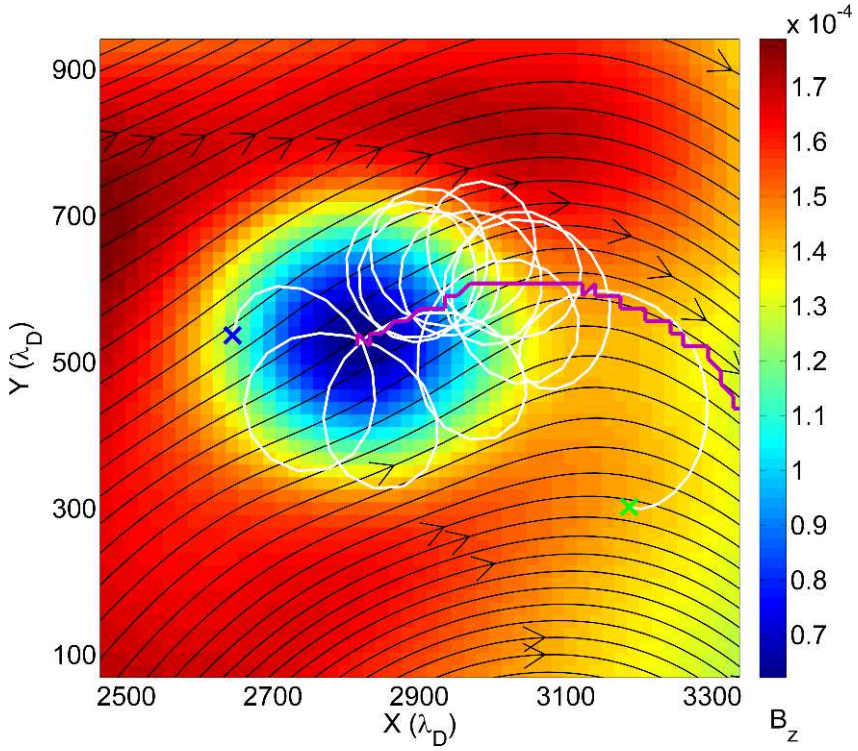

Figure 5.7.: Magnetic field lines (black) and out-of-plane magnetic field, B_z. The solid line (white) shows an example electron trajectory as it interacts with the vortex. The green and blue crosses mark the start and end locations respectively. The purple line indicates the trajectory of the centre of the vortex.

The trajectory in Fig. 5.7 shows that the electron orbits in an anti-clockwise direction, consistent with the guide field directed out of the page. Its average, or guiding centre motion is at first anti-clockwise, but towards the end of the recorded data, is clearly in a clockwise motion. The gyro-radius of the electrons orbit is of the order the magnetic hole radius, and fluctuates in size depending on its location within the hole. This is clearly visible in Fig. 5.7 in the last two gyro-orbits which arc tightly along the outside edge of the magnetic hole, where the magnetic field strength is stronger, and the orbit follows wider arcs as the electron passes near the holes centre, where the magnetic field strength is reduced.

Animations of this trajectory suggests that this electron is trapped, or partially trapped, within the magnetic hole. What is not obvious from Fig. 5.7 is that the EVMH itself is slowly moving, from right to left, as indicated by the purple line. Its exact centre was tracked by searching for the minimum value of B_z in the region over the times of interest. To check that this electron is indeed trapped, we re-plot the same data in Fig. 5.8 in a frame relative to the centre of the magnetic hole.

The black lines show the electrons relative trajectory. The white circle indicates the approximate size of the magnetic hole, estimated to have a radius of 15 cells/255 Debye lengths. The green cross, again shows the relative start location of the electron, and the blue cross shows its last recorded position. The background colour shows a 2D map of electron temperature anisotropy at $t = 200\Omega_e^{-1}$, showing that the highest perpendicular anisotropy corresponds to the region where the electron is trapped.

Figure 5.8 shows that the electron initially follows a (relatively) stationary circular orbit, trapped along the left hand side of the hole. Then, eventually falls into a petal-like orbit with a guiding centre motion clockwise relative to the vortex centre. It is clear from this orbit, that only electrons with a gyro-radius approaching the radius of the EVMH, can be influenced by it in this way. Electrons above a certain energy have the potential to enter these trapped orbits, as they sample reduced fields towards the holes centre and increased field at its edges during a single gyro-orbit, the net effect being a drift perpendicular to the radial direction, and can be described as a cylindrically symmetric gradient drift. In an EVMH field structure as the one seen here, $\nabla|\mathbf{B}|$ points in a direction from the centre towards the edges of the EVMH. (See the vectors drawn in Fig. 5.8.) The direction of the gradient drift velocity, $\mathbf{V}_{\nabla\mathbf{B}}$, is in the direction $\pm\mathbf{B} \times \nabla|\mathbf{B}|$, where the $\pm$ should be applied for the charge of the particle in motion. With the guide field out of the simulation plane, this results in a clockwise drift for an electron and anti-clockwise drift for a proton.

Therefore the direction of $\mathbf{V}_{\nabla\mathbf{B}}$ for electrons appears incompatible with the required direction of current, as Fig. 5.2(a) shows that the average electron motion is anticlockwise, not clockwise. However it is the collective motion of these trapped electrons that will generate total current. We have examined 676 electron trajectories from the plateaus of the VDFs of all four boxes in Fig. 5.2(c). Most of them show similar petal shaped orbits, but they are not always completely trapped. Some, like the electron in Fig. 5.8 do not initially interact with the structure, and then become trapped. Others initially interact, and can escape after time. Therefore they appear quasi-trapped.

We can infer the collective affect of many such trajectories, by examining Fig. 5.8 and imagining at the same moment in time, there is an electron at every point of the plotted trajectory that will follow the same path. The trajectories along the radial direction often come close to electrons moving radially in the opposite direction, so their contribution to overall current will cancel. Only the trajectories along the outer edges of the "petals" will not see any cancellation of their contribution to

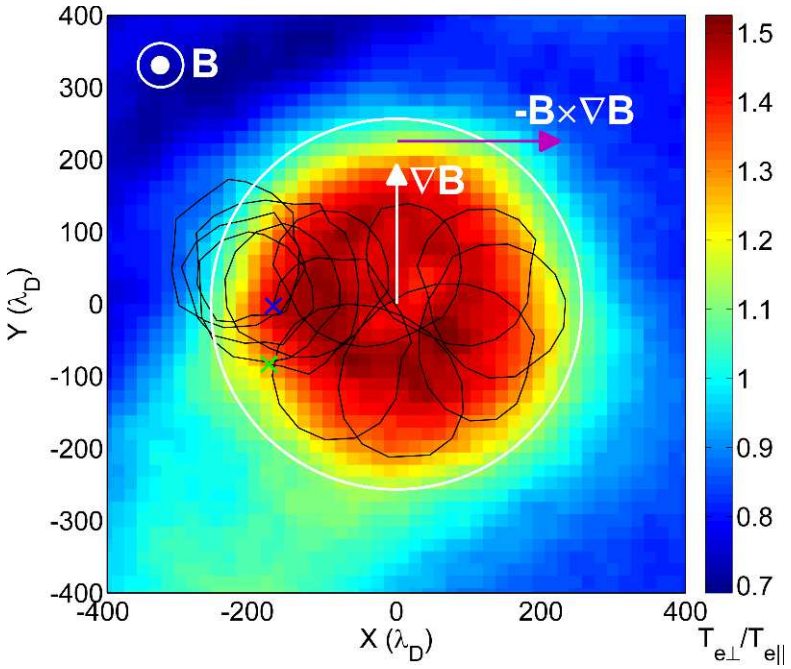

Figure 5.8.: An electrons trajectory (black) relative to the magnetic holes centre. The green and blue crosses mark the start and end locations respectively. The circle (white) shows the approximate radius of the magnetic hole. The colour scale shows $T_{e\perp}/T_{e\|}$ at time $t = 200\Omega_e^{-1}$.

current, except with non trapped electrons outside the structure. However, there is an increased perpendicular anisotropy within the hole. Therefore, electrons with a centre of gyration outside the hole, have lower perpendicular energies, and their trajectories would not cancel all of this current at the edge of the "petal".

This explains how a thin ring shaped current could form from a collection of petal orbits. In order to create a much wider ring current, many types, and possibly different shaped trapped orbits would be required within the MH at any one time. A group tracking analysis was performed, like the methods shown previously in Section 4.3.6, in order to confirm that the electrons within the plateau regions of the VDF are quasi trapped within the MH. The results of the analysis are shown in Fig. 5.9.

A total of 3076 electrons were used to generate these images. The electrons were chosen from the four boxes of Fig. 5.2(c), plus one additional box located at the centre of the vortex. Different group of electrons are given different label numbers. The 676 electrons from the plateau regions of the VDFs were labelled 4 (yellow). Electrons from the VDF peaks of the four outer boxes were labelled 2 (light blue), whilst electrons from the VDF peak of the central box were labelled 1 (darker blue). As in the previous analysis, the position of these electrons at previous timesteps

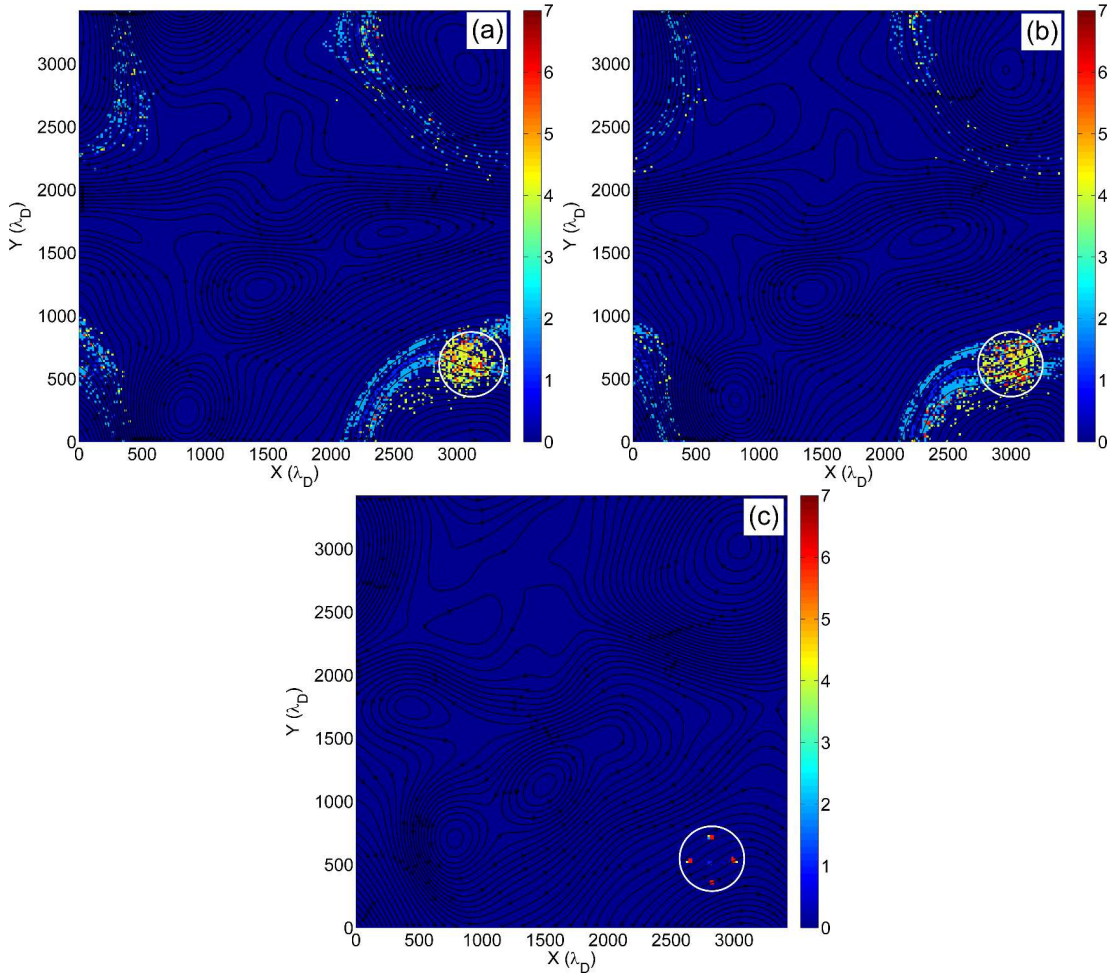

Figure 5.9.: Particle group tracking plots at a) $t = 132\Omega_e^{-1}$, b) $t = 150\Omega_e^{-1}$, c) $t = 200\Omega_e^{-1}$. Yellow cells (4) contain only electrons from the plateau of the VDF (Fig. 5.6). Lighter blue cells (2) contain only electrons from the peak of the VDF. Darker blue cells (1) show cells that contain electron from the peaks, from the centre of the vortex. Other values show combinations of electrons within that cell. The white circle is centred at the lowest value of B_z, the centre of the vortex, with 15 cell radius.

are used to create colourmaps which show where different groups of these electrons were. Combinations of the label numbers indicates that the cell contains mixes of the three labelled groups. Zero (darkest blue) indicates none of the labelled electrons were present in that cell. Figure 5.9(a) shows the group tracking plot at $t = 132\Omega_e^{-1}$. Figure 5.9(b) shows the same analysis at $t = 150\Omega_e^{-1}$, and Fig. 5.9(c) shows the plot at $t = 200\Omega_e^{-1}$, where the VDFs were plotted and the electrons selected from. The four boxes and additional central box is clearly visible. In all three plots magnetic field lines are plotted in black. A white circle with a radius of 15 cells is plotted in

each case to show the current position of the vortex.

The movement of the vortex from right to left is clearly visible between Figs. 5.9(a) and (b). The group of electrons from the plateaus of the VDFs (yellow) form a circular shape, filling the white circle, which shows the approximate location of magnetic depletion. Animations of these figures confirm that this group of electron are quasi-trapped, as the circular yellow area moves with the location of the vortex. A small number of these "plateau" electrons are plotted outside the hole, which demonstrates their quasi-trapped nature. Both groups of electrons (labels 1 and 2) from the peaks of the VDFs closely follow the in-plane field lines. This can be seen in the two light blue arcs and darker blue ark (between the two) in Fig. 5.9(a) and (b). The electrons from the peaks of the Maxwellian-like distributions of Fig. 5.5, have smaller energies, reduced $V_\perp$, smaller gyroradii, and closely trace the field lines. They sample a small change in magnetic field strength over an individual gyro-orbit, and therefore are unaffected by the EVMH.

This evidence suggests that the quasi-trapped electrons are responsible for the ring shaped current in the EVMH. The hypothesis being that radially directed parts of the trajectories of the electrons within the hole are cancelled out by the presence of oppositely directed electron trajectories. Only azimuthal directions contribute to current at locations, such as at the edge of the petal orbits where no oppositely directed trapped orbits exists, and the non-trapped electrons outside the hole have lower energies so that the current at these locations cannot completely cancel. In order to show this a more idealized analysis of the types of trapped orbits is required. We will explore particle trapping in more detail in Section 5.3.

5.2.3. Signatures of intermittency

In Section 2.1 we discussed intermittency in turbulence, and noted that it is often associated with coherent structures. In Section 2.3.3 the partial variance of increments (PVI) method was discussed as a way of identifying intermittency in observational data. We now apply this same technique to the simulation data.

Firstly, a single timestep is chosen. The intention was to use the entire spatial grid of data (40000 cells) at that moment as a single cross-section of data, from which PVI values (Eq. 2.36) could be calculated. One way of doing this would be to use the periodic nature of the simulation, and draw a single line through the simulation domain at a small angle to the y axis. This line would wrap around the box, drawing a single trajectory from which the data can be interpolated onto, and PVI values calculated. For simplicity, PVI values were calculated on each column of spatial data

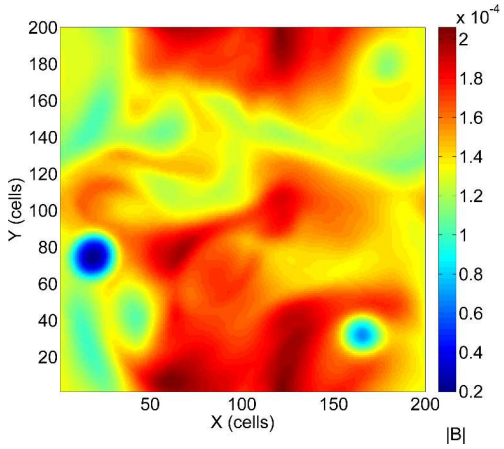

Figure 5.10.: Magnitude of magnetic field strength $|\mathbf{B}|$ in the turbulence simulation at $t = 200\Omega_e^{-1}$.

separately, and then combined as a single dataset, as initial tests showed there was little difference in the final results, and this technique did not require any additional interpolation. Using this technique, the variable in Eq. 2.36 is now a function of space, and not time as in Section 2.3.3. $\Delta\tau$ (now ΔS) was chosen in terms of cell lengths so that $\Delta S = 1$ means that the differences between adjacent cell values were calculated. The PVI was calculated (Eq. 2.37) using magnetic field strength data, at $t = 0$ and $t = 200\Omega_e^{-1}$, using $\Delta S = 100$, 25 and 1 cells. A colourmap of magnetic field strength data at $t = 200\Omega_e^{-1}$ is shown in Fig. 5.10. The two EVMHs are clearly visible as blue circles in the lower left and lower right hand sides.

As discussed in Section 2.3.3, when ΔS is large, the probability distribution function (PDF) of PVI values should represent uniform Gaussian fluctuations. As ΔS is reduced, increased probability at large values of σ is an indication of intermittency. This is shown in Figs. 5.11, 5.12 and 5.13. In each figure, Panel (a) shows a colourmap of the PVI value normalised to the standard deviation. Panel (b) shows a colourmap of the PVI values above an absolute value of 3. Panel (c) plots the PDF of the PVI at $t = 0$ (green x's), $t = 200\Omega_e^{-1}$ (blue +'s) and also shows a unit variance Gaussian distribution (red circles) for reference.

Panel (b) in Figs. 5.12 and 5.13 show that the highest values of PVI corresponds to the locations of the EVMHs, however with the largest ΔS (Fig. 5.11) only the EVMH on the left hand side of the simulation has a PVI greater than 3. In all three figures, the initial PDF (green) is Gaussian. Figure 5.11 shows that the PDF at $t = 200\Omega_e^{-1}$ is also Gaussian when ΔS is large. When ΔS is reduced (Fig. 5.12) the distribution at $t = 200\Omega_e^{-1}$ starts to develop super Gaussian "wings" at large values of σ. The distribution also begins to show a super Gaussian core around PVI = 0, and sub-

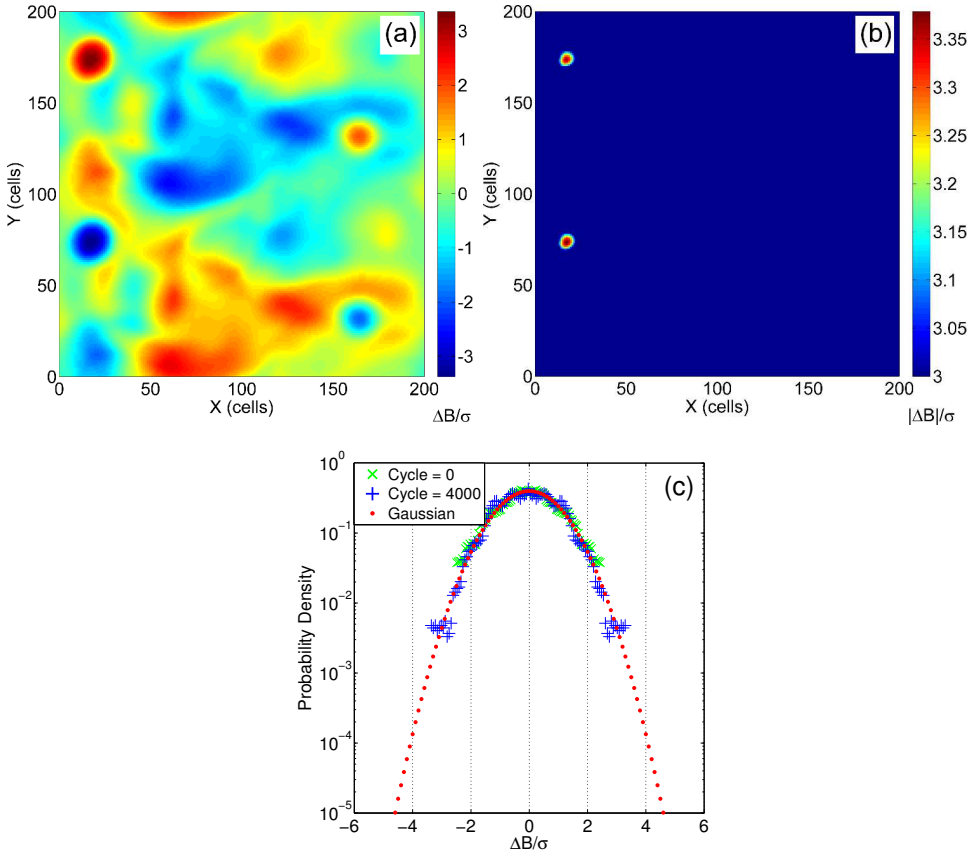

Figure 5.11.: PVI plots using a separation of $\Delta S = 100$ cells.
(a) PVI values of magnetic field strength, $|\mathbf{B}|$ (refer to Fig. 5.10).
(b) Magnitude of the PVI of magnetic field strength.
(c) Probability distribution functions (PDFs) of the PVI of $|\mathbf{B}|$ at $t = 0$ (green), $t = 200\Omega_e^{-1}$ (blue). A unit variance Gaussian is shown in red.

Gaussian areas between these two regions. As ΔS is reduced further (Fig. 5.13) all of these are features are enhanced. Figures 5.13 and Fig. 2.17 have similar features, however a larger simulation dataset would be required in order to achieve such smoothly varying distributions. Figure 5.13(b) confirms that the wings in the PDFs (PVI values greater than 3) are definitely associated with the EVMH structures. The sharp decrease in magnetic field strength are highly localised and result in large departures in PVI from a Gaussian probability distribution. In summary, these electron scale structures will contribute to intermittency in turbulence at sub proton scales.

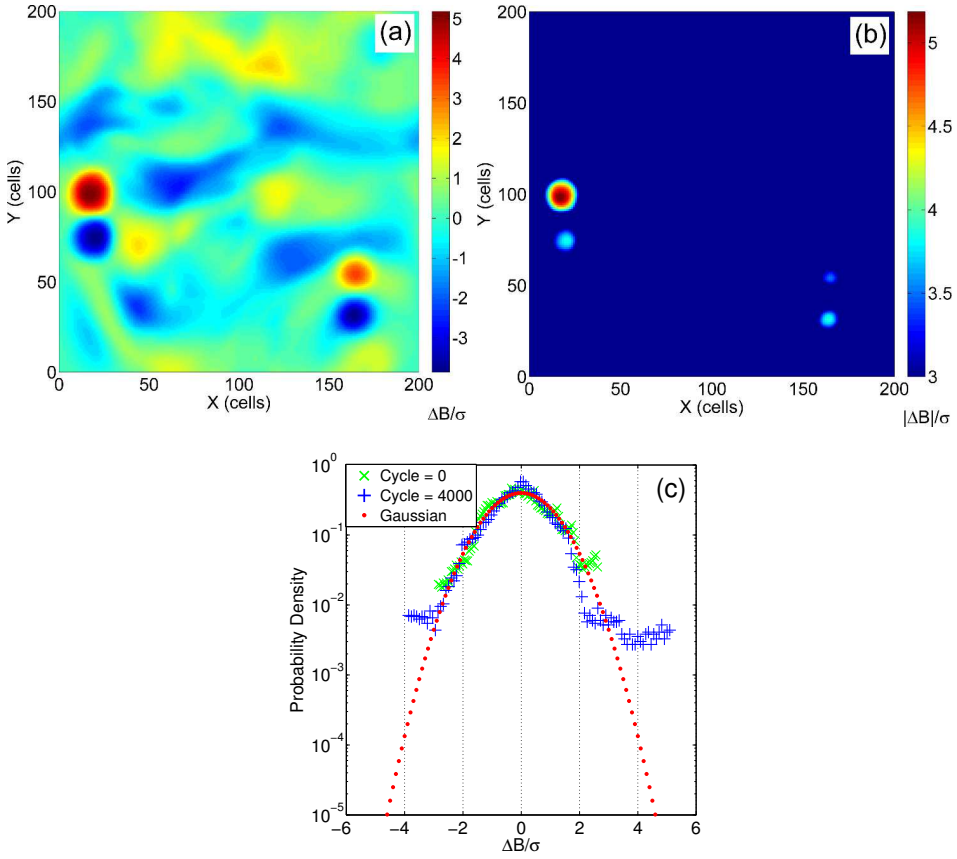

Figure 5.12.: PVI plots using a separation of $\Delta S = 25$ cells.
(a) PVI values of magnetic field strength, $|\mathbf{B}|$ (refer to Fig. 5.10).
(b) Magnitude of the PVI of magnetic field strength.
(c) Probability distribution functions (PDFs) of the PVI of $|\mathbf{B}|$ at $t = 0$ (green), $t = 200\Omega_e^{-1}$ (blue). A unit variance Gaussian is shown in red.

5.3. Test particle experiments

In Section 5.2.2 the orbits of the particles suggested that the collective effect of trapped or quasi-trapped electrons may be responsible for the ring shaped current, as seen in Fig. 5.2(c). To test this hypotheses, a test particle code was developed that uses static magnetic and electric fields to calculate the trajectory of an individual particle, in order to categorize the various electron orbits near/within an EVMH.

A simple magnetic hole configuration was set up similar to those seen in the 2D turbulence simulations. The magnetic field was directed in the x-z plane, at an angle of 15° to the z-axis, with a total magnetic field strength set to the arbitrary value of 1. Electric fields were set to zero. A circular magnetic hole was imposed in the simulation plane, with a quarter period sinusoidal radial profile and a 50% drop in B_z at its centre, compared to B_z outside the hole (consistent with Fig. 5.3). The radius

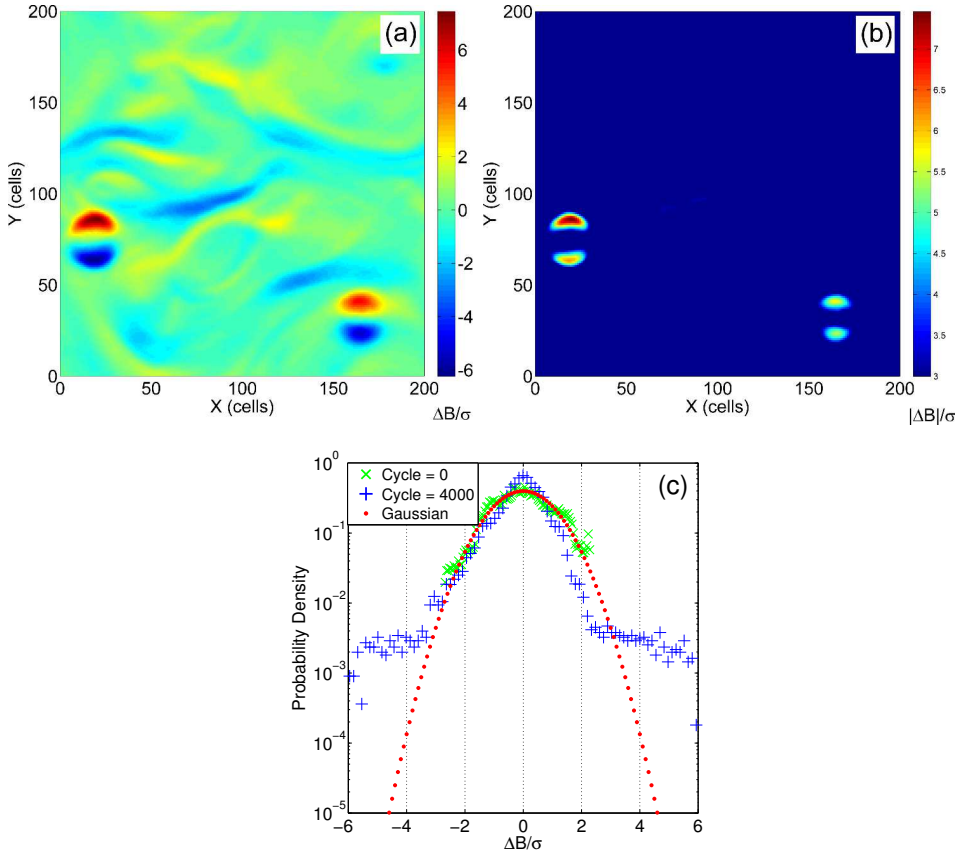

Figure 5.13.: PVI plots using a separation of $\Delta S = 1$ cell.
(a) PVI values of magnetic field strength, $|\mathbf{B}|$ (refer to Fig. 5.10).
(b) Magnitude of the PVI of magnetic field strength.
(c) Probability distribution functions (PDFs) of the PVI of $|\mathbf{B}|$ at $t = 0$ (green), $t = 200\Omega_e^{-1}$ (blue). A unit variance Gaussian is shown in red.

of the hole, R_H, was set to match that seen in the turbulence simulation, which was $\sim 300\lambda_D$ (17 cells), or $\sim 5.66\rho_e$ (where $\rho_e = 3$ cells). The electron thermal velocity was determined in the test code by setting the value of electron beta, β_e, equal to 0.5. Velocities are normalised to the speed of light, c, and time is normalised to the electron plasma frequency, ω_{pe}. The electrons were initially positioned randomly within a radius twice that of the EVMH (Fig. 5.14), so that the behaviour of electrons entering or escaping the MH and those trapped inside could be investigated. Initial velocities were also randomised, using an isotropic Maxwellian distribution function so that statistical data could be gathered. Electron trajectories were calculated and recorded for a maximum of 200 gyro-periods, or until the electron was $\sim 7R_H$ away from the centre of the hole (in order to reduce unnecessary calculation time for electrons that are not trapped and escape the hole). The timestep, Δt, used to calculate each particle's position and velocity was chosen such that 200 steps were

calculated for every gyro-period.

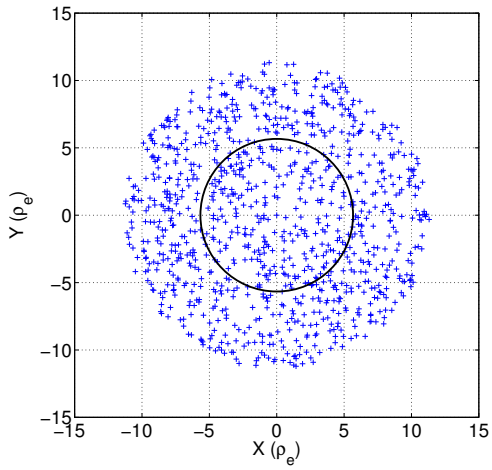

Figure 5.14.: Initial position of the first 1000 test particles (blue crosses). The radius of the EVMH is shown in black.

This analysis showed that there are several types of electron trajectory possible near a MH. The first are trajectories that are not trapped by the MH, as shown in Fig. 5.15. The relative magnitudes of the electrons perpendicular velocity, $V_\perp$, can be inferred from the radii of their gyration outside the hole where the field is constant. When an electrons $V_\perp$ is small, and its gyro-radius is considerably smaller than the MH radius, R_H, then the MH only slightly deflects the electrons path. Figs. 5.15(a) and (b) show two examples. The electron in Panel (a) has a gyroradius $\sim 1/10th$ the size of R_H and its trajectory starts on the right hand side. The electron in Panel (b) has a gyroradius of $\sim 1/4$ the size of R_H (larger $V_\perp$) and its trajectory starts on the left hand side. The effect of the MH in both cases is to slightly deflect the electrons gyro-centre motion as it passes through the hole, but both electrons exit/escape at the other side. It is clear that the MH has a larger effect on the trajectory of an electron with larger $V_\perp$, as the electron in Panel (b) is deflected more that the electron in Panel (a). This figure also shows that the electrons $V_\perp$, initial position and direction are all important factors determining if an electron will become trapped. Figure 5.15(c) shows the trajectory of an electron with similar $V_\perp$ to the electron in Panel (b), but because it is initially travelling in a direction away from the MH it does not interact with the hole.

Figure 5.16 shows example electron trajectories that are quasi-trapped by the MH. These can be split into two types, those whose orbits are not entirely contained within the MH, but do not escape (Figs. 5.16(a) and (b)) and electrons that are significantly diverted/reflected by the MH but eventually escape (Figs. 5.16(c) and

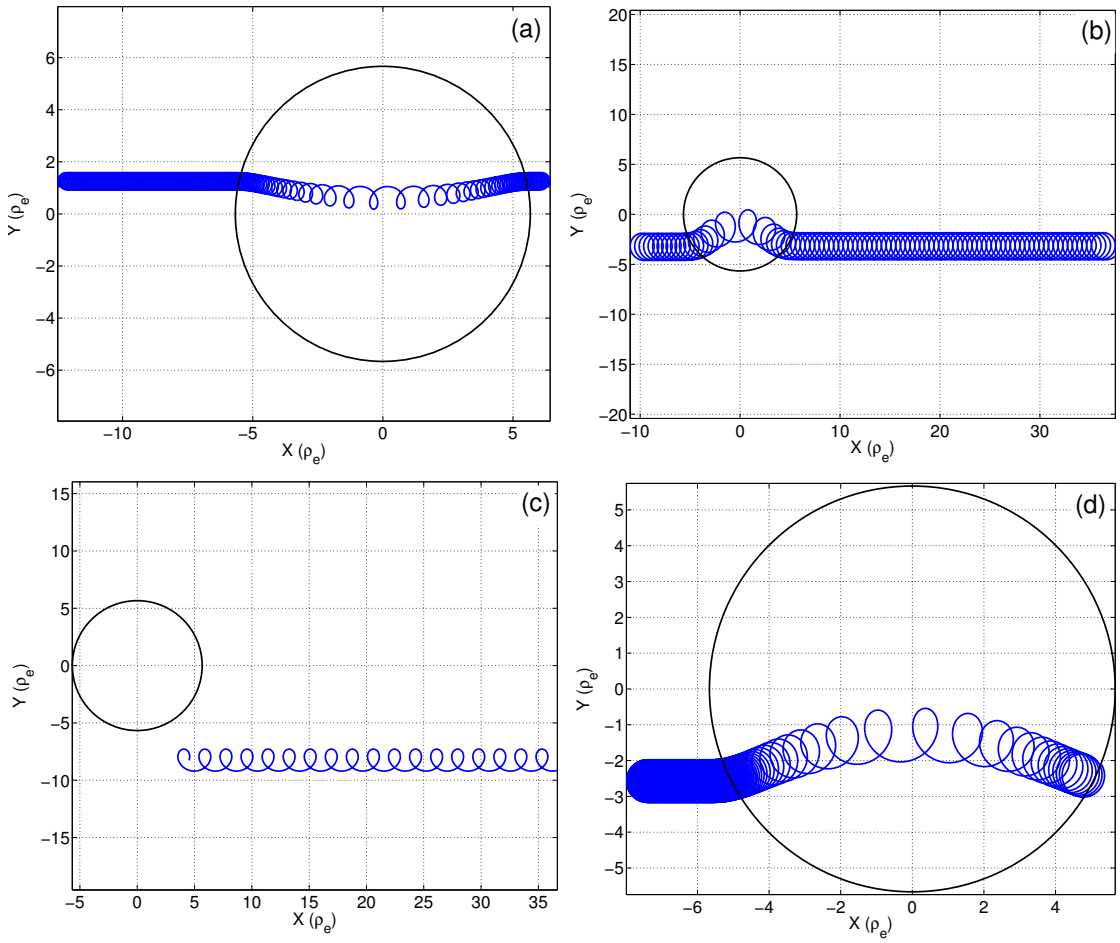

Figure 5.15.: Example test particle trajectories for electrons which are not trapped by the MH.

(d)). An obvious difference between Fig. 5.15 and Figs. 5.16 is that the electrons $V_\perp$ is larger in the latter figure, as their gyroradius is approaching 1/2 R_H. This supports the theory suggested in Section 5.2.2 that electrons with Larmor radii approaching that of the hole radius are more likely to be trapped by it.

Figure 5.17 shows electrons that are fully trapped within the MH. These have similar $V_\perp$ to the electrons in Fig. 5.16, but have initial positions and directions, so that the electrons can form "petal" shaped orbits (Figs. 5.17(a)-(d)). The trajectories in Fig. 5.17(a) and (b) most closely resemble the example trajectory seen in the turbulence simulation in Fig. 5.8. This figure also shows that when $V_\perp$ is even larger the trajectory can become circular (Fig. 5.17(e)).

Whilst examining trajectories can help us to understand the basic electron dynamics and individual behaviour within an EVMH, we also use a statistical approach in order to better characterize the population of trapped electrons in these structures. A test was developed that determined automatically whether a particle was part of

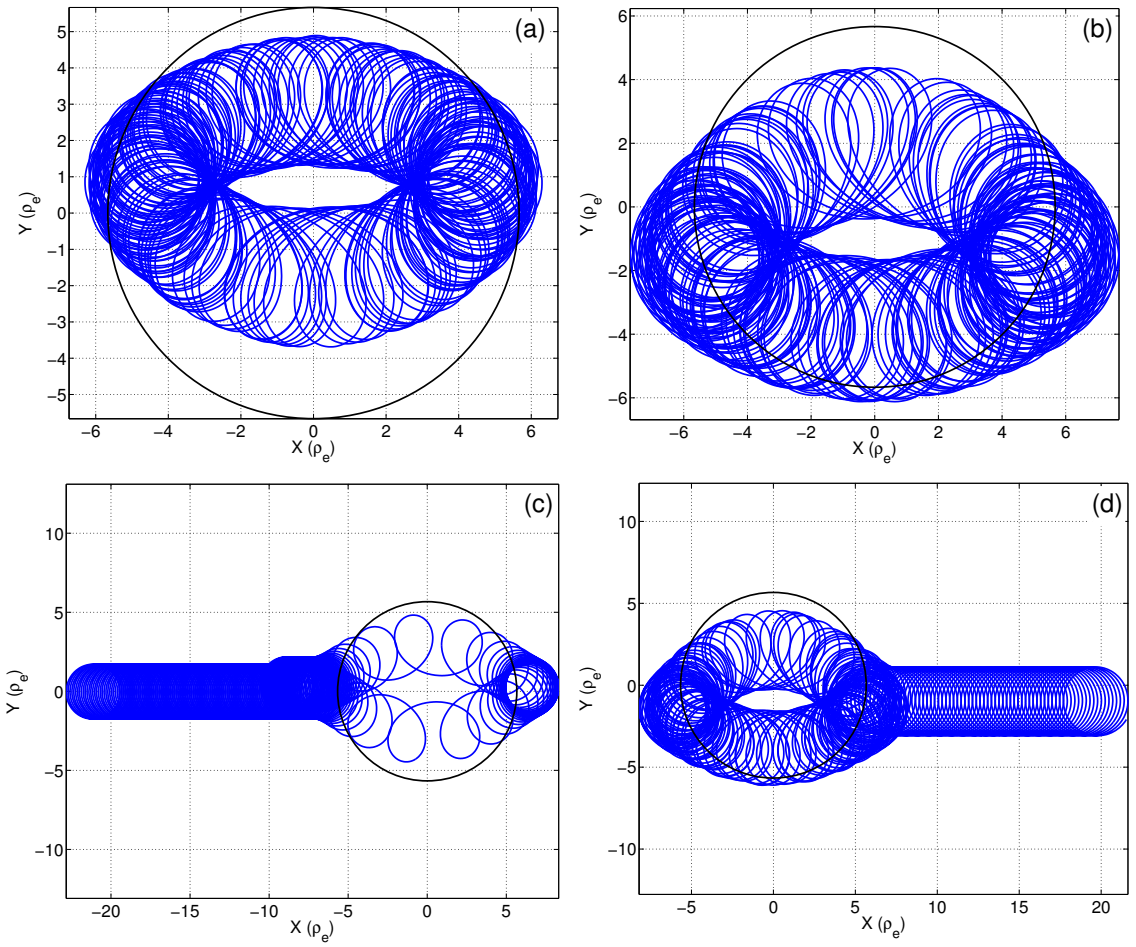

Figure 5.16.: Example test particle trajectories for electrons which are quasi-trapped by the MH.

the trapped population. This was done according to the following rules: After 200 gyro-periods, if the electrons maximum position is within a square box of length four times the EVMH radius (centred on the hole) then the particle is considered trapped. This logic ensures that quasi-trapped particles (Figs. 5.16(a) and (b)) that can orbit considerably outside the hole, are considered part of the population, whilst those that eventually escape (Figs. 5.16(c) and (d)) are discounted.

An additional piece of logic was also added after initial analysis due to a number of false positives that were discovered in the data at low energies. These were attributed to electrons with small $V_\perp$ that were only deflected by the MH, rather than trapped, but even after 200 gyro-periods were still within a distance of $2R_H$ in the x and y directions. An example of this type of false positive is shown in Fig. 5.15(d). In order to remove these from the analysis, a electron was only considered part of the trapped population if it entered all four quadrants of the MH at least once. This

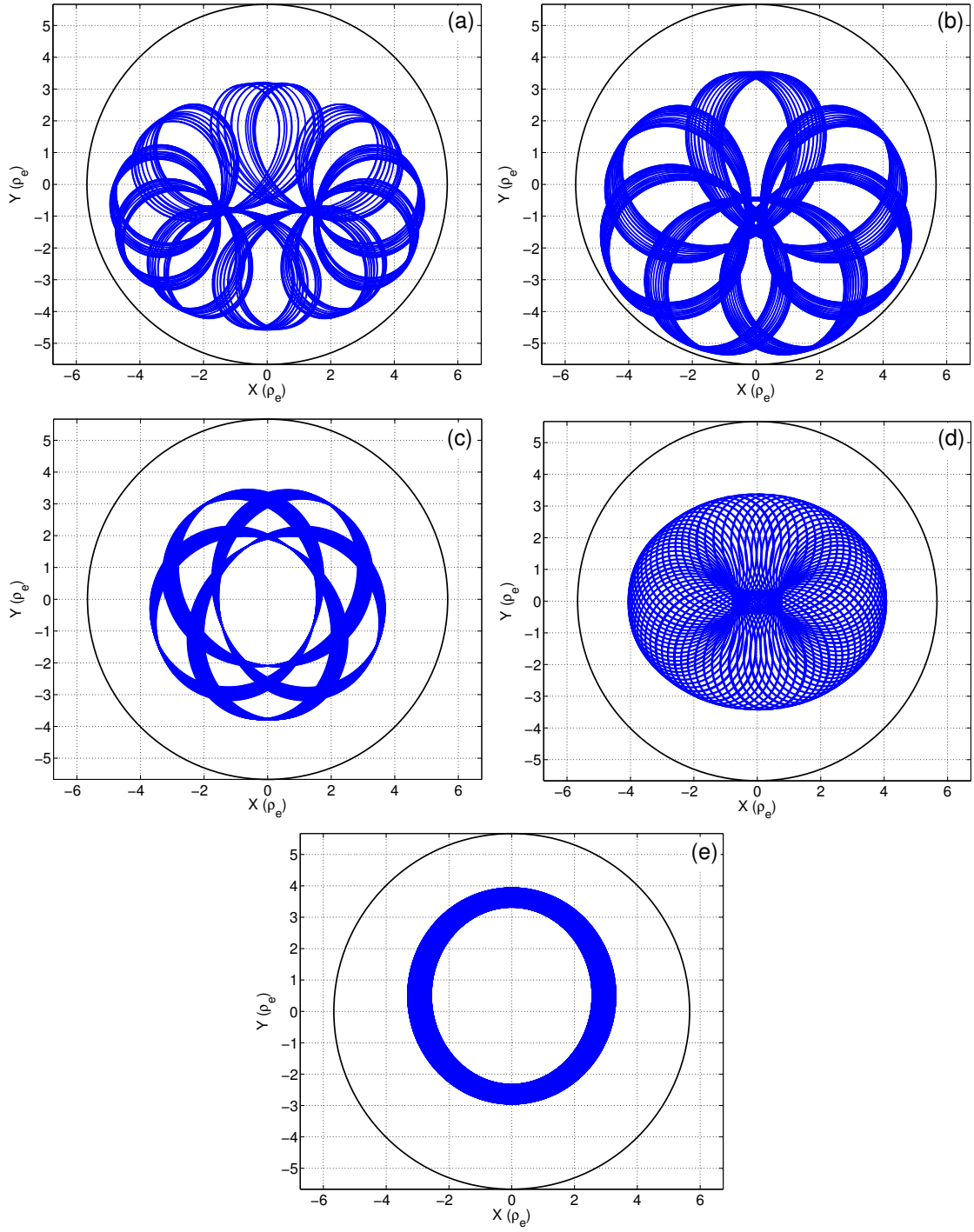

Figure 5.17.: Example test particle trajectories for electrons which are trapped by the MH.

"quadrant logic" removes most of the electrons erroneously tagged as trapped, but some false positives are still possible if the electron gyrates near/around the centre of the MH.

In order to build up statistics that are comparable to the PIC studies, we use a similar number of test particles as in the previous simulation. Using a hole radius of 17 cells with 6400 particles per cell, results in $\sim 6\times10^6$ super-particles in the EVMH. Our initial work with the test code showed that $\sim$ 10% of test particles become trapped, so to be able to demonstrate the shape of any instantaneous current due to trapped electrons, we would like to have trapped trajectory data for $\sim 6\times10^5$ electrons.

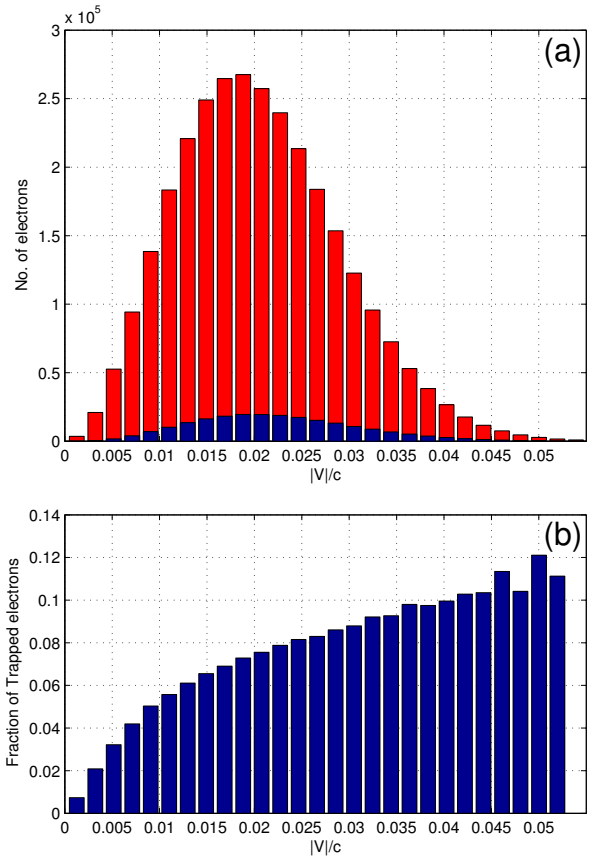

Figure 5.18.: (a) Speed distribution of total (red) and trapped (blue) electrons. (b) Distribution of the fraction of trapped electrons. Velocities are normalised to the speed of light, c.

The statistical data we show used an initial population of 3×10^6 electrons, initially distributed randomly within a radius of $2R_H$ as previously shown in Fig. 5.14, with velocities set to an isotropic Maxwellian distribution. This results in a speed distribution that ranges from $\sim 0-4.5V_{th}$. Using the selection method described above, the code recorded 218 013 trapped electrons, which is of the order of the number expected in the turbulence simulation. The speed distribution of the total number of electrons (red), and trapped population (blue) is shown in Fig. 5.18(a).

This graph confirms that the initial population was in a Maxwellian distribution. Plotting the fraction of trapped electrons (Fig. 5.18(b)) confirms the previous statements that the larger the velocity, the more likely the particle will be trapped in the EVMH, as the histogram follows a smoothly increasing curve. The maximum fraction of trapped electrons is 12%, with an average over the speed distribution of 7.3%.

Particles with $|v|/c > 0.055$ are not shown in Fig. 5.18 as the fraction becomes statistically unreliable, producing erroneous data spikes. The total number of electrons in each bin, shown in Fig. 5.18, is greater than 1000. A similar spike was initially also seen at the lower end of this histogram due to a high number of false positives from low energy electrons (as previously discussed, and shown in Fig. 5.15(d)) that were tagged as trapped. This erroneous peak was successfully removed in Fig. 5.18(b) by the inclusion of the additional "quadrant logic."

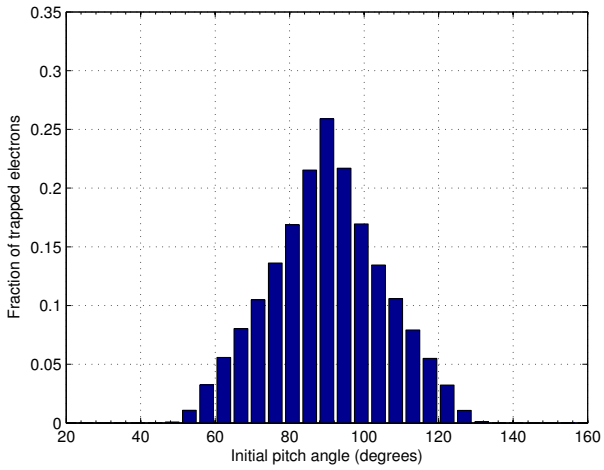

Figure 5.19.: Distribution of initial pitch angles for trapped electrons.

We now examine the initial pitch angle, defined as $\arctan(V_\perp/V_\parallel)$, of the trapped electron population. The Maxwellian distribution algorithm produces an initial distribution of pitch angles peaking at 90° in a cosine form. Figure 5.19 shows the ratio of the number of trapped particles to the number of total particles in each angular bin. This shows a distinctive peak, that is symmetric around 90°, meaning that particles with a large ratio of $V_\perp$ to $V_\parallel$ are more likely to get trapped. Therefore, within the EVMH, there will be an increase in the number of electrons that have a high value of $V_\perp$. This, as we have seen in Fig. 5.4, will result in an increase in perpendicular pressure, and therefore $T_{e\perp}$ within the hole. This also explains why a high value of $T_{e\perp}/T_{e\parallel}$ was observed within these EVMH structures in Figs. 5.4 and 5.8.

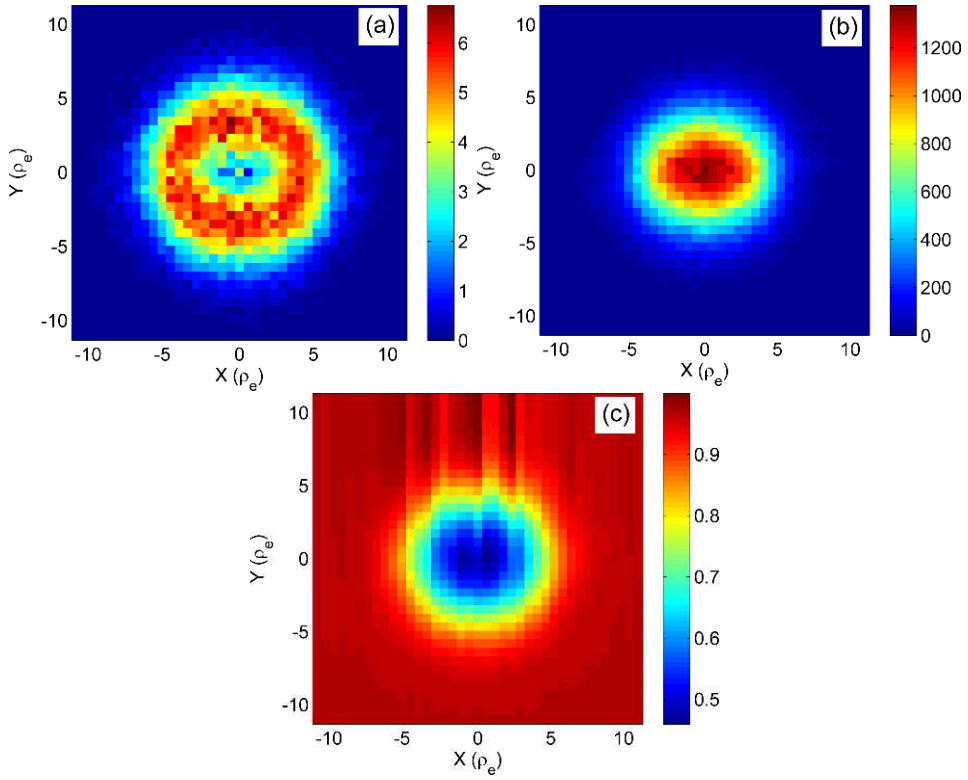

Figure 5.20.: a) Total current calculated from the trapped electron trajectories at cycle 3000.
b) Number of electrons in each bin.
c) Induced B_z calculated from the total current.

To see if the collective trajectories of these these trapped particles could be responsible for the ring shaped current, a series of 2D histograms were created using the test particle code. A square box, $4R_H$ wide was centred around the EVMH and divided into 40×40 square cells. After the position of a test particle was calculated, its location within this grid was determined and various velocity sums calculated for each grid point, (e.g. $J_x \sim \sum V_x = N\langle V_x \rangle$) in order to build up a picture of the current these trapped electrons could create.

Figure 5.20(a) shows the magnitude of the total current calculated from the population of trapped electrons ($\sim 2 \times 10^5$ electrons) binned into a 2D histogram, at timestep 3000. This shows that the combination of multiple trapped orbits sum to form a distinctive ring current, mostly contained within the radius of the magnetic hole ($5.66\rho_e$). This matches the form of current seen in the turbulence simulation in Fig. 5.2(c). A similar histogram (not shown) that sums only the azimuthal component of the electrons in-plane velocity, also forms a similar ring shape. The histogram formed of the radial component of velocity, does not show a ring, but instead is circular, with values approximately 1/10th that of the total current. This

confirms the hypothesis made at the end of Section 5.2.2 that the radial parts of the electron trajectories within the MH cancel out when the average current is calculated, and it is the azimuthal component that is the strongest contributor to the overall current.

The out-of-plane magnetic field that would be induced by this current was calculated using the equation $\mathbf{J} = \nabla \times \mathbf{B}$, and the in-plane components of current shown in Fig. 5.20(a), via the integration method described in Appendix C. The ring current creates a circular depression in the B_z component of the magnetic field, as shown in Fig. 5.20(c). A cross section of the initial B_z profile and the induced B_z is shown in Fig. 5.21. A density weighting of 0.0032 was applied to each test particle in order to match the depth of the B_z depletion.

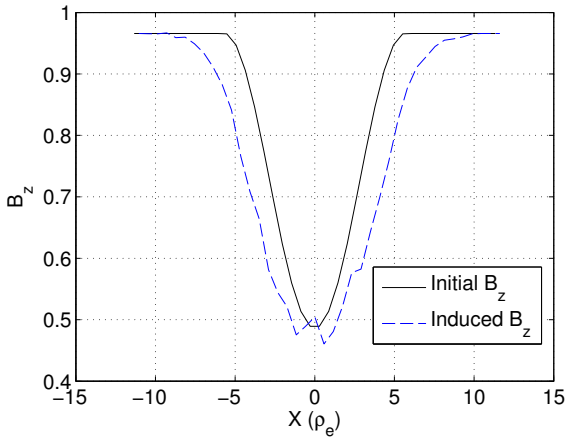

Figure 5.21.: Initial and induced B_z cross section.

Due to the fact that test particles can travel outside the hole radius and still remain trapped, the induced B_z profile is slightly wider than the initial hole width. This is only an estimate of what fields might be produced in a self consistent model. There will be electrons, not trapped, gyrating outside the hole (not included in this calculation of current) that form opposing currents at the outer edges of these trapped orbits, which would alter (perhaps reduce further) the amount of B_z depletion at the edge of the structure. However, the similarity of the original imposed field profile and that inferred from the trapped particles suggests that it might be possible for electrons trapped in such a structure to find a stable Vlasov equilibrium.

Figure 5.20(b) shows a similar 2D histogram as Fig. 5.20(a) but sums the electron counts in each bin location at the same timestep. This value will be proportional to number density multiplied by a weighting factor. This shows a high density of trapped electrons at the centre of the EVMH, gradually reducing with circular symmetry towards the outer edges of the hole. This matches the previous observation

in the turbulence simulation of increased electron density in the EVMH centre in Fig. 5.3(c). The increased electron density in the region suggests that there should also be an increased ion density in the EVMH in order to maintain charge neutrality, for $\mathbf{E} = 0$, but the electron test particle analysis does not provide any information about this. The data in the turbulence simulation in which these were first observed, suggests that there was a corresponding ion density increase in the area, but this is of the order of the other random density fluctuations in the simulation. It is difficult to say whether this increased ion density is a crucial factor in the formation of an EVMH. To investigate if an EVMH can be formed, and reach a natural Vlasov equilibrium, without the presence of turbulence, a series of self consistent simulations were performed.

5.4. Isolated simulation results

We now show results from PIC simulations, using Parsek2D, designed to recreate a simple EVMH, in a quiet uniform plasma. The intent is to show that an EVMH can be "seeded" within the plasma, by adjusting the initial properties of the plasma in a localised area. The simulations were initialized with the same plasma properties as in the initial turbulence simulation (Section 5.2), but in a smaller box; $\sim 1/2$ ion inertial length, and with an increased number of particles per cell (100×100).

A number of PIC simulations were run, designed to examine what plasma properties were required for a EVMH to achieve an equilibrium, the first of which only had a quiet magnetic field, set at an angle of 15° to the z axis in the x-z plane, as in the test particle experiments. This was seeded with a circular, half sinusoidal drop in the B_z component of magnetic field, with a maximum drop at its centre of 50%. These initial PIC simulations showed that with only an initial magnetic depression, and uniform plasma, the MH was not stable. The structure did initially form a ring current, however the depletion in the magnetic field slowly reduced until the MH was completely gone. This implied that a depression in magnetic field was not enough for the system to reach an equilibrium. Therefore a series of tests were performed which changed the initial values of electron temperature anisotropy in a circular region within the magnetic depression.

The velocity distributions of the ions and electrons in the simulation were initialized with Maxwellian distributions. The ions distributions were isotropic, however the thermal velocities of the electrons were adjusted to produce a perpendicular temperature anisotropy of 0.8 outside the hole, and 1.4 inside the hole. These pa-

rameters were successful at forming a stable MH, which remains stationary at the centre of the simulation.

5.4.1. Simulation results

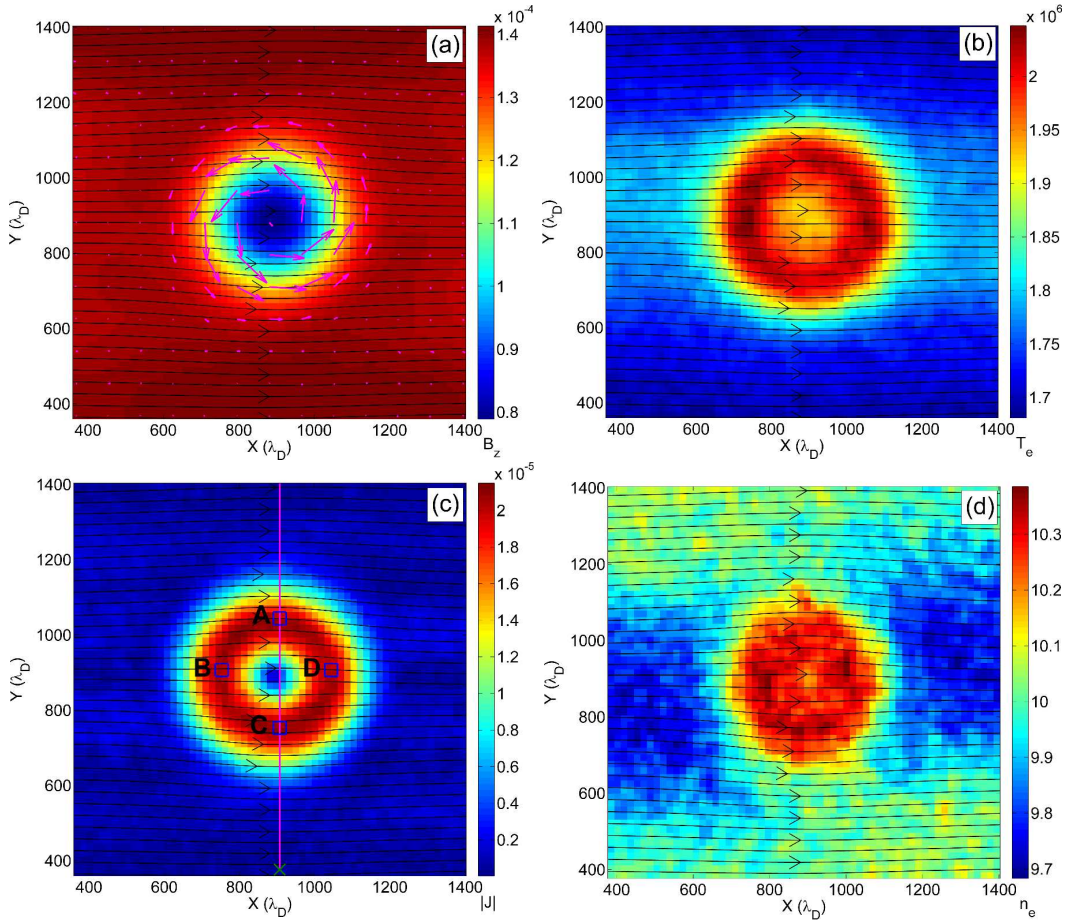

Figure 5.22.: Magnetic field lines (black) and (a) out-of-plane magnetic field B_z with electron flow vectors (magenta), (b) total electron temperature, T_e, (c) magnitude of current J and (d) electron number density, n_e (cm^{-3}) at cycle 5000. The vertical line shows where cross sections of the parameters will be taken. The four marked regions are discussed in the text.

The simulation initialised with a magnetic depletion and perpendicular temperature anisotropy within the EVMH is shown in Fig. 5.22 at $t = 250\Omega_e^{-1}$ (5000 cycles). Panel (a) shows the circular depletion in B_z. Panel (b) shows the electron temperature, which as in Section 5.2.1 shows higher temperature within the EVMH. Panel (c) shows the current density within the vortex, which again shows the characteristic ring shape. The vertical line again shows the location where a cross section

of plasma parameters will be taken. The labelled boxes are the locations where we will calculate electron VDFs. Panel (d) shows an increase in electron number density of $\sim 3\%$ within the EVMH. This also shows a horizontal band of reduced density outside the hole, which is not seen in the turbulence simulations. This area of the plasma has lost electrons to the MH, as only electrons in this central portion of the simulation domain can follow trajectories which intersect with the MH. The density above and below this central band is approximately the value assigned as the particle background density, 10 particles cm^{-3}. Overall, the final configuration is remarkably similar to that seen in the turbulence simulations (Fig. 5.2).

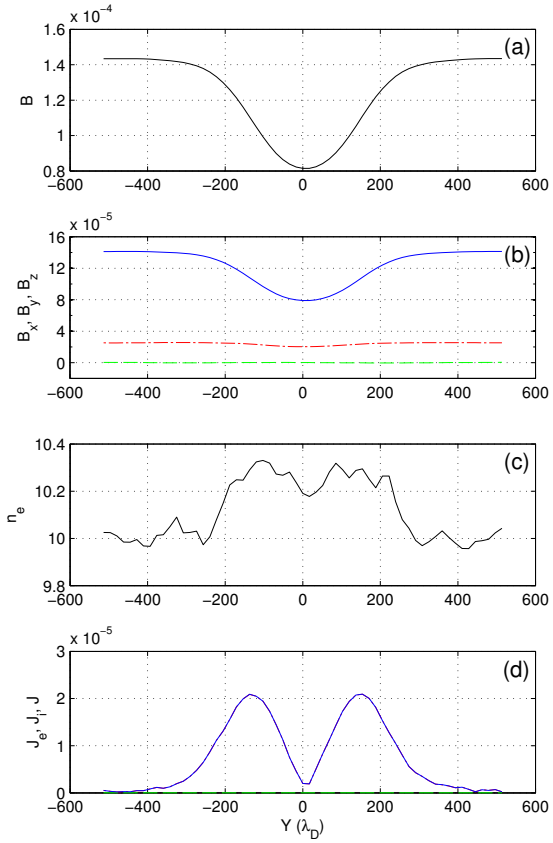

Figure 5.23.: Cross section of field and current parameters through the line indicated on Fig. 5.22(c).

Figures 5.23 and 5.24 show cross sections of the properties of the EVMH through the line shown in Fig. 5.22(c), in the same style as Figs. 5.3 and 5.4. These show a 40% reduction in B_z (Fig. 5.23(b)) and a $\sim 3\%$ increase in electron density within the structure (Fig. 5.23(c)). The current is again formed by electron flow, as the J (blue) and J_e (red) lines completely overlap (Fig. 5.23(d)).

Figure 5.24(a) shows the increased electron temperature within the hole, and

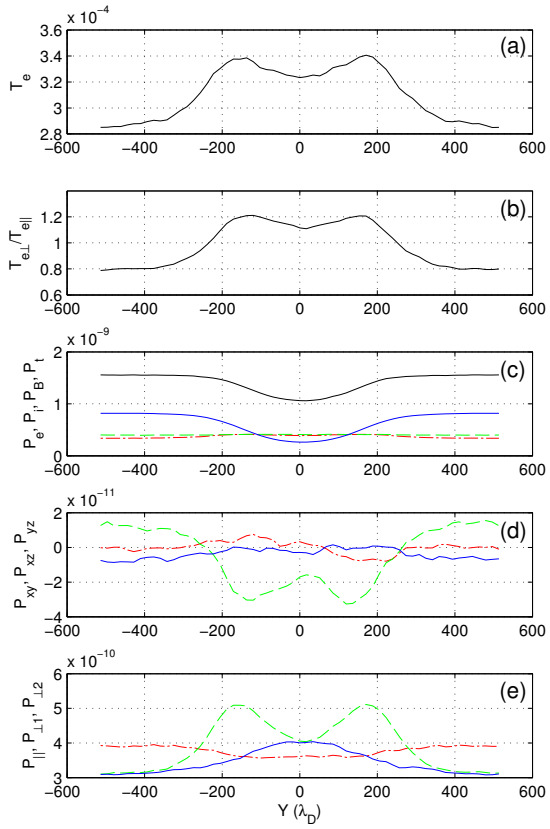

Figure 5.24.: Cross section of plasma temperature and pressure parameters through the line indicated on Fig. 5.22(c).

Fig. 5.24(b) shows the increased perpendicular temperature anisotropy. The magnetic pressure reduces below the electron and ion pressure (Fig. 5.24(c)) as seen in Section 5.2.1. Non symmetric off diagonal terms are again present in the pressure tensor (Fig. 5.24(d)), and the difference in the $P_{\perp 1}$ and $P_{\perp 2}$ components of the pressure tensor show non-gyrotropic behaviour.

An increase in ion density (not shown) matching that of the electrons is also present in the MH, which implies that an electrostatic potential has been set-up in the region, in order to reach a stable equilibrium. In order to see if this was the case, the in-plane components of electric field, E_x and E_y were integrated in order to calculate the electrostatic potential, Φ, using the equation $\mathbf{E} = -\nabla\Phi$. Figure 5.25 shows that a negative potential has been created within this EVMH. This means that positively charged particles would actually lose potential energy as they enter this region, and are attracted/accelerated into the area. This explains the increase in ion density in the region, which matches the electron density in the hole.

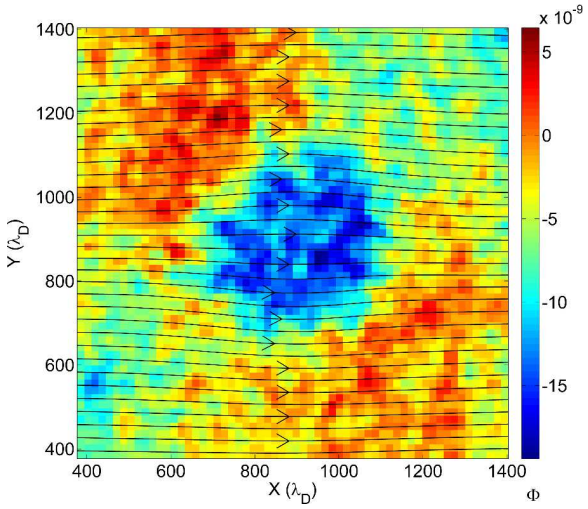

Figure 5.25.: Magnetic field lines (black) and electrostatic potential, Φ, at cycle 5000.

5.4.2. Electron velocity distributions and particle tracking.

Calculating the electron VDFs from electrons in the four boxes labelled A, B, C and D (Fig. 5.22(c)) reveals similar distributions to those seen in Section 5.2.2. Figure 5.26 is plotted in the same style as Fig. 5.5, and shows the same characteristics: anticlockwise electron current (average velocity in each VDF is indicated by a small black cross), and electron VDFs with extended tails. The shape of the distribution is seen more clearly in Fig. 5.27, which is calculated using the same method as in Fig. 5.6, but for the electron VDF from box C (Fig. 5.22(c)). A small plateau is present in the positive V_x side of the distribution, with an increased population of higher energy electrons located at higher values of V_x.

Particle tracking also shows a range of trapped trajectories, of both the petal and circular type. Electrons with higher perpendicular velocities tend to circular, whereas lower energy electrons follow petal shaped orbits, as discussed in Section 5.3. An example petal trajectory is shown in Fig. 5.28, with the background colour indicating B_z at cycle 5000. This particle was chosen from the plateau region of Box C (Fig. 5.22(c)).

These simulations show that a circular sinusoidal magnetic depletion in B_z can form an electron structure, which can achieve a Vlasov equilibrium over many electron gyroperiods. This structure will only be stable if it is populated by electrons with a higher perpendicular temperature anisotropy than those outside the EVMH. These trapped electrons then create a negative electrostatic potential that can attract positive ions into the region, which ensure charge neutrality, and allow the

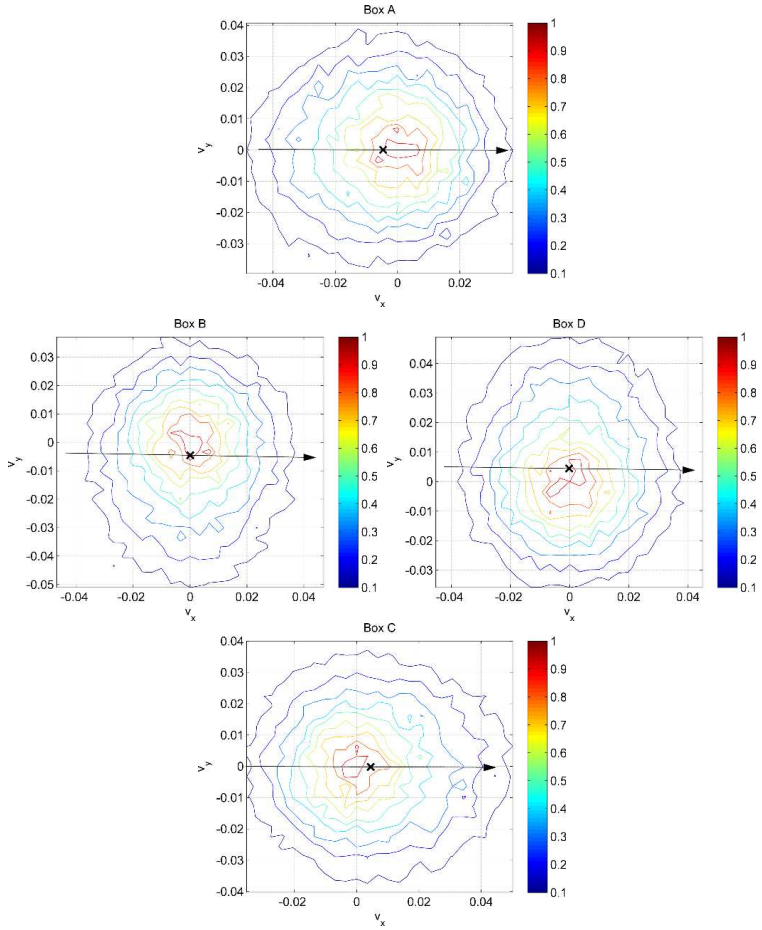

Figure 5.26.: Electron velocity distribution functions in the $v_x - v_y$ plane for Boxes A, B, C and D. (Refer to Fig. 5.22(c).)

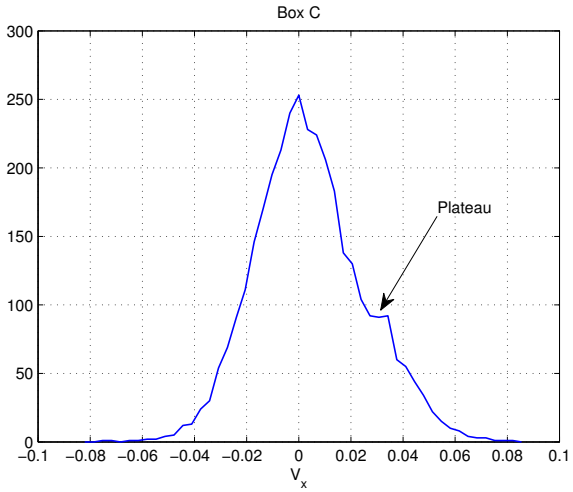

Figure 5.27.: Maximum value of electron VDF along the V_y direction, for Box C. (Refer to Fig. 5.22(c).)

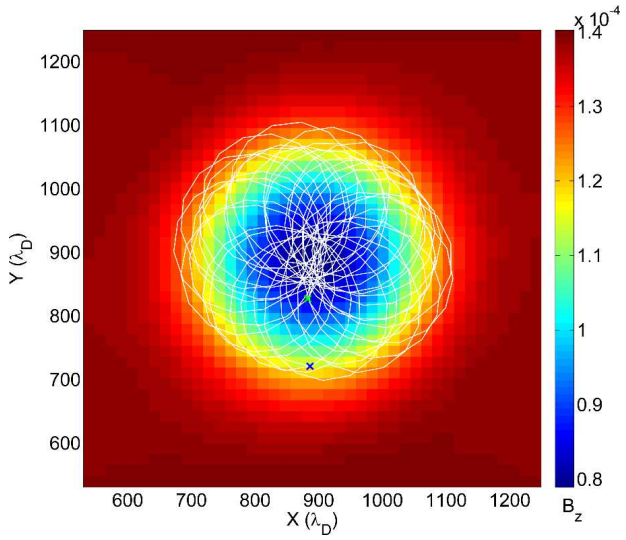

Figure 5.28.: Example petal trajectory (white) for an electron selected from the plateau region of Box C. (Refer to Fig. 5.22(c).) The start and end position are indicated by a green and blue cross respectively. The colourmap shows the out-of-plane magnetic field, B_z.

structure to stabilize.

5.5. MH observations in the plasma sheet

We now present spacecraft observational data that shows that these structures may have been observed in the Earth's plasma sheet. This data is taken from Sun et al. [2012], in which they analyse data from the Cluster and TC-1 spacecraft. Magnetic holes were identified in this data using a search criterion of $B_{min}/B < 0.75$, and a change in field direction of less than 15° across the event.

In Fig. 5.29 we plot data from one of the events from Sun et al. [2012] in minimum variance coordinates (Figure provided by Sundberg [2014]). This shows a good agreement to the EVMH cross sections plotted in Figs. 5.3 and 5.23, as the change in magnetic field is only in one direction, and it has a similar relative drop in magnetic field strength of $\sim 50\%$.

Most of the MHs they found had a range of sizes that were less than the proton thermal gyroradius, ρ_p. Figure 5.30 shows the distribution of sizes, and has a peak at $\sim 0.55\rho_p$. The MH that developed in the turbulence simulation in Section 5.2 has a diameter of 34 cells, and the local ρ_p in the area was ~ 100 cells, giving a length of $0.34\rho_p$, so they are of comparable size. Crucially because Sun et al. [2012] used four spacecraft data from Cluster, they were able to confirm the observed MHs are

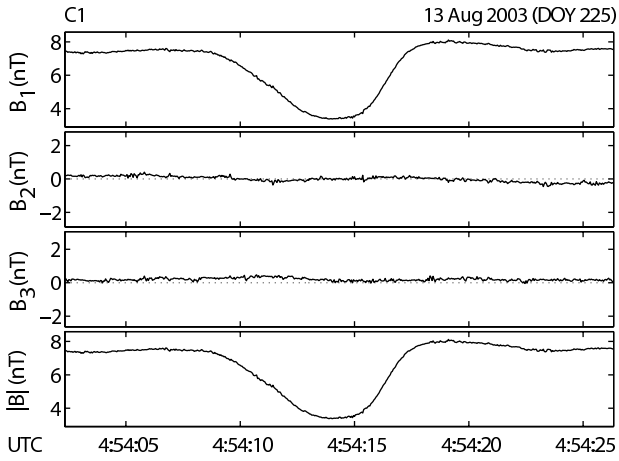

Figure 5.29.: Cluster MH event rotated to a minimum variance coordinate system. (Figure provided by Sundberg [2014].)

spatial structures and not just temporal fluctuations in field strength (using interlaced magnetic field patterns). No comment is made of the two dimensional shape of these structure due to the lack of data, but we would suggest if more spacecraft were present, that these would be observed to be circular as in our simulations.

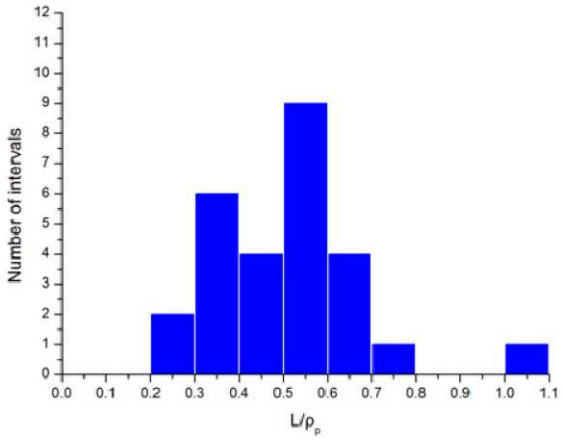

Figure 5.30.: Histogram of the ratios of magnetic hole scale sizes to proton Larmor radii. The proton Larmor radius is calculated from their background parameters. This data in this histogram is from the Cluster spacecraft. Larmor radius was calculated from timing velocity. (Image from Sun et al. [2012].)

The Cluster data also shows that the MHs had an electron energy flux enhancement at a 90° pitch angle. This is in good agreement with our test particle run that showed electrons with 90° pitch angles are more likely to get caught in an EVMH (Fig. 5.19). They also state that in most cases the electron total temperature increased inside the observed MHs, and that the perpendicular temperature

also increased (consistent with the 90° pitch angle). This is consistent with what we have observed in our simulations (Fig. 5.2(b), Fig. 5.4(a) and (b), Fig. 5.22(b), Fig. 5.24(a) and (b)). The observations also showed a slight increase in electron density, but not much change in total pressure within the hole, mainly due to the presence of much hotter ions, which we would not see in the PIC simulations, as the ions and electrons were initialised at the same temperature.

Finally the authors discuss whether the formation of the MHs could be via mirror mode instabilities. They use the following equation (from Istomin et al. [2009]) to calculate if the surrounding plasma was mirror unstable,

$$L = \frac{T_\perp}{T_\parallel} - 1 - \frac{1}{\beta_\perp} - \frac{(T_\perp/T_\parallel - 1)^2 T_e}{2T_\perp(1 + T_e/T_\parallel)}, \tag{5.1}$$

where $L > 0$ is unstable. They found that most events were mirror stable, and therefore could not conclude that the mirror mode was invoked during the MHs formation, a conclusion supported by Balikhin et al. [2012]. Using the same formula on the turbulence simulation data (Section 5.2) shows that the plasma was also never mirror unstable. In the turbulence simulation, the field fluctuations are provided by the initial magnetic perturbation, and further fluctuations are the result of ongoing turbulence and reconnection. The formation of the second magnetic hole must have been due to a field depression that "caught" or trapped electrons with pitch angles of around 90°, which formed a trapped ring current, and allowed the structure to stabilize.

All the data we have presented is highly suggestive that the MHs observed and analysed by Sun et al. [2012] are the same as EVMHs we have presented here, and provides a theoretical explanation for this type of sub-proton scale MH.

5.6. Conclusions

We have presented the results of 2-D simulations that show coherent nonlinear magnetic structures can form within sub-proton plasma turbulence. The structures are circular, have a depletion in B in the guide field direction, and contain a population of hot electrons, with a characteristic ring shaped current density. These "magnetic holes" are $\sim 300\lambda_D$ or $\sim 5.66\rho_e$ in radius. The current density is entirely formed by azimuthal mean electron flow, and thus we call them electron vortex magnetic holes (EVMHs). The holes we observe have a high perpendicular temperature anisotropy within them, and a central density increase of $\sim$ 10%. There is a dip in total pressure, P_t in the region, resulting in increased values of β within the hole. Mag-

netic pressure is seen to dip below both the ion and electron pressure. Off diagonal terms of the pressure tensor are non-zero, and non-symmetric, and the pressure tensor rotated into the parallel and perpendicular directions shows non-gyrotropic behaviour. Particle VDFs show a Maxwellian-like part of the distribution and an additional population of high $V_\perp$ current carrying electrons, forming a plateau and extended tail in the distribution function. Tracking particles confirms that these electrons are trapped within the hole, and trajectory plots show that they follow petal shaped orbits. These orbits are the result of the reduced B_z field in the region, and are similar to orbits produced by electrons drifting in a magnetic field gradient, where the field gradient here is circularly symmetric.

An analysis of groups of particles from various parts of the VDFs confirmed that the higher energy electrons were a group of trapped electrons, potentially responsible for the circular ring current in the region, as they collectively followed the circular form of the vortex as the MH drifted in space.

We also showed that the EVMHs contribute to the intermittency by plotting probability distribution functions (PDF) of the normalised partial variance of increments (PVI). We formed the PVI dataset using the difference between the points (separated by ΔS) in the original magnetic field map. We showed that high values of PVI were located at the locations of the two MHs in the simulation. Reducing the values of ΔS changed the PDF of partial variance of increment (PVI) values from a Gaussian shape, to one with extended tails, which is an indicator of intermittency.

Test particle simulations were used to demonstrate the different types of trapped trajectories which are possible within a static, circular sinusoidal depletion in magnetic field. For an ensemble of test particles one can calculate the effective current and density that they would produce (assuming some particle weighting). Assuming the test particles have a Maxwellian velocity distribution at some temperature, each type of orbit contributes to the instantaneous current with the EVMH. We showed that these collectively form a ring shaped current within the MH. The ring shaped current has a diamagnetic effect, and can induce a similarly shaped magnetic field to the initial drop in B_z, implying a solution to the Vlasov equation might be possible in a self consistent field model. Using a statistically significant number of particles, we showed that $\sim 7\%$ of test particles become trapped, and the probability of a particle being trapped was an increasing function of the magnitude of its velocity.

We also found that particles with 90° pitch angles are most likely to be trapped within these structures, and a small increase in the electron density should be observed within the structure, due to the overlapping orbits of the trapped electron population.

We then showed that we can seed a stable EVMH in a self consistent PIC simulation with a "quiet" plasma background, using a perturbation consisting of a circular drop in B_z and increase in perpendicular electron temperature anisotropy within the hole. These results show that B_z induced by these trapped electrons appears to reach a quasi-stable solution, at least on sub-proton timescales, so that an EVMH can exist without the presence of turbulence. The trapped population of electrons within the MH generates a negative electrostatic potential, which attract ions into the region, allowing an increase in electron density and corresponding ion density increase. However, no negative potentials were seen in the holes within the turbulence simulations which suggests that this potential is not a necessary requirement for the stability of an EVMH.

And finally we showed that these simulated EVMHs are consistent with the scale sizes and electron properties of the population of linear MHs surveyed in the Earth's plasma sheet by the Cluster and TC-1 spacecraft [Sun et al., 2012]. We suggest that the EVMHs described in this chapter provide a theoretical description for the sub-proton scale MHs seen in the plasma sheet that have an increased electron energy flux at 90° pitch angles.

6. Dissipation at electron scales

In this chapter we attempt to address the issue of dissipation within our simulations of electron scale collisionless plasma turbulence. We will do this by examining the energy budgets in the previous simulation (Chapter 4), and by using a dissipation diagnostic, D_e, which has been used in previous studies of both magnetic reconnection and turbulence [Karimabadi et al., 2013, Wan et al., 2012, Zenitani et al., 2011]. Before we discuss the definition of this parameter it is useful to discuss exactly what we mean by the term "dissipation" in the context of collisionless plasmas.

The term has a very specific meaning in hydrodynamic turbulence, as previously described in Chapter 2. It is the process by which energy is removed from the fluctuations involved in the turbulent cascade, and is deposited back into the medium. Since the cascade process involves a constant rate of energy transfer between waves of different wavenumbers, the dissipation process needs to have an energy removal rate the same as the energy injection rate at large scales (see Fig. 2.2). It also needs to be an irreversible process, so the energy deposited from the waves cannot regenerate waves, and thus terminate the cascade. In hydrodynamics, dissipation is often linked to heating of the medium, due to the action of viscosity in shear flows at small scales, as there is no other way in which the energy can be transferred from flow energy (fluctuations in fluid velocity) to thermal energy. Therefore people often use the terms "dissipation" and "heating" interchangeably, which may be misleading and incorrect, especially when talking about kinetic scale collisionless plasma dissipation.

So what is dissipation in a collisionless plasma? There are no collisions and therefore no viscosity, but since turbulence has been observed in the solar wind (Section 2.3) we assume there should be an equivalent dissipation mechanism in plasma. Therefore plasma dissipation is the mechanism (or mechanisms) that redistribute wave energy back into the plasma medium. We do not mean necessarily in the form of temperature increase, and we will discuss why later. What is also more complex is the term: wave energy. In hydrodynamics wave energy is contained in the bulk kinetic energy of the fluid. This has one dissipation mechanism, via viscosity, which transfers the bulk kinetic energy into heat. In a plasma the kinetic energy is split

between the separate particle species, ions and electrons. There is also electromagnetic energy contained in the magnetic and electric fields, and across many types of wave mode. Therefore more energy transfer mechanisms exist in the medium. It follows then that dissipation in a collisionless plasma is, most probably, a multi-staged process and dissipation must exist in many types, e.g. cyclotron or Landau interactions, in order to remove energy from the different types of wave mode.

To explore this concept in the simulations, we will first use the dissipation diagnostic, D, defined as:

$$D = \mathbf{J}.\mathbf{E}, \tag{6.1}$$

where $\mathbf{J}$ is the current density and $\mathbf{E}$ is the electric field. This definition describes the rate of work done by the electric field per unit volume, on both the ions and electrons. This can be transformed into a frame of reference moving with the electron bulk motion using,

$$\mathbf{J}' = qn_i\mathbf{V}'_\mathbf{e} = qn_i(\mathbf{V_i} - \mathbf{V_e}) = \mathbf{J} - \rho_q\mathbf{V_e}, \tag{6.2}$$

where q is the charge, n_i is the ion number density, ρ_q is the total charge density, V_i and V_e are the ion and electron bulk velocities. Dashed values represent values transformed into the moving frame. The electric field must also be transformed into the electron frame via $\mathbf{E}' = \mathbf{E} + \mathbf{V_e} \times \mathbf{B}$. Therefore, D_e, the dissipation parameter in the electron frame is,

$$D_e = \mathbf{J}'.\mathbf{E}' = (\mathbf{J} - \rho_q\mathbf{V_e}).(\mathbf{E} + \mathbf{V_e} \times \mathbf{B}). \tag{6.3}$$

The dissipation parameter in the ion frame, D_i, can be found by replacing $\mathbf{V_e}$ with $\mathbf{V_i}$ in Eq. 6.3. It is also useful to calculate the rate of work done by the electric field, in a direction parallel to the magnetic field, which is given by,

$$D_\parallel = \frac{(\mathbf{J}'.\mathbf{B})(\mathbf{E}'.\mathbf{B})}{|\mathbf{B}|^2}, \tag{6.4}$$

and in the electron frame gives,

$$D_{e\parallel} = \frac{(\mathbf{J}.\mathbf{B} - \rho_q\mathbf{V_e}.\mathbf{B})(\mathbf{E}.\mathbf{B})}{|\mathbf{B}|^2}. \tag{6.5}$$

These dissipation parameters all return scalar quantities. A positive value indicates that on average, energy has been given to the plasma, and the plasma has been accelerated by the local electric field. This is useful, since only the electric field can

do work on an single particle in the plasma, whereas (in a static field) the magnetic field, only changes the direction, not magnitude of the particle velocity, and does no work. A negative value means the medium has given kinetic energy back to the electric field. This parameter is not a unique marker for plasma dissipation, in our definition, but positive values do indicate where dissipation could be occurring in the simulation. It has also been useful at identifying waves in the simulations.

This chapter is split into three main sections. In Section 6.1 we apply the dissipation parameter to the previous simulation (Chapter 4), and discuss its implications. In Section 6.2 we revisit data from another turbulence simulation, run by Camporeale and Burgess [2011], which supports parallel wave modes, and apply the dissipation parameter to the data. In doing so, we find several electrostatic wave-modes which we analyse in detail. Finally in Section 6.3 we draw conclusions from both simulations and discuss the nature of dissipation in electron scale turbulence.

6.1. Simulation 1: Out-of-plane guide field

In Chapter 4 we showed results from a simulation of turbulence, which had an out-of-plane guide field, and showed how the reconnection sites in this configuration were responsible for the generation of parallel electron temperature anisotropy. The energy was input by a magnetic perturbation, which releases additional energy into the plasma as the field relaxes, forming turbulence in the process.

6.1.1. Energy budget

Since turbulence is often associated with general heating of the medium, it is useful to plot the average temperature of the cells in the simulation, and also look at the energy exchange of the four main types of energy contained in the plasma. These are the electron and proton total kinetic energy (calculated by summing the square of the velocities for each super-particle in the simulation), magnetic energy, and electric energy. The results are shown in Figs. 6.1 and 6.2.

Figure 6.1(c) confirms that magnetic energy is falling throughout the simulation, as the field relaxes. Panel (d) also shows that the electric field energy jumps from zero soon after the start of the simulation and falls steadily. The electron kinetic energy (Fig. 6.1(a)) also receives a large jump in energy soon after the start of the simulation, and actually finishes at the same value of energy at the end of the simulation after a short period of increase. The proton kinetic energy is constantly increasing throughout the entire simulation. Figure 6.2 confirms that the proton

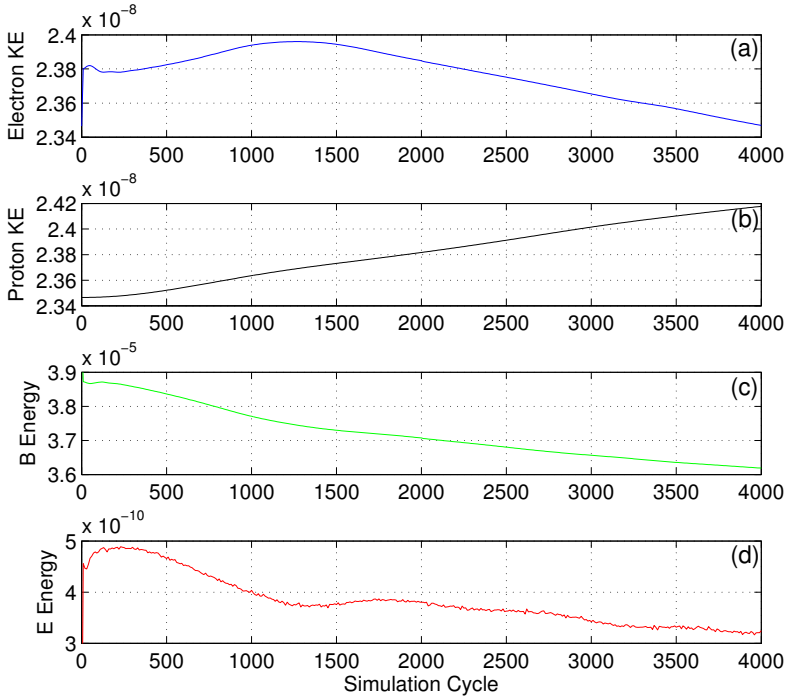

Figure 6.1.: Timeseries of (a) electron kinetic energy, (b) proton kinetic energy, (c) magnetic energy and (d) electric energy.

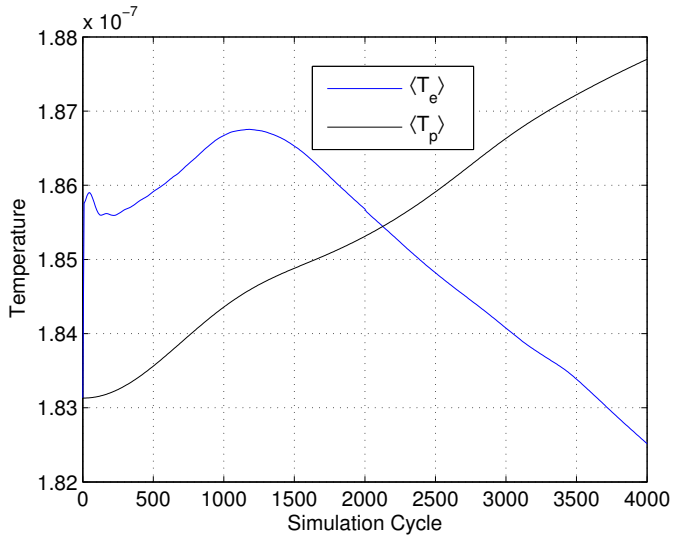

Figure 6.2.: Timeseries of average electron temperature, $\langle T_e \rangle$, and average ion temperature, $\langle T_p \rangle$.

temperature increases, and that the electron temperature also initially increases, but then returns to approximately its start value by the end of the simulation. These figures confirm that energy has been transferred from the magnetic field to

the plasma, and it mainly ends up in the form of proton kinetic energy. This is consistent with observational evidence in the solar wind that turbulence leads to proton perpendicular temperature increase (see Fig. 1.7 and associated text in Section 1.1).

6.1.2. Dissipation parameter

We now apply Eqs. 6.3 and 6.5 to the out-of-plane guide field simulation, in order to see where energy transfer is occurring, noting that positive values of D_e indicate net energy transfer from the electric field to the particles. Two timesteps of interest were chosen. $t = 90\Omega_e^{-1}$, which corresponds to the maximum reconnection rate of reconnection site 2 (refer to Fig. 4.6 and Fig. 4.16(a)), and $t = 180\Omega_e^{-1}$, which corresponds to the maximum reconnection rate of reconnection site 3 (refer to Fig. 4.6 and Fig. 4.17(a)).

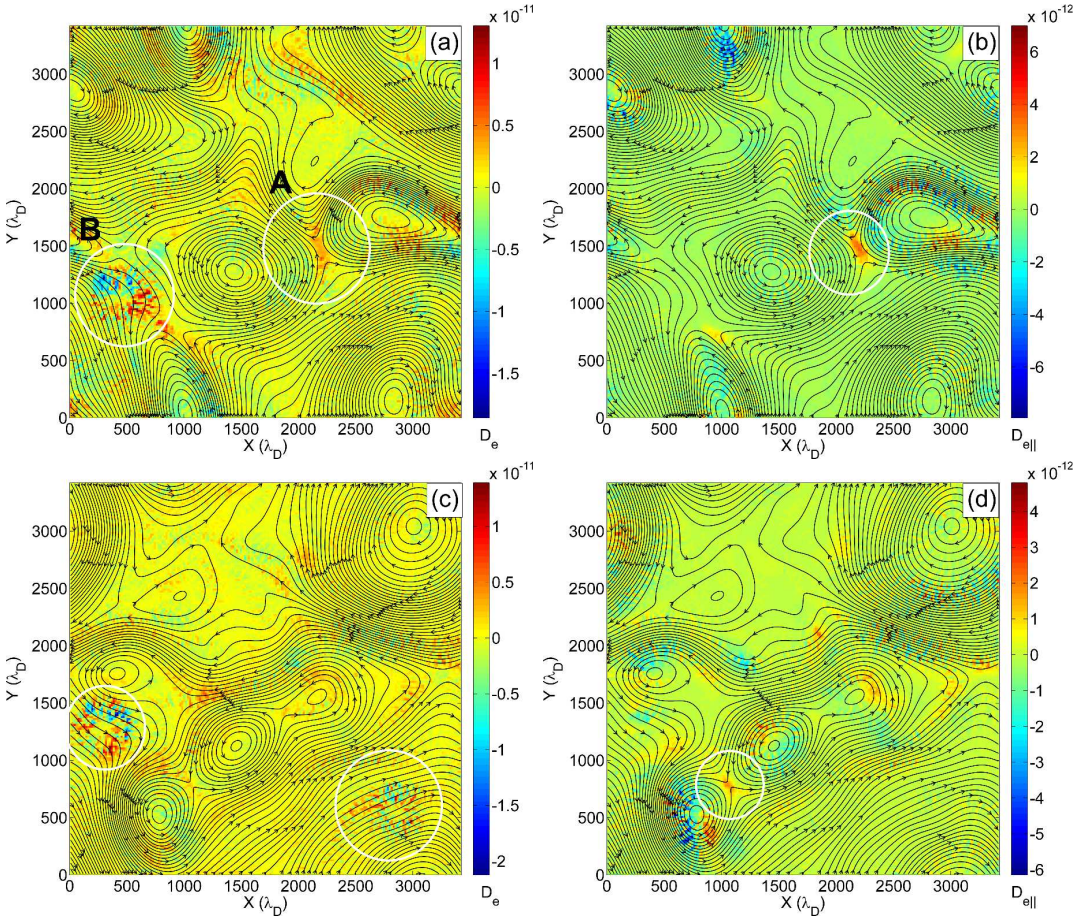

Figure 6.3.: Dissipation parameters. (a) D_e, at $t = 90\Omega_e^{-1}$. (b) $D_{e\|}$ for $t = 90\Omega_e^{-1}$. (c) D_e, at $t = 180\Omega_e^{-1}$. (d) $D_{e\|}$ for $t = 180\Omega_e^{-1}$. Magnetic field lines are shown in black. Highlighted areas are discussed in the text.

Figures 6.3(a) and 6.3(b) show D_e and $D_{e\parallel}$ at the moment of reconnection site 2's maximum reconnection rate. The reconnection site is labelled A in Panel (a) and is highlighted by a circle in Panel (b). These show that in both cases, dissipation (energy transfer to the particles from the electric field) is taking place, as both D_e and $D_{e\parallel}$ are positive. In this configuration, $D_{e\parallel}$ highlights the reconnection site much more effectively, as the in-plane magnetic field is zero due to the reconnecting fields, and E_z (parallel to the guide field) is large and negative (Fig. 4.16(a)). At this moment in time, only one of the two EVMHs (Chapter 5) is present in the simulation, as the second one had not yet formed. Figure 6.3(a) shows a circular feature in D_e corresponding to the location of this vortex (labelled B), but is not present in $D_{e\parallel}$ (Fig. 6.3(b)). The D_e signatures appear to be a mixed pattern of positive and negative values. This suggests that there is a weak electric field operating within the EVMH, likely in the perpendicular direction, although no circular features were identified when looking at components of **E**.

Figures 6.3(c) and 6.3(d) shows D_e and $D_{e\parallel}$ at the moment of reconnection site 3's maximum reconnection rate. The location of site 3 is indicated by the circle in Panel (d). Both figures have a positive value in the region of reconnection, indicating that energy is transferring from the electric field to the plasma, and is more distinct in the value of $D_{e\parallel}$. This is consistent with the out-of-plane reconnection electric field accelerating particles in the parallel direction, and the formation of beam like features in the electron VDFs (Chapter 4). At this time, both EVMHs are present, and again can only be seen in the D_e parameter (Fig. 6.3(c)), and not the parallel component of D_e.

Interestingly, there are also other areas in the simulation that have similarly positive values of D_e that are not necessarily located around reconnection sites, particularly around some of the magnetic islands in Panel (a). This, as in Section 4.3.7 strongly suggests the presence of waves at these locations, which could be propagating quasi-perpendicularly to the field. This is also consistent with the suggestion that dissipation is no larger at reconnection sites within turbulence, than elsewhere in the simulation, as mentioned in previous statements about dissipation (Chapter 4).

Finally, it is worth mentioning that the dissipation parameter will have an enhanced value in the presence of large electric fields. Therefore, if a reconnection site has a slow reconnection rate, E_z will be small, and the site will not be highlighted by the D_e parameter, despite it having a magnetic field geometry the resembles magnetic reconnection.

6.2. Simulation 2: In-plane guide field

Camporeale and Burgess [2011] used Parsek2D to study the properties of electron scale turbulence in 2D, but with a guide field set in the in-plane (x) direction. A magnetic perturbation was applied in order to inject energy into the largest 3 wave-modes that the simulation domain would support. As the simulation was allowed to evolve, the magnetic energy relaxed over time to a lower energy state. The results showed that a turbulent energy cascade was formed down to the electron gyro-radius scales. These results are broadly similar to those already discussed in Chapter 4. Several observations were made about electron temperature anisotropies that formed within the simulation, by plotting the VDFs of electrons contained within boxes of varying sizes. The results showed that non-thermal features appeared in the VDFs when the box size was relatively small, and the VDFs were nearly isotropic when larger box sizes were used. The simulation also used a perturbation size of $\delta B/B_0 \approx 3$. The large amplitude was so that magnetic fluctuations could be resolved above the PIC noise floor at small scales.

Several questions remained unanswered whilst reviewing this paper. The first was that of the nature of the observed temperature anisotropy. The initial suggestion was that small scale topological structures were formed, and could be the cause of these anisotropies. Another question, not answered in the original paper, was whether magnetic reconnection was occurring in the simulation. This could be possible in the simulation given the large magnetic perturbation, and may play a role in forming the observed small scale temperature anisotropies.

The simulation data had to be reproduced in order to answer these questions, with the same methodology, and plasma parameters described by Camporeale and Burgess [2011]. First, we confirm that the data resembles that of the original paper, by comparing the newly generated plots of the magnetic power spectra, in 1D and 2D. We will then examine the magnetic topology to look for magnetic reconnection, before looking at the energy budget and the dissipation parameter, D_e, in the following section.

The 1D magnetic power spectra are shown in Fig. 6.4. The initial three modes excited by the perturbation are shown by the green line at $k\rho_e = 0.1$ to 0.3. The spectra calculated at time, $t = 100\Omega_e^{-1}$ are shown in blue for the x (solid line) and y (dashed line) directions. Note that the x direction is the direction of the original guide field. At $t = 100\Omega_e^{-1}$ the x and y spectra are qualitatively similar, with marginally more power in the perpendicular direction than in the parallel one, matching previous observations [Camporeale and Burgess, 2011]. The slopes of the

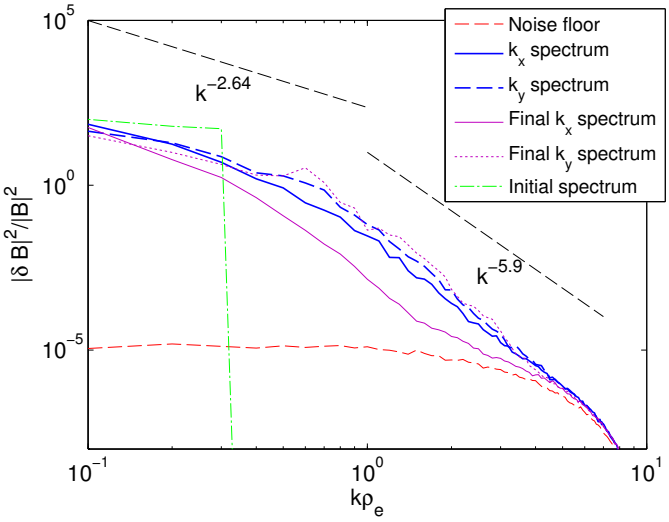

Figure 6.4.: Power spectra of $|\delta B|^2/|B_0|^2$ as functions of k_x (solid lines) and k_y (dashed lines), at $t = 100\Omega_e^{-1}$ (blue) and $t = 200\Omega_e^{-1}$ (purple). The straight lines show the original power law values from Camporeale and Burgess [2011]. The initial perturbation spectrum is shown in green. The red dot dashed line shows the simulation noise floor.

lines are similar and approximately match the original power law values of -2.64 and -5.9. The spectra are not above the noise floor at $k\rho_e \sim 5$, so the fluctuations beyond this point are not meaningful. The purple lines show the spectra plotted at the end of the simulation at $t = 200\Omega_e^{-1}$. The parallel spectra (solid purple) has less power compared to the perpendicular spectrum (dashed purple line) and this is consistent with the development of the magnetic topology, as we will show shortly.

Figure 6.5 shows contours of magnetic power in k space. Initially there is only magnetic power at $k\rho_e = 0.1$ to 0.3 (not shown). At $t = 100\Omega_e^{-1}$ (Panels (a) and (b)) the contours show a slight power anisotropy with more power in the perpendicular direction than in the parallel one, consistent with Fig. 6.4 and Camporeale and Burgess [2011]. Beyond $k\rho_e = 5$ (small scales) the magnetic power drops off rapidly and is nearly isotropic. By $t = 200\Omega_e^{-1}$ (Fig. 6.5(c) and (d)) the power is highly anisotropic with power constrained to large scales with more power in the perpendicular direction, in agreement with the 1D spectra of Fig. 6.4. These results suggest that the simulation has relaxed to a lower energy state. These figures show that the new simulation has successfully recreated the original results of Camporeale and Burgess [2011].

Animations of the simulation data were created, plotting field lines and adding potential reconnection sites using the method described in Section 4.2.2. Figure 6.6(a) shows the initial magnetic perturbation with four reconnection sites. The field lines

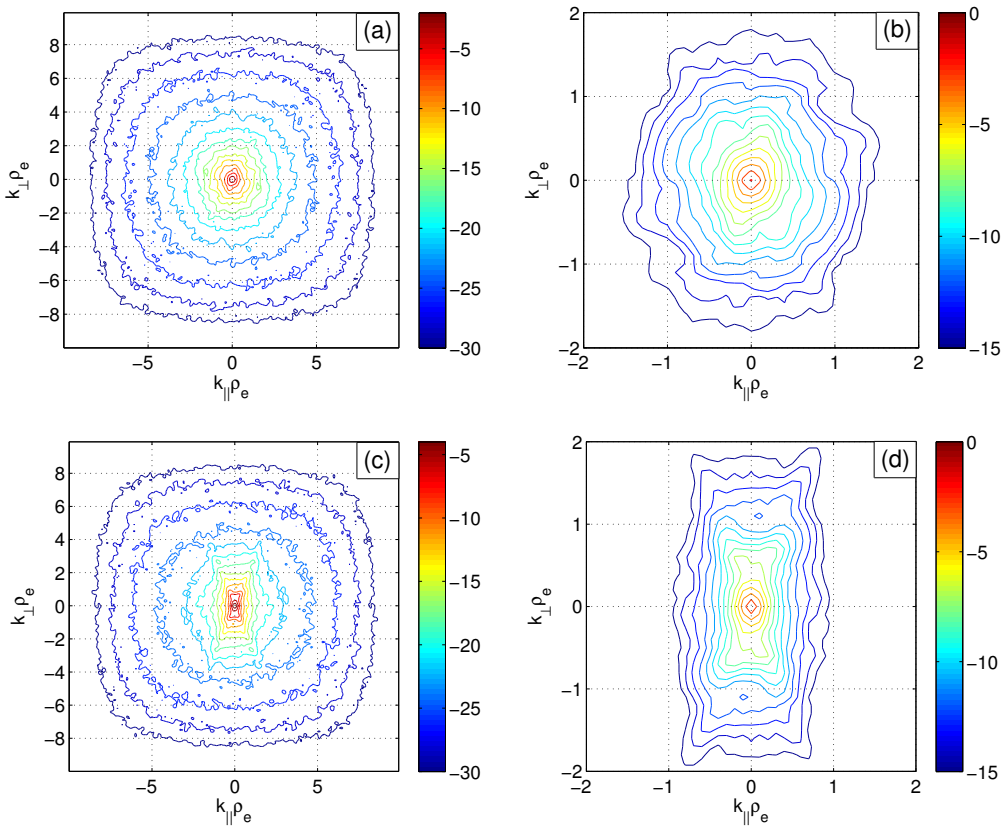

Figure 6.5.: Contour plots of the spectrum of magnetic fluctuations $|\delta B|^2/|B0|^2$ in the parallel and perpendicular directions. (a) $t = 100\Omega_e^{-1}$ and (b) $t = 100\Omega_e^{-1}$ zoomed in. (c) $t = 200\Omega_e^{-1}$ and (d) $t = 200\Omega_e^{-1}$ zoomed in.

flex and move, with reconnection occurring as they do so. Two reconnection sites exist for the majority of the simulation as shown in Fig. 6.6(b). These have the appearance of magnetic peninsulas, encompassing small magnetic islands, with reconnection occurring in both directions as the field fluctuates. Eventually the field relaxes so B_x is dominant (Fig. 6.6(c)). The total magnetic field strength is also shown in Fig. 6.6(c) as the background colour. In the x direction, the magnetic field appears to contain a transverse wave with a wavelength approximately equal to the length of the box. The y direction appears to show smaller wavelength fluctuations, of $\sim 400\lambda_D$ wavelength, which is ~ 20 cells or $k\rho_e \sim 1$. This is consistent with the flattened 2D FFT shown in Fig. 6.5(d), which shows there is still more power in the perpendicular direction at $k\rho_e > 1$. This topology is also consistent with Fig. 6.4 where the k_x spectrum has less power than the k_y spectrum.

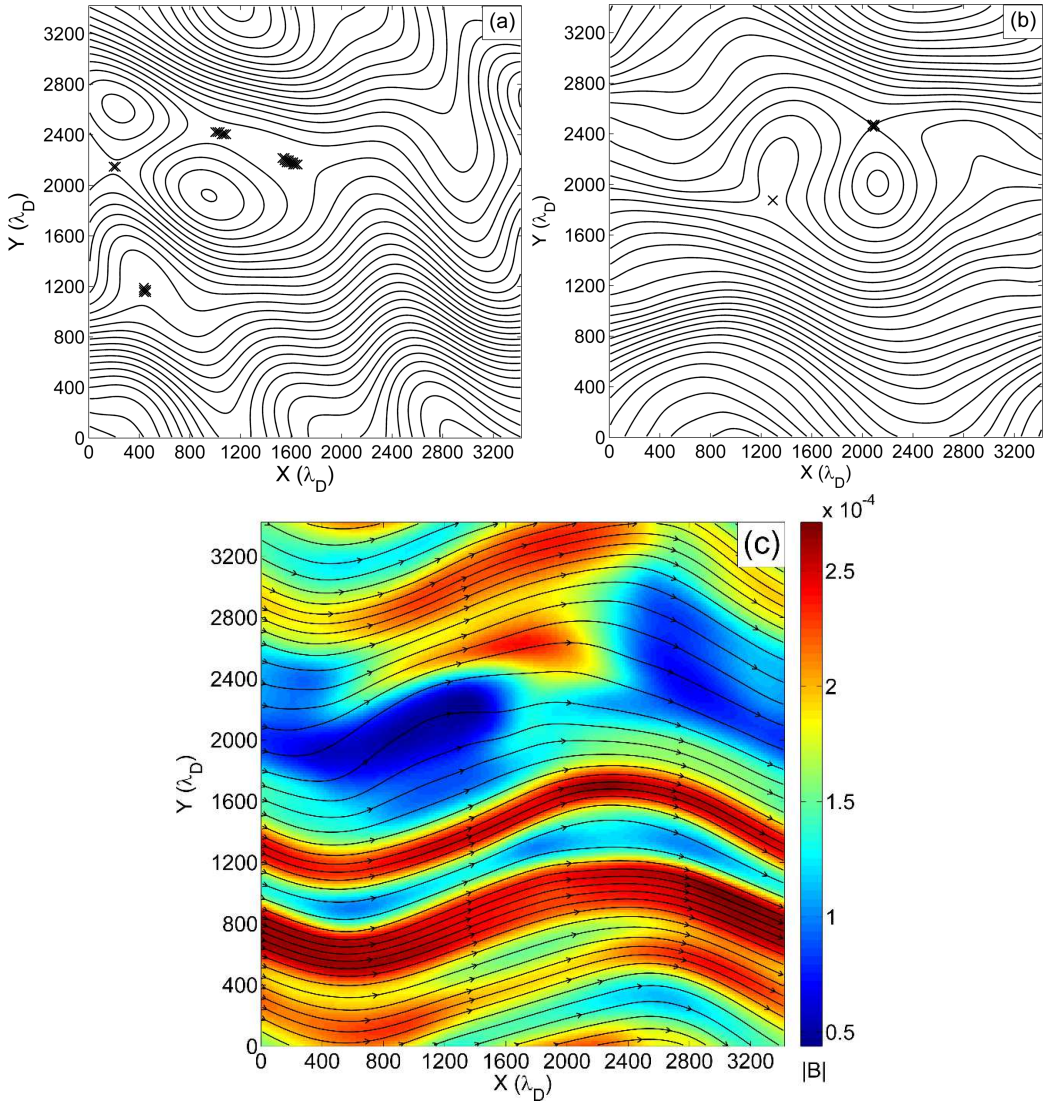

Figure 6.6.: Initial, intermediate and final magnetic field line configurations at (a) $t = 0$, (b) $t = 70\Omega_e^{-1}$, (c) $t = 200\Omega_e^{-1}$. Background colour in (c) is $|\mathbf{B}|$. Lengths in units of λ_D. Potential reconnection sites are marked by black crosses.

6.2.1. Energy budget

Figure 6.7 shows time-series for electron kinetic energy, proton kinetic energy, magnetic energy and electric energy. The initial magnetic energy, introduced by the perturbation reduces over time, consistent with the field relaxing. The electric field energy jumps from zero soon after the start of the simulation and falls steadily. Both electrons and ion start at the same total energy, and gain kinetic energy over time.

The average temperature of the electrons and ions are shown in Fig. 6.8. It confirms that both species gain energy with more thermal energy being deposited

into the electrons.

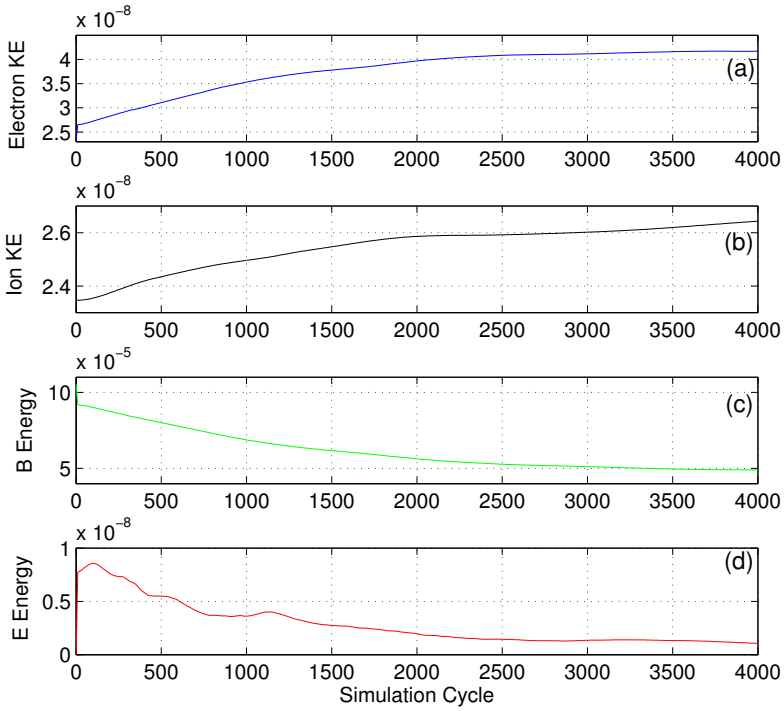

Figure 6.7.: Timeseries of (a) electron kinetic energy, (b) ion kinetic energy, (c) magnetic energy and (d) electric energy.

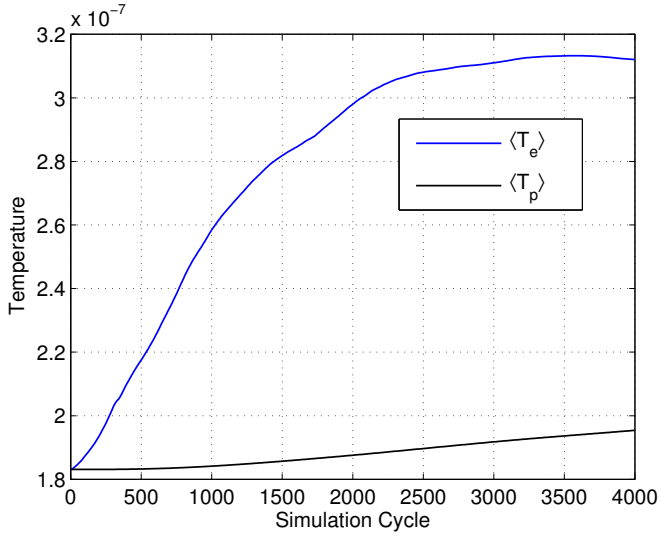

Figure 6.8.: Timeseries of average electron temperature, $\langle T_e \rangle$, and average ion temperature, $\langle T_p \rangle$.

6.2.2. Dissipation parameter

Figure 6.9 shows the dissipation parameter, D_e at $t = 31\Omega_e^{-1}$. The two reconnection sites are clearly visible, and highlighted by the circles labelled A and B. Both reconnection sites show positive values (indicating dissipation) whilst they are in the process of reconnecting. Notice, as in the previous simulation, the positive values of D_e in Fig. 6.9 are not limited to the reconnection zones, but are dispersed throughout the box.

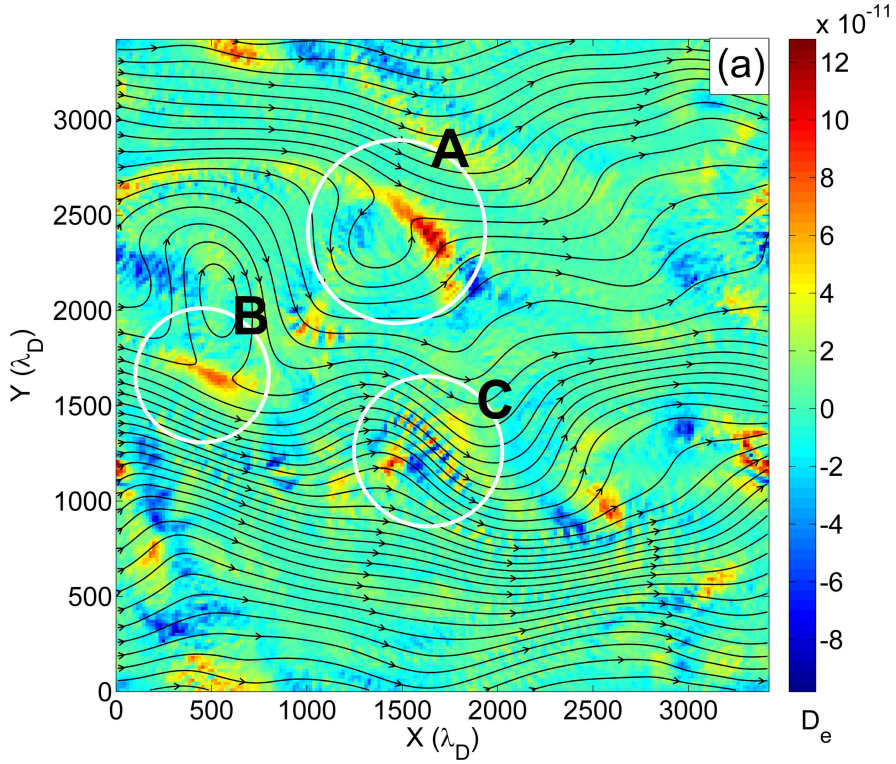

Figure 6.9.: (a) Dissipation parameter, D_e, at $t = 31\Omega_e^{-1}$. Magnetic field lines are shown in black. Highlighted areas are discussed in the text.

What is not obvious in screenshots are the number of visible parallel propagating wave packets present in this simulation. These waves have a small wavelength, and are highly localised. One of these wave packets is visible in Fig. 6.9, highlighted by the circle labelled C, in the positive and negative bands in the value of D_e. Approximately 8 wavelengths are visible. This particular wave is propagating to the right along the magnetic field lines. Another wave is also visible between the three white circles in Fig. 6.3.

These waves, are also easily identifiable using the parameter $|\mathbf{E} + \mathbf{V_e} \times \mathbf{B}|$, in which they appear as positive values. In ideal MHD, this parameter should be zero. Therefore a non-zero number, indicates that some kind of kinetic effect is at work.

There are far too many kinetic signatures/waves to examine all of them, therefore we focus on one strong wave signature in the dissipation parameter, D_e, and examine this wave in detail.

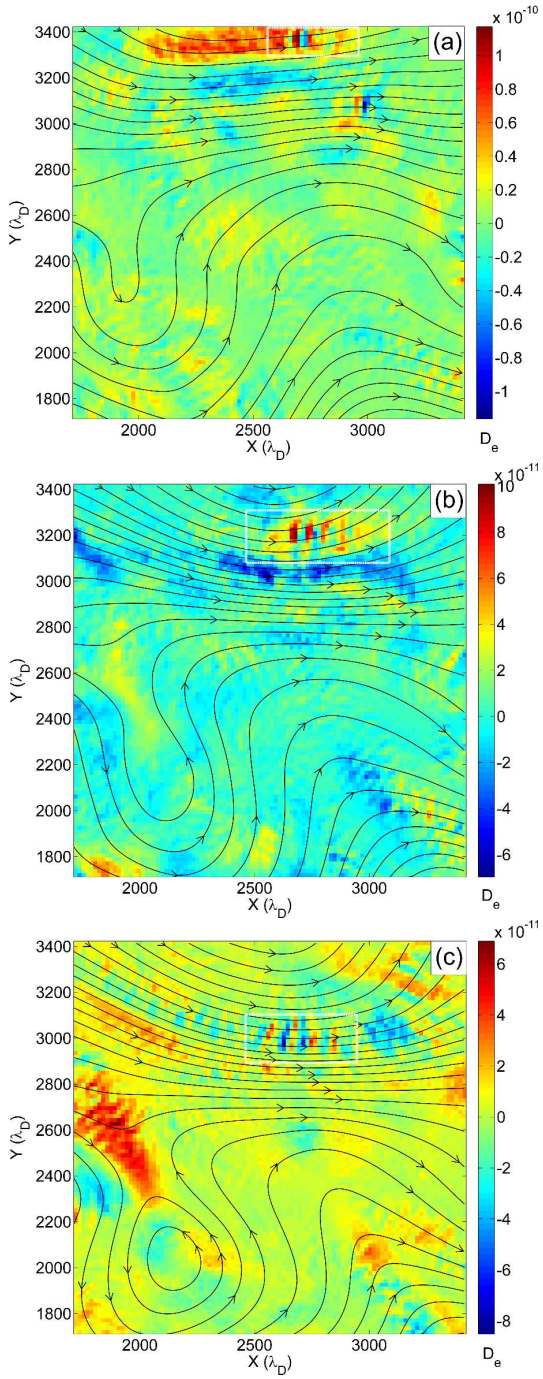

Figure 6.10.: Magnetic field lines (black) and the parameter, D_e, at time (a) $t = 44\Omega_e^{-1}$, (b) $t = 52\Omega_e^{-1}$, and (c) $t = 62\Omega_e^{-1}$.

6.2.3. Wave analysis

Figure 6.10 shows, D_e for the top right hand corner of the simulation at $t = 44\Omega_e^{-1}$, $t = 52\Omega_e^{-1}$ and $t = 62\Omega_e^{-1}$. In all three panels the white box highlights the location of a parallel propagating wave.

Animations of D_e reveal that this wave appears at $\sim$ cycle 800 in the lower half of the simulation box, but the field line it is propagating on is also moving in the negative y-direction. The wave wraps around due to the periodic boundaries of the simulation, and in Fig. 6.10(a) is now at the top of the box, with the field line still moving down. Between Panels (a) and (b) the wave has moved down (due to the field line movement) and also propagates in the positive x-direction. More careful analysis revealed that the highlighted wave in Panel (c) is actually a second wave packet, that propagates from right to left.

Another feature highlighted in these three panels is the reconnection site on the left hand side. This is in the process of reconnecting in Panel (b) and (c) but not in Panel (a). The value of D_e also only positive in the reconnection region in Panel (b) and (c). This shows that the dissipation parameter, D_e, will only indicate a positive value if the site is active and is in the process of reconnecting.

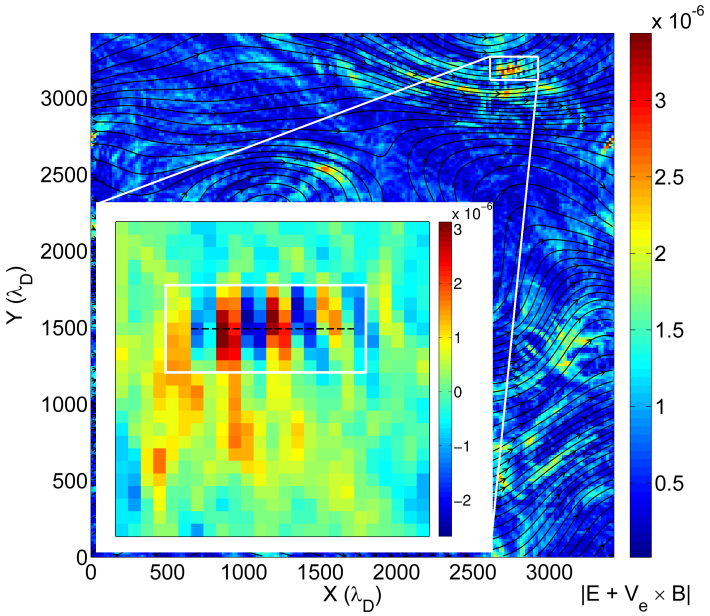

Figure 6.11.: Magnetic field lines (black) and the parameter $|\mathbf{E} + \mathbf{V_e} \times \mathbf{B}|$ at $t = 52\Omega_e^{-1}$ for the full simulation domain. The wave discussed in the text is marked by a white box. The inset shows $E_{\|}$ in the locality of the wave. The white box in the inset shows the area of strong local wave activity. The dashed line (black) shows the cells where electron VDFs will be calculated.

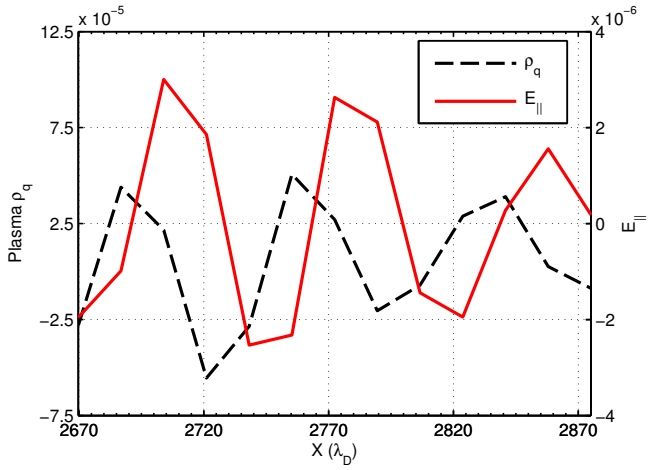

Figure 6.12.: $E_\parallel$ and plasma charge density, ρ_q from the dashed line (black) indicated in the inset of Fig. 6.11.

Figure 6.11 plots the parameter, $|\mathbf{E} + \mathbf{V_e} \times \mathbf{B}|$ throughout the whole simulation domain at time $t = 52\Omega_e^{-1}$. The same wave as in Fig. 6.10(b) is highlighted by a white rectangle. The inset of Fig. 6.11 shows a graph of $E_\parallel$ within the white rectangle. An oscillating pattern of positive and negative $E_\parallel$ is clearly visible, again outlined by a white box in the inset. The dotted line (black) in the inset of Fig. 6.11 shows the cells we will use to analyse the wave. First, we use these cells to plot a cross section of $E_\parallel$ and charge density ρ_q, as shown in Fig. 6.12.

Figure 6.12 shows approximately three wavelengths of a wave, with $E_\parallel$ plotted as a solid line (red), and charge density, ρ_q in dashed line (black). The gradient of $E_\parallel$ is proportional to the charge density in the region, consistent with Gauss's law. The amplitude of the wave appears to be decreasing in the x-direction. Although not plotted, the magnetic field in this region is slowly changing, but does not show any variation consistent with the waveform of $E_\parallel$ or ρ_q indicating that this wave is electrostatic. While the in-plane magnetic field components remains roughly constant, there is a slowly increasing B_z, such that the angle of $\mathbf{B}$ to the simulation plane varies along this wave from 20° on the left edge to 0° on the right.

We now characterize the phase speed of the wave in the x-direction only as this is the dominant direction of propagation. We calculate a mean $E_\parallel$ over 25 cells in the y-direction, plotting the result spatially in x. We then repeat this for the same cells in time. The resulting time-space diagram is shown in Fig. 6.13 and shows the phase fronts of the wave as it moves. The positive slopes indicate the wave propagates in the positive x-direction, in agreement with animations of $E_\parallel$ and the dissipation parameter. The two black lines in Fig. 6.13 show that the phase speed is constant.

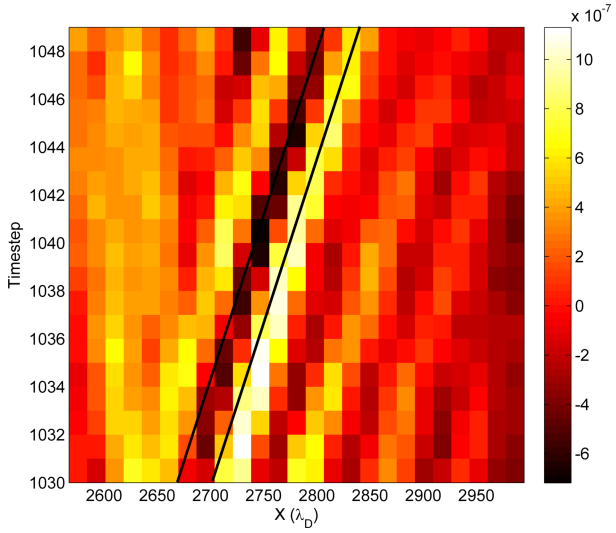

Figure 6.13.: $E_{\parallel}$ averaged over 25 cells in the y-direction in the vicinity of the wave identified in Fig. 6.11, showing propagation direction and phase speed of $0.044c$.

The wave travels ~ 7.5 cells in 19 timesteps, resulting in a phase speed of $0.044c$ (where c is the speed of light) in the x-direction. Figure 6.13 also shows the localized nature of the wave, as its amplitude is largest over a couple of wavelengths in the x direction, and the phase fronts fade in time as it propagates.

We now examine the electron velocity distribution function (VDF) in the area local to the wave. The electron VDF plotted in Fig. 6.14 uses the electrons from the same cells used to generate the cross section in Fig. 6.12. The VDF has been normalized to 1, with a higher density of electrons indicated by dark red contours, and blue contours indicating low density. The arrow (black) indicates the average in-plane magnetic field in the cells. The cross (black) indicates the electron bulk velocity. All velocities have been normalized to the speed of light, c.

Figure 6.14 shows that the electrons are almost gyrotropic, as shown by the symmetry on either side of the magnetic field. The bulk drift of the electrons is in the negative y direction (down) matching animations of the field line motion. The shape of the distribution indicates a main population of electrons with a perpendicular anisotropy (assuming the field is mainly in the x direction.) There is a beam travelling in the anti-parallel direction. In the parallel direction, there is a plateau. This strongly hints that there is a wave acting in this area. Note that the observed wave has a phase speed of $0.044c$ which is in the centre of the plateau in Fig. 6.14.

The solid line (blue) in Fig. 6.15 shows a 1D cross section of the VDF from Fig. 6.14. This cross section was calculated by taking the maximum value of the

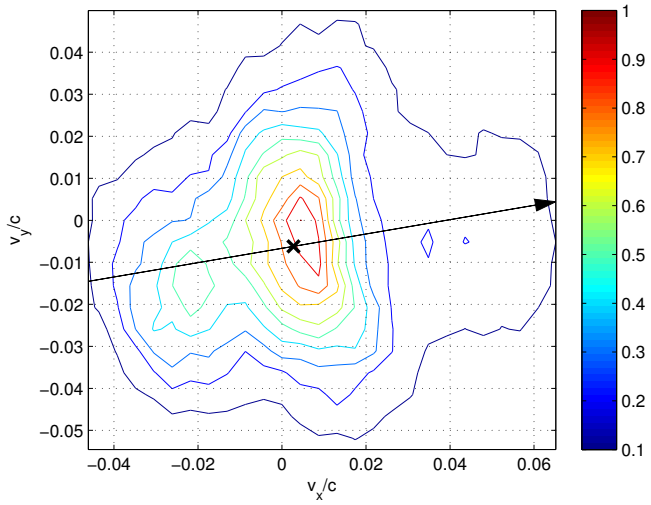

Figure 6.14.: Electron velocity distribution function (VDF) for v_x and v_y for the a group of cells indicated by the dashed line (black) in Fig. 6.11. The black arrow indicates the average magnetic field direction. The black cross indicates electron bulk drift. All velocities normalized to c.

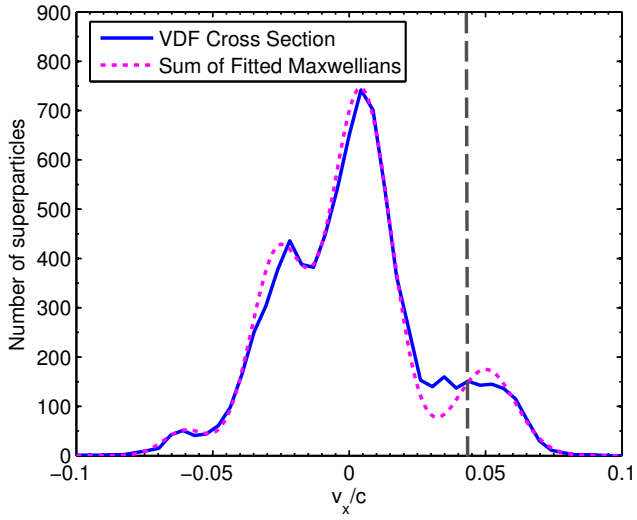

Figure 6.15.: Cross section of the electron VDF (blue) shown in Fig.6.14, taken along the x-direction. Sum of fitted Maxwellian distributions (magenta). Grey line is phase speed of the observed wave at $0.044c$.

2D VDF along the y direction, so by symmetry will be approximately equal to the VDF along the in-plane field. The dashed line (magenta) shows a sum of four Maxwellian distributions fitted to match this line and will be discussed later. The vertical dashed line (grey) indicates the phase speed of the observed wave at $0.044c$ (refer to Fig. 6.13).

Figure 6.15 demonstrates how the wave could have formed, assuming that an

electron beam was initially located to the right of the vertical dashed line, as indicated by the magenta distribution. Electrons slightly faster than the wave phase speed (to the right of the dashed vertical line) must give up some energy to the wave, while electrons slightly slower than the phase speed, must take energy from the wave. This interaction would occur if there was a positive slope in the electron distribution function (as shown by the magenta dashed line in Fig. 6.15) and would result in a flattened distribution as the wave is generated.

1D Kempo simulation

To confirm if this wave formed through parallel beam interactions, we decided to simplify the problem, by using a 1-dimensional code, Kempo1 [Omura, 2007]. The code is an electromagnetic particle in cell code that can be run in Matlab. A simulation was set-up, using the VDF in Fig. 6.15, assuming that the magnetic field is directed in the x direction. This is not strictly identical to the conditions seen in the Parsek2D simulation as the magnetic field in the location of the wave varied in angle to the x axis from 0° to 20°, but it is a reasonable assumption to simplify the simulation parameters. The density in the region was approximately that of

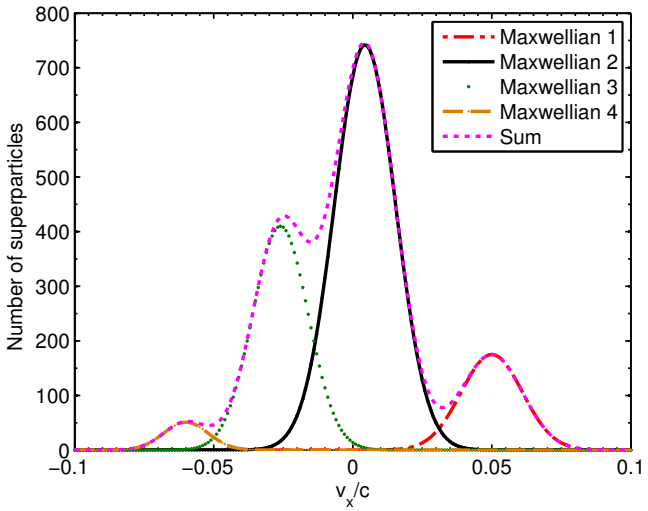

Figure 6.16.: Four Maxwellians used to create a fit to the VDF cross section (Fig. 6.15) and used as the initial conditions in the 1D Kempo1 simulation.

the starting conditions, 10 particles cm^{-3}. The average magnetic field strength for the cells containing the wave was 4.3×10^{-4} G. Kempo1 uses Gaussian CGS units and we chose the following normalizations: Velocities are normalized to the speed of light, time is normalized to $10\omega_{pe}^{-1}$, and charge per unit mass is normalized to the proton charge per unit mass. The simulation assumes a charge neutralising

background of ions is always present, and therefore only has electrons as species inputs. The electrons were modelled as four separate species, matching the velocity distributions of the four Maxwellians shown in Fig. 6.16.

Parameter	Maxwellian 1	Maxwellian 2	Maxwellian 3	Maxwellian 4
N_{Max}	175	742	410	51
v_D	0.05	0.0044	-0.026	-0.06
v_{th}	0.011	0.011	0.01	0.008
Density Ratio	0.1319	0.5592	0.2809	0.028
$\Delta x/\lambda_D$	0.53	1.09	0.85	0.34

Table 6.1.: Electron species distribution information. (Refer to Fig. 6.16.)

The properties of these Maxwellian distributions are shown in Table 6.1. This shows for each species, the maximum number of superparticles (in Parsek2D), N_{max}, the central location of the distribution, or drift velocity, v_D, its thermal velocity, v_{th} and its density ratio. This is the proportion of electrons that the species should contain compared to the total number of electrons. This is calculated by integrating each distribution, and dividing by their sum. As previously shown, the sum of these distributions combine to approximately match the VDF seen in the x direction in Parsek2D (Fig. 6.15), except for a beam included on the right hand side. This was chosen to have a shape that matched the outer edges of the Parsek2D distribution, and a height that (in theory) could form the observed wave at the correct phase speed. The length of the simulation was the equivalent to 13 Parsek2D cells/$200\lambda_D$, the same as the cross section shown in Fig. 6.12. The timestep and cell size of the simulation in Kempo1 was chosen in order to meet the Courant condition. This results in very small cell sizes and timesteps, such that the simulation was run for 10000 cycles which is the equivalent of $\sim$50 cycles in Parsek2D, and contained 180 cells. (This demonstrates the amount of time saving that can be achieved from the implicit algorithm used in Parsek2D.) The final check was that the cell size (Δx) was less than $2\lambda_D$ as specified in the Kempo1 instruction manual [Omura, 2007]. Using the original number density of 10 particles cm^{-3}, and the standard deviation of the combined distribution (which was ~ 0.027) $\Delta x/\lambda_D = 0.6$. As an additional check, since each electron species has a separate λ_D associated with it, we chose a cell size to make sure they all met this requirement (see Table 6.1).

Figures 6.17 and 6.18 show the results of the Kempo1 simulation. Figure 6.17 shows the electron v_x VDF at the end of the simulation (green), compared to the Parsek2D VDF cross section (blue). This shows a very good agreement. Crucially, the beam introduced on the right hand side has formed a flat plateau in the location

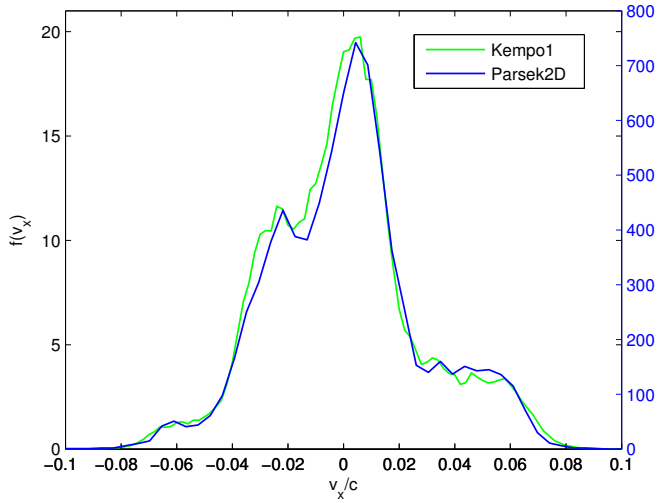

Figure 6.17.: Final electron VDF from the Kempo1 simulation (green) compared to the Parsek2D VDF cross section (blue).

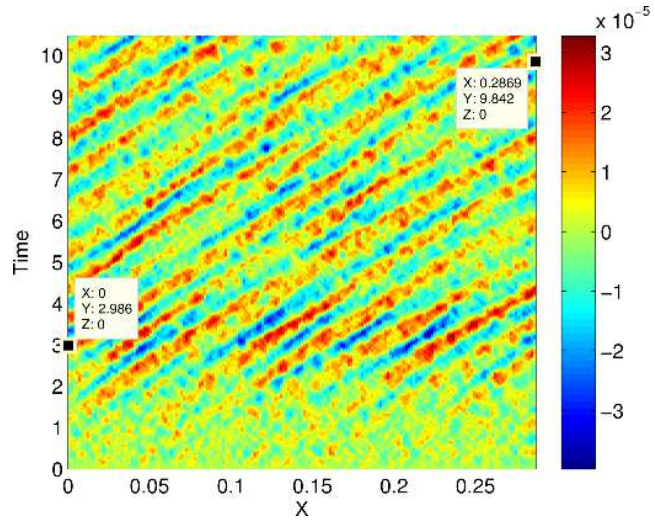

Figure 6.18.: E_x space-time diagram from Kempo1, showing phase fronts of an electro-static wave.

of $v_x/c = 0.04$. Figure 6.18 shows a space time diagram of E_x (parallel electric field) from the Kempo1 simulation. This clearly shows that waves with an E_x component have been produced in the simulation, which propagate in the positive x-direction. No corresponding fluctuations are seen in E_y, E_z or in the magnetic field, indicating that it is electrostatic. Using the two points shown, the wave phase can be calculated as $v_{ph} = 0.2869/(9.842 - 2.986) = 0.042$. This is also in good agreement with the observed wave phase of 0.044 seen in Parsek2D (Fig. 6.13). The only discrepancy is the wavelength of the Kempo1 wave. There appears to be ~ 7 wavelengths in the same space where the Parsek2D simulation had approximately

3 wavelengths (Fig. 6.12). This factor of 2 could be associated with the resolution of Parsek2D. Perhaps a higher resolution Parsek2D simulation could resolve the smaller wavelength, and could be investigated in the future.

To identify this wave mode we refer to Gary [1993], Chapter 3, Eq. 3.2.8a and Eq. 3.2.8b. This chapter describes electrostatic component/component instabilities in uniform plasmas, which is what we have observed here between electrons. These two equations describe how to differentiate between the Langmuir beam instability and the electron-electron beam instability. In both instabilities a wave is generated from a Maxwellian electron core and a weaker electron beam, and the instability can be identified using the threshold:

$$LB = (v_{Db}/v_{thb})^3(n_b/n_e), \tag{6.6}$$

where v_{Db} is the drift velocity of the beam distribution (assuming beam and core are current cancelling). v_{thb} is the thermal velocity of the beam distribution. n_b and n_e are the beam and total electron number density respectively. If the threshold $LB \geq 1$ then the plasma is unstable to the electron-electron beam instability. If $LB < 1$ then the plasma is unstable to the Langmuir beam instability. Both instabilities are kinetic, and rely on a positive slope in the distribution function at the phase speed of the wave, however the Langmuir instability describes the mode generated for low drift speeds and/or low beam densities. In order to apply this equation to our results, we have to chose the two Maxwellian distributions involved in the wave generation. In our case, Maxwellian 1 is the beam distribution and Maxwellian 2 is the electron core (see Fig. 6.16 and Table 6.1). We then calculate the location where these two electron distributions would be current cancelling, given a charge cancelling ion background. This is done by using the values of v_D and density ratios in Table 6.1 like moments. In doing so, the location of the new zero current axis should be $0.013c$ and the beam offset, $v_{Db} = 0.037$, relative to the zero current axis. We use the density ratios in place of number density, and assume n_e is the sum of the density ratios from Maxwellian 1 and Maxwellian 2. Substituting these values into Eq. 6.6 gives $LB = 7.2$, indicating that plasma is unstable to the electron-electron beam instability.

In doing this analysis we have assumed that only the parallel beam plays a role in the instability, which is reasonable given the confirmed phase of the wave in relation to the VDF. We have also run a simplified Kempo1 simulation with just these two Maxwellians in current cancelling locations, and get very similar results to Fig. 6.17, i.e. the formation of a plateau on the right hand side of the VDF, and the same

phase fronts as seen in Fig. 6.18.

In summary, this work proves that the wave identified in Fig. 6.10(b) and Figs. 6.11 and 6.12 was formed via the electron-electron beam instability. This strongly implies that the fluctuating magnetic field created a parallel electric field in order to create the beam, which then generated this wave when it meets plasma with the necessary electron VDF for instability. Given the similarity of the other parallel propagating waves seen in the simulation animations (e.g. Fig. 6.9) this would seem to be a common method of wave generation within large amplitude turbulence.

6.3. Conclusions/Discussion

In this chapter we have attempted to address the question: "what is dissipation in a collisionless plasma?" We have done this by using the frame shifted (electron frame) dissipation parameter, D_e on two different simulations. This parameter effectively shows the work done by the electric field on the plasma. We argue that D_e is only a good indicator of dissipation when it is positive, and the particles have gained energy from the electric field.

In Section 6.1, in the simulation with a guide field in the z-direction, the reconnection sites are associated with positive values of D_e only when they are reconnecting, which makes sense, as reconnection is the conversion of magnetic energy to plasma kinetic energy. Reconnection sites are highlighted/isolated in positive values of $D_{e\parallel}$. D_e also highlights many other areas in the simulation where an electric field is at work. Comparing D_e and $D_{e\parallel}$ can help understand which direction the dissipation is occurring. The EVMHs discussed in Chapter 5 only appear via the D_e and not the $D_{e\parallel}$ parameter indicating that there is some interaction between the electric field and electrons in a non-parallel, perhaps perpendicular direction. D_e is both positive and negative within the EVMHs, suggesting that no net dissipation (positive work) occurs in them, consistent with the electrons being trapped by the magnetic field geometry, rather than being accelerated/trapped by an electric field.

In Section 6.2, the simulation has an in-plane guide field, and the data shows that reconnection sites are also regions of dissipation (when reconnection is occurring). Furthermore, the D_e parameter also revealed many parallel propagating waves in the box. Analysis of one of these waves indicates that it was generated by an electron-electron beam instability. These waves were not seen in the simulation discussed earlier in Chapter 4 as that simulation, on average, did not support waves in the parallel direction. It did, however, produce large parallel electron temperature

anisotropies, especially around reconnection sites. Combining the results from these two simulations, we can begin to build a picture of the process of dissipation that occurs in a fully 3D collisionless plasma.

Reconnection can produce parallel anisotropies (refer to Figs. 4.19 and 4.20). These multi-peaked distributions look very similar to the ones that generated the electron-electron beam mode in Fig. 6.15. If the reconnection rate is fast enough, the reconnection site will shift the electrons VDF in a particular direction, and when those electrons travel and mix with other groups of electrons, a beam instability may be generated. An electrostatic wave will travel parallel to the magnetic field. This beam will then be damped as it reaches plasma with properties that no longer support it. It is likely that in a fully 3D simulation this process would occur so quickly that the stages of the waves creation may not be observed. So waves will act as a method of moving energy around in space as well as reducing the temperature anisotropy introduced by the reconnection sites.

The dissipation parameter, corresponds to the rate of work done by the electric field (per unit volume), or $\mathbf{J}.\mathbf{E}$, but masks the nature of the dissipation, which is contained more fully in the velocity distribution functions of the species. At the smallest scales, in the presence of an electric field, an individual ion and electron are accelerated in opposite directions, and a magnetic field only changes a particles direction, doing no work. Once a particle has been accelerated, it travels to a new location with potentially different plasma parameters, and then it is the collective distribution of the particles that forms waves through instabilities.

Dissipation at kinetic scales, is a multi-staged process, that begins with the generation of an electric field, and the redistribution of kinetic energy, via non-Maxwellian features in VDFs and instabilities. We argue that this is why it is difficult to formulate a single definition of plasma dissipation. In a collisionless plasma, there are many instabilities associated with non-Maxwellian distribution functions, and they all redistribute energy back to the plasma. There are three main types of energy: kinetic energy (ions and electrons), magnetic energy, and electric energy. Like any physical system, a plasma always tries to reach an equilibrium. Dissipation is then conversion of energy into a stable equilibrium, and should be non reversible.

In a collisional plasma the non-reversibility is provided by collisions, which provides a source of randomness, and therefore the entropy (defined as the natural logarithm of the number of microscopic states that can be mapped onto the macroscopic state of a system) increases. In a collisionless plasma, this mechanism is removed, and additionally, the collisionless Vlasov equation conserves entropy (Bellan [2006, p. 474]). In order to provide this non reversibility we must introduce the

concept of mixing. This concept breaks the natural assumption of classical thermodynamics, where the system is comprised only of macroscopic physical objects. At kinetic scales, it is the microscopic states of the system, (waves, particles) described by VDFs that define the plasma behaviour.

We therefore suggest there are four distinct stages to dissipation at electrons scales: 1) Acceleration, via localised kinetic scale electric fields (e.g. reconnection or another localised phenomena) forms a bump/beam in the local VDF. These accelerated electrons then travel and mix with other groups of electrons into areas where their combined presence can cause an instability. 2) Wave generation: The particle kinetic energy is converted to the wave electromagnetic (or electric) field. 3) Wave propagation: The generated wave will travel in space, the direction and distance will be determined by the local magnetic field and the plasma properties, which all vary within turbulence. 4) Damping: The wave will be damped when it reaches an area with a VDF, or plasma properties that no longer support it. Energy from the wave will be given back to local particles, which raises local average kinetic energy.

This final stage is often wrongly associated with temperature increases. On a macroscopic scale where enough of these events happen randomly, then the distribution may look Maxwellian. However, locally, on kinetic scales, dissipation could be a spreading, levelling, or flattening of the plasma VDFs, so not just a general widening of the Maxwellian distribution, that is associated with the concept of increasing temperature.

For an individual wave-particle interaction, the process is reversible. However, the addition of mixing, and the interaction between an ensemble of waves in the system adds a degree of randomisation, and therefore irreversibility, especially when we consider that turbulence is inherently associated with stochastic properties of the plasma. The wave propagation direction ensures that the energy is carried away from the location of the instability that caused it, it will mix with the plasma, and the final location of the wave is at a location in the plasma that results in damping, wave destruction, and the conversion of wave energy to kinetic energy, so it is unlikely that the same wave could be re-created at this "final" location, such that a wave could propagate back to where it came from, and reverse the process. Here we have only focussed on electron dynamics, and this is only a simplified description of what is naturally an extremely complex process, with larger scale structures being dominated by ion dynamics.

7. Conclusions and further work

In this thesis we have explored the nature of electron scale turbulence using 2D particle in cell simulations. In Chapter 4 we examined how magnetic power is transferred to small scales in a simulation of decaying magnetic fluctuations. A fluctuation power spectrum with approximately power law form quickly evolves, and remained relatively time steady over the period simulated. The spectra extends to small scales of order the electron gyroradius, indicating the generation of a turbulent cascade.

Animations of the magnetic field evolution show that X-points (i.e., potential reconnection sites) evolve dynamically, responding to the motion of surrounding magnetic islands in the turbulence. The regions around X-points have signatures which indicate that magnetic reconnection is occurring, with the motion of field lines and the pattern of electron bulk drifts consistent with reconnection inflows and outflows, and an asymmetric quadrupolar signature in B_z, similar to that found in Hall reconnection due to the decoupled electron and ion motion.

Applying the eigenvector analysis of Servidio et al. [2010] revealed that the shape of the electron diffusion region is similar to the ratios seen in MHD asymmetric Sweet Parker reconnection. Similar to the asymmetric model of Cassak and Shay [2007] reconnection sites appear to have electron flow stagnation points offset towards the lower value of density divided by reconnecting field strength, or $-\rho_{qe}/|B(x,y)|$.

Animations of the evolution of the electron temperature anisotropy ratio $T_{e\parallel}/T_{e\perp}$ indicate the dynamic appearance of regions of enhanced parallel anisotropy in reconnection outflow regions at some X-points, during periods of strong reconnection, and these correspond to multi-peaked electron VDFs.

We tracked electrons from the VDF peaks and found that electrons are accelerated by the reconnection electric field E_z, in the direction of the guide field. Acceleration can therefore occur in both positive and negative z directions depending on the sense of reconnection at a particular X-point. We then described a new mechanism of temperature anisotropy generation, involving multiple X-points with opposite senses of reconnection (see Fig. 4.30). These accelerate electrons, double peaked distributions are seen. In this model the reconnection sites act as both acceleration

regions and mixing zones.

In a fully 3D simulation we suggest that these multi-peaked distributions would produce additional waves via beam or anisotropy instabilities, which is supported by the additional simulation performed in Chapter 6. This simulation had an in-plane guide field, and therefore supports parallel propagating waves. In this scenario we see that these parallel "bumps" in velocity distribution function often lead to electron-electron beam instabilities and the generation of wave packets. This would lead to the reduction of the anisotropy and the redistribution of energy throughout the plasma.

Turbulence plays an active role in increasing electron parallel temperature anisotropy. This has implications for the study of the evolution of solar wind parameters. These parameters should be constrained by kinetic linear instability thresholds, which limit temperature anisotropy in response to Coulomb collisions, and the expansion of the solar wind. We suggest that reconnection can be another driver of electron temperature anisotropy, in localised areas of the turbulence.

The fluctuations contributing to the power spectrum, in the range $k > 1$ were isolated using a FFT technique in Section 4.3.7. This showed that the fluctuations appear aligned with the local magnetic field lines, and bear a striking resemblance to the KAW simulation data shown in Fig. 2.20. This, given with the lack of a parallel spatial direction to allow parallel propagating whistler waves suggests that these are kinetic Alfvén waves. A correlation analysis showed that electron density and magnetic field strength had a negative correlation. With the strongest correlation occurring with electron density 500 cycles ($25\Omega_e^{-1}$) behind the magnetic field. Further investigation is required to understand this effect, but the lower mass ratio run indicates the electron density fluctuations could be related to the speed of the ion movement.

In future work, we would like to formally identify the fluctuations revealed by the FFT filtering technique, possibly by attempting to simulate KAWs or whistler waves in a similar plasma parameter space, and comparing the results. We would also like to simulate a much larger simulation domain, to include more of the ion scale phenomenon. This can be done using non realistic mass ratio, as we have already shown this produces similar results (Fig. 4.29), and should show the coupling of effects at ion and electron scales, and will reveal more information about the shape and location of the electron scale breakpoint.

In Chapter 5 we analyzed one of two nonlinear coherent structures that spontaneously formed during the simulations of sub-proton scale turbulence. The structures appear to be new to plasma literature. They are circular, and have a depletion

in **B** in the guide field direction, and contain a population of hot electrons, with a characteristic ring shaped current density. These "magnetic holes" are $\sim 300\lambda_D$ or $\sim 5.66\rho_e$ in radius. The current density is entirely formed by azimuthal mean electron flow, and thus we call them electron vortex magnetic holes (EVMHs). The holes we observe have a high perpendicular temperature anisotropy within them, and a central density increase of $\sim 10\%$. There is a dip in total pressure, P_t in the region, resulting in increased values of β within the hole. Magnetic pressure is seen to dip below both the ion and electron pressure. Off diagonal terms of the pressure tensor are non-zero, and non-symmetric, and the pressure tensor rotated into the parallel and perpendicular directions shows non-gyrotropic behaviour.

Particle VDFs show a Maxwellian-like part of the distribution and an additional population of high $V_\perp$ current carrying electrons, forming a plateau and extended tail in the distribution function. Tracking particles confirms that these electrons are trapped within the hole, and trajectory plots show that they follow petal shaped orbits. These orbits are the result of the reduced B_z field in the region, and are similar to orbits produced by electrons drifting in a magnetic field gradient, where the field gradient here is circularly symmetric.

We showed that the EVMHs contribute to the intermittency of the simulations are high values of PVI were located at the locations of the two MHs in the simulation, and reduced values of ΔS changes the PDF of partial variance of increment (PVI) values from a Gaussian shape, to one with extended tails.

Test particle simulations were used to demonstrate the different types of trapped trajectories that are possible within a static, circular sinusoidal depletion in magnetic field. Assuming an ensemble of test particles form a Maxwellian velocity distribution at some temperature we showed that these collectively form a ring shaped current within the MH. The ring shaped current has a diamagnetic effect, and can induce a similarly shaped magnetic field to the initial drop in B_z. We also found that particles with 90° pitch angles are most likely to be trapped within these structures.

We then showed that we can seed a stable EVMH in a self consistent PIC simulation with a "quiet" plasma background, using a perturbation consisting of a circular drop in B_z and increase in perpendicular electron temperature anisotropy within the hole. These results show that these structures are quasi-stable, at least on sub-proton timescales, so that an EVMH can exist without the presence of turbulence.

We also showed that these simulated EVMHs are consistent with the scale sizes and electron properties of the population of linear MHs surveyed in the Earth's plasma sheet by the Cluster and TC-1 spacecraft [Sun et al., 2012]. We suggest that the EVMHs described in this chapter provide a theoretical description for the sub-

proton scale MHs seen in the plasma sheet that have an increased electron energy flux at 90° pitch angles.

In future work, we would like to see if these features spontaneously appear in turbulence simulations with larger box sizes, and determine what governs the size of the EVMH. We would also like to run simulations with different plasma parameters, such as beta, to try and characterise the type of plasmas the EVMHs "prefer" to exist in. We will also experiment with the "toy" model, using different initial hole perturbations, and characterise the electron trapping statistics using the test particle code. We expect to see that smaller holes are more selective, and have a 'preferred" energy range when trapping electrons, and higher energy electron are not trapped. This theory will make an interesting investigation. We would also like to answer the question, can these structure exist over ion timescales or will ion dynamics destroy them? One final interesting thought would be if the equivalent ion "bump" could exist, which requires further analysis.

In Chapter 6 we attempted to address the question: "what is dissipation in a collisionless plasma?" We used the frame shifted (electron frame) dissipation parameter, D_e on two different simulations. We argue that D_e is only a good indicator of dissipation when it is positive, and the particles have gained energy from the electric field.

We showed that in the simulation with a guide field in the z direction, reconnection sites are associated with positive values of D_e only when they are reconnecting, as reconnection is the conversion of magnetic energy to plasma kinetic energy. Reconnection sites are also highlighted/isolated in positive values of $D_{e\parallel}$. D_e also highlights many other areas in the simulation where an electric field is at work. Comparing D_e and $D_{e\parallel}$ can help understand which direction the dissipation is occurring.

We showed for another simulation that has an in-plane guide field, that reconnection sites are also regions of dissipation. The D_e parameter also revealed many parallel propagating electrostatic waves in the box. Analysis of one of these waves indicates that it was generated by an electron-electron beam instability. These waves were not seen in the simulation discussed earlier in Chapter 4 as that simulation, on average did not support waves in the parallel direction. It did, however, produce large parallel electron temperature anisotropies, especially around reconnection sites. Combining the results from these two simulations, we can infer that the reconnection anisotropies (Chapter 4) would produce similar electron beam-beam instabilities, and produce an electrostatic wave, which will travel parallel to the magnetic field. This beam will then be damped as it reaches plasma with properties that no longer support it. So waves will act as a method of moving energy

around in space as well as reducing the temperature anisotropy introduced by the reconnection sites.

We then discussed dissipation needs to be an irreversible process, even in the absence of collisions. In order to provide this non reversibility we introduced the concept of mixing. This concept breaks the natural assumption of classical thermodynamics, where the system is comprised only of macroscopic physical objects. At kinetic scales, it is the microscopic states of the system, (waves, particles) described by VDFs that define the plasma behaviour.

We then suggested there are four distinct stages to dissipation at electrons scales: 1) Acceleration: Via localised kinetic scale electric fields (e.g. reconnection or another localised phenomena) forms a bump/beam in the local VDF. These accelerated electrons then travel and mix with other groups of electrons into areas where their combined presence can cause an instability. 2) Wave generation: The particle kinetic energy is converted to the wave electromagnetic (or electric) field. 3) Wave propagation: The generated wave will travel in space, the direction and distance will be determined by the local magnetic field and the plasma properties, which all vary within turbulence. 4) Damping. The wave will be damped when it reaches an area with a VDF, or plasma properties that no longer support it. Energy from the wave will be given back to local particles, which raises local average kinetic energy.

The addition of mixing, and the interaction between an ensemble of waves in the system adds a degree of randomisation, and therefore irreversibility, especially when we consider that turbulence is inherently associated with stochastic properties of the plasma. Here we have only focussed on electron dynamics, and this is only a simplified description of what is naturally an extremely complex process, with larger scale structures being dominated by ion dynamics.

Extending the simulation domain to cover both ion and electron scales would be a challenging and next logical step in our research into dissipation mechanisms. We would also like to introduce additional energy budget analysis, both globally, and locally, in order to quantify dissipation within collisionless plasma turbulence.

Appendix A.

Parsek2D description

We use the implicit particle-in-cell (PIC) code Parsek2D. The implicit method allows larger time steps and box sizes compared with other explicit PIC methods. A full description of the solver is provided in Markidis et al. [2009], and Camporeale [2008] however a brief summary is presented below.

Parsek2D solves Maxwell's second order equation for the electric field:

$$\nabla^2 \mathbf{E} - \frac{1}{c^2}\frac{\partial^2 \mathbf{E}}{\partial t^2} = \frac{4\pi}{c^2}\frac{\partial \mathbf{J}}{\partial t} + 4\pi\nabla\rho. \tag{A.1}$$

This is converted into a discrete equation for the new electric field, $\mathbf{E^{i+1}}$, expressed only as a function of old variables (see Camporeale [2008]), using the implicit moment method for time advance of the electromagnetic fields. This new equation can be expressed in the following matrix form:

$$Ax = b, \tag{A.2}$$

where b is a 1D array of known source terms, which originate from the position and velocity of the particles, such as ρ_q and $\mathbf{J}$. x is a 1-D matrix representing the unknown 2D electric field, $\mathbf{E^{i+1}}$ at the new timestep, and A is a 2-D matrix, or image, representing the required relationships between knowns and unknowns. This is then solved for x using the generalised Minimal residual solver (GMRes). This is an iterative solver that reduces the error of an initial guess for x at every iteration.

Once the new electric field, $\mathbf{E^{i+1}}$, has been calculated, the new magnetic field can be calculated using $\frac{\partial \mathbf{B}}{\partial t} = -c\nabla \times \mathbf{E}$, expressed discretely as:

$$\mathbf{B^{i+1}} = \mathbf{B^{i}} - c\Delta t(\nabla \times \mathbf{E^{i+1}}). \tag{A.3}$$

A predictor-corrector method is used for the particle mover. This uses the equation of motion for a particle:

$$\frac{d\mathbf{x}}{dt} = \mathbf{v}, \tag{A.4}$$

$$\frac{d\mathbf{v}}{dt} = \frac{q}{m}\left(\mathbf{E} + \frac{\mathbf{v}}{c} \times \mathbf{B}\right). \tag{A.5}$$

These equations can be expressed in discrete form as:

$$\mathbf{x}^{i+1} = \mathbf{x^i} + \mathbf{v^{i+1/2}}\Delta t, \tag{A.6}$$

$$\tilde{\mathbf{v}} = \mathbf{v^i} + \frac{q\Delta t}{2m}\mathbf{E^{i+1}}, \tag{A.7}$$

$$\mathbf{v^{i+1/2}} = \frac{\tilde{\mathbf{v}} + \frac{q\Delta t}{2mc}\left(\tilde{\mathbf{v}} \times \mathbf{B^{i+1}} + \frac{q\Delta t}{2mc}\left(\tilde{\mathbf{v}}.\mathbf{B^{i+1}}\right)\mathbf{B^{i+1}}\right)}{\left(1 + \frac{q^2\Delta t^2}{4m^2c^2}B^{i+1^2}\right)}. \tag{A.8}$$

The updated particle position, (Eq. A.6) is solved iteratively, using an initial guess for the new position. This new position is used to calculate the field at that point, and $\mathbf{v^{i+1/2}}$ (using Eqs. A.8 and A.7). Eq. A.6 is again used to calculate an updated position. This process is repeated until there is convergence between the guess and the recalculated position.

Appendix B.

Normalisation description

Parsek2D uses the Gaussian CGS system of units: centimetres (cm), grams (g) and seconds (s). Charge is in Franklin (Fr), force is in Dynes (dyn) and the magnetic field is in Gauss (G). The unit of charge is redefined in CGS such that two unit charges, 1 cm apart exert a force on each other of 1 dyn using $F = \frac{q_1 q_2}{r^2}$ (removing the factor of $4\pi\epsilon_0$ in SI units). Therefore charge, q, has dimensional units of $q = \mathrm{g}^{1/2}\ \mathrm{cm}^{3/2}\ \mathrm{s}^{-1}$. Additionally this means that the magnetic field, $\mathbf{B}$, and electric field, $\mathbf{E}$, have the same dimensional units, $\mathrm{g}^{1/2}\ \mathrm{cm}^{-1/2}\ \mathrm{s}^{-1}$.

A Matlab script is used to help the user calculate the appropriate simulation parameters for input into Parsek2D, and to provide normalisation. The following variables must be chosen by the user: ion and electron temperature (eV), electron/ion number density (cm^{-3}), magnetic field (G), simulation size, L (cm), number of cells (to determine grid spacing, Δx), and also the proton to electron mass ratio, m_i/m_e. Once these values have been selected, the ion mass is set using $m_i = m_e \times m_i/m_e$. A range of plasma frequency parameters are then calculated, such as the electron and ion cyclotron frequencies, Ω_{ce}, and Ω_{ci}, electron and ion plasma frequency, ω_{pe} and ω_{pi}. The electron and ion thermal velocities (v_{the} and v_{thi}) are calculated from the input temperatures (and mass ratios), followed by the thermal larmor radii for each species. The Debye length, λ_D, and Alfvén velocity, V_A are also calculated.

This wide range of plasma parameters can then be used to select normalised units. Appropriate values are chosen to normalise time (N_{time}), velocity ($N_{velocity}$) and charge to mass ratio (N_{qom}). Units are then normalised by dividing the CGS unit by its corresponding normalisation value. Normalisation values for other units

can all be calculated from these three selected values, using the relations:

$$N_{space} = N_{time} \times N_{velocity}, \tag{B.1}$$

$$N_B = N_{space}^{-1} \times (N_{velocity}^2 / N_{qom}), \tag{B.2}$$

$$N_{\rho_q} = N_B / N_{space}. \tag{B.3}$$

where N_{space} is the length normalisation value, N_B is the magnetic field normalisation value, and N_{ρ_q} is the charge density normalisation value. Equations B.1 to B.3 provide the dimensional relationships between units in the Gaussian CGS system.

In addition the user is required to take into account several parameter constraints that can affect the numerical stability of the code. The first is $v_{the} \times \Delta t / \Delta x > 0.1$. Where Δx is grid size, and Δt is the simulation timestep. If this condition is not met it can produce finite grid instability. The second condition is $v_{the} \times \Delta t / \Delta x < 1$, which ensures that the majority of the electrons do not move more than 1 cell in a single timestep. The user must adjust Δt, and Δx in order to ensure these stability criteria are met.

Appendix C.

Field line calculation in 2-D

Magnetic field lines pictorially depict the direction and strength of a magnetic field located in a plane. Field lines that are closer together indicate stronger magnetic field strength, **B**. Magnetic field lines in the x-y plane can be plotted as contours of the z component of the magnetic vector potential, **A**. This is due to the relationship between B and A:

$$\mathbf{B} = \nabla \times \mathbf{A}. \tag{C.1}$$

The Parsek2D code, however, does not use vector potential in its internal solver, so the variable A_z is not available. In order to plot field lines, the magnetic field must be integrated, to calculate A_z. The curl of **A** is,

$$\mathbf{B} = \nabla \times \mathbf{A} = \left(\frac{\partial A_z}{\partial y} - \frac{\partial A_y}{\partial z}\right)\hat{\mathbf{i}} + \left(\frac{\partial A_x}{\partial z} - \frac{\partial A_z}{\partial x}\right)\hat{\mathbf{j}} + \left(\frac{\partial A_y}{\partial x} - \frac{\partial A_x}{\partial y}\right)\hat{\mathbf{k}}. \tag{C.2}$$

In the 2D geometry, differentials in the z direction are zero giving:

$$\mathbf{B} = \nabla \times \mathbf{A} = \left(\frac{\partial A_z}{\partial y}\right)\hat{\mathbf{i}} + \left(-\frac{\partial A_z}{\partial x}\right)\hat{\mathbf{j}} + \left(\frac{\partial A_y}{\partial x} - \frac{\partial A_x}{\partial y}\right)\hat{\mathbf{k}}. \tag{C.3}$$

Comparing $\hat{\mathbf{i}}$ and $\hat{\mathbf{j}}$ components then gives,

$$\frac{\partial A_z}{\partial y} = B_x, \tag{C.4}$$

$$\frac{\partial A_z}{\partial x} = -B_y. \tag{C.5}$$

We therefore use B_x and B_y as the gradients of A_z in the corresponding direction. The analysis code initialises A_z to zero in a corner, and calculates A_z in a nested loop, adding $-B_y\Delta x$ to A_z for each step in the x direction and $B_x\Delta y$ to A_z for each step in the y direction (where Δx and Δy are the simulation grid sizes). Magnetic

field values from cell edges are used as appropriate. This correctly reconstructs the geometry of A_z in 2-D space. Contours of equally spaced values of A_z allows field lines to be visualized, with the addition of arrows to depict the in-plane field direction.

In order to follow the same field line between simulation cycles $\frac{\partial A_z}{\partial t}$ is also required. This time derivative can be calculated from the general equation for any electric field, **E**:

$$\mathbf{E} = -\nabla V - \frac{\partial \mathbf{A}}{\partial t}, \tag{C.6}$$

where V is the electrostatic potential. Given the 2D geometry, z is an ignorable coordinate, it follows that the z component of Eq. C.6 is:

$$E_z = -\frac{\partial A_z}{\partial t}. \tag{C.7}$$

Eq. C.7, shows that a local value of E_z can be used to calculate the time derivative of A_z. Therefore, before the spatial integration is performed at a new timestep, the initial value of A_z is adjusted by $-E_z \Delta t$, where Δt is the simulation timestep. Additionally Eq. C.7 also shows that the rate of in-plane reconnection is equal to the out of plane electric field E_z at the centre of a reconnection site.

References

O. Alexandrova, V. Carbone, P. Veltri, and L. Sorriso-Valvo. Small-scale energy cascade of the solar wind turbulence. *The Astrophysical Journal*, 674(2):1153, 2008. URL http://stacks.iop.org/0004-637X/674/i=2/a=1153.

O. Alexandrova, J. Saur, C. Lacombe, A. Mangeney, J. Mitchell, S. J. Schwartz, and P. Robert. Universality of Solar-Wind Turbulent Spectrum from MHD to Electron Scales. *Physical Review Letters*, 103(16):165003, October 2009. doi: 10.1103/PhysRevLett.103.165003.

O. Alexandrova, C. Lacombe, A. Mangeney, R. Grappin, and M. Maksimovic. Solar wind turbulent spectrum at plasma kinetic scales. *The Astrophysical Journal*, 760 (2):121, 2012. URL http://stacks.iop.org/0004-637X/760/i=2/a=121.

S. D. Bale, P. J. Kellogg, F. S. Mozer, T. S. Horbury, and H. Reme. Measurement of the electric fluctuation spectrum of magnetohydrodynamic turbulence. *Phys. Rev. Lett.*, 94:215002, Jun 2005. doi: 10.1103/PhysRevLett.94.215002. URL http://link.aps.org/doi/10.1103/PhysRevLett.94.215002.

M. A. Balikhin, D. G. Sibeck, A. Runov, and S. N. Walker. Magnetic holes in the vicinity of dipolarization fronts: Mirror or tearing structures? *Journal of Geophysical Research: Space Physics*, 117(A8):n/a–n/a, 2012. ISSN 2156-2202. doi: 10.1029/2012JA017552. URL http://dx.doi.org/10.1029/2012JA017552.

Klaus Baumgärtel. Soliton approach to magnetic holes. *Journal of Geophysical Research: Space Physics*, 104(A12):28295–28308, 1999. ISSN 2156-2202. doi: 10.1029/1999JA900393. URL http://dx.doi.org/10.1029/1999JA900393.

H. J. Beinroth and F. M. Neubauer. Properties of whistler mode waves between 0.3 and 1.0 au from helios observations. *Journal of Geophysical Research: Space Physics*, 86(A9):7755–7760, 1981. ISSN 2156-2202. doi: 10.1029/JA086iA09p07755. URL http://dx.doi.org/10.1029/JA086iA09p07755.

Paul M. Bellan. *Fundamentals of Plasma Physics*. Cambridge University Press, 2006.

J. Birn, J. F. Drake, M. A. Shay, B. N. Rogers, R. E. Denton, M. Hesse, M. Kuznetsova, Z. W. Ma, A. Bhattacharjee, A. Otto, and P. L. Pritchett. Geospace environmental modeling (gem) magnetic reconnection challenge. *Journal of Geophysical Research: Space Physics*, 106(A3):3715–3719, 2001. ISSN 2156-2202. doi: 10.1029/1999JA900449. URL http://dx.doi.org/10.1029/1999JA900449.

D. Biskamp. Magnetic reconnection via current sheets. *Physics of Fluids (1958-1988)*, 29(5):1520–1531, 1986. doi: http://dx.doi.org/10.1063/1.865670. URL http://scitation.aip.org/content/aip/journal/pof1/29/5/10.1063/1.865670.

Stanislav Boldyrev. Spectrum of magnetohydrodynamic turbulence. *Phys. Rev. Lett.*, 96:115002, Mar 2006. doi: 10.1103/PhysRevLett.96.115002. URL http://link.aps.org/doi/10.1103/PhysRevLett.96.115002.

Stanislav Boldyrev and Jean Carlos Perez. Spectrum of kinetic-alfvén turbulence. *The Astrophysical Journal Letters*, 758(2):L44, 2012. URL http://stacks.iop.org/2041-8205/758/i=2/a=L44.

Stanislav Boldyrev, Jean Carlos Perez, Joseph E. Borovsky, and John J. Podesta. Spectral scaling laws in magnetohydrodynamic turbulence simulations and in the solar wind. *The Astrophysical Journal Letters*, 741(1):L19, 2011. URL http://stacks.iop.org/2041-8205/741/i=1/a=L19.

Joseph E. Borovsky. Flux tube texture of the solar wind: Strands of the magnetic carpet at 1 au? *Journal of Geophysical Research: Space Physics*, 113(A8):n/a–n/a, 2008. ISSN 2156-2202. doi: 10.1029/2007JA012684. URL http://dx.doi.org/10.1029/2007JA012684.

S. Bourouaine, O. Alexandrova, E. Marsch, and M. Maksimovic. On spectral breaks in the power spectra of magnetic fluctuations in fast solar wind between 0.3and0.9au. *The Astrophysical Journal*, 749(2):102, 2012. URL http://stacks.iop.org/0004-637X/749/i=2/a=102.

R. Bruno, V. Carbone, P. Veltri, E. Pietropaolo, and B. Bavassano. Identifying intermittency events in the solar wind. *Planetary and Space Science*, 49(12):1201 – 1210, 2001. ISSN 0032-0633. doi: http://dx.doi.org/10.1016/S0032-0633(01)00061-7. URL http://www.sciencedirect.com/science/article/pii/S0032063301000617. ¡ce:title¿Nonlinear Dynamics and Fraactals in Space¡/ce:title¿.

Roberto Bruno and Vincenzo Carbone. The solar wind as a turbulence laboratory. *Living Reviews in Solar Physics*, 10(2), 2013. doi: 10.12942/lrsp-2013-2. URL http://www.livingreviews.org/lrsp-2013-2.

L. F. Burlaga and J. F. Lemaire. Interplanetary magnetic holes: Theory. *Journal of Geophysical Research: Space Physics*, 83(A11):5157–5160, 1978. ISSN 2156-2202. doi: 10.1029/JA083iA11p05157. URL http://dx.doi.org/10.1029/JA083iA11p05157.

L. F. Burlaga, N. F. Ness, and M. H. Acuna. Trains of magnetic holes and magnetic humps in the heliosheath. *Geophysical Research Letters*, 33(21):n/a–n/a, 2006. ISSN 1944-8007. doi: 10.1029/2006GL027276. URL http://dx.doi.org/10.1029/2006GL027276.

E. Camporeale and D. Burgess. The Dissipation of Solar Wind Turbulent Fluctuations at Electron Scales. *Astrophys. J.*, 730:114, April 2011. doi: 10.1088/0004-637X/730/2/114.

Enrico Camporeale. *Kinetic aspects of Solar Wind turbulence*. PhD thesis, Queen Mary University London, 2008.

Enrico Camporeale and David Burgess. Electron firehose instability: Kinetic linear theory and two-dimensional particle-in-cell simulations. *Journal of Geophysical Research: Space Physics*, 113(A7):n/a–n/a, 2008. ISSN 2156-2202. doi: 10.1029/2008JA013043. URL http://dx.doi.org/10.1029/2008JA013043.

P. A. Cassak and M. A. Shay. Scaling of asymmetric magnetic reconnection: General theory and collisional simulations. *Physics of Plasmas (1994-present)*, 14(10): 102114, 2007. URL http://dx.doi.org/10.1063/1.2795630.

M. B. Bavassano Cattaneo, C. Basile, G. Moreno, and J. D. Richardson. Evolution of mirror structures in the magnetosheath of saturn from the bow shock to the magnetopause. *Journal of Geophysical Research: Space Physics*, 103(A6):11961–11972, 1998. ISSN 2156-2202. doi: 10.1029/97JA03683. URL http://dx.doi.org/10.1029/97JA03683.

Benjamin D. G. Chandran. Perpendicular ion heating by low-frequency alfven-wave turbulence in the corona and solar wind, 2011. URL http://solarorbiter4.org/assets/docs/oralpresentations/Chandran_session2_032811.pdf. URL accessed: 04-07-2014.

Benjamin D. G. Chandran and Joseph V. Hollweg. Alfvén wave reflection and turbulent heating in the solar wind from 1 solar radius to 1au: An analytical treatment. *The Astrophysical Journal*, 707(2):1659, 2009. URL http://stacks.iop.org/0004-637X/707/i=2/a=1659.

O. Chang, S. Peter Gary, and J. Wang. Whistler turbulence forward cascade: Three-dimensional particle-in-cell simulations. *Geophys. Res. Lett.*, 38:L22102, November 2011. doi: 10.1029/2011GL049827.

C. H. K. Chen, T. S. Horbury, A. A. Schekochihin, R. T. Wicks, O. Alexandrova, and J. Mitchell. Anisotropy of solar wind turbulence between ion and electron scales. *Phys. Rev. Lett.*, 104:255002, Jun 2010. doi: 10.1103/PhysRevLett.104.255002. URL http://link.aps.org/doi/10.1103/PhysRevLett.104.255002.

C. H. K. Chen, A. Mallet, A. A. Schekochihin, T. S. Horbury, R. T. Wicks, and S. D. Bale. Three-dimensional structure of solar wind turbulence. *The Astrophysical Journal*, 758(2):120, 2012. URL http://stacks.iop.org/0004-637X/758/i=2/a=120.

C. H. K. Chen, S. Boldyrev, Q. Xia, and J. C. Perez. Nature of Subproton Scale Turbulence in the Solar Wind. *Physical Review Letters*, 110(22):225002, May 2013. doi: 10.1103/PhysRevLett.110.225002.

P. J. Coleman, Jr. Turbulence, Viscosity, and Dissipation in the Solar-Wind Plasma. *Astrophys. J.*, 153:371, August 1968. doi: 10.1086/149674.

S. Dasso, L. J. Milano, W. H. Matthaeus, and C. W. Smith. Anisotropy in fast and slow solar wind fluctuations. *The Astrophysical Journal Letters*, 635(2):L181, 2005. URL http://stacks.iop.org/1538-4357/635/i=2/a=L181.

J. Drake and M. Shay. Fundamentals of collisionless reconnection. In J. Birn and E. Priest, editors, *Reconnection of Magnetic Fields*. Cambridge Press, 2007.

J. P. Eastwood, M. A. Shay, T. D. Phan, and M. Øieroset. Asymmetry of the ion diffusion region hall electric and magnetic fields during guide field reconnection: Observations and comparison with simulations. *Physical Review Letters*, 104(20), June 2010. doi: 10.1103/PhysRevLett.104.205001. URL http://link.aps.org/doi/10.1103/PhysRevLett.104.205001.

R. W. Ebert, D. J. McComas, H. A. Elliott, R. J. Forsyth, and J. T. Gosling. Bulk properties of the slow and fast solar wind and interplanetary coronal mass ejections measured by ulysses: Three polar orbits of observations. *Journal of Geophysical Research: Space Physics*, 114(A1):n/a–n/a, 2009. ISSN 2156-2202. doi: 10.1029/2008JA013631. URL http://dx.doi.org/10.1029/2008JA013631.

J. Egedal, W. Daughton, and Le A. Large-scale electron acceleration by parallel electric fields during magnetic reconnection. *Nature Physics*, 8(4):321–324, March 2012. doi: 10.1038/nphys2249. URL http://www.nature.com/doifinder/10.1038/nphys2249.

T. G. Forbes. The nature of Petschek-type reconnection. *Earth, Planets, and Space*, 53:423–429, June 2001.

M. Franz, D. Burgess, and T. S. Horbury. Magnetic field depressions in the solar wind. *Journal of Geophysical Research: Space Physics*, 105(A6):12725–12732, 2000. ISSN 2156-2202. doi: 10.1029/2000JA900026. URL http://dx.doi.org/10.1029/2000JA900026.

S. P. Gary, O. Chang, and J. Wang. Forward Cascade of Whistler Turbulence: Three-dimensional Particle-in-cell Simulations. *The Astrophysical Journal*, 755: 142, August 2012. doi: 10.1088/0004-637X/755/2/142.

S. Peter. Gary. *Theory of Space Plasma Microinstabilities*. Cambridge University Press, 1993. URL http://dx.doi.org/10.1017/CBO9780511551512.

S. Peter Gary, Shinji Saito, and Hui Li. Cascade of whistler turbulence: Particle-in-cell simulations. *Geophysical Research Letters*, 35(2):n/a–n/a, 2008. ISSN 1944-8007. doi: 10.1029/2007GL032327. URL http://dx.doi.org/10.1029/2007GL032327.

Y. S. Ge, J. P. McFadden, J. Raeder, V. Angelopoulos, D. Larson, and O. D. Constantinescu. Case studies of mirror-mode structures observed by themis in

the near-earth tail during substorms. *Journal of Geophysical Research: Space Physics*, 116(A1):n/a–n/a, 2011. ISSN 2156-2202. doi: 10.1029/2010JA015546. URL http://dx.doi.org/10.1029/2010JA015546.

V. Génot, E. Budnik, P. Hellinger, T. Passot, G. Belmont, P. M. Trávníček, P.-L. Sulem, E. Lucek, and I. Dandouras. Mirror structures above and below the linear instability threshold: Cluster observations, fluid model and hybrid simulations. *Annales Geophysicae*, 27(2):601–615, 2009. doi: 10.5194/angeo-27-601-2009. URL http://www.ann-geophys.net/27/601/2009/.

P. Goldreich and S. Sridhar. Toward a theory of interstellar turbulence. 2: Strong alfvenic turbulence. *The Astrophysical Journal*, 438:763–775, January 1995. doi: 10.1086/175121.

J. T. Gosling and A. Szabo. Bifurcated current sheets produced by magnetic reconnection in the solar wind. *J. Geophys. Res.*, 113(A12):A10103, October 2008. doi: 10.1029/2008JA013473.

J.T. Gosling and V.J. Pizzo. Formation and evolution of corotating interaction regions and their three dimensional structure. *Space Science Reviews*, 89(1-2): 21–52, 1999. ISSN 0038-6308. doi: 10.1023/A:1005291711900. URL http://dx.doi.org/10.1023/A%3A1005291711900.

A. Greco, W. H. Matthaeus, S. Servidio, P. Chuychai, and P. Dmitruk. Statistical analysis of discontinuities in solar wind ace data and comparison with intermittent mhd turbulence. *The Astrophysical Journal Letters*, 691(2):L111, 2009. URL http://stacks.iop.org/1538-4357/691/i=2/a=L111.

C. T. Haynes, D. Burgess, and E. Camporeale. Reconnection and electron temperature anisotropy in sub-proton scale plasma turbulence. *The Astrophysical Journal*, 783(1):38, 2014. URL http://stacks.iop.org/0004-637X/783/i=1/a=38.

Petr Hellinger, Pavel Trávníček, Justin C. Kasper, and Alan J. Lazarus. Solar wind proton temperature anisotropy: Linear theory and wind/swe observations. *Geophysical Research Letters*, 33(9):n/a–n/a, 2006. ISSN 1944-8007. doi: 10.1029/2006GL025925. URL http://dx.doi.org/10.1029/2006GL025925.

Michael Hesse, Thomas Neukirch, Karl Schindler, Masha Kuznetsova, and Seiji Zenitani. The diffusion region in collisionless magnetic reconnection. *Space Science Reviews*, 160(1-4):3–23, 2011. ISSN 0038-6308. doi: 10.1007/s11214-010-9740-1. URL http://dx.doi.org/10.1007/s11214-010-9740-1.

T S Horbury, M A Forman, and S Oughton. Spacecraft observations of solar wind turbulence: an overview. *Plasma Physics and Controlled Fusion*, 47(12B):B703, 2005. URL http://stacks.iop.org/0741-3335/47/i=12B/a=S52.

T.S. Horbury, R.T. Wicks, and C.H.K. Chen. Anisotropy in space plasma turbulence: Solar wind observations. *Space Science Reviews*, 172(1-4):325–342, 2012.

ISSN 0038-6308. doi: 10.1007/s11214-011-9821-9. URL http://dx.doi.org/10.1007/s11214-011-9821-9.

Ya. N. Istomin, O. A. Pokhotelov, and M. A. Balikhin. Nonzero electron temperature effects in nonlinear mirror modes. *Physics of Plasmas (1994-present)*, 16(12):122901, 2009. doi: http://dx.doi.org/10.1063/1.3275787. URL http://scitation.aip.org/content/aip/journal/pop/16/12/10.1063/1.3275787.

H. Karimabadi, D. Krauss-Varban, N. Omidi, and H. X. Vu. Magnetic structure of the reconnection layer and core field generation in plasmoids. *Journal of Geophysical Research, Volume 104, Issue A6, p. 12313-12326*, 104:12313–12326, July 1999. doi: 10.1029/1999JA900089. URL http://adsabs.harvard.edu/abs/1999JGR...10412313K.

H. Karimabadi, J. D. Huba, D. Krauss, and N. Omidi. On the generation and structure of the quadrupole magnetic field in the reconnection process: Comparative simulation study. *Geophysical Research Letters*, 31(7), 2004. doi: 10.1029/2004GL019553. URL http://dx.doi.org/10.1029/2004GL019553.

H. Karimabadi, V. Roytershteyn, M. Wan, W. H. Matthaeus, W. Daughton, P. Wu, M. Shay, B. Loring, J. Borovsky, E. Leonardis, S. C. Chapman, and T. K. M. Nakamura. Coherent structures, intermittent turbulence, and dissipation in high-temperature plasmas. *Physics of Plasmas*, 20(1):012303, 2013. doi: 10.1063/1.4773205. URL http://link.aip.org/link/?PHP/20/012303/1.

K. H. Kiyani, S. C. Chapman, Y. V. Khotyaintsev, M. W. Dunlop, and F. Sahraoui. Global Scale-Invariant Dissipation in Collisionless Plasma Turbulence. *Physical Review Letters*, 103(7):075006, August 2009. doi: 10.1103/PhysRevLett.103.075006.

A. Kolmogorov. The Local Structure of Turbulence in Incompressible Viscous Fluid for Very Large Reynolds' Numbers. *Akademiia Nauk SSSR Doklady*, 30:301–305, 1941.

G. Kowal, A. Lazarian, E. T. Vishniac, and K. Otmianowska-Mazur. Reconnection studies under different types of turbulence driving. *Nonlinear Processes in Geophysics*, 19(2):297–314, 2012. doi: 10.5194/npg-19-297-2012. URL http://www.nonlin-processes-geophys.net/19/297/2012/.

G. Lapenta, S. Markidis, A. Divin, M. V. Goldman, and D. L. Newman. Bipolar electric field signatures of reconnection separatrices for a hydrogen plasma at realistic guide fields. *Geophysical Research Letters*, 38(17):n/a–n/a, 2011. ISSN 1944-8007. doi: 10.1029/2011GL048572. URL http://dx.doi.org/10.1029/2011GL048572.

A. Lazarian and Ethan T. Vishniac. Reconnection in a weakly stochastic field. *The Astrophysical Journal*, 517(2):700, 1999. URL http://stacks.iop.org/0004-637X/517/i=2/a=700.

A. Lazarian, Ethan T. Vishniac, and Jungyeon Cho. Magnetic field structure and stochastic reconnection in a partially ionized gas. *The Astrophysical Journal*, 603 (1):180, 2004. URL http://stacks.iop.org/0004-637X/603/i=1/a=180.

R. J. Leamon, C. W. Smith, N. F. Ness, W. H. Matthaeus, and H. K. Wong. Observational constraints on the dynamics of the interplanetary magnetic field dissipation range. *J. Geophys. Res.*, 103:4775, March 1998. doi: 10.1029/97JA03394.

D. Lengyel-Frey, R. A. Hess, R. J. MacDowall, R. G. Stone, N. Lin, A. Balogh, and R. Forsyth. Ulysses observations of whistler waves at interplanetary shocks and in the solar wind. *Journal of Geophysical Research: Space Physics*, 101(A12): 27555–27564, 1996. ISSN 2156-2202. doi: 10.1029/96JA00548. URL http://dx.doi.org/10.1029/96JA00548.

S. Markidis, E. Camporeale, D. Burgess, Rizwan-Uddin, and G. Lapenta. Parsek2D: An Implicit Parallel Particle-in-Cell Code. In N. V. Pogorelov, E. Audit, P. Colella, and G. P. Zank, editors, *Numerical Modeling of Space Plasma Flows: ASTRONUM-2008*, volume 406 of *Astronomical Society of the Pacific Conference Series*, page 237, April 2009.

Jason Maron and Peter Goldreich. Simulations of incompressible magnetohydrodynamic turbulence. *The Astrophysical Journal*, 554(2):1175, 2001. URL http://stacks.iop.org/0004-637X/554/i=2/a=1175.

E. Marsch. *Kinetic Physics of the Solar Wind Plasma*. Springer-Verlag, 1991.

E. Marsch, K.-H. Mühlhäuser, R. Schwenn, H. Rosenbauer, W. Pilipp, and F. M. Neubauer. Solar wind protons: Three-dimensional velocity distributions and derived plasma parameters measured between 0.3 and 1 au. *Journal of Geophysical Research: Space Physics*, 87(A1):52–72, 1982. ISSN 2156-2202. doi: 10.1029/JA087iA01p00052. URL http://dx.doi.org/10.1029/JA087iA01p00052.

E. Marsch, X.-Z. Ao, and C.-Y. Tu. On the temperature anisotropy of the core part of the proton velocity distribution function in the solar wind. *Journal of Geophysical Research: Space Physics*, 109(A4):n/a–n/a, 2004. ISSN 2156-2202. doi: 10.1029/2003JA010330. URL http://dx.doi.org/10.1029/2003JA010330.

Eckart Marsch. Kinetic physics of the solar corona and solar wind. *Living Reviews in Solar Physics*, 3(1), 2006. doi: 10.12942/lrsp-2006-1. URL http://www.livingreviews.org/lrsp-2006-1.

Lorenzo Matteini, Simone Landi, Petr Hellinger, Filippo Pantellini, Milan Maksimovic, Marco Velli, Bruce E. Goldstein, and Eckart Marsch. Evolution of the solar wind proton temperature anisotropy from 0.3 to 2.5 au. *Geophysical Research Letters*, 34(20):n/a–n/a, 2007. ISSN 1944-8007. doi: 10.1029/2007GL030920. URL http://dx.doi.org/10.1029/2007GL030920.

Lorenzo Matteini, Petr Hellinger, PavelM. Landi, Simone, and Marco Velli. Ion kinetics in the solar wind: Coupling global expansion to local microphysics.

Space Science Reviews, 172:373–396, 2012. ISSN 0038-6308. doi: 10.1007/s11214-011-9774-z. URL http://dx.doi.org/10.1007/s11214-011-9774-z.

William H. Matthaeus, Melvyn L. Goldstein, and D. Aaron Roberts. Evidence for the presence of quasi-two-dimensional nearly incompressible fluctuations in the solar wind. *Journal of Geophysical Research: Space Physics*, 95(A12):20673–20683, 1990. ISSN 2156-2202. doi: 10.1029/JA095iA12p20673. URL http://dx.doi.org/10.1029/JA095iA12p20673.

D. J. McComas, H. A. Elliott, N. A. Schwadron, J. T. Gosling, R. M. Skoug, and B. E. Goldstein. The three-dimensional solar wind around solar maximum. *Geophysical Research Letters*, 30(10):n/a–n/a, 2003. ISSN 1944-8007. doi: 10.1029/2003GL017136. URL http://dx.doi.org/10.1029/2003GL017136.

Yoshiharu Omura. One-dimensional electromagnetic particle code: Kempo1. In *Advanced methods for Space Simulations*, pages 1–21. TERRAPUB, 2007. ISBN 978-4-88704-138-7. URL http://www.terrapub.co.jp/e-library/amss/.

S. A. Orszag and C.-M. Tang. Small-scale structure of two-dimensional magnetohydrodynamic turbulence. *Journal of Fluid Mechanics*, 90:129–143, January 1979. doi: 10.1017/S002211207900210X.

K. T. Osman and T. S. Horbury. Multispacecraft measurement of anisotropic correlation functions in solar wind turbulence. *The Astrophysical Journal Letters*, 654 (1):L103, 2007. URL http://stacks.iop.org/1538-4357/654/i=1/a=L103.

K. T. Osman, W. H. Matthaeus, A. Greco, and S. Servidio. Evidence for Inhomogeneous Heating in the Solar Wind. *Astrophys. J. Lett.*, 727:L11, January 2011. doi: 10.1088/2041-8205/727/1/L11.

E. N. Parker. Dynamics of the Interplanetary Gas and Magnetic Fields. *Astrophys. J.*, 128:664, November 1958. doi: 10.1086/146579.

E. N. Parker. Comments on the reconnexion rate of magnetic fields. *Journal of Plasma Physics*, 9:49, February 1973. doi: 10.1017/S0022377800007327.

H. E. Petschek. Magnetic Field Annihilation. *NASA Special Publication*, 50:425, 1964.

T. D. Phan, M. A. Shay, J. T. Gosling, M. Fujimoto, J. F. Drake, G. Paschmann, M. Oieroset, J. P. Eastwood, and V. Angelopoulos. Electron bulk heating in magnetic reconnection at earth's magnetopause: Dependence on the inflow alfvén speed and magnetic shear. *Geophysical Research Letters*, pages n/a–n/a, 2013. ISSN 1944-8007. doi: 10.1002/grl.50917. URL http://dx.doi.org/10.1002/grl.50917.

J. J. Podesta, D. A. Roberts, and M. L. Goldstein. Spectral exponents of kinetic and magnetic energy spectra in solar wind turbulence. *The Astrophysical Journal*, 664(1):543, 2007. URL http://stacks.iop.org/0004-637X/664/i=1/a=543.

A. Retinò, D. Sundkvist, A. Vaivads, F. Mozer, M. André, and C. J. Owen. In situ evidence of magnetic reconnection in turbulent plasma. *Nature Phys.*, 3:236–238, April 2007. doi: 10.1038/nphys574.

Paolo Ricci, Giovanni Lapenta, and J. U. Brackbill. Gem reconnection challenge: Implicit kinetic simulations with the physical mass ratio. *Geophysical Research Letters*, 29(23):3–1–3–4, 2002. ISSN 1944-8007. doi: 10.1029/2002GL015314. URL http://dx.doi.org/10.1029/2002GL015314.

D. Aaron Roberts. Evolution of the spectrum of solar wind velocity fluctuations from 0.3 to 5 au. *Journal of Geophysical Research: Space Physics*, 115(A12):n/a–n/a, 2010. ISSN 2156-2202. doi: 10.1029/2009JA015120. URL http://dx.doi.org/10.1029/2009JA015120.

F. Sahraoui, M. L. Goldstein, P. Robert, and Y. V. Khotyaintsev. Evidence of a Cascade and Dissipation of Solar-Wind Turbulence at the Electron Gyroscale. *Physical Review Letters*, 102(23):231102, June 2009. doi: 10.1103/PhysRevLett.102.231102.

F. Sahraoui, S. Y. Huang, G. Belmont, M. L. Goldstein, A. Retinò, P. Robert, and J. De Patoul. Scaling of the electron dissipation range of solar wind turbulence. *The Astrophysical Journal*, 777(1):15, 2013. URL http://stacks.iop.org/0004-637X/777/i=1/a=15.

Manfred Scholer. Undriven magnetic reconnection in an isolated current sheet. *Journal of Geophysical Research: Space Physics*, 94(A7):8805–8812, 1989. ISSN 2156-2202. doi: 10.1029/JA094iA07p08805. URL http://dx.doi.org/10.1029/JA094iA07p08805.

S. Servidio, W. H. Matthaeus, M. A. Shay, P. Dmitruk, P. A. Cassak, and M. Wan. Statistics of magnetic reconnection in two-dimensional magnetohydrodynamic turbulence. *Physics of Plasmas*, 17(3):032315, March 2010. doi: 10.1063/1.3368798.

S. Servidio, F. Valentini, F. Califano, and P. Veltri. Local kinetic effects in two-dimensional plasma turbulence. *Phys. Rev. Lett.*, 108:045001, Jan 2012. doi: 10.1103/PhysRevLett.108.045001. URL http://link.aps.org/doi/10.1103/PhysRevLett.108.045001.

S. Servidio, W. H. Matthaeus, M. A. Shay, P. A. Cassak, and P. Dmitruk. Magnetic Reconnection in Two-Dimensional Magnetohydrodynamic Turbulence. *Phys. Rev. Lett.*, 102(11), MAR 20 2009. ISSN 0031-9007. doi: {10.1103/PhysRevLett.102.115003}.

M. A. Shay and J. F. Drake. The role of electron dissipation on the rate of collisionless magnetic reconnection. *Geophysical Research Letters*, 25(20):3759–3762, 1998. ISSN 1944-8007. doi: 10.1029/1998GL900036. URL http://dx.doi.org/10.1029/1998GL900036.

M. A. Shay, J. F. Drake, and M. Swisdak. Two-scale structure of the electron dissipation region during collisionless magnetic reconnection. *Phys. Rev. Lett.*, 99:155002, Oct 2007. doi: 10.1103/PhysRevLett.99.155002. URL http://link.aps.org/doi/10.1103/PhysRevLett.99.155002.

Kazunari Shibata and Tetsuya Magara. Solar flares: Magnetohydrodynamic processes. *Living Reviews in Solar Physics*, 8(6), 2011. doi: 10.12942/lrsp-2011-6. URL http://www.livingreviews.org/lrsp-2011-6.

C. W. Smith, K. Hamilton, B. J. Vasquez, and R. J. Leamon. Dependence of the Dissipation Range Spectrum of Interplanetary Magnetic Fluctuationson the Rate of Energy Cascade. *Astrophys. J. Lett.*, 645:L85–L88, July 2006. doi: 10.1086/506151.

BUO Sonnerup. Solar system plasma physics. *Vol. Ill,(LT Lanzerotti, CF Kennel, and EN Parker, eds.), North Holland*, page 45, 1979.

Luca Sorriso-Valvo, Vincenzo Carbone, Pierluigi Veltri, Giuseppe Consolini, and Roberto Bruno. Intermittency in the solar wind turbulence through probability distribution functions of fluctuations. *Geophysical Research Letters*, 26(13):1801–1804, 1999. ISSN 1944-8007. doi: 10.1029/1999GL900270. URL http://dx.doi.org/10.1029/1999GL900270.

Olaf Stawicki, S. Peter Gary, and Hui Li. Solar wind magnetic fluctuation spectra: Dispersion versus damping. *Journal of Geophysical Research: Space Physics*, 106(A5):8273–8281, 2001. ISSN 2156-2202. doi: 10.1029/2000JA000446. URL http://dx.doi.org/10.1029/2000JA000446.

W. J. Sun, Q. Q. Shi, S. Y. Fu, Z. Y. Pu, M. W. Dunlop, A. P. Walsh, Q. G. Zong, T. Xiao, C. L. Tang, H. Reme, C. Carr, E. Lucek, and A. Fazakerley. Cluster and tc-1 observation of magnetic holes in the plasma sheet. *Annales Geophysicae*, 30(3):583–595, 2012. doi: 10.5194/angeo-30-583-2012. URL http://www.ann-geophys.net/30/583/2012/.

Torbjorn Sundberg. Private communication (email), 2014.

David Sundkvist, Alessandro Retinò, Andris Vaivads, and Stuart D. Bale. Dissipation in turbulent plasma due to reconnection in thin current sheets. *Phys. Rev. Lett.*, 99:025004, Jul 2007. doi: 10.1103/PhysRevLett.99.025004. URL http://link.aps.org/doi/10.1103/PhysRevLett.99.025004.

G. I. Taylor. The Spectrum of Turbulence. *Royal Society of London Proceedings Series A*, 164:476–490, February 1938. doi: 10.1098/rspa.1938.0032.

Toshio Terasawa. Hall current effect on tearing mode instability. *Geophysical Research Letters*, 10(6):475–478, 1983. ISSN 1944-8007. doi: 10.1029/GL010i006p00475. URL http://dx.doi.org/10.1029/GL010i006p00475.

Bruce T. Tsurutani, Gurbax S. Lakhina, Olga P. Verkhoglyadova, Ezequiel Echer, Fernando L. Guarnieri, Yasuhito Narita, and Dragos O. Constantinescu. Magnetosheath and heliosheath mirror mode structures, interplanetary magnetic decreases, and linear magnetic decreases: Differences and distinguishing features. *Journal of Geophysical Research: Space Physics*, 116(A2):n/a–n/a, 2011. ISSN 2156-2202. doi: 10.1029/2010JA015913. URL http://dx.doi.org/10.1029/2010JA015913.

J. M. Turner, L. F. Burlaga, N. F. Ness, and J. F. Lemaire. Magnetic holes in the solar wind. *Journal of Geophysical Research*, 82(13):1921–1924, 1977. ISSN 2156-2202. doi: 10.1029/JA082i013p01921. URL http://dx.doi.org/10.1029/JA082i013p01921.

M. Ugai. Computer studies on development of the fast reconnection mechanism for different resistivity models. *Physics of Fluids B: Plasma Physics (1989-1993)*, 4(9):2953–2963, 1992. doi: http://dx.doi.org/10.1063/1.860458. URL http://scitation.aip.org/content/aip/journal/pofb/4/9/10.1063/1.860458.

M. Ugai and T. Tsuda. Magnetic field-line reconnexion by localized enhancement of resistivity. I - Evolution in a compressible MHD fluid. *Journal of Plasma Physics*, 17:337–356, June 1977. doi: 10.1017/S0022377800020663.

D. A. Uzdensky and R. M. Kulsrud. Two-dimensional numerical simulation of the resistive reconnection layer. *Physics of Plasmas (1994-present)*, 7(10):4018–4030, 2000. doi: http://dx.doi.org/10.1063/1.1308081. URL http://scitation.aip.org/content/aip/journal/pop/7/10/10.1063/1.1308081.

Š. Štverák, P. Trávníček, M. Maksimovic, E. Marsch, A. N. Fazakerley, and E. E. Scime. Electron temperature anisotropy constraints in the solar wind. *Journal of Geophysical Research (Space Physics)*, 113:A03103, March 2008. doi: 10.1029/2007JA012733.

Štěpán Štverák, Milan Maksimovic, Pavel M. Trávníček, Eckart Marsch, Andrew N. Fazakerley, and Earl E. Scime. Radial evolution of nonthermal electron populations in the low-latitude solar wind: Helios, cluster, and ulysses observations. *Journal of Geophysical Research: Space Physics*, 114(A5):n/a–n/a, 2009. ISSN 2156-2202. doi: 10.1029/2008JA013883. URL http://dx.doi.org/10.1029/2008JA013883.

A. Verdini, M. Velli, and E. Buchlin. Turbulence in the sub-alfvénic solar wind driven by reflection of low-frequency alfvén waves. *The Astrophysical Journal Letters*, 700(1):L39, 2009. URL http://stacks.iop.org/1538-4357/700/i=1/a=L39.

M. Wan, W. H. Matthaeus, H. Karimabadi, V. Roytershteyn, M. Shay, P. Wu, W. Daughton, B. Loring, and S. C. Chapman. Intermittent dissipation at kinetic scales in collisionless plasma turbulence. *Physical Review Letters*, 109(19), December 2012. doi: 10.1103/PhysRevLett.109.195001. URL http://link.aps.org/doi/10.1103/PhysRevLett.109.195001.

Daniel Winterhalter, Marcia Neugebauer, Bruce E. Goldstein, Edward J. Smith, Samuel J. Bame, and André Balogh. Ulysses field and plasma observations of magnetic holes in the solar wind and their relation to mirror-mode structures. *Journal of Geophysical Research: Space Physics*, 99(A12):23371–23381, 1994. ISSN 2156-2202. doi: 10.1029/94JA01977. URL http://dx.doi.org/10.1029/94JA01977.

Masaaki Yamada, Russell Kulsrud, and Hantao Ji. Magnetic reconnection. *Rev. Mod. Phys.*, 82:603–664, Mar 2010. doi: 10.1103/RevModPhys.82.603. URL http://link.aps.org/doi/10.1103/RevModPhys.82.603.

M. Yan, L. C. Lee, and E. R. Priest. Fast magnetic reconnection with small shock angles. *Journal of Geophysical Research: Space Physics*, 97(A6):8277–8293, 1992. ISSN 2156-2202. doi: 10.1029/92JA00170. URL http://dx.doi.org/10.1029/92JA00170.

Seiji Zenitani, Michael Hesse, Alex Klimas, and Masha Kuznetsova. New measure of the dissipation region in collisionless magnetic reconnection. *Phys. Rev. Lett.*, 106: 195003, May 2011. doi: 10.1103/PhysRevLett.106.195003. URL http://link.aps.org/doi/10.1103/PhysRevLett.106.195003.

T. L. Zhang, W. Baumjohann, C. T. Russell, L. K. Jian, C. Wang, J. B. Cao, M. Balikhin, X. Blanco-Cano, M. Delva, and M. Volwerk. Mirror mode structures in the solar wind at 0.72 au. *Journal of Geophysical Research: Space Physics*, 114(A10):n/a–n/a, 2009. ISSN 2156-2202. doi: 10.1029/2009JA014103. URL http://dx.doi.org/10.1029/2009JA014103.